

DISSERTATION
SUBMITTED TO THE
COMBINED FACULTIES OF THE NATURAL SCIENCES AND
MATHEMATICS
FOR THE DEGREE OF
DOCTOR OF NATURAL SCIENCES

PUT FORWARD BY
MANUEL RIENER
BORN IN
STEYR, AUSTRIA

ORAL EXAMINATION: 10.07.2020

THE DETAILED VELOCITY STRUCTURE AND
DISTRIBUTION OF ^{13}CO EMISSION
IN THE GALACTIC PLANE

MANUEL RIENER

REFEREES:

APL. PROF. DR. HENRIK BEUTHER

APL. PROF. DR. CHRISTIAN FENDT

ABSTRACT

Studying the detailed velocity structure of molecular gas in our Galaxy is of fundamental importance for understanding structure formation in the interstellar medium. Knowledge about the detailed gas kinematics is moreover essential to map the distribution and dynamics of the molecular gas in the Milky Way.

In this thesis I use the method of spectral decomposition to analyse the ^{13}CO (1–0) observations of the Galactic Ring Survey (GRS). I developed the `GAUSSPY+` package, specifically designed for the fully automated decomposition of large Galactic plane surveys, to fit the ~ 2.3 million spectra of this large emission line data set. After extensive validation of the algorithm using synthetic spectra and a GRS test field, I use `GAUSSPY+` to fit the entire data set of the GRS, resulting in ~ 4.6 million Gaussian fit components.

These decomposition results provide a new way to analyse the dynamics of the molecular gas over a wide extent of the Galactic plane and study how its velocity structure looks like and varies at Galactic to sub-cloud scales. I find that the velocity dispersion of the gas is increased in the midplane and towards the inner Galaxy, and establish that the integrated emission of the velocity components correlates well with the complexity of the gas emission and the amount of dust emission along the line of sight. Moreover, I uncover qualitatively similar fluctuations in the centroid velocities of the gas components throughout the entire GRS data set, and demonstrate how the fitted linewidths enable the separation of blended gas emission features that originate from nearby regions and far distances.

Finally, I use a Bayesian approach to obtain the current best assessment of the Galactic distribution of ^{13}CO . As prior information, I use the presently most precise knowledge about the structure and kinematics of the Milky Way and an extensive compilation of distances from literature. I perform two different distance calculations that either include or exclude a prior for a model of Galactic features, which allows me to characterise possible biases of the distance estimates and establish more reliable limits on the ^{13}CO distribution. I establish that the majority (76% to 84%) of the ^{13}CO emission is associated with spiral arm features. However, I do not find significant differences between the gas emission properties associated with spiral arm and interarm features.

I conclude that the decomposition results provide a wealth of data enabling new and unexplored ways to interpret the detailed gas velocity structure of large Galactic plane surveys. The methodology and results presented in this thesis allowed for a homogeneous study of the dynamics and distribution of the molecular gas over a large fraction of the Galactic disk. As demonstrated in this work, the information extracted from the detailed gas kinematics and its combination with complementary tracers of the interstellar medium has enormous potential to further our knowledge about the physical processes and mechanisms shaping the interstellar medium.

ZUSAMMENFASSUNG

Um zu verstehen wie sich Strukturen im interstellaren Medium bilden ist es wichtig die detaillierte Geschwindigkeitsstruktur des molekularen Gases in unserer Galaxie zu untersuchen. Diese kinematische Analyse ermöglicht zudem Rückschlüsse über die Verteilung und Dynamik des molekularen Gases in der Milchstraße.

In dieser Dissertation verwende ich die Methode der spektralen Zerlegung, um ^{13}CO (1–0)-Emissionslinien des Galactic Ring Surveys (GRS) zu analysieren. Für die spektrale Zerlegung verwende ich den Algorithmus GAUSSPY+, den ich speziell für das automatisierte Fitten von Emissionslinien großer Beobachtungsdatensätze der galaktischen Ebene entwickelt habe. Nach umfangreicher Validierung des Algorithmus an synthetischen Spektren und einem GRS-Testfeld verwende ich GAUSSPY+ um die $\sim 2,3$ Millionen Spektren des GRS-Datensatzes mittels $\sim 4,6$ Millionen Gausskomponenten zu fitten.

Diese Ergebnisse ermöglichen neue Ansätze die Dynamik des molekularen Gases über einen weiten Bereich der galaktischen Ebene zu analysieren. So stelle ich fest, dass die Geschwindigkeitsdispersion des Gases in der galaktischen Ebene und zum galaktischen Zentrum hin zunimmt und die integrierte Emission der Geschwindigkeitskomponenten mit der Komplexität der Gasemission und der Menge der Staubemission entlang der Sichtlinie korreliert. Zudem kann ich demonstrieren, dass die mittleren Geschwindigkeiten der Gaskomponenten über den gesamten GRS-Datensatz qualitativ ähnliche Fluktuationen aufweisen, und die gefitteten Linienbreiten die Trennung miteinander verwobener Gaskomponenten ermöglichen, welche aus nahen und fernen Regionen stammen.

Ein probabilistischer Ansatz – welcher Kenntnisse über die Struktur und Kinematik der Milchstraße sowie eine umfangreiche Zusammenstellung von Distanzen aus der Literatur beinhaltet – ermöglicht es mir schließlich die bisher präziseste galaktische Verteilung des ^{13}CO -Gases zu erhalten. Die Distanzbestimmung mit und ohne Berücksichtigung eines Modells der galaktischen Struktur erlaubt es mir mögliche Problematiken der beiden Ansätze zu charakterisieren und die Verteilung des Gases verlässlicher einzugrenzen. Der Großteil der ^{13}CO -Emission (76% bis 84%) ist mit Spiralarmen assoziiert; die Eigenschaften der Gasemission in Spiralarmen und Interarm-Regionen zeigen jedoch keine signifikanten Unterschiede.

Zusammenfassend schließe ich, dass die hierin präsentierten Ergebnisse und Resultate neue und unerforschte Wege zur Interpretation der detaillierten Geschwindigkeitsstruktur des Gases großer Beobachtungsdatensätze der galaktischen Ebene ermöglichen. Die in dieser Dissertation vorgestellten Methodiken und Ergebnisse erlauben eine homogene Studie der Dynamik und Verteilung des molekularen Gases über einen weiten Bereich der galaktischen Scheibe. Diese Arbeit zeigt zudem, dass die detaillierten kinematischen Informationen des Gases in Kombination mit komplementären Beobachtungsdatensätzen enormes Potenzial aufweisen unser Wissen über die physikalischen Prozesse und Mechanismen des interstellaren Mediums zu bereichern.

Dedicated to all who ever looked up at the stars and wondered.

*We all travel the Milky Way together,
trees and men.*

— John Muir

FOREWORD

The study of the interstellar medium in the Milky Way is a rich field with a long history. Many brilliant minds have devoted their life and work to understanding how structures in the interstellar medium form and evolve. We have realised that the matter distributed in between the stars plays a fundamental role in the evolution of galaxies as it regulates the formation of stellar systems and the amount of their destructive feedback. We know that star formation—and with it the origin of planetary systems—is intimately coupled to the formation and evolution of structures in the interstellar medium. Physical processes in the interstellar medium are thus of immense importance in regulating the structure of entire galaxies down to the formation of individual stars and planets, which have ultimately led to the evolution of sentient human beings that can look up at the sky and try to understand this process. Studying the interstellar medium is therefore definitely a worthwhile endeavour.

It can be humbling to discover that many of the questions that have been discussed for decades still remain largely unanswered today. But it is also exhilarating to look back at the enormous progress that has been made over the years. Observational astrophysics is driven by new instrumentation and facilities, and there is an ever increasing push towards higher sensitivity and spatial resolution. As expected, more detailed observations and larger samples have brought more complexity and challenges for our simplified theories. It is however necessary to embrace this complexity and use different approaches and new analysis tools to discover hidden or obscured results in our observations.

Throughout the last decades we have accumulated a vast legacy of large archival data sets that are not yet fully explored and promise a rich untapped ground for new discoveries. Given the enormous complexity contained within these data sets, their analysis can sometimes seem overwhelming and it is often necessary to simplify the data, ideally while preserving its intricate details. The work presented herein goes in this direction. Throughout the main text I have included spectra from the original data set in the bottom part of the page. All results and conclusions of this work are based on the emission lines contained in these and many other spectra; it never ceases to astound me how much meaning we can infer from these observations.

I am immensely thankful for the opportunity of having been able to devote many years of my life to this incredibly interesting scientific journey. I hope my analysis tools and results can be of use to other researchers and my work is a helpful contribution to our understanding of the interstellar medium.

April 6, Manuel Riener

CONTENTS

List of Figures	xv
List of Tables	xix
1 INTRODUCTION	1
1.1 The interstellar medium	1
1.1.1 Components of the ISM	1
1.1.2 The evolution and lifecycle of the ISM	2
1.1.3 The importance of ISM dynamics in the context of star formation	4
1.1.4 The velocity structure of gas as a probe of physical processes	6
1.2 Observations of CO line emission	7
1.2.1 Fundamentals of molecular line emission	8
1.2.2 Information contained in CO emission lines	10
1.2.3 The advantage of ^{13}CO	12
1.3 The distribution of CO in the Milky Way	13
1.3.1 The importance of Galactic plane surveys	13
1.3.2 The presence of Galactic features in longitude-velocity diagrams	16
1.3.3 Kinematic distances	18
1.3.4 The impact of spiral arms on molecular gas properties	20
1.4 Structure identification in the ISM	20
1.4.1 The segmentation approach	21
1.4.2 Going beyond cloud segmentation	22
1.5 Motivation	24
1.6 Scope of this thesis	26
2 GAUSSPY+: A NOVEL DECOMPOSITION PACKAGE FOR EMISSION LINE SPECTRA	27
2.1 The GaussPy algorithm	28
2.2 Overview about the GaussPy+ package	29
2.3 Preparatory steps	30
2.3.1 Noise estimation	30
2.3.2 Identification of signal intervals	33
2.3.3 Masking noise artefacts	34
2.3.4 Creation of the training set	34
2.4 Improving the GaussPy decomposition	36
2.4.1 In-built quality control	36
2.4.2 Optional quality control	41
2.4.3 Improved fitting routine	44
2.5 Spatially coherent refitting	47
2.5.1 Phase 1: Refitting of the flagged fits	48
2.5.2 Phase 2: Refitting of the spatially incoherent fits	52
2.6 Performance of GaussPy+ on samples of synthetic spectra	55
2.7 Performance of GaussPy+ on a GRS test field	57

2.7.1	Optimal flux estimate for fair comparisons between the data set and decomposition results	58
2.7.2	Noise map	59
2.7.3	Comparison between the decomposition runs with GaussPy and GaussPy+	61
2.8	Discussion	67
2.8.1	Applications and limitations of GaussPy+	67
2.8.2	Recommended settings for GaussPy+	68
2.9	Summary	69
3	GLOBAL STATISTICS AND PROPERTIES OF THE GRS ^{13}CO EMISSION	71
3.1	Observational data sets	72
3.1.1	Galactic Ring Survey	72
3.1.2	Hi-GAL	72
3.2	Gaussian decomposition of the GRS data	72
3.2.1	Catalogue description	73
3.2.2	Flux recovery	75
3.3	Statistics of the Gaussian components	79
3.3.1	Number of fitted components	79
3.3.2	Intensity values	81
3.3.3	Centroid velocity values	82
3.3.4	Velocity dispersion values	83
3.3.5	Relationships between the parameters	85
3.4	Global properties of the gas emission	87
3.4.1	Distribution of velocity dispersion values as a function of Galactic coordinates	87
3.4.2	Complexity along the line of sight	89
3.5	Disentangling emission from the near and far side of the Galaxy	91
3.5.1	Considerations based on Galactic kinematics	91
3.5.2	Expected location and extent of the Galactic disk	92
3.5.3	Expected velocity dispersion values	93
3.5.4	Information contained in the velocity dispersion values	94
3.6	Velocity fluctuations	96
3.7	Summary	99
4	THE GALACTIC DISTRIBUTION OF THE GRS ^{13}CO EMISSION	101
4.1	Distance estimation	102
4.1.1	Bayesian distance calculator	102
4.1.2	Modification of the BDC and setting of prior weights	103
4.1.3	Prior for the kinematic distance ambiguity	105
4.1.4	Prior for the fitted linewidth	106
4.1.5	Choice of distance solution	111
4.2	Galactic distribution of the gas emission	112
4.2.1	Face-on view of the ^{13}CO emission	112
4.2.2	Comparison of the distance results	115
4.2.3	Gas fraction in spiral arm and interarm regions	117
4.2.4	Velocity dispersion in spiral arm and interarm regions	118
4.2.5	Galactocentric variation of the gas properties	120

4.2.6	Vertical distribution of the ^{13}CO emission	123
4.2.7	Potential problems, artefacts, and biases	125
4.2.8	Comparison with previous results	129
4.3	Summary	130
5	CONCLUSIONS & OUTLOOK	133
A	SUPPLEMENTARY MATERIAL FOR CHAPTER 2	139
A.1	Markov Chain	139
A.2	Testing GaussPy+ on synthetic spectra	141
A.2.1	Sample of synthetic spectra	141
A.2.2	Performance of the automated noise estimation routine	144
A.2.3	Performance of the identification of signal intervals	145
A.2.4	Performance of the masking of noise artefacts	146
A.2.5	Performance of the automated decomposition routine for the training set	147
A.2.6	Performance of the Gaussian decomposition	148
A.2.7	Recovery of identical components with different S/N ratios and degrees of blendedness	152
A.3	Performance details for GaussPy+	153
A.3.1	Performance and execution time for the decomposition of the training set	153
A.3.2	Execution time for the GRS test field	154
A.3.3	Effect of varying minimum S/N ratio and significance	155
A.3.4	Performance of in-built and optional quality control procedures	156
A.3.5	Refit iterations of the spatially coherent refitting phases	158
A.4	Normality tests	159
A.5	χ^2_{red} calculations for the GRS test field	161
A.6	GaussPy+ keywords and default values	162
B	SUPPLEMENTARY MATERIAL FOR CHAPTER 3	165
B.1	Chosen parameters, data preparation, and decomposition runs	165
B.1.1	Preparatory steps	165
B.1.2	Choice of the GaussPy smoothing parameters	165
B.1.3	Decomposition parameters and steps	168
B.1.4	Additional remarks on the decomposition results	170
B.2	Quality assurance metrics	170
B.2.1	Noise values	170
B.2.2	Goodness of fit statistics	172
B.3	Effects of optical depth on the decomposition results	174
B.3.1	Depletion, freeze-out, and self-absorption of ^{13}CO	175
B.3.2	Calculation of optical depth values	175
B.3.3	Optical depth effects in the G24 region	177
B.3.4	Effects on the decomposition	183
C	SUPPLEMENTARY MATERIAL FOR CHAPTER 4	185
C.1	Further details about the KDA prior	185
C.1.1	Calculation of priors	185
C.1.2	Inferring literature KDA solutions	187

c.1.3	Literature results used in the KDA prior	188
c.1.4	Effect of the KDA prior	193
c.2	Effects of beam averaging on the observed linewidth	196
c.3	Characterisation of the BDC performance	198
c.3.1	Effect of v_{LSR} uncertainties	198
c.3.2	Distance results without P_{far} priors	198
c.3.3	Estimated probabilities, P_{far} weights, and distance choices	200
c.3.4	Deviation from Galactic rotation curve	202
	List of Symbols	203
	Acronyms	206
	Publications	207
	Bibliography	209
	Acknowledgments	221

LIST OF FIGURES

Figure 1.1	Various stages in the lifecycle of the interstellar medium	3
Figure 1.2	Illustration of a spectral cube	11
Figure 1.3	Overview about recent Galactic plane surveys	13
Figure 1.4	Appearance of Galactic features in PV diagrams	17
Figure 1.5	Illustration of Galactic rotation and observed radial velocities	19
Figure 1.6	Comparison between moment analysis and spectral decomposition	23
Figure 2.1	Methods and procedures included in GAUSSPY+	30
Figure 2.2	Illustration of automated noise estimation routine	31
Figure 2.3	Flowchart of in-built quality controls	36
Figure 2.4	Illustration of significance criterion	38
Figure 2.5	Illustration of optional flagging criteria	41
Figure 2.6	Illustration of flagging criterion based on neighbouring fit solutions	44
Figure 2.7	Flowchart of improved fitting routine	45
Figure 2.8	Flowchart of first phase of spatial refitting routine	48
Figure 2.9	Illustration of grouping routine	49
Figure 2.10	Flowchart of second phase of spatial refitting routine	52
Figure 2.11	Illustration of second phase of the spatial refitting routine	53
Figure 2.12	Performance results for GAUSSPY+ and GAUSSPY decompositions	57
Figure 2.13	Zereth moment maps of GRS test field	58
Figure 2.14	Noise maps of GRS test field	60
Figure 2.15	Comparison of noise estimation for GRS test field	60
Figure 2.16	Decomposition results of GAUSSPY+ stages for GRS test field	63
Figure 2.17	Fit results of GAUSSPY+ stages for GRS test field spectra	64
Figure 2.18	Distribution of fit parameters for GRS test field	66
Figure 3.1	Average spectra of entire GRS data set	75
Figure 3.2	Zereth moment and normalised residual maps of the GRS data set	77
Figure 3.3	PV and normalised residual maps of the GRS data set	78
Figure 3.4	Map of the number of fit components per spectrum for the full GRS data set	80
Figure 3.5	Histogram of the number of fit components per spectrum for the full GRS data set	81
Figure 3.6	Histogram of intensity values for GRS fit components	82
Figure 3.7	Histogram of centroid velocity values for GRS fit components	83

Figure 3.8	Histogram of velocity dispersion values for GRS fit components	84
Figure 3.9	Distribution of intensity and velocity dispersion values	85
Figure 3.10	Distribution of centroid velocity and velocity dispersion values	86
Figure 3.11	Distribution of centroid velocity and intensity values	86
Figure 3.12	Distribution of the velocity dispersion values against their Galactic latitude positions	88
Figure 3.13	Distribution of velocity dispersion values against their Galactic longitude positions	89
Figure 3.14	Ridge plots of integrated ^{13}CO emission and H_2 surface density PDFs	90
Figure 3.15	Schematic face-on view of the Galactic plane	92
Figure 3.16	Zeroth moment and velocity dispersion maps within $-5 < v_{\text{LSR}} < 20 \text{ km s}^{-1}$ range	95
Figure 3.17	Velocity fluctuations throughout the GRS data set	97
Figure 3.18	Velocity fluctuations in the Aquila Spur region	98
Figure 4.1	Overview about the spiral arm model and maser parallax sources	104
Figure 4.2	Effect of BDC priors on the distance estimation	105
Figure 4.3	Illustration of BDC bias for sources with low v_{LSR} velocities	107
Figure 4.4	Illustration of linewidth broadening caused by beam averaging	108
Figure 4.5	PDFs of fitted velocity dispersion values in different v_{LSR} ranges	109
Figure 4.6	Illustration of the distance prior based on the fitted linewidth	110
Figure 4.7	Example of final distance choice for BDC results	111
Figure 4.8	Face-on view of the integrated ^{13}CO emission	113
Figure 4.9	Face-on view of the number of Gaussian fit components	113
Figure 4.10	Face-on view of the median velocity dispersion values	114
Figure 4.11	PDFs for estimated heliocentric distances and corresponding uncertainties	115
Figure 4.12	2D histograms of estimated distance values against intensity and velocity dispersion values	116
Figure 4.13	PDFs of velocity dispersion values associated with Galactic features	119
Figure 4.14	PDFs of velocity dispersion values for 2 kpc heliocentric distance bins	121
Figure 4.15	2D histograms of estimated Galactocentric distance values against intensity and velocity dispersion values	122
Figure 4.16	Face-on view of the median z_{gal} values	123
Figure 4.17	PDFs of the vertical distribution of the ^{13}CO emission	124
Figure 4.18	2D histograms of velocity dispersion and estimated vertical distances z_{gal}	125

Figure 4.19	Face-on view with diagnostics to illustrate potential issues in the distance assignment	126
Figure 4.20	Face-on view of the median v_{LSR} values	127
Figure 4.21	Face-on view of the median distance uncertainty	127
Figure 5.1	Spatial coverage of GRS, SEDIGISM, and PROMISE	136
Figure A.1	Illustration of one-step Markov chain results	141
Figure A.2	Example synthetic spectra	142
Figure A.3	Probability distribution functions for parameters of the synthetic spectra	143
Figure A.4	Noise estimation results for the synthetic spectra	145
Figure A.5	Signal interval identification results for synthetic spectra	146
Figure A.6	Performance of the GAUSSPY and GAUSSPY+ decompositions of the synthetic spectra	148
Figure A.7	Cumulative distributions of GAUSSPY and GAUSSPY+ decomposition results	150
Figure A.8	Example spectra illustrating the performance of GAUSSPY+	151
Figure A.9	Decomposition results for synthetic spectra with two identical Gaussian components	152
Figure A.10	Percentage of correctly identified mean positions for the synthetic spectra	155
Figure A.11	Percentage of incorrectly identified mean positions for the synthetic spectra	155
Figure A.12	Number of refit attempts and successful refits of spectra of the GRS test field	158
Figure A.13	Comparison of the performance of different normality tests	160
Figure A.14	χ_{red}^2 maps for GAUSSPY and GAUSSPY+ decompositions of GRS test field	161
Figure A.15	χ_{red}^2 distribution for GAUSSPY and GAUSSPY+ decompositions of GRS test field	162
Figure B.1	Map of determined rms noise	171
Figure B.2	Histogram of determined rms noise	171
Figure B.3	Histogram of resulting p -values from normality tests	172
Figure B.4	Histogram of χ_{red}^2 values	173
Figure B.5	Map of χ_{red}^2 values	174
Figure B.6	Optical depth of ^{13}CO as function of brightness temperature	176
Figure B.7	Maps for G24 region	178
Figure B.8	2D histograms of GRS and MWISP fit parameters	180
Figure B.9	2D distribution of determined T_{ex} and τ_0^{13} values	182
Figure C.1	Flowchart outlining the use of literature distances for the KDA prior	186
Figure C.2	Comparison between associated Hi-GAL and ATLASGAL sources	191
Figure C.3	BDC results for the ATLASGAL clump sample compared to their literature values	195

Figure C.4	Increase in observed velocity dispersion with decreasing spatial resolution	197
Figure C.5	Effect of v_{LSR} uncertainties on BDC results	198
Figure C.6	Face-on view of integrated emission obtained with BDC default settings	199
Figure C.7	Face-on view of the median velocity dispersion values without the size-linewidth prior	199
Figure C.8	Face-on view of the median probability values	201
Figure C.9	Cumulative distributions for estimated probabilities, P_{far} prior values, and distance choices	201
Figure C.10	Face-on view of components associated with v_{LSR} deviations	202

LIST OF TABLES

Table 1.1	Phases of the interstellar gas	2
Table 1.2	Details about ^{13}CO Galactic plane surveys	14
Table 2.1	Performance of GAUSSPY and GAUSSPY+ on the synthetic spectra	55
Table 2.2	Comparison of parameters and flagged spectra for the decomposition runs with GAUSSPY and GAUSSPY+	65
Table 3.1	Decomposition results	74
Table 3.2	Expected velocity dispersion values based on a size-linewidth relationship	93
Table 4.1	Galactic rotation curve parameters used in the BDC runs	103
Table 4.2	Distance results for the two BDC runs	117
Table A.1	Comparison of smoothing parameter values for different training sets	147
Table A.2	Execution times for synthetic spectra	154
Table A.3	Execution times for GAUSSPY+ decomposition of GRS test field	154
Table A.4	Performance of in-built quality control procedures	157
Table A.5	Performance of optional quality control procedures	157
Table A.6	Performance of normality tests	161
Table A.7	GAUSSPY+ keywords	163
Table B.1	Smoothing parameters for GAUSSPY+ training sets	166
Table B.2	Comparison of smoothing parameters for SCOUSEPY and GAUSSPY+ training sets	167
Table B.3	Decomposition performance of GAUSSPY+ stages	169
Table B.4	Threshold between optically thin and thick emission	177
Table B.5	Smoothing parameters for ^{13}CO and C^{18}O MWISP data sets	179
Table C.1	Overview of the catalogues used as KDA solutions	189
Table C.2	BDC results for the ATLASGAL clump sample for different catalogue weights and prior values	194
Table C.3	BDC results for ATLASGAL sample for different spiral arm and KDA priors	195
Table C.4	BDC results for the remaining catalogues	196

INTRODUCTION

*I don't pretend we have all the answers.
But the questions are certainly worth thinking about.*

— Arthur C. Clarke

We have come a long way ever since Galileo Galilei first pointed his telescope towards the band of the Milky Way to resolve its observed diffuse structure into countless individual stars. In particular, we have learned that the regions in between the stars are not empty; they harbour the ingredients out of which structures can form that ultimately give birth to stars, which subsequently shape and return material to their surroundings. This environment—called the interstellar medium—is of fundamental importance for understanding the formation of stars, which in turn impact galaxy evolution. Given this significance, a vast amount of research has been dedicated to addressing the following key questions: *how are structures in the interstellar medium created, what are they like, and how do they evolve?*

1.1 THE INTERSTELLAR MEDIUM

To understand the processes and conditions that shape the interstellar medium (ISM), we first have to understand the composition of its constituents. The ISM consists of different phases that are shaped by a multitude of physical processes and forces such as turbulence, gravity, and magnetic fields. The complex interplay between these processes governs how overdensities and structures in the ISM are formed. In the following I provide a short overview about the ISM phases, discuss how they interact and evolve, and highlight the important role of the velocity structure of molecular gas.

1.1.1 Components of the ISM

The total mass of the ISM is dominated by hydrogen (H, $\sim 70\%$) and helium (He, $\sim 28\%$). The remaining fraction of mass is constituted by heavier elements, with carbon (C), nitrogen (N), and oxygen (O) being the most important contributors both in terms of abundance and fractional mass contribution (e.g. [Draine, 2011](#)). The ISM is mostly composed of gas and has only a small contribution of dust ($\sim 1\%$, e.g. [Lilley 1955](#) and [Savage & Mathis 1979](#)). In the Milky Way, most of the H mass is in its neutral atomic form (H I, $\sim 60\%$), followed by its ionised atomic form (H II, $\sim 23\%$), and its molecular form (H₂, $\sim 17\%$) ([Draine, 2011](#)).

The diffuse component of the ISM with number densities, n_{H} , less than 10^2 cm^{-3} , is usually classified into four phases, characterised by their temperatures and densities (Table 1.1). The first model proposed by [Field et al. \(1969\)](#) contained two thermally stable gas phases coexisting in pressure equilibrium: a cold neutral medium (CNM)

TABLE 1.1: Phases of the interstellar gas.

Phase	T_k [K]	n_H [cm^{-3}]
DIFFUSE ISM		
Hot ionised medium (HIM); coronal gas	$\geq 10^{5.5}$	~ 0.004
Warm ionised medium (WIM); H II gas	$\sim 10^4$	~ 0.3
Warm neutral medium (WNM); warm H I	$5000 - 10^4$	$\sim 0.2 - 0.9$
Cold neutral medium (CNM); cool H I	$\sim 60 - 260$	$\sim 7 - 70$
DENSE ISM		
H II regions	$\sim 10^4$	10^4
Molecular gas; diffuse H ₂	~ 50	$\sim 10^2$
Molecular gas; dense H ₂	$10 - 50$	$\sim 10^3 - 10^6$

Notes. Based on [Ferrière \(2001\)](#) and [Draine \(2011\)](#). T_k is the kinetic temperature and n_H is the number density of hydrogen nuclei.

containing dense and largely neutral H I clouds, and a warm neutral medium (WNM) surrounding the cold clouds. [McKee & Ostriker \(1977\)](#) expanded this model by a third phase, the hot ionised intercloud medium (HIM), which is characterised by very low densities and high temperatures and is produced by supernova explosions. Based on observations of H α emission, a fourth phase of highly ionised warm hydrogen (warm ionised medium, WIM) was introduced (see e.g. [Kulkarni & Heiles, 1988](#)). H II regions and molecular clouds are the main constituents of the dense ($n_H \gtrsim 10^2 \text{ cm}^{-3}$) ISM but are often not considered as phases of the ISM since due to self-gravity and expansion they are overpressured compared to the four diffuse phases ([Stanimirović & Zweibel, 2018](#)).

This characterisation into distinct phases is likely an oversimplification, as the presence of strong turbulence in the ISM will mix the different phases ([Klessen & Glover, 2016](#)). For example, [Heiles & Troland \(2003\)](#) reported that half of the WNM could be found in the thermally unstable region with temperatures ranging between 500 – 5000 K. Nonetheless, this simplified model has been very useful in the description of how the interstellar gas transitions between different phases and in the process forms and evolves structures.

1.1.2 The evolution and lifecycle of the ISM

The evolution of structures in the ISM is driven by physical processes and forces that govern the complex interaction between the ISM phases presented in Table 1.1, which ultimately constitutes a continuous causal loop of formation and destruction (see Fig. 1.1). In the following, I describe this evolutionary cycle starting with the formation of cold H I clouds.

The accumulation of cold H I in cloudy structures is a natural outcome of the simple two-phase model proposed by [Field et al. \(1969\)](#), in which the CNM and



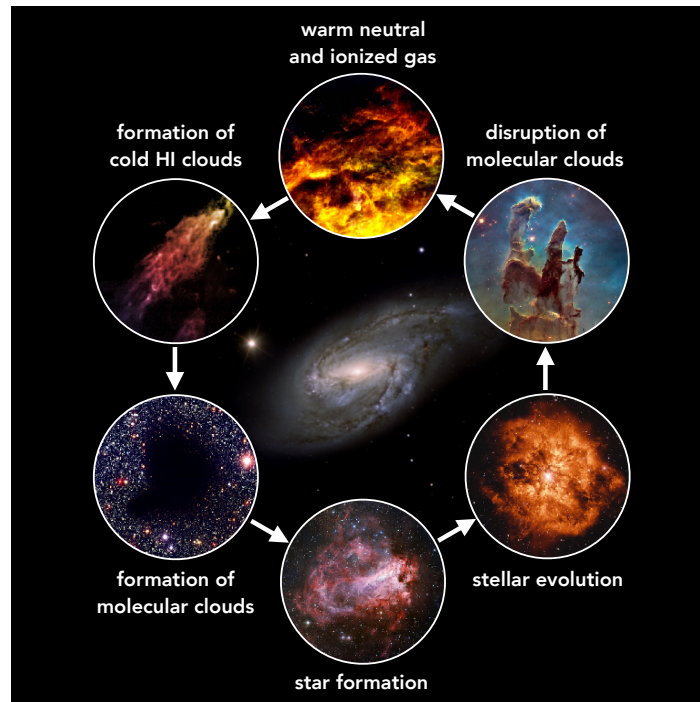


FIGURE 1.1: Various stages in the lifecycle of the interstellar medium. Inspired by Fig. 3 in [Kulesa \(2011\)](#). Credits for individual images from left to right and top to bottom: Infrared cirrus, IPAC, Caltech/JPL; Smith’s cloud, Bill Saxton, NRAO/AUI/NSF; Pillars of creation, NASA, ESA, and the Hubble Heritage Team (STScI/AURA); NGC 3627, ESO; B68, ESO; M1-67, Judy Schmidt, Hubble Legacy Archive; M17, ESO.

WNM phases are in thermal equilibrium. Gas at temperatures between the CNM and WNM will either heat up and decrease its density or cool down and increase its density and thus become part of the WNM or CNM, respectively, leading to cold H I clouds that are confined by the WNM. A number of simulations have also shown that compression via shocks can lead to a destabilisation of the WNM and the formation of cold H I clouds (e.g. [Hennebelle & Pérault, 1999](#); [Koyama & Inutsuka, 2002](#)). Another potential formation mechanism for H I clouds could be the galactic fountain model, in which hot gas from the HIM rises above the galactic disk, cools and condenses into H I clouds that fall back onto the disk as high-velocity clouds ([Shapiro & Field, 1976](#); [Breitschwerdt & Komossa, 2000](#)).

The next step in the evolutionary cycle of the ISM involves the transition from diffuse H I to dense H₂. For this transition interstellar dust acts as a vital catalyst because H₂ is predominantly formed on dust grain surfaces ([Gould & Salpeter, 1963](#); [Hollenbach & Salpeter, 1971](#)). Once molecular hydrogen has formed, it requires sufficient shielding from the interstellar radiation field, as high energy photons can dissociate H₂. Enough gas needs to be accumulated to increase the column density of the gas, so that H₂ self-shielding effects at the exterior (in addition to shielding by dust) can enable the formation of denser molecular structures in the interior. There are multiple possible mechanisms by which H I structures could be transformed into giant molecular clouds (GMCs; see [Dobbs et al., 2014](#), and references therein), for example via collisions of smaller clouds in spiral arms, or large-scale instabilities due



to a combination of gravitational and magnetic forces in the rotating galactic disk (e.g. [Toomre, 1964](#); [Parker, 1966](#); [Elmegreen, 1987](#)). These instabilities or feedback from already ongoing star formation can also drive converging turbulent flows of lower density gas, which can collide and form molecular clouds in the dense, post-shock regions (e.g. [Klessen & Glover, 2016](#), and references therein).

It is currently not fully understood how the complex and hierarchical internal structure of molecular clouds arises. Most likely it is a combination of multiple physical effects, for instance due to turbulence and magnetic forces that can create overdensities within molecular clouds, which can lead to gravitational contraction (e.g. [McKee & Ostriker, 2007](#)). This results in inhomogeneous and hierarchical molecular cloud structures characterised by filamentary mass distributions (e.g. [Schneider & Elmegreen, 1979](#); [André et al., 2014](#)). Higher-density substructures in molecular clouds are usually classified into clumps (with sizes of 0.3 – 3 pc and densities of $10^3 - 10^4 \text{ cm}^{-3}$) and cores (with sizes up to ~ 0.3 pc and densities of $10^4 - 10^5 \text{ cm}^{-3}$; [Bergin & Tafalla 2007](#)). Clumps can be the site of star cluster formation, whereas cores are the formation sites of individual stars or small multiple stellar systems (e.g. [McKee & Ostriker, 2007](#)).

Once stars are forming in the high-density regions of molecular clouds, they begin to impact their environment. Massive ($\geq 8 M_{\odot}$) stars can inject a large amount of momentum and energy back into the parent cloud via multiple feedback processes, such as protostellar outflows and jets, radiation pressure, radiative heating, strong stellar winds, ionising radiation from H II regions, and supernova explosions (for a review see [Krumholz et al., 2014](#)). Massive stars also produce heavier elements (such as C, N, and O) in their interior via nucleosynthetic processes and due to their strong stellar winds and short lifetimes on the order of a few Myr these elements are soon returned to the ISM to enrich and increase its metallicity ([Woosley et al., 2002](#)). In the late phases of the evolution of low- to intermediate-mass ($0.6 - 8 M_{\odot}$) stars, nucleosynthetic processes in the atmospheres of these so-called asymptotic giant branch stars also produce heavy elements that end up in the ISM through mass loss from strong stellar winds ([Busso et al., 1999](#)).

The combined effects of these feedback mechanisms from the newly formed stars contribute to turbulent motions within the clouds, and can even disrupt and destroy the parent molecular cloud (e.g. [Matzner, 2002](#); [Rogers & Pittard, 2013](#)). Moreover, feedback from star-forming regions introduces turbulence and shocks into the surrounding warm atomic ISM, which can lead to renewed formation of cold H I structures, thus starting the evolutionary cycle of the ISM anew.

1.1.3 *The importance of ISM dynamics in the context of star formation*

A fundamental reason for our interest in the dynamics of the ISM is its intimate connection with star formation. As discussed in the previous section, the ISM is shaped by multiple physical processes and forces—such as gravity, turbulence, and magnetic fields—whose interaction governs how the ISM evolves. In particular turbulence plays an important key role in regulating structure formation in the



ISM, in that it creates density contrasts¹ leading to overdense regions but also acts to stabilise or destroy these structures again via turbulent pressure support or feedback mechanisms. Supersonic turbulence has thus been put forward as a dominant mechanism shaping the ISM and ultimately controlling star formation (e.g. Elmegreen & Scalo, 2004; Mac Low & Klessen, 2004; Ballesteros-Paredes et al., 2007; McKee & Ostriker, 2007). In this picture, turbulent energy introduced on larger scales, for example by colliding gas flows, is transmitted down to smaller scales (known as the ‘turbulent cascade’) until it is dissipated. In what is referred to as gravoturbulent fragmentation, random supersonic motions can lead to shock waves that compress material locally to form denser regions, and provide conditions for gravity to take over and proceed until gravitational collapse ensues and forms stars (Mac Low & Klessen, 2004). A host of numerical simulations support this picture of turbulence-regulated star formation (e.g. Federrath & Klessen, 2012; Padoan et al., 2014), which has thus become the current paradigm in star formation studies.

The dynamic state of ISM structures, that means the effects of self-gravity on a turbulent cloud or clump, can be analysed with the virial theorem², which in its full form is given as

$$\frac{1}{2}\ddot{I} = 2(\mathcal{T} - \mathcal{T}_S) + \mathcal{B} + \mathcal{W} + \mathcal{S}. \quad (1.1)$$

The left-hand side of this equation includes the second time derivative of the moment of inertia I defined as

$$I = \int_V \rho r^2 dV, \quad (1.2)$$

with ρ , r , and V being the density, radius, and volume of the cloud. The right-hand side of the equation contains different energy terms. \mathcal{T} is the sum of the total kinetic and thermal energy of the cloud given as

$$\mathcal{T} = \int_V \left(\frac{3}{2} P_{\text{th}} + \frac{1}{2} \rho v^2 \right) dV, \quad (1.3)$$

where P_{th} is the thermal pressure and v is the velocity. The surface kinetic term \mathcal{T}_S is given as

$$\mathcal{T}_S = \oint_S P_{\text{th}} \mathbf{r} \cdot d\mathbf{S} \quad (1.4)$$

and defines the confining pressure on the cloud surface S . The net magnetic energy \mathcal{B} is given as

$$\mathcal{B} = \frac{1}{8\pi} \int_V B^2 dV + \frac{1}{4\pi} \oint_S \mathbf{r} \cdot \left(\mathbf{B}\mathbf{B} - \frac{1}{2} B^2 \mathbf{I} \cdot d\mathbf{S} \right), \quad (1.5)$$

¹ For isothermal gas, supersonic turbulence creates density fluctuations that scale with the Mach number to the second power, so Mach numbers of 5 and 10 are expected to create density contrasts of 25 and 100, respectively (Klessen, 2011).

² The following discussion about the virial theorem is based on McKee & Ostriker (2007) and Krumholz (2015). We refer to these works for more information about the equations and details about their derivations.



which is the difference between the magnetic pressure in the cloud interior and the magnetic tension plus magnetic pressure at the cloud surface. \mathcal{W} is the gravitational energy of the cloud given as

$$\mathcal{W} = - \int_V \rho \mathbf{r} \cdot \nabla \phi dV, \quad (1.6)$$

with ϕ being the gravitational potential. Finally, \mathcal{S} is the rate of change of the momentum flux across the cloud surface

$$\mathcal{S} = - \frac{1}{2} \frac{d}{dt} \oint_S (\rho \mathbf{v} r^2) \cdot d\mathbf{S}. \quad (1.7)$$

If magnetic and surface forces are negligible and no gas crosses the cloud surface (i.e. $\mathbf{v} = 0$ at S), the virial theorem for a cloud in equilibrium ($\dot{I} = 0$) simplifies to $2\mathcal{T} = -\mathcal{W}$ and we can define the virial ratio as

$$\alpha_{\text{vir}} = \frac{2\mathcal{T}}{|\mathcal{W}|}, \quad (1.8)$$

with $\alpha_{\text{vir}} = 1$ in case of virial equilibrium and $\alpha_{\text{vir}} = 2$ in case of equipartition between the gravitational and kinetic energy of the system. For $\alpha_{\text{vir}} < 1$ the internal pressure and turbulent support of the cloud would not be sufficient to prevent it from gravitational collapse.

Equation 1.8 can be reformulated into quantities that can be inferred from observations. The gravitational energy \mathcal{W} can be written as

$$\mathcal{W} = -a \frac{GM^2}{R}, \quad (1.9)$$

with M and R being the mass and radius of the cloud, and the factor a describing the internal density structure. The total kinetic and thermal energy can be reformulated as

$$\mathcal{T} = \frac{3}{2} M \sigma_v^2, \quad (1.10)$$

where σ_v^2 is the one-dimensional mean square velocity measured over the whole system, which is a combination of the thermal and non-thermal contributions. The one-dimensional velocity dispersion σ_v can be directly measured from the emission lines in spectroscopic data sets.

1.1.4 The velocity structure of gas as a probe of physical processes

As established in the previous section, information about the gas kinematics is crucial for analysing the dynamical state of molecular clouds and clumps and to establish whether these structures are supported against gravitational collapse. Molecular clouds are highly turbulent with Reynolds numbers (Re)³ on the order of $\sim 10^7$ (e.g. Myers & Khersonsky, 1995), which is also reflected in their observed suprathermal linewidths. Supersonic turbulence has therefore been invoked as one of the main

³ The Reynolds number is a measure for the importance of viscous forces and is defined as $\text{Re} = vl/\nu$, with v being the typical velocity on the scale l and ν being the kinetic viscosity.



sources of kinetic energy and support in molecular clouds. Larson (1981) found that the velocity dispersion and size of molecular clouds follow a power-law scaling, which is referred to as the size-linewidth relationship, and has been recovered in several follow-up works (e.g. Solomon et al., 1987; Heyer & Brunt, 2004). However, many studies have found large scatter for this relation and more recent works have uncovered a more robust relation that also accounts for the surface density of the clouds (Heyer & Dame, 2015, and references therein). Nonetheless, the size-linewidth relation is often interpreted as indicating a universal ISM property, namely the presence of the aforementioned supersonic turbulent cascade (Larson, 1981; Kritsuk et al., 2013). However, the large observed linewidths could also be explained by a global collapse scenario in which clumps, filaments, and GMCs constitute a hierarchical system dominated by accretion via gravitational collapse instead of random turbulence (Dobbs et al., 2014, and references therein).

Observationally, there is a tremendous wealth of physically interesting information that can be gleaned from studying the detailed velocity structure of molecular gas. These include fundamental insights about: properties of turbulence in the ISM and molecular clouds and their implications for star formation (e.g. Larson 1981, for reviews, see Elmegreen & Scalo 2004, Scalo & Elmegreen 2004, and Hennebelle & Falgarone 2012); the driving scale and dissipative processes of supersonic turbulence in molecular clouds (e.g. Ossenkopf & Mac Low, 2002); the universality of turbulence in the molecular ISM (e.g. Heyer & Brunt, 2004); inference about imprints of shear in molecular clouds (e.g. Hily-Blant & Falgarone, 2009); the ratio between solenoidal and compressive modes of turbulence (e.g. Orkisz et al., 2017); the manifestations of intermittency of turbulence (i.e. strong spatial or temporal fluctuations of the density and velocity structure) in dense cores (e.g. Falgarone et al., 2009); the transition to coherence, that means the transition from supersonic to subsonic motions, at the boundary of dense cores (e.g. Pineda et al., 2010; Chen et al., 2019); velocity signatures that can distinguish different hypotheses for the collapse of cores (e.g. Keto et al., 2015); the identification of velocity-coherent filamentary substructures within molecular clouds (e.g. Hacar et al., 2013; Henshaw et al., 2014); and the characterisation of the kinematics and gas velocity dispersion of filaments (e.g. Arzoumanian et al., 2013; Orkisz et al., 2019).

A detailed investigation of the molecular gas is thus of prime importance to fully understand the formation and evolution of dense ISM structures and the mechanisms controlling star formation. However, this requires detailed analysis of the kinematic and dynamic information contained in observations of the molecular gas. In the next section, I discuss how the required information about the gas velocity structure can be extracted from molecular line observations.

1.2 OBSERVATIONS OF CO LINE EMISSION

Observations of emission lines are of fundamental importance for obtaining information about the ISM. Starting with the first detections of H I via the 21 cm line at 1420.4 MHz by Ewen & Purcell (1951), followed by the first observation of interstellar



CO⁴ in the Orion nebula by [Wilson et al. \(1970\)](#) and the first detections of two other major CO isotopologues⁵ by [Penzias et al. \(1971\)](#), the study of emission lines at radio wavelengths has led to groundbreaking astrophysical insights. Our knowledge about the ISM—especially information about its dynamic state—is largely shaped by the emission properties of its molecules in the gas phase. In particular our insight into the state of the molecular gas has been largely driven by observations of CO and its isotopologues.

The molecular gas phase of the ISM is characterised by very low temperatures of about 10 – 50 K (Table 1.1). Therefore direct observations of H₂—the main molecular building block of the ISM—are challenging or effectively impossible, since the low mass and homonuclear configuration of H₂ put its lowest energy transition ($J = 2 \rightarrow 0$) at ~ 510 K above the ground state. CO, which is the most abundant molecule in the ISM after H₂, has multiple transitions that are excited at the low temperatures prevalent in the molecular part of the ISM and can be observed in the radio and sub-millimetre part of the electromagnetic spectrum. Since its low transitions of the rotational quantum number J are predominantly excited by collisions with H₂ molecules, CO is often used to infer the underlying distribution of H₂ (for a review see [Bolatto et al., 2013](#)). In the following sections I briefly go over some fundamentals about molecular line emission and discuss how useful velocity information can be extracted from the position and shape of CO emission lines.

1.2.1 Fundamentals of molecular line emission

The rotational energy state of a diatomic molecule with a dipole moment such as CO can be calculated in the rigid rotor approximation as

$$E_{\text{rot}}(J) = \frac{h^2}{8\pi^2 I_M} J(J+1), \quad (1.11)$$

where I_M is the moment of inertia, and h is the Planck constant. For rotational transitions the specific selection rule only allows for transitions between successive states ($\Delta J = \pm 1$), with $J = 0$ corresponding to the ground state or lowest energy configuration. For a transition from successive rotational states the energy difference $\Delta E = E(J+1) - E(J)$ is released and propagated as electromagnetic radiation. The equation of radiative transfer describes how the intensity of this radiation is affected by absorption and emission along the line of sight (for simplicity we do not consider scattering effects)⁶. The radiative transfer equation can be written as

$$\frac{dI_\nu}{ds} = -\kappa_\nu I_\nu + j_\nu, \quad (1.12)$$

where I_ν is the specific intensity, s is the path of propagation along the line of sight, and j_ν and κ_ν are the frequency-dependent emissivity and absorption coefficients, respectively.

⁴ More specifically the lowest rotational transition $J = 1 \rightarrow 0$ for ¹²C¹⁶O at 115.2712 GHz.

⁵ ¹³C¹⁶O at 110.2014 GHz and ¹²C¹⁸O at 109.7822 GHz.

⁶ The following discussion about radiative transfer is based on [Draine \(2011\)](#), [Wilson et al. \(2014\)](#), and [Mangum & Shirley \(2015\)](#). We refer to these works for more information about the equations and details about their derivations.



Under local thermodynamic equilibrium (LTE)—that means assuming that the emitted radiation is only dependent on intrinsic properties and the temperature of the radiating matter—we obtain Kirchhoff's law:

$$\frac{j_\nu}{\kappa_\nu} = B_\nu(T). \quad (1.13)$$

Here $B_\nu(T)$ is the Planck function describing the radiation of a black body, which only depends on the thermodynamic temperature T , and is defined as

$$B_\nu(T) = \frac{2h\nu^3}{c^2} \frac{1}{e^{h\nu/kT} - 1} \quad (1.14)$$

at frequency ν , with c being the speed of light, and k the Boltzmann constant. In the Rayleigh-Jeans limit ($h\nu \ll kT$), Eq. 1.14 can be approximated as

$$B_\nu(T) = \frac{2\nu^2}{c^2} kT. \quad (1.15)$$

From this relation we can define the brightness temperature T_B as

$$T_B(\nu) = \frac{c^2}{2k\nu^2} I_\nu, \quad (1.16)$$

using $B_\nu(T) = I_\nu$ under the LTE assumption. To solve for the radiative transfer equation (Eq. 1.12) in terms of $B_\nu(T)$, we first define the optical depth τ_ν as

$$d\tau_\nu = -\kappa_\nu ds. \quad (1.17)$$

We further define the excitation temperature T_{ex} as

$$T_{\text{ex}} = \frac{\Delta E}{k} \left[\ln \left(\frac{n_l g_u}{n_u g_l} \right) \right], \quad (1.18)$$

where n_u and n_l are the densities in an upper (e.g. excited) and lower (e.g. ground) state with g_u and g_l as their respective statistical weights and ΔE the difference in energy between the upper and lower levels. Assuming that T_{ex} is constant, the resulting intensity at frequency ν can be written as

$$I_\nu = I_{\nu,0} \cdot e^{-\tau_\nu} + B_\nu(T_{\text{ex}}) [1 - e^{-\tau_\nu}], \quad (1.19)$$

where $I_{\nu,0} \cdot e^{-\tau_\nu}$ describes the attenuated background intensity. For molecular line measurements the intensity at the source position is corrected for the background temperature T_{bg} . This background intensity is measured from an offset or reference position containing only contributions from the background, yielding the measured intrinsic source intensity $\Delta I_\nu = I_\nu - I_{\nu,0}$. Plugging in the relation from Eq. 1.19 this can be converted to

$$\Delta I_\nu = [B_\nu(T_{\text{ex}}) - B_\nu(T_{\text{bg}})] [1 - e^{-\tau_\nu}]. \quad (1.20)$$

Using the definition of the brightness temperature T_B (Eq. 1.16), Eq. 1.20 can be rewritten as



$$T_{\text{B}}(\nu) = f \cdot \frac{h\nu}{k} \left[\left(e^{h\nu/kT_{\text{ex}}} - 1 \right)^{-1} - \left(e^{h\nu/kT_{\text{bg}}} - 1 \right)^{-1} \right] [1 - e^{-\tau_{\nu}}], \quad (1.21)$$

where f is the filling factor, which describes the extent by which the spatial resolution element is filled by the source (i.e. $f = 1$ for extended sources filling the beam). For $T_{\text{ex}} > T_{\text{bg}}$ we observe the resulting line in emission, whereas for $T_{\text{ex}} < T_{\text{bg}}$ the line would be observed in absorption.

For the ^{12}CO (1–0) emission line that is optically thick ($\tau_{\nu} \gg 1$), Eq. 1.21 can be used to estimate T_{ex} from the observed emission T_{B} in the absence of background continuum sources. Assuming that the different CO isotopologues have the same excitation temperature, Eq. 1.21 can then be solved for τ_{ν} for a different isotopologue of CO assumed to be optically thin ($\tau_{\nu} \ll 1$). The optical depth can then be further used with the measured T_{B} of the emission line to estimate the column density of the respective CO isotopologue (see Eq. 15.31 and Eq. 15.38 in [Wilson et al. 2014](#) for an example using the ^{13}CO (1–0) line).

1.2.2 Information contained in CO emission lines

Figure 1.2 illustrates the typical data product resulting from CO emission line observations, which is called a spectral or Position-Position-Velocity (PPV) cube. A PPV cube consists of two spatial axes and one spectral axis, so each pixel in the spatial domain contains a spectral dimension.

The position and shape of the emission line contains useful information about the velocity structure of the gas. The Doppler shift of the centroid frequency of the line, compared to the rest frequency in the Local Standard of Rest (LSR), is typically interpreted as the bulk motion of the gas⁷. This is illustrated with the channel maps in Fig. 1.2, which correspond to different velocity channels along the spectral axis and immediately let us identify the main gas motions.

The width of the emission line apart from natural line broadening⁸ and pressure broadening⁹ is caused by the following two contributions: thermal (or Doppler) broadening that is due to random thermal motions of the gas molecules, which in case of an underlying Maxwellian velocity distribution leads to a projected Gaussian velocity distribution along the line of sight; and non-thermal (often interpreted as ‘turbulent’) broadening, which usually includes all other effects that might introduce motion in the gas, such as velocity gradients or internal (turbulent) motions within molecular clouds. However, the ‘turbulent’ broadening can be affected by projection effects, such as unresolved blended lines caused by overlapping structures along the line of sight.

In case of low optical depth, the observed total width of CO emission lines (including all thermal and non-thermal contributions) is well-described by a Gaussian shape.

⁷ The PPV data is a convolution of velocity, density, and excitation, which effectively prevents the extraction of pure velocity information. See Sect. 1.4.1 for more information.

⁸ The natural line broadening is a consequence of the Heisenberg uncertainty principle and gives the minimum width of a spectral line for an excited state with a finite lifetime.

⁹ Also referred to as collisional broadening. Increases in the temperature and density of the gas can lead to increasing collisional de-excitations that lower the lifetime of an excited state and thus broaden the spectral line.



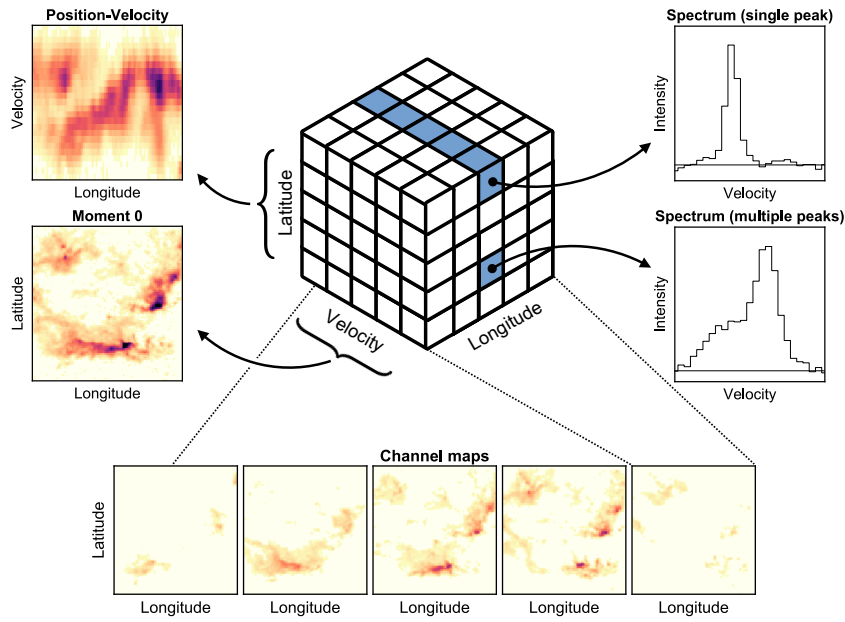


FIGURE 1.2: Illustration of a spectral cube. Inspired by Fig. 1 of [Loomis et al. \(2018\)](#). The data is taken from ^{12}CO (1–0) observations of the Orion and Monoceros region from [Wilson et al. \(2005\)](#).

If the gas temperature is known, it is straightforward to account for the thermal contribution to the linewidth and in turn determine the non-thermal contribution.

One way to try to understand the observed emission is to hypothesise that it can be described as a sum of many individual ideal Gaussian components, all of which arise from some well defined volume of gas. Identifying such Gaussian components from the observed data would then be a useful tool to study the properties of those volumes of gas. Figure 1.2 illustrates this concept with two example spectra for the case of a single component and two blended emission lines. For the single emission line the approximation with the Gaussian component yields straightforward information about the column density, bulk motion, and line of sight velocity dispersion of the gas that can be determined from the integrated area, centroid position, and dispersion of the Gaussian. In the case of the spectrum consisting of two blended emission peaks, a separation or Gaussian decomposition of the emission profile into individual components is necessary to obtain the correct bulk motions of the gas and avoid overestimating the amount of the non-thermal contribution to the linewidth.

PPV cubes offer the advantage of a straightforward visualisation of the intensity and velocity distribution of the gas. By integrating all the emission along the velocity axis we obtain a zeroth moment map, which shows us the integrated emission along the line of sight that can be further converted into an H_2 column density (assuming a conversion factor $X_{\text{CO}} = 2 \times 10^{20} \text{ cm}^{-2}/(\text{K km/s})^{-1}$, see [Bolatto et al. 2013](#)). We can also integrate the PPV cube over one of the spatial axes; this gives us a Position-Velocity (PV) diagram, which can be used to identify velocity gradients and can be helpful in separating physically unrelated structures along the line of sight that are



blended in position-position (PP) space but show distinct unconnected features in PV space. The width of the emission along the velocity axis in a PV diagram also gives a first indication about the velocity dispersion present in the molecular gas.

The analysis of CO emission lines is not entirely straightforward, as the line shape can be impacted by various effects, such as optical depth. Knowledge about the behaviour of the different CO isotopologues and their limitations and advantages is thus essential for interpreting the observations. In the following, I discuss why ^{13}CO has emerged as a useful tracer for large mapping surveys.

1.2.3 The advantage of ^{13}CO

As already mentioned, CO is the most abundant molecule in the ISM after H_2 . Although the CO abundance can show strong variations, a canonical $^{12}\text{CO}/\text{H}_2$ abundance ratio of $\sim 1 - 2 \times 10^{-4}$ is in conformity with many independent observations of different ISM environments (e.g. [van Dishoeck et al., 1992](#); [Bergin & Williams, 2017](#), and references therein). Due to its low dipole moment and its low energy spacing between the rotational levels, CO is easily excited at the low temperatures and densities typical for the molecular ISM. The low J transitions of ^{12}CO have thus been the most commonly used tracers of the cold molecular ISM, given their strong emission lines that are easily observed also for more diffuse regions. Unfortunately, the large abundance of ^{12}CO can often lead to optically thick emission, which is especially severe for the $J = 1 - 0$ transition. Photons emitted from CO molecules in the $J = 1$ state in the interior of molecular gas structures will be rapidly absorbed by CO molecules in the $J = 0$ state at the surface layers. Thus the observed CO emission does not reliably trace the full volume of the molecular gas structure. The high optical depths of ^{12}CO result in broader linewidths, which makes it more difficult to separate blended emission lines along the line of sight. Moreover, increased optical depth effects can cause flat-topped or self-absorbed emission features. In addition, opacity effects lead to further broadening of the linewidth ([Hacar et al., 2016](#)).

These problems can be alleviated by switching to less abundant CO isotopologues, such as ^{13}CO . The abundance of ^{13}CO relative to ^{12}CO is determined by the isotopic ratio $^{12}\text{C}/^{13}\text{C}$, which shows a strong decrease with Galactocentric distance, with values of ~ 50 at a distance of about 4 kpc and ~ 70 for the local ISM ([Wilson, 1999](#); [Giannetti et al., 2014](#)). Compared to ^{12}CO , the optical depth of ^{13}CO is much smaller and this tracer is often assumed to be optically thin; however its lower rotational transitions can get optically thick in very dense regions within molecular clouds (e.g. [Hernandez et al., 2011](#); [Pitann et al., 2013](#); [Giannetti et al., 2014](#); [Pon et al., 2016](#); [Barnes et al., 2018](#)). In addition, opacity broadening effects can still be relevant ([Hacar et al., 2016](#)). While observations of higher rotational transitions or even less abundant CO isotopologues (such as C^{18}O) would improve these problems even further, these tracers are more suited for observations of higher density ($n_{\text{H}} \gtrsim 10^3 \text{ cm}^{-3}$) regions¹⁰, as they only show weak emission in lower density regions due to their low abundances. The lowest rotational transitions of ^{13}CO are thus best suited for large

¹⁰ We note that within the densest regions of cores CO isotopologues including C^{18}O can freeze out from the gas-phase onto dust grain surfaces (e.g. [Bergin et al., 2006](#)).



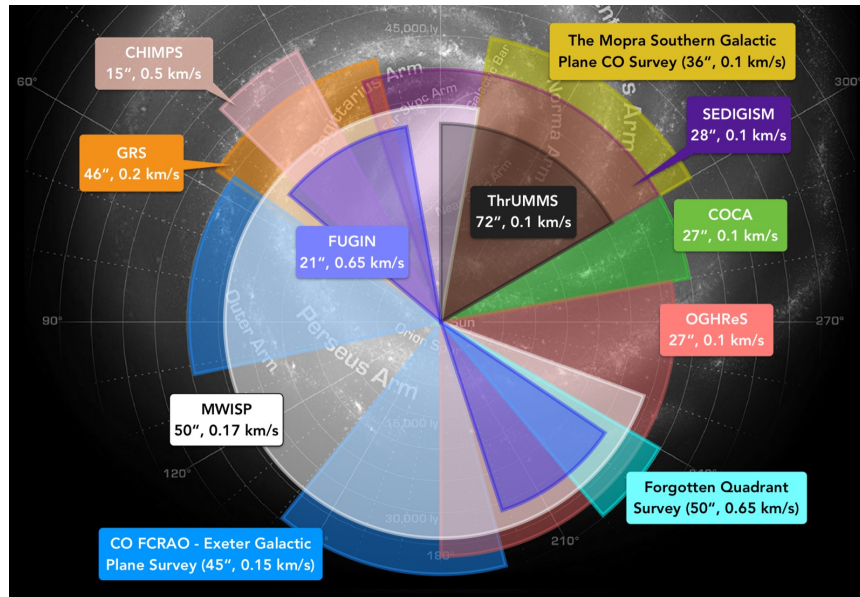


FIGURE 1.3: Overview about recent Galactic plane surveys that targeted a transition of ^{13}CO . Inspired by Fig. 1 in Stanke et al. (2019). Credit background image: NASA/JPL-Caltech/R. Hurt.

mapping observations in the Milky Way, as they offer a good compromise between sensitivity and issues related to optical depth.

1.3 THE DISTRIBUTION OF CO IN THE MILKY WAY

A long-standing problem in astrophysics is how molecular gas, in particular the isotopologues of CO, is distributed in the Milky Way (Combes, 1991; Heyer & Dame, 2015). Knowledge about the location of the molecular gas in our Galaxy is essential to answer important open questions in ISM research, such as the impact and importance of different Galactic environments (e.g. spiral arm and interarm regions) on star formation and ISM structure formation and evolution. Addressing these questions in an unbiased and systematic way requires the detailed analysis of large CO emission line surveys of the Galactic plane.

1.3.1 The importance of Galactic plane surveys

Given the relative ease of observation and the plethora of information they encode, the rotational transitions of the most abundant isotopologues of CO— ^{12}CO , ^{13}CO , and C^{18}O —have been prime targets for large mapping surveys of the Milky Way's disk for a long time. Figure 2 in Heyer & Dame (2015) gives a thorough overview about all large CO surveys of the Galactic plane up until 2015. From the 59 surveys listed, about two thirds were conducted in ^{12}CO (1–0), with the remaining surveys covering either ^{12}CO (2–1) or ^{13}CO (1–0).

^{13}CO has emerged as a prime target for Galactic plane surveys. In Fig. 1.3 and Table 1.2 we give an overview about recent and ongoing large Galactic plane surveys



TABLE 1.2: Details about the Galactic plane surveys shown in Fig. 1.3.

Survey	ℓ coverage	b coverage	^{13}CO	Ref. ^a
Exeter FCRAO CO Galactic Plane Survey	55° – 102°, 141° – 195°	$\geq 1^\circ $, -3.5° – 5.5°	(1-0)	1
FOREST Unbiased Galactic plane Imaging survey with the Nobeyama 45-m telescope (FUGIN)	10° – 50°, 198° – 236°	$\leq 1^\circ $	(1-0)	2
Forgotton Quadrant Survey (FQS)	220° – 240°	0° to -2°	(1-0)	3
Galactic Ring Survey (GRS)	14° – 56°	$\leq 1.1^\circ $	(1-0)	4
Milky Way Imaging Scroll Painting (MWISP)	-10° – 250°	$\leq 5.2^\circ $	(1-0)	5
Mopra Southern Galactic Plane CO Survey	300° – 350°	$\leq 0.5^\circ $	(1-0)	6
Three-mm Ultimate Mopra Milky Way Survey (ThrUMMS)	300° – 360°	$\leq 1^\circ $	(1-0)	7
COCA	280° – 300°	N/A	(2-1)	8
Outer Galaxy High Resolution Survey (OGHReS) ^b	180° – 280°	-2° to 0.5°	(2-1)	9
Structure, excitation, and dynamics of the inner Galactic interstellar medium (SEDIGISM)	-60° – 18°	$\leq 0.5^\circ $	(2-1)	10
$^{13}\text{CO}/\text{C}^{18}\text{O}$ Heterodyne Inner Milky Way Plane Survey (CHIMPS)	28° – 46°	$\leq 0.5^\circ $	(3-2)	11

Notes. Some of the surveys also cover other CO isotopologues, but we only give details about the ^{13}CO observations.

^(a) (1) [Mottram & Brunt \(2010\)](#) and Brunt et al., in prep.; (2) [Umemoto et al. \(2017\)](#); (3) [Benedettini et al. \(2020\)](#); (4) [Jackson et al. \(2006\)](#); (5) [Su et al. \(2019\)](#); (6) [Burton et al. \(2013\)](#) and [Braiding et al. \(2018\)](#); (7) [Barnes et al. \(2015\)](#); (8) Yeh et al., in prep.; (9) König et al., in prep.; (10) [Schuller et al. \(2017\)](#); (11) [Rigby et al. \(2016\)](#).

^(b) The survey follows the warp of the Galactic disk; the latitude coverage is $-2^\circ < b < -1^\circ$ for $280^\circ > \ell > 225^\circ$, then goes up in latitude until $\ell = 205^\circ$, from where the coverage is $-0.5^\circ < b < 0.5^\circ$.

that target a rotational transition of ^{13}CO . Figure 1.3 shows that essentially the entire Galactic disk is covered by ^{13}CO observations in sub-arcmin spatial resolution and sufficient spectral resolution to resolve the thermal linewidth of the cold molecular gas ($\sim 0.2 \text{ km s}^{-1}$), resulting in vast data sets containing hundreds of thousands to millions of spectra.

The prime importance for Galactic plane studies has always been the drive to understand the distribution of the molecular gas within our Galaxy and to make inferences about the structure of the Milky Way (for reviews see [Burton, 1976](#); [Combes, 1991](#); [Heyer & Dame, 2015](#)). Large Galactic plane surveys are also crucial for our understanding of physical processes and structure formation in the ISM of our Galaxy, which requires to go beyond individual case studies and to probe a volume that is relevant for and representative of the Milky Way.

Recent years have seen detailed mapping projects in the main CO isotopologues of nearby molecular clouds, such as Ophiuchus and Perseus ([Ridge et al., 2006](#)), Taurus ([Goldsmith et al., 2008](#)), or Orion ([Kong et al., 2018](#)). These studies focus on a detailed analysis of the physics of star formation on scales that range from a few parsec down to $\sim 10^3 \text{ au}$ and thus provide invaluable insight on the microphysics of star formation—that means the details about how individual stars or multiple-star systems form—on the highest spatial resolution scales attainable. However, these nearby molecular clouds only give a limited sampling of environments within the solar neighbourhood ($\lesssim 500 \text{ pc}$) and are not representative of massive star-forming regions in the Galactic disk. [Murray \(2011\)](#) estimated that about 30% of the star formation in the Milky Way takes place in 32 GMCs that account for $\sim 6\%$ of the molecular gas mass of our Galaxy; the average mass of these GMCs ($1.5 \times 10^6 M_{\odot}$) exceeds the average mass of nearby ($\lesssim 300 \text{ pc}$) molecular clouds by almost 3 orders of magnitude ([Heiderman et al., 2010](#)). To put the results of nearby molecular clouds into a galactic context and probe a larger sample of environmental conditions and ISM structures we thus need observations of a significant fraction of the molecular ISM of the Milky Way with at least moderate spatial and spectral resolutions, which is provided by Galactic plane surveys.

Moreover, large single-dish Galactic plane surveys are essential to link Galactic ISM and star formation studies with extragalactic work. Interferometric observations and surveys of the molecular ISM in nearby galaxies, such as the Physics at High Angular resolution in Nearby GalaxieS–Atacama Large Millimetre/Submillimetre Array survey (PHANGS–ALMA, e.g. [Schinnerer et al., 2019](#); [Sun et al., 2020](#)), probe the relevant physics at the typical scale of molecular clouds for tens of thousands of these objects. Dedicated studies—such as the Line Emission in Galaxy Observations (LEGO) project ([Kauffmann et al., 2017](#))—will provide detailed line emission analyses for a representative sample of molecular clouds in the Milky Way to help interpret the extragalactic observations. However, Galactic plane surveys are needed to complement these studies by providing the larger Galactic context (that means the Galactic environment) and to enable large statistical analyses and comparisons with the work on nearby galaxies. Galactic plane surveys thus bridge the gap between more dedicated studies of individual molecular clouds and the large cloud statistics provided by extragalactic studies.



The data sets of Galactic plane surveys have provided and continue to provide invaluable information about the CO content and kinematics for individual case studies or samples of molecular clouds (e.g. [Heyer & Dame, 2015](#); [Miville-Deschênes et al., 2017](#)), infrared dark clouds (IRDCs; e.g. [Simon et al., 2006a](#); [Kainulainen & Tan, 2013](#); [Barnes et al., 2018](#); [Zhou et al., 2019](#)), molecular clumps (e.g. [Urquhart et al., 2018](#)), or filaments (e.g. [Zucker et al., 2018](#); [Zhang et al., 2019](#)) covered by these surveys. While for many works the average kinematic properties of the observations have been of prime interest, some studies have further analysed the detailed velocity structure of their objects by exploiting the full spatial and spectral resolution of one or more of these surveys (e.g. [Barnes et al., 2018](#)).

There are also studies that used the entire data set of one of the Galactic plane surveys; so far, these have mostly focussed on either the global properties of the gas emission at larger scales to obtain information about the Galactic structure (e.g. [Dame et al., 2001](#); [Nakanishi & Sofue, 2006](#); [Rigby et al., 2016](#); [Roman-Duval et al., 2016](#)) or on segmenting the observed gas emission into molecular clouds, clumps, or filaments (e.g. [Solomon et al., 1987](#); [Rathborne et al., 2009](#); [Rice et al., 2016](#); [Miville-Deschênes et al., 2017](#); [Colombo et al., 2019](#)) to infer useful average physical properties of the gas emission on the scales of these objects in order to put them into context with their location within our Galaxy (e.g. [Roman-Duval et al., 2010](#); [Heyer & Dame, 2015](#); [Miville-Deschênes et al., 2017](#)). However, the analysis of Galactic plane surveys requires the determination of distances to the gas emission to permit a homogeneous analysis and comparison across different Galactic environments, accounting for differences in spatial resolution introduced by our vantage point inside the Galactic disk.

1.3.2 *The presence of Galactic features in longitude-velocity diagrams*

I now discuss how the presence of Galactic features such as spiral arms manifests itself in our observations, providing important context for our discussions about Galactic structure in Chapters 3 and 4. We assume a flat rotation curve, $\Theta(R_{\text{gal}}) = \Theta_0$, meaning the value of the rotation curve at a Galactocentric radius R_{gal} is assumed to be equal to the rotational velocity Θ_0 of the orbit of the Sun at a radius of R_0 (the distance to the Galactic centre). Using $R_0 = 8.15$ kpc and $\Theta_0 = 236$ km s⁻¹ from [Reid et al. \(2019\)](#), we overplot curves of constant projected v_{LSR} (i.e. the velocity difference to the local standard of rest) on an artist’s impression of a face-on view of the Milky Way (left panels in Fig. 1.4). Assuming that the gas motion is strictly determined by the Galactic rotation curve, each curve of constant projected v_{LSR} thus gives the location of all the gas that would cause these observed v_{LSR} values. Inside the solar circle ($R_{\text{gal}} < R_0$) the emission lines in the first and fourth quadrant are ‘redshifted’ and ‘blueshifted’ with respect to an emission line in the LSR frame, whereas this is reversed for locations outside the solar circle ($R_{\text{gal}} > R_0$). Gas moving on the same orbit as the Sun has v_{LSR} values close to zero.

In the upper panel of Fig. 1.4, I illustrate how three circular gas orbits at different Galactic radii would appear in our observations in a longitude-velocity (or PV) diagram (Sect. 1.2), using real data from the CfA 1.2 m CO Survey ([Dame et al. 2001](#); right panels in Fig. 1.4). I further show the intersection points of a line of sight at



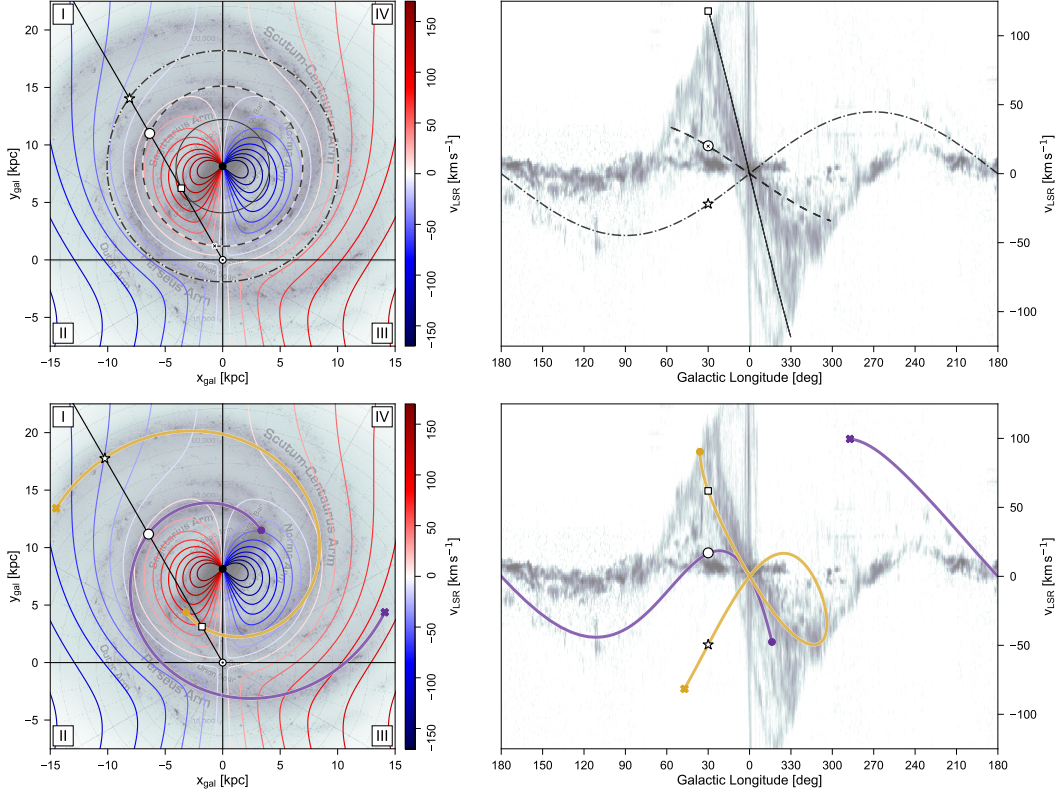


FIGURE 1.4: Illustration of the appearance of Galactic features in emission line observations. The *left panels* show face-on views of an artist's impression of the Milky Way (credit: NASA/JPL-Caltech/R. Hurt), with the four Galactic quadrants marked with Roman numerals. The coloured lines show curves of constant projected v_{LSR} based on an assumed flat Galactic rotation curve. Consecutive v_{LSR} curves differ by 20 km s^{-1} . The \odot symbol and the filled black circle indicate the position of the Sun and the Galactic centre, respectively. The *right panels* show observed PV or longitude-velocity diagrams of the CfA 1.2 m CO Survey from Dame et al. (2001). In the *upper left panel* we show three circular orbits with radii of 4 kpc (solid), 7 kpc (dashed), and 10 kpc (dash-dotted). The black line indicates a line of sight at $\ell = 30^\circ$ that intersects with the three orbits on either the near side (cross), the tangent point (square), or the far side (circle and star). In the *lower left panel* we trace the position of the Scutum-Centaurus and Perseus arms with logarithmic spirals (in gold and purple, respectively). The coloured dots and crosses mark the start and end positions of the arms for easier identification in the longitude-velocity diagram. The black line again indicates a line of sight at $\ell = 30^\circ$ with the corresponding intersections with the logarithmic spirals marked with the square, circle, and star symbols. The *right panels* show how the circular orbits and logarithmic spirals would appear in the observations. See Sect. 1.3.3 for more details.



$\ell = 30^\circ$ with these orbits. For the outermost orbit beyond the solar circle (dash-dotted line) there is a unique mapping of locations in the face-on view to points in the PV diagram, which means that the observed v_{LSR} values can be transformed to a single distance solution. For an orbit inside the solar circle (dashed line) the mapping of locations in the face-on view to points in the PV diagram is not unique and for each line of sight two distance solutions are compatible with an observed v_{LSR} value. The PV diagram shows that in this case the circular orbit approximates a straight line. The minimum and maximum v_{LSR} values associated with a circular orbit correspond to the so-called tangent point positions. The tangent point is the only location inside the solar orbit where an observed v_{LSR} value yields a unique distance solution.

In the lower panels of Fig. 1.4, I illustrate how spiral arm structures would appear in the PV diagram. For distances $\lesssim 8$ kpc the assumed spiral arm model corresponds well with observed CO structures, whereas for farther distances there is only weak detection of CO emission due to the limited spatial resolution and sensitivity of the survey, obscuration of the far Galactic disk by the Galactic centre, and a decrease in the number density of molecular clouds (which have lower surface densities) in the outskirts of the Galaxy (Dame et al., 2001; Rice et al., 2016; Miville-Deschênes et al., 2017). We can also see that spiral arm positions can show a substantial overlap in the PV diagram. This can make it very difficult to correctly separate large-scale Galactic structure in observational data. Nonetheless, Fig. 1.4 shows that we can translate data points from the PPV observations into so-called kinematic distances, which is the most commonly used method to establish distances to molecular gas structures. In the following, I introduce the kinematic distance method and discuss some of its major shortcomings.

1.3.3 Kinematic distances

As we have seen, molecular gas observations entail information about the radial velocity of the gas emission along the line of sight (v_{LSR}), which many Galactic plane studies have used in conjunction with an assumed model for the rotation curve of our Galaxy to estimate distances via the kinematic distance (KD) method (e.g. Roman-Duval et al., 2009; Roman-Duval et al., 2016; Elia et al., 2017; Miville-Deschênes et al., 2017).

Figure 1.5 illustrates the basic geometric configuration relevant for the determination of kinematic distances. For simplicity we assume that the gas moves in perfectly circular orbits around the Galactic centre and that its orbital velocity is determined by a Galactic rotation curve. The observed v_{LSR} position of an emission line then corresponds to the line of sight component of this orbital velocity. This observed radial velocity v_{LSR} of a point along Galactic longitude ℓ is given as

$$v_{\text{LSR}} = R_0 \sin \ell \left(\frac{\Theta(R_{\text{gal}})}{R_{\text{gal}}} - \frac{\Theta_0}{R_0} \right). \quad (1.22)$$

By rearranging this equation we can solve for R_{gal} and use it to determine the heliocentric or kinematic distance to the position along the respective orbit that yields the observed v_{LSR} value. However, inside the solar circle (i.e. $R_{\text{gal}} < R_0$) there are two points along the line of sight that produce the same radial velocity v_{LSR} and



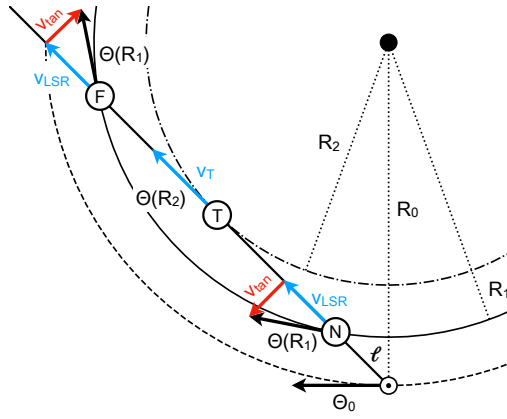


FIGURE 1.5: Illustration of Galactic rotation and observed radial velocities. The \odot symbol and the filled black circle indicate the position of the Sun and the Galactic centre. Vectors indicate the orbital velocity (Θ , black), tangential velocity (v_{tan} , red), and radial velocity (v_{LSR} , blue). Inside the solar orbit (dashed), there are two points along the line of sight that result in the same observed v_{LSR} , the near (N) and far (F) position; the observed radial velocity is at a maximum at the tangent point (T) position. See Sect. 1.3.3 for more details.

we consequently get two distance solutions, the *near* and *far* kinematic distance (see Fig. 1.5). This problem has been termed the kinematic distance ambiguity (KDA). Additional information is needed to resolve the KDA and previous studies have utilised an abundance of methods to solve for it by using, for example, H I self absorption (e.g. Jackson et al., 2002; Anderson & Bania, 2009; Roman-Duval et al., 2009; Wienen et al., 2012; Urquhart et al., 2018), H I emission/absorption (e.g. Anderson & Bania, 2009), association with IRDCs (e.g. Simon et al., 2006a), or the use of scaling relationships (e.g. Rice et al., 2016; Miville-Deschênes et al., 2017). The only exception to this ambiguity occurs at the tangent point, where the observed v_{LSR} value corresponds exactly to the orbital velocity. For a given line of sight, this tangent point also corresponds to the smallest observable R_{gal} distance and an extreme value in the measured v_{LSR} .

Another problem of the kinematic distance method is that since it is based on a model for the Galactic rotation curve it assumes the gas to be in rotational equilibrium, whereas the Milky Way is characterised by streaming motions (e.g. Combes, 1991; Reid et al., 2009; López-Corredoira & Sylos Labini, 2019; Reid et al., 2019). Especially around spiral arms we expect strong deviations from purely circular rotation that can reach values of up to 10 km s^{-1} and can lead to large kinematic distance uncertainties of up to 2 – 3 kpc (e.g. Burton, 1971; Liszt & Burton, 1981; Stark & Brand, 1989; Gómez, 2006; Reid et al., 2009; Ramón-Fox & Bonnell, 2018). Moreover, the non-axisymmetric potential introduced by the Galactic bar causes large non-circular motions in the gas within Galactocentric distances of $\sim 5 \text{ kpc}$ (e.g. Reid et al., 2019). Near the Galactic centre and close to the Sun the observed gas velocity has also almost no radial component which yields large distance uncertainties (see e.g. the kinematic distance avoidance zones in Fig. 1 of Ellsworth-Bowers et al., 2015).



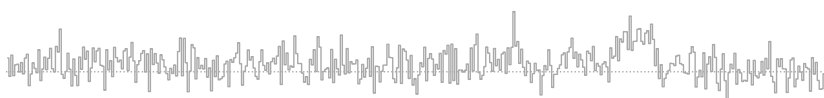
1.3.4 *The impact of spiral arms on molecular gas properties*

Notwithstanding all the issues in establishing reliable distances, many studies of molecular clouds obtained from $^{12}\text{CO}(1-0)$ or $^{13}\text{CO}(1-0)$ surveys have tried to identify their position within the Galaxy (e.g. [Combes, 1991](#); [Heyer & Dame, 2015](#); [Rice et al., 2016](#); [Miville-Deschênes et al., 2017](#)) and have found large variations in how well the clouds trace the gaseous spiral arm structure and the fraction of clouds located in interarm regions. In terms of star formation, some theories predict an enhancement in spiral arms due to effects of gravitational instabilities, cloud collisions, and orbit crowding (e.g. [Elmegreen, 2009](#)). Even though sites of massive star formation seem to be predominantly associated with gaseous spiral arms (e.g. [Urquhart et al., 2018](#)), recent studies have found no significant impact of Galactic structure on the (star) formation efficiency of dense clumps (e.g. [Moore et al., 2012](#); [Eden et al., 2013](#); [2015](#); [Ragan et al., 2016](#); [2018](#)), or the physical properties of filaments ([Schisano et al., 2019](#)) and molecular clumps ([Rigby et al., 2019](#)). However, the last study reported differences in the linewidths between clumps located in interarm and spiral arm structures. A recent study by [Wang et al. \(2020\)](#) also found clear differences in the ratio of atomic to molecular gas between arm and interarm regions.

However, many of these studies used different Galactic rotation curve models and rotation parameters (e.g. [Clemens, 1985](#); [Brand & Blitz, 1993](#); [Reid et al., 2014](#)) in their distance estimation; also different spiral arm models (e.g. [Taylor & Cordes, 1993](#); [Vallee, 1995](#); [Reid et al., 2014](#)) have been used for comparison. The nature, number, and location of the gaseous spiral arms in the Milky Way is still under debate, even though recent years have seen huge progress in our understanding of Galactic structure (see e.g. the recent review from [Xu et al., 2018](#)). In particular, big advances have been made by precise parallax measurements of masers associated with high-mass star-forming regions (e.g. [Reid et al., 2009](#); [2014](#); [2019](#); [VERA collaboration et al., 2020](#)). New distance estimation approaches have emerged that use a Bayesian approach to combine these parallax measurements with additional information from CO and HI surveys ([Reid et al., 2016](#); [2019](#)), which has already been used in estimating distances to molecular clouds and clumps (e.g. [Rice et al., 2016](#); [Urquhart et al., 2018](#); [Rigby et al., 2019](#)). This Bayesian approach is also employed in the distance determinations discussed in Chapter 4.

1.4 STRUCTURE IDENTIFICATION IN THE ISM

In the previous section I discussed why it is important to know how the molecular gas is distributed at large scales within our Galaxy. However, to better understand to what extent physical processes such as turbulence contribute to star formation, we also need to analyse how the gas is distributed more locally, on the scale of individual structures that can range from a few to hundreds of parsec. Many studies have already focussed on defining such structures from Galactic plane surveys, which have been compiled into catalogues of physical objects such as molecular clouds and clumps (e.g. [Solomon et al., 1987](#); [Rathborne et al., 2009](#); [Rice et al., 2016](#); [Miville-Deschênes et al., 2017](#); [Rigby et al., 2019](#)). In this section I give a brief overview about why and how this segmentation is done, discuss problems with this



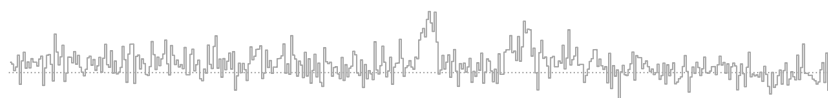
approach, and present an alternative method that is more suited for the analysis of the gas velocity structure.

1.4.1 *The segmentation approach*

The concept of ‘molecular clouds’ has been a staple of observational and theoretical astronomy ever since the first detection of interstellar molecules, such as OH (Weinreb et al., 1963), NH₃ (Cheung et al., 1968), H₂O (Cheung et al., 1969), and CO (Wilson et al., 1970). Compared to H I emission, the CO emission was observed to have a much more clumpy nature (e.g. Burton et al., 1975; Bania, 1977; Clemens et al., 1986), which at least in the earlier observations was partly due to low spatial resolution and low sensitivity. The classification or segmentation of CO emission into cloud- or clump-like structures has thus been a natural and apt description for the observed structures in the earliest CO data sets. Common ISM classifiers—such as clouds and clumps—always had more of an operational function rather than a physical one and are reflective of these former observational limitations. Observations with higher spatial resolution and sensitivity have demonstrated that the cloud-like structures are not isolated entities and show a complex, fractal distribution of the molecular gas (e.g. Scalo, 1990; Falgarone et al., 1991; Elmegreen & Falgarone, 1996). Rather than discrete quasi-static equilibrium structures, molecular clouds seem to be transient high-density regions within a more extended turbulent gas flow (Klessen & Glover, 2016). Most of what we classify as giant molecular clouds might not even be gravitationally bound structures (e.g. Dobbs et al., 2011). Moreover, a significant fraction of the molecular gas can be found in a diffuse state rather than in denser more readily identifiable cloud-like structures (e.g. Pety et al., 2013; Shetty et al., 2014; Roman-Duval et al., 2016).

However, given that a full description of the molecular gas distribution is a difficult and complex endeavour, the segmentation approach has retained its popularity, as it allows for a straightforward way to describe the gas distribution and calculate average quantities for the obtained structures. It is thus not surprising that the analysis of molecular gas structures in the Galactic plane has so far been largely driven by segmentation approaches based on ‘cloud-finding’ or ‘clump-finding’ techniques. Two established algorithms that have been widely used in the identification of molecular cloud structure are GAUSSCLUMPS (Stutzki & Guesten, 1990; Kramer et al., 1998), which iteratively fits and subtracts three-dimensional Gaussians to the data set, and CLUMPFIND (Williams et al., 1994), which is a watershed algorithm that separates structures based on contours defined around local emission peaks. Newer algorithms introduced in recent years perform a more intricate extraction of PPV structures. Examples of such algorithms are FELLWALKER (Berry, 2015), which is an improved version of the CLUMPFIND algorithm; FILFINDER (Koch & Rosolowsky, 2015), which uses the techniques of mathematical morphology to extract filamentary structure; and SCIMES (Colombo et al., 2015), which uses a clustering algorithm on top of the dendrogram method (Rosolowsky et al., 2008) to extract hierarchical structures from the molecular gas observations.

There is no doubt that segmentation approaches are useful and the resulting catalogues of ISM structures have been important for quantifying the mean properties



of cloud-, filament-, or clump-like structures (e.g. [Heyer & Dame, 2015](#)). However, the main problem in segmenting the molecular gas into pre-defined structures is that there is no consensus on the exact definitions and properties of such structures. It can also be challenging to compare the outputs of the segmentation algorithms, as the extracted structures are strongly dependent on the respective algorithm and parameter settings.

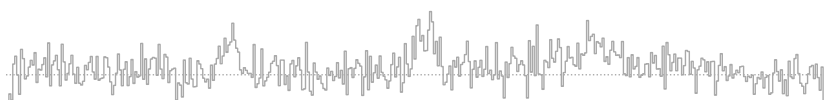
Furthermore, coherent structures identified in the PPV data need not necessarily correspond to contiguous structures in real (position-position-position or PPP) space. The main issue is that the PPV data is a superposition of the density fluctuations and the velocity field, which renders it difficult to infer the true three-dimensional density distribution from it. The morphology present in PPV data is dominated by the line of sight velocity component, which can introduce spurious small-scale structures not present in the density field ([Pichardo et al., 2000](#)). For supersonic turbulence there is in general good correspondence between PPV and PPP structures, whereas for subsonic turbulence the PPV space is dominated by the velocity field ([Burkhart et al., 2013](#)). [Beaumont et al. \(2013\)](#) found that compared to $^{12}\text{CO} (1-0)$ and $^{12}\text{CO} (3-2)$, $^{13}\text{CO} (1-0)$ represents PPP structures in PPV space more faithfully, which they link back to the reduced opacity of this transition. However, care has to be taken when attributing velocity-coherent PPV structures to coherent PPP structures, as the latter can have large velocity gradients and even velocity discontinuities and the PPV representation can suffer from significant line of sight confusion ([Clarke et al., 2018](#)).

Given these pitfalls and caveats of defining structure from PPV data, it seems preferable to complement it with an analysis approach that does not segment the data first into pre-defined physical structures. Such an approach is in particular useful for analysing the velocity structure.

1.4.2 *Going beyond cloud segmentation*

An alternative method to the segmentation approach discussed in the previous section is the statistical analysis of the gas emission, which can give access to information that is not available for segmented data. For instance, turbulence is predicted to manifest itself dominantly in the statistical properties of the gas, and has already been studied extensively in nearby clouds over the last few decades. Examples for velocity statistics that have been used for the characterisation of turbulence properties in molecular clouds are (centroid) velocity probability distribution functions, which can be used to determine the total turbulent mixing energy and large-scale flows or ordered motions such as velocity gradients (e.g. [Miesch et al., 1999](#); [Ossenkopf & Mac Low, 2002](#); [Federrath et al., 2016](#); [Henshaw et al., 2019](#)), and structure functions (e.g. [Ossenkopf & Mac Low, 2002](#); [Heyer & Brunt, 2004](#); [Federrath et al., 2010](#)), which characterise the velocity difference across various spatial scales and are thus sensitive to periodicity in the velocity structure ([Henshaw et al., in press](#)). However, these statistical methods require a good description of the gas kinematics as input, which can be challenging to extract from the observations.

The moment analysis technique is the simplest and most commonly used technique to extract information about the gas kinematics. I have already introduced the zeroth moment (Fig. 1.2), which corresponds to the integrated emission along the spectral



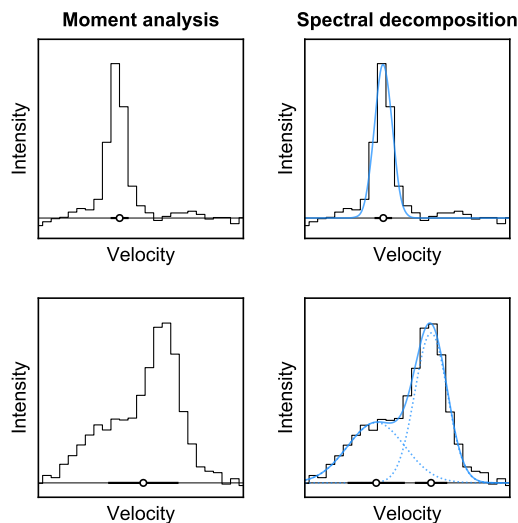


FIGURE 1.6: Comparison between moment analysis and spectral decomposition for a single emission peak (upper panels) and two blended emission lines (lower panels). Open circles and horizontal bars indicate the estimated line centroid positions and velocity dispersion values. Blue lines indicate individual fit components (dotted) and their combined sum (solid).

axis; the first moment defines the intensity-weighted velocity of a spectral line and can be interpreted as the mean or centroid velocity of the gas (open circles in the left panels of Fig. 1.6); and the second moment is defined as the intensity-weighted dispersion of the emission feature (horizontal bars in the left panels of Fig. 1.6) and is a measure for the gas velocity dispersion. Moment analysis generally works well if the integration can be restricted to individual isolated emission lines like the example in the upper panel of Fig. 1.6. However, moment analysis does not yield correct results about the gas kinematics when there are multiple blended emission components along the line of sight (e.g. [Henshaw et al. 2016a](#); see also lower left panel of Fig. 1.6), which is generally the case for observations of the Galactic plane.

A better approach to characterise the gas kinematics is the decomposition of spectra into individual emission peaks (also referred to as velocity components), which allows to disentangle blended emission lines along the line of sight (lower right panel in Fig. 1.6). As already mentioned, Gaussian components are a good match to the observed line shapes of the CO isotopologues in case of low optical depth. Moreover, adopting the Gaussian shape is mathematically simple and leads to a significant reduction in complexity and enables the use of a rich set of available Gaussian statistics tools.

The basic methods of spectral decomposition—in particular using Gaussian fit components—have been in use for a long time, mostly for fitting H I spectra (e.g. [Kaper et al. 1966](#) and references therein; [Mebold 1972](#)). The biggest difference to previously mentioned segmentation algorithms, such as `GAUSSCLUMPS`, is that the spectral decomposition algorithms do not make any assumption on the spatial extent of the gas structures. They are therefore suitable tools for analysing the properties and statistics of the gas velocity structure from large to small scales. In addition, velocity-coherent PPV structures can be recovered from the decomposition results



by running an additional clustering routine on top of the fitting results (see e.g. [Hacar et al., 2013](#); [Miville-Deschênes et al., 2017](#); [Henshaw et al., 2019](#)). This post-hoc segmentation has the advantage that issues due to the blending of individual PPV structures have already been accounted for in the decomposition. Using the spectral decomposition results of Galactic plane surveys as input for a Bayesian distance determination (Sect. 1.3.4) also has enormous potential to improve our knowledge about the Galactic distribution of the molecular gas contained in these data sets.

1.5 MOTIVATION

It has become clear from the discussion so far that many important topics in ISM research, such as the prevalent conditions for the creation and development of large-scale structures and in particular the onset of star formation, are intricately tied to the physics of the molecular gas. We have also seen that there is an enormous amount of useful kinematic information contained in these molecular gas observations, the analysis of which constitutes an essential contribution to our knowledge about which physical processes shape ISM structure. My main motivation for this work is therefore to exploit the detailed velocity structure of molecular gas from Galactic to sub-cloud scales to learn more about the global gas emission properties and possible variations thereof over a significant extent of the Galactic disk. In the following I further outline and motivate the main questions I address in this thesis.

How can we best approach the enormous data sets of Galactic plane surveys without resorting to commonly used segmentation methods? What can be inferred by such an analysis that can complement and go beyond the information that has already been obtained from existing catalogues of clouds and clumps? In recent years, Galactic ISM research has entered a data-intensive era with a rapid increase in large Galactic plane surveys. We require new tools that are able to deal with the complexity of these data sets and that allow us to obtain useful quantities, for example about the detailed kinematics of the gas, without averaging out essential information on small scales. While the categorisation into molecular clouds has been successful in providing us with useful information about the average properties of such structures, this segmentation approach is by design not sensitive to variations and information in between or within the extracted features. Moreover, it is very challenging to compare the results of different segmentation algorithms, especially between different data sets. It is therefore crucial to complement the cloud-scale analyses with an approach that does not segment the gas. To facilitate this, we would ideally like to apply the methods and techniques established for small-scale studies to the large surveys of the Galactic plane. However, studying the detailed velocity structure of any of these Galactic plane surveys requires a significant reduction of the complexity of these data sets. One possible approach is the Gaussian decomposition of the emission lines of each spectrum into individual (velocity) components, which can provide us with invaluable knowledge about the detailed gas velocity structure.

How does the detailed velocity structure of molecular gas look like over a large portion of our Galaxy? How can we use this velocity structure to identify systematic trends linked to physical processes important in the formation of ISM structures? We still lack a study of



the detailed velocity structure of the molecular gas covering a large section of our Galaxy, with sufficient spatial resolution to resolve the inner structure of molecular clouds ($\lesssim 1'$) and sufficient spectral resolution to resolve the thermal linewidth of the cold molecular gas ($\sim 0.2 \text{ km s}^{-1}$). Such a study requires to take advantage of the full data set of one of the more recent large Galactic plane surveys without losing or discarding details of the data by smoothing. Presently, we do not know what this velocity structure looks like and studying it could reveal systematic trends linked to physical processes, for instance, the effects of spiral arms on the gas kinematics in the context of star formation. Knowledge about the detailed dynamics is also of fundamental importance for understanding the cycling of gas within galaxies and it connects ISM research within the Milky Way with new work on nearby galaxies.

How can we use the detailed analysis of the Galactic molecular gas structure to explore synergies with complementary observational tracers? How can such synergies help to better characterise the complexity of the observed features along the line of sight? While molecular gas observations contain plenty of crucial information about the state of the ISM, it is important and instructive to compare and complement this information with other existing large observational studies using different tracers, such as surveys of dust emission and dust extinction. While we fundamentally expect the dust and gas to be well mixed in the ISM, a global comparison of these two tracers can provide critical information about the sensitivity of each of the tracers and can test whether the degree of their correspondence is a function of Galactic environment. Since the velocity information provided by the gas observations allows for a more straightforward separation of structures along the line of sight, it is also a critical key element in disentangling the dust structures, for which such a separation can be more challenging.

How is the molecular gas distributed in our Milky Way? How do the gas properties vary between different Galactic environments, such as spiral arm and interarm regions? The impact of Galactic structure on the properties of interstellar gas and the efficiency of star formation is still under debate. While studies of nearby galaxies already identified intriguing differences between the state of the interstellar gas in different Galactic environments (Colombo et al., 2014), such an analysis is difficult for our own Galaxy given our location within the disk of the Milky Way. One of my main motivations here is to use the currently most precise information about the structure and kinematics of the Milky Way to study the distribution of molecular gas within the Galactic disk. Important key results of such an analysis are the fraction of gas residing in spiral arm and interarm locations and possible variations (or the lack thereof) of gas emission properties with Galactic environment or Galactocentric distance.

In addition to addressing these questions, another main motivation for this work is to present an alternative complementary approach to currently common analysis methods of large ISM surveys. By demonstrating the utility of alternative analysis tools and its data products, the science results presented in this thesis can serve as a guideline and foundation for future investigations of the molecular ISM.



1.6 SCOPE OF THIS THESIS

In this thesis I present a study of the detailed velocity structure of the Galactic Ring Survey, which is a large ^{13}CO (1–0) survey of the inner Galactic plane. I use a new fully automated spectral decomposition package to automatically fit the millions of spectra of this survey at their full spatial and spectral resolution. This approach allows me to simplify the complexity of the observations while retaining their detailed velocity structure and to study the global gas emission properties that can be obtained from it.

In the following chapter I present the newly developed spectral decomposition package `GAUSSPY+`, which is used to automatically fit the ^{13}CO spectra. I discuss in detail the methods and procedures used by `GAUSSPY+` and verify its performance via thorough tests on synthetic spectra and a GRS test field.

In Chapter 3 I expand the spectral decomposition to the entire GRS data set. I discuss the global gas emission properties that can be obtained from the fit results, and use it to characterise the complexity and confusion of the gas emission along the line of sight. I also describe how spectral decomposition can provide a new view about the detailed velocity structure of the gas.

In Chapter 4 I use a Bayesian approach to estimate distances to all fit components from the decomposition results of the GRS. With these distance results, I discuss the Galactic distribution of the ^{13}CO emission and check whether the gas emission properties vary between different Galactic environments.

In Chapter 5 I provide a summary and discuss possible avenues for future work.



GAUSSPY+: A NOVEL DECOMPOSITION PACKAGE FOR EMISSION LINE SPECTRA

Ask her to wait a moment – I am almost done.

— Carl Friedrich Gauss [When told, while working, that his wife was dying.]

Based on [Riener et al. \(2019\)](#), published in *Astronomy & Astrophysics* (628, A78).

As discussed in the previous chapter, the detailed velocity structure of molecular gas contains vital information for addressing the questions of ISM structure formation and evolution and the characterisation of interstellar turbulence. However, the molecular gas data sets can consist of hundreds of thousand to millions of spectra with complex emission line profiles, thus requiring a significant reduction in complexity to enable any further analysis. One approach that has substantial potential is quantifying and analysing the complex spectra by decomposing them into velocity components and then analysing the properties and statistics of these components.

Recently, several semi-automatic (e.g. [Ginsburg & Mirocha, 2011](#); [Hacar et al., 2013](#); [Henshaw et al., 2016a](#); [2019](#)) and fully automated (e.g. [Haud, 2000](#); [Lindner et al., 2015](#); [Miville-Deschênes et al., 2017](#); [Clarke et al., 2018](#); [Marchal et al., 2019](#)) spectral fitting techniques have been introduced. The semi-automated techniques require user interaction, usually in deciding how many velocity components to fit. This can be achieved, for instance, by using spatially smoothed spectra to inform the fit. However, the user-dependent decisions introduce subjectivity to the fitting procedure that reduces reproducibility of the results. The required interactivity with the user can also make it difficult to distribute the analysis to multiple processors. Therefore, while semi-automated approaches are well-suited for small data sets (individual molecular clouds or nearby galaxies at high or low spatial resolution), they can become prohibitively time-consuming for the analysis of big surveys with millions of spectra and components.

The automated methods overcome these drawbacks by removing the user interaction. The initial number of components can either be a guess ([Miville-Deschênes et al., 2017](#); [Marchal et al., 2019](#)) or can be based on the derivatives of the spectrum ([Lindner et al., 2015](#); [Clarke et al., 2018](#)). However, currently these automated routines either: fit the spectra independently from each other ([Lindner et al., 2015](#); [Clarke et al., 2018](#)), which might introduce unphysical differences between the fit results in neighbouring spectra; use a fixed number of velocity components as an initial guess ([Miville-Deschênes et al., 2017](#); [Marchal et al., 2019](#)), which can be computationally expensive; or are not freely available to the community. Also, the current versions of the automated methods listed above are of the ‘first generation’, so there is still potential to improve the decomposition techniques and their applicability to different data sets.

In this chapter I present GAUSSPY+, an automated decomposition package that is based on the existing GAUSSPY algorithm (Lindner et al., 2015), but with physically-motivated developments specifically designed for analysing the dynamics of the ISM. Moreover, I developed GAUSSPY+ with the specific aim of analysing CO surveys of the Galactic plane, such as the GRS (Jackson et al., 2006) and SEDIGISM (Schuller et al., 2017).

The structure of this chapter is as follows. I describe the original GAUSSPY algorithm in Sect. 2.1. I give an overview about the GAUSSPY+ package in Sect. 2.2. In Sects. 2.3–2.5 I present the methods and procedures of GAUSSPY+. I report performance results of GAUSSPY+ on synthetic spectra in Sect. 2.6. In Sect. 2.7 I test the performance of GAUSSPY+ on a GRS test field. I discuss applications, limitations, and recommended settings of the algorithm in Sect. 2.8. I summarise the content of this chapter in Sect. 2.9.

2.1 THE GAUSSPY ALGORITHM

The GAUSSPY¹ algorithm (Lindner et al., 2015) is an autonomous Gaussian decomposition technique for automatically decomposing spectra into Gaussian components. While GAUSSPY was developed for the decomposition of HI spectra (e.g. Murray et al., 2018; Dénes et al., 2018) it can in principle be used for the decomposition of any spectra that can be approximated well by Gaussian functions (e.g. CO).

One of the strengths of the GAUSSPY algorithm is that it automatically determines the initial guesses for Gaussian fit components for each spectrum with a technique called derivative spectroscopy. This technique is based on finding functional maxima and minima in the spectrum to gauge which of the features are real signal peaks. Since the estimation of maxima and minima requires the calculation of higher derivatives (up to the fourth order), an essential preparatory step in GAUSSPY is to smooth the spectra in such a way as to get rid of the noise peaks without smoothing over signal peaks (see Fig. 2 in Lindner et al., 2015). If the data set contains signal peaks that show a limited range in widths, smoothing with a single parameter α_1 may already lead to good results in the fitting. In the original GAUSSPY algorithm users can choose between two different versions of denoising the spectrum before derivatives of the data are calculated: a total variation regularisation algorithm and filtering with a Gaussian kernel. We use exclusively the latter approach, in which the parameter α_1 refers to the size of the Gaussian kernel that is used to Gaussian-filter the spectrum. The decomposition of data sets that show a mix of both narrow and broad linewidths likely requires an additional smoothing parameter α_2 to yield good fitting outcomes. The fitting procedure using a single or two smoothing parameters is referred to as one-phase or two-phase decomposition, respectively.

It is essential for the best performance of the derivative spectroscopy technique to find the optimal smoothing parameters for the original spectra. The GAUSSPY algorithm achieves this via an incorporated supervised machine learning technique, for which the user has to supply the algorithm with a couple of hundred well-fit spectra, from which the algorithm then deduces the best smoothing parameters.

¹ <https://ascl.net/1907.019>



In the training step of GAUSSPY, the algorithm essentially iterates in a controlled manner through different values for the two smoothing parameters and compares the resulting decompositions of the training set with the user-provided corresponding best fit solutions for the spectra. More specifically, GAUSSPY uses the gradient descent technique—a first-order iterative optimisation algorithm—to find values for α_1 and α_2 that yield the most accurate decomposition of the training set. This accuracy is measured via the F_1 score, which is defined as:

$$F_1 = 2 \cdot \frac{\text{precision} \cdot \text{recall}}{\text{precision} + \text{recall}}, \quad (2.1)$$

where precision refers to the fraction of fit components that are correct and recall refers to the fraction of true components that were found in the decomposition of the training set with guesses for α_1 and α_2 . See [Lindner et al. \(2015\)](#) for more details on how the training set is evaluated.

2.2 OVERVIEW ABOUT THE GAUSSPY+ PACKAGE

The methods and procedures described in Sects. 2.3–2.5 are all either new preparatory steps for, or extensions to, the original GAUSSPY algorithm. They aim at either improving the performance of GAUSSPY or automating required preparatory steps. Figure 2.1 presents a schematic outline of the GAUSSPY+ algorithm.

The main shortcomings of the original GAUSSPY algorithm that we aim at improving are: i) the noise values are calculated from a fixed fraction of channels in the spectrum, which is not ideal in cases where signal peaks might occur at all spectral channels; ii) the user has to supply the training set; iii) there is no in-built quality control of the fit results; iv) the fit of each spectrum is treated independently of its neighbours. The last point might lead to drastic jumps between the number of Gaussian components between neighbouring spectra. From a physical point of view we would not expect such component jumps for resolved extended objects with sizes larger than the beam. Moreover, observations are often Nyquist sampled, in which case the beam size or resolution element is larger than the pixel size. Therefore neighbouring pixels will contain part of the same emission, which also introduces coherence between the number of components between neighbouring spectra.

To develop a fitting algorithm that improves on the above points, we have included in GAUSSPY+: i) automated preparatory steps for the noise calculation and creation of the training set (see Sect. 2.3); ii) automated quality checks for the decomposition, some of which can be customised by the user and are used to flag and refit unphysical or unwanted fit solutions (see Sect. 2.4); iii) automated routines that check the spatial coherence of the decomposition and in case of conflicting results try to refit the spectrum based on neighbouring fits (see Sect. 2.5).

In the next section, the GAUSSPY+ algorithm is described in detail, following the outline presented in Fig. 2.1. A description of GAUSSPY+ keywords including their default values and other symbols used throughout the thesis can be found in the App. A.7.



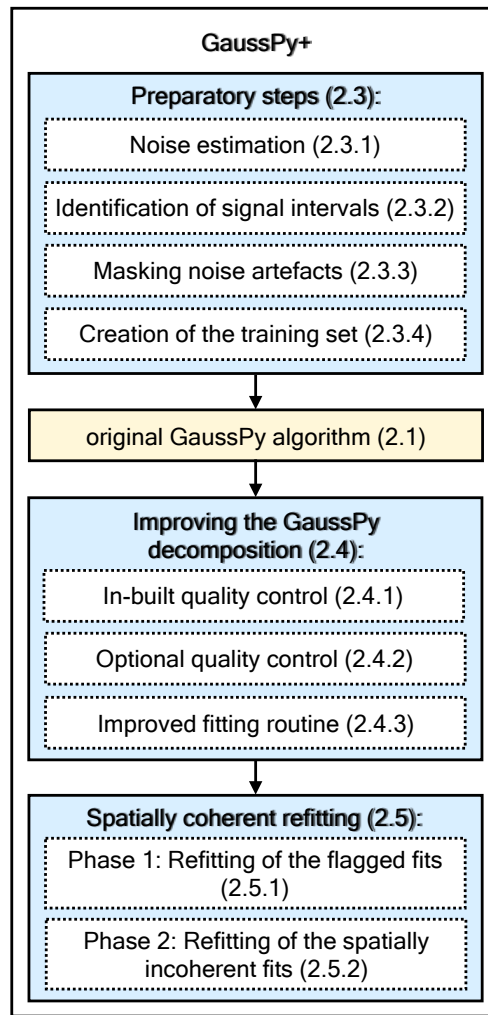


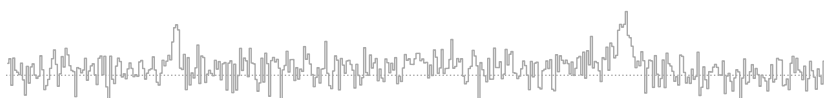
FIGURE 2.1: Schematic outline describing new automated methods and procedures included in GAUSSPY+, along with corresponding sections in this chapter.

2.3 PREPARATORY STEPS

2.3.1 *Noise estimation*

The original GAUSSPY algorithm either requires the user to supply noise estimates or uses a certain fraction of the spectral channels, assumed to contain no signal, for the noise estimation. However, the latter approach only leads to correct noise estimates if one can exclude the presence of signal peaks in the spectral channels used to calculate the noise.

A reliable noise estimation is of fundamental importance for the decomposition—key steps of GAUSSPY depend on the noise value, and also the new procedures in GAUSSPY+ rely on accurate noise estimation: the signal-to-noise (S/N) threshold is used for the initial guess for the number of components in GAUSSPY and the noise estimate is needed for the quality assessments of the fit components in GAUSSPY+.



Because of the key role of the noise, we developed a new, automated noise estimation routine as a preparatory step for the decomposition.

The fundamental, underlying assumptions in our noise estimation process are: i) the noise statistics are Gaussian, meaning ‘white noise’; ii) the spectral channels are uncorrelated; and iii) the noise is fluctuating around a baseline of zero. These assumptions enable us to make use of the number statistics of negative and positive channels in the noise estimation process (elaborated further in item 1 below).

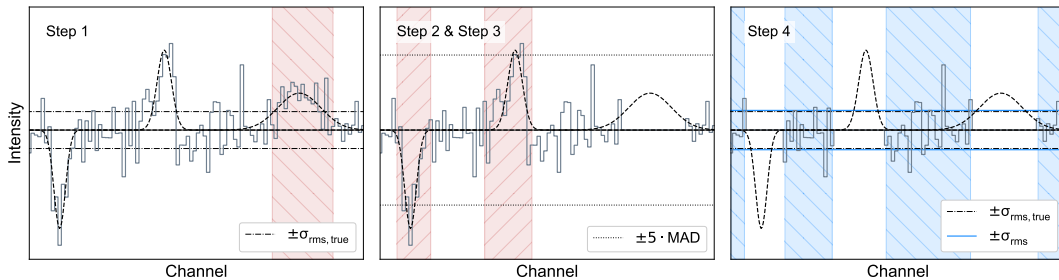


FIGURE 2.2: Illustration of our automated noise estimation routine for a mock spectrum containing two signal peaks and a negative noise spike. Hatched red areas indicate spectral channels that are masked out and hatched blue areas indicate all remaining spectral channels used in the noise calculation. *Right panel:* Comparison of the true noise value ($\sigma_{\text{rms, true}}$; black dash-dotted lines) with the noise value estimated by our automated routine (σ_{rms} , blue solid lines). See Sect. 2.3.1 for more details.

In the following, we describe how our automated noise estimation proceeds. The overall idea is to identify the spectral channels that can be used for noise estimation and maximise their number. To do so, the routine has to identify as many channels as possible that are free from signal and instrumental effects. We demonstrate the steps of the process for a mock spectrum in Fig. 2.2. The spectrum has 100 channels and contains two challenging features for the noise estimation: a negative noise spike in the first few channels and a broad signal feature with a maximum amplitude of two times the root-mean-square (rms) noise σ_{rms} .

The steps to estimate the noise are the following:

1. Mask out broad features in the spectrum; such features are likely to be either positive signal or instrumental artefacts due to, for instance, insufficient baseline corrections. Given our basic assumptions (see above), spectra containing (only) noise have the same number of positive and negative spectral channels on average. We can use this fact to determine the probability of having a number of consecutive positive or negative channels in the spectrum, meaning the probability that a given feature is noise (instead of a signal peak or an artefact). This provides a mean to mask out features that are likely not noise. We estimate the probability that a consecutive number of positive or negative channels is due to noise with a Markov chain (see App. A.1 for more details). We then mask out all features whose probability to be caused by noise is below a user-defined threshold P_{Limit} . For the example spectrum in Fig. 2.2 we used the default value



of $P_{\text{Limit}} = 2\%^2$. From the Markov chain calculations for a spectrum with 100 spectral channels we get that all features with more than twelve consecutive positive or negative channels have a probability less than $P_{\text{Limit}} = 2\%$ to be the result of random noise fluctuations and are thus masked out (one spectral feature; see left panel in Fig. 2.2). In many cases, peaks will still continue on both sides of the identified consecutive channels. To take this into account, the user can specify how many additional channels N_{pad} will be masked out on both sides of the identified feature. In the example spectrum (Fig. 2.2) we set $N_{\text{pad}} = 2$, so two additional channels on both sides of the identified features got masked out.

2. Use the unmasked negative channels to calculate their median absolute deviation (MAD). We use the MAD statistic because it is very robust against outliers in the data set, such as noise spikes. The relationship of MAD to the standard deviation σ is $\text{MAD} \approx 0.67\sigma$. We restrict the calculation of the MAD to spectral channels with negative values, since the positive channels can still contain multiple narrow high signal peaks that were not identified in the previous step. Narrow negative spikes will still be included in this calculation but we assume that their presence is sufficiently uncommon so that they will not significantly affect the estimation of the MAD.
3. Identify intensity values with absolute value higher than $5 \times \text{MAD}$. We then mask out all consecutively negative or positive channels of all features that contain an intensity value higher than $\pm 5 \times \text{MAD}$.³ The mask is extended again on both sides by the user-defined number of channels N_{pad} . In the example spectrum, two regions are masked out in this step (middle panel in Fig. 2.2), corresponding to the second positive signal and the negative noise spike in the spectrum.
4. Use all remaining unmasked channels to calculate the rms noise. The example spectrum is left with 51 unmasked channels (blue hatched areas in the right panel of Fig. 2.2) from which the noise is estimated.

The right panel of Fig. 2.2 shows the determined σ_{rms} value (blue solid line), which is very close to the true value $\sigma_{\text{rms,true}}$ (black dash-dotted line) that was used to generate the noise. This example represents a case in which estimating the noise from a fixed fraction of channels in the beginning or the end of the spectrum would obviously not work well. Had we estimated the noise with the first or last 20% of spectral channels, we would have overestimated the noise by factors of 2.3 and 1.3, respectively.

In case of residual continuum in the spectrum or signal peaks covering almost all of the spectral channels, the noise estimation can be skewed and biased towards low

² $P_{\text{Limit}} = 2\%$ yielded good results in our tests and represents a good compromise between excluding signal peaks with low-amplitude values from the noise estimation without masking out too many noise features.

³ We choose $\pm 5 \times \text{MAD}$ as our threshold because it is a good trade-off: lower thresholds would remove too many valid noise peaks and higher thresholds could miss too many narrow signal peaks with low amplitude values.



values. To circumvent this problem, the user can supply an average noise value $\langle\sigma_{\text{rms}}\rangle$ or calculate $\langle\sigma_{\text{rms}}\rangle$ directly from the data cube by randomly sampling a specified number of spectra throughout the cube. This $\langle\sigma_{\text{rms}}\rangle$ value is adopted instead of the value resulting from steps 1–4 above, if 1) the fraction of spectral channels available for noise calculation from steps 1–4 is less than a user-defined value (default: 10%), and 2) the noise value resulting from steps 1–4 is less than a user-defined fraction of $\langle\sigma_{\text{rms}}\rangle$ (default: 10%)⁴. If no $\langle\sigma_{\text{rms}}\rangle$ value is supplied or calculated, the spectra that do not reach the required minimum fraction of spectral channels for the noise calculation are masked out.

We performed thorough testing of the effects of random noise fluctuations on our noise estimation routine. A detailed description of the tests is given in App. A.2.2. The tests showed that the routine is robust in typical situations (pure white noise, white noise with signal, white noise with signal and negative noise spikes, white noise with weak signal and negative noise spikes).

2.3.2 Identification of signal intervals

If a spectrum contains a high fraction of signal-free spectral channels, goodness of fit calculations can be completely dominated by noise and their value thus may decrease to acceptable numbers even in cases for which the fit did not work out. Therefore, we added a routine to GAUSSPY+ that automatically identifies intervals of spectral channels that contain signal; goodness of fit calculations are subsequently restricted to these channels⁵. However, the fitting itself is still performed on all spectral channels.

As part of our automated noise estimation routine (outlined in Sect. 2.3.1) we already identify consecutive positive spectral channels that can potentially contain signal (see Fig. 2.2). We identify these features as signal intervals using a criterion that takes both the S/N ratio and the extent of the feature into account (this criterion is described in more detail in Sect. 2.4.1.3). For spectra that contain a single narrow peak, only a small fraction of the spectrum might be identified as signal interval. To ensure that for such cases the goodness of fit values are not artificially increased by a too small number of spectral channels, the user can require that a minimum number of spectral channels be adopted as signal intervals (N_{min} ; default value: 100). If the signal intervals identified in the spectrum contain fewer channels than required by N_{min} , the size of all individual signal intervals identified in the spectrum is incrementally increased on both sides by N_{pad} , until N_{min} is reached. This incremental padding will not include regions masked out as negative noise spikes (see next section). If no signal intervals could be identified in the spectrum, all channels are used for goodness of fit calculations, even though it is unlikely in this case that there are peaks in the spectrum that will be fit. We tested the performance of the signal interval identification on synthetic spectra and found that it is able to reliably determine

⁴ The default values are deliberately set to low values to target only spectra with anomalies such as severe baseline effects.

⁵ With the exception of one normality test that we perform over the whole channel range. See Sect. 2.4.1.5 and App. A.4.



weak and strong signal peaks without being sensitive to smaller peaks caused by random noise fluctuations (see App. A.2.3).

2.3.3 *Masking noise artefacts*

Spectra can sometimes contain negative noise spikes, which can bias the goodness of fit calculations. In principle, candidate regions with negative noise spikes are already identified in the automated noise estimation routine (Sect. 2.3.1). However, since the MAD-based threshold is set to a conservative value to exclude most of the narrow signal peaks from the noise estimation, it will also incorrectly remove an increased fraction of regular noise peaks or false positives (see the distribution for sample A of our synthetic spectra in Fig. A.2.2). To avoid such contamination of identified noise artefacts by regular noise peaks, the user can decide below which negative value features get masked out by supplying the value in terms of the S/N-ratio (S/N_{spike} ; default value: 5). Setting $S/N_{\text{spike}} = 5$ means that any region of consecutive negative channels that contains at least one channel with a value lower than $-5 \times \sigma_{\text{rms}}$ will get masked out. We tested the performance of the identification of noise spikes on synthetic spectra and found that we are able to reliably mask such features out (see App. A.2.4).

2.3.4 *Creation of the training set*

As described in Sect. 2.1, GAUSSPY needs a sample of already decomposed spectra to determine the smoothing parameters used in the decomposition. In principle, this training set can be composed of synthetic spectra whose noise and emission properties are similar to the data set the user wants to analyse. Another approach is to use actual spectra from the data set for which the user can supply a reliable decomposition. We added a routine to GAUSSPY+ that adopts the latter approach and automatically decomposes a user-defined number of spectra from the data set. These decomposition results are then supplied to GAUSSPY, which uses its machine learning functionality to infer the most appropriate smoothing parameters for the data set.

In principle, we could use GAUSSPY itself to construct decompositions for this training sample by first guessing the smoothing parameters and correcting them accordingly to get good fitting results. However, since it can be tricky and time-consuming to guess the correct smoothing parameters for a data set we added a routine to GAUSSPY+ that decomposes spectra for a training set.

Our key requirement for this decomposition routine was that it should be able to produce high quality fits for a small subset of the data set. We recommend to use training set sizes of about 200–500 decomposed spectra, as these should already give very good values for the smoothing parameter. In principle also larger training sets can be created, but users should be aware that in this case it can become time-consuming to train GAUSSPY, as it might be necessary to use different starting values for the smoothing parameters α_1 and α_2 to make sure that the search for optimal smoothing parameters explored the parameter space properly and did not get stuck



in a local minimum (see Fig. 3 in Lindner et al. 2015). Training sets containing < 200 spectra bear the risk of higher uncertainties for the resulting smoothing parameter values, as incorrectly fitted features in the training set may have a large negative impact on the F_1 score. While deviations of the smoothing parameters from the optimal values will impact the decomposition with GAUSSPY, the improved fitting (Sect. 2.4.3) and spatially coherent refitting (Sect. 2.5) routines in GAUSSPY+ should be able to mitigate such incorrect or insufficient decomposition results. Thus the decomposition of GAUSSPY+ also has a bigger margin for deviations of the smoothing parameters from their optimal values than the decomposition with GAUSSPY, which allows the use of smaller training set sizes.

For the decomposition of the spectra for the training set we use the SLSQP optimisation algorithm and least squares statistic (SLSQPLSQFITTER) of the ASTROPY.MODELING package, which produced good fits to the spectra in our tests of the routine. We have to supply the SLSQPLSQFITTER routine with initial guesses for possible Gaussian fit components. We determine the number of Gaussian fit component candidates and their initial guesses by estimating how many local positive extreme values or maxima are present in the spectrum. To find these local extreme values, we first set all values to zero that are below a user defined S/N threshold (S/N_{\min} ; default value: 3). The remaining positive values are then searched for local maxima. We define a local maximum as a peak that exceeds all values for a minimum number of neighbouring spectral channels on either side of the peak. This required minimum number of spectral channels on either side can be defined by the user with the ζ parameter (default value: 6). To infer a good value for ζ , users are advised to check the shape of the components present in the spectra or make a test run for a small training set size and check the decomposition results (routines for plotting the spectra, decomposition results, and residuals are contained in our method).

Our routine then tries to fit a number of Gaussian components according to the inferred peaks of local positive maxima present in the spectrum. We therefore likely start out with the maximum possible number of Gaussian fit components for the spectrum. The individual fit parameters of each Gaussian parameter (amplitude a_i , mean position μ_i , standard deviation σ_i) are then checked for the following criteria:

- amplitude $a_i \geq S/N_{\min} \times \sigma_{\text{rms}}$
- significance $\mathcal{S}_{\text{fit}} \geq \mathcal{S}_{\min}$. See Sect. 2.4.1.3 for more information about this criterion.
- the standard deviation σ_i is between user defined limits: $\sigma_{\min} \leq \sigma_i \leq \sigma_{\max}$, where the limits for the standard deviation can be specified in terms of the full width at half maximum (FWHM) given as fraction of channels (Θ_{\min} and Θ_{\max} ; default values: 1 and None, respectively).

We do not check if components are blended in the creation of the training set. If any of the individual Gaussian components do not satisfy all these requirements, their values are removed from the list of initial guess values and a new fit is performed. These checks and the subsequent refitting is performed as long as some of the individual Gaussians are not satisfying all the criteria or there are no more Gaussian



parameters remaining. In the process of refitting a spectrum we do not add any new fit component candidates.

We thoroughly tested the routine outlined in this section on samples of synthetic spectra and found that it is able to create reliable training sets that allow inferring optimal smoothing parameters with GAUSSPY (see App. A.2.5). However, we did not optimise the SLSQPLSQFITTER decomposition routine for speed, which is why we recommend to only use this fitting technique for the creation of training sets. See App. A.3.1 for a quantitative comparison between the SLSQPLSQFITTER fitting routine and the improved fitting routine of GAUSSPY+ (Sect. 2.4.3) in terms of execution time and performance of the decomposition.

2.4 IMPROVING THE GAUSSPY DECOMPOSITION

2.4.1 In-built quality control

In this section we describe the automated quality checks for the decomposition results we implemented in GAUSSPY+. If individual Gaussian components do not satisfy one of the criteria outlined in Sects. 2.4.1.1–2.4.1.4 they get discarded.

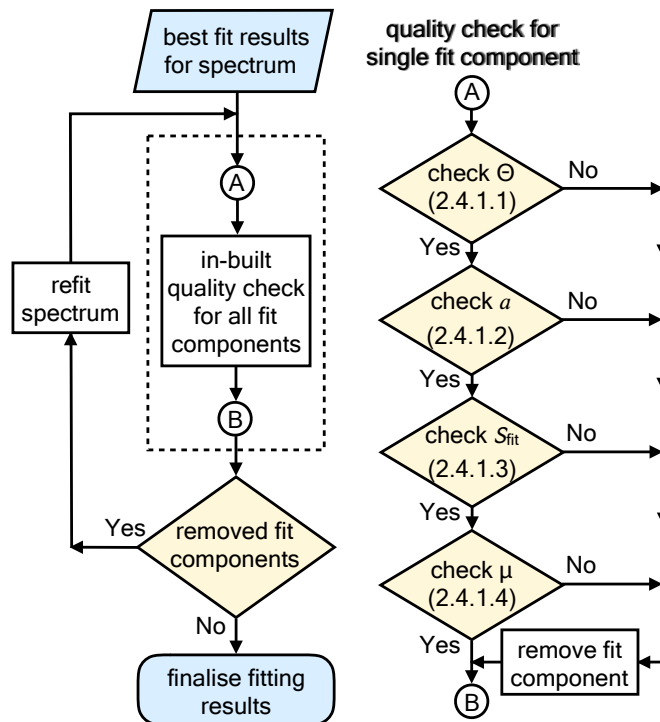


FIGURE 2.3: Flowchart outlining how in-built quality controls from Sects. 2.4.1.1–2.4.1.4 are applied to fit results of a spectrum.

Figure 2.3 illustrates how the in-built quality controls explained in Sects. 2.4.1.1–2.4.1.4 are used to improve the fit results for a spectrum. This refitting procedure using the in-built quality controls is applied to all fit solutions obtained in the decomposition steps of GAUSSPY+ (Sect. 2.4.3–2.5.2). The corrected Akaike information criterion and normality tests for the normalised residual are used to decide



between different fit solutions of a spectrum and to assess whether a spectrum needs to be refitted, respectively; both methods are described in Sect. 2.4.1.5. See also App. A.3.4 for a discussion about the performance of the in-built quality controls on the decomposition results of the synthetic spectra (Sect. 2.6) and the GRS test field (Sect. 2.7).

2.4.1.1 FWHM value

If users supply limits for the lower and upper values of the FWHM (Θ_{\min} and Θ_{\max} , respectively) all fitted components with FWHM values outside this defined range are removed. In the GAUSSPY+ default settings $\Theta_{\min} = 1$, which means that the FWHM value of a fit component has to be at least one spectral channel. By default, GAUSSPY+ does not set any value for Θ_{\max} . Users are advised to use the Θ_{\max} parameter with caution, as it can produce artefacts in the decomposition, such as an increase of the number of fit components whose widths are close to or exactly at this predefined upper limit.

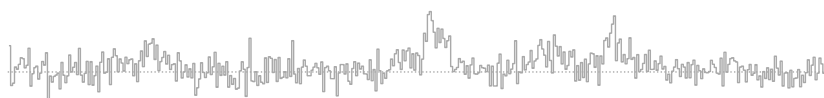
2.4.1.2 Signal-to-noise ratio

The user-defined minimum S/N ratio S/N_{\min} (default value: 3) is in the default settings used as the S/N threshold for: i) the original spectrum and the second derivative of the smoothed spectrum in the GAUSSPY decomposition (i.e. $SNR_1 = S/N_{\min}$ and $SNR_2 = S/N_{\min}$); ii) the search for new peaks in the residual (Sect. 2.4.3); iii) the search for negative residual peaks (i.e. $S/N_{\min, \text{neg}} = S/N_{\min}$, Sect. 2.4.2.1); iv) the decomposition of the training set (Sect. 2.3.4). These parameters can all be set to different values from each other to improve the fitting results but we advise to keep them at the same value for consistency.

The minimum required amplitude values of Gaussian fit components are determined by the $S/N_{\min, \text{fit}}$ parameter, whose default value is half the value of S/N_{\min} . All Gaussian components with $a_i < S/N_{\min, \text{fit}} \times \sigma_{\text{rms}}$ will be removed from the fit. We recommend setting $S/N_{\min, \text{fit}} < S/N_{\min}$ to allow fit components to also converge to an amplitude value that is below S/N_{\min} , as such smaller unfit peaks might otherwise negatively influence the fitting results of higher signal peaks that are close by (see panel b in Fig. 2.5). A smaller value for $S/N_{\min, \text{fit}}$ can also be beneficial if it cannot be excluded that some of the spectra might be affected by insufficient baseline subtraction effects, in which case the spectra would show a very broad but low-amplitude feature that can stretch over all spectral channels. However, the $S/N_{\min, \text{fit}}$ can also be supplied by the user directly in case the default settings do not yield good results.

2.4.1.3 Significance

To further check the validity of fitted Gaussian components, we use the integrated area of the Gaussian as a proxy for the significance of the component. Assuming that the noise properties are Gaussian (white noise), random noise fluctuations are more likely to cause narrow features with a higher amplitude than broader, extended features with a lower amplitude. With this significance criterion we basically require



that the fit components, or data peaks, have either very high intensity or are extended over a wide channel range.

The integrated area W_i of a Gaussian component can be calculated from its amplitude and FWHM value Θ in terms of spectral channels:

$$W_i = a_i \cdot c \cdot \sqrt{2\pi} \quad (2.2)$$

with the parameter c defined as

$$c = \frac{\Theta_i}{2\sqrt{2\ln 2}}. \quad (2.3)$$

For the calculation of the significance value, we compare the area of the Gaussian component to the integrated σ_{rms} interval of the channels from the interval $\mu_i \pm \Theta_i$, which gives a good approximation for the total width of the emission line:

$$\mathcal{S}_{\text{fit}} = \frac{W_i}{\sqrt{2} \cdot \Theta_i \cdot \sigma_{\text{rms}}}. \quad (2.4)$$

The \mathcal{S}_{fit} value is then compared to a user-defined minimum \mathcal{S}_{min} (default value: 5) and the Gaussian component is discarded if $\mathcal{S}_{\text{fit}} < \mathcal{S}_{\text{min}}$. This check helps to remove noise peaks that might have been fit and were not discarded in the checks for the S/N ratio.

We can use the significance parameter also as a threshold to decide whether peaks in the data are valid signal peaks. For this estimate of the significance ($\mathcal{S}_{\text{data}}$), we first search for peaks in the data above the user-defined S/N threshold and then compare the integrated intensity of all positive consecutive channels belonging to this feature to the integrated σ_{rms} interval of the channels spanned by this feature. We discard the peak as a valid signal feature if $\mathcal{S}_{\text{data}} < \mathcal{S}_{\text{min}}$.

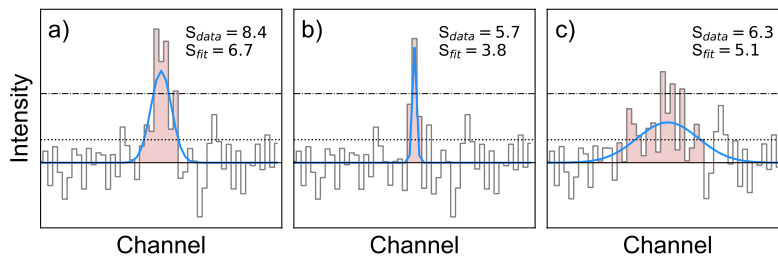


FIGURE 2.4: Calculation of the significance for Gaussian fit components (\mathcal{S}_{fit} ; blue solid lines) or peaks in the data ($\mathcal{S}_{\text{data}}$; red-shaded areas). The dotted and dash-dotted horizontal lines indicate the σ_{rms} value and S/N thresholds of 3, respectively.

Figure 2.4 illustrates this significance measure for three different cases. Panel (a) shows a signal peak and fit component that is very likely corresponding to a true signal, with the significance measures for the data peak and the fit both above the critical default value of 5. Panel (b) shows a data peak with narrow linewidth that might be caused by random fluctuations of the noise. The $\mathcal{S}_{\text{data}}$ value of this feature passes the threshold value $\mathcal{S}_{\text{min}} = 5$, but the depicted Gaussian fit component for this data feature only has a \mathcal{S}_{fit} value of 3.8. This low \mathcal{S}_{fit} value would cause the algorithm to reject this fit component even though its peak has a high S/N ratio of



about 5. Panel (c) shows a broader feature, which has only low S/N values. However, since this feature is spread over more spectral channels than the feature shown in panel (b), we would accept it based on its $\mathcal{S}_{\text{data}}$ value. With the default settings of GAUSSPY+ we would also keep the depicted fit component. As already mentioned in Sect. 2.4.1.2, it can be beneficial to keep Gaussian components with such low S/N ratios in the decomposition results, as to not negatively influence the fitting of nearby data peaks (see panel b in Fig. 2.5).

For a fitted feature or signal peak containing N_{feat} spectral channels, the \mathcal{S}_{min} parameter implies an average S/N ratio $\langle \text{S/N} \rangle$ of

$$\langle \text{S/N} \rangle = \frac{\mathcal{S}_{\text{min}}}{\sqrt{N_{\text{feat}}}}. \quad (2.5)$$

Users can apply this relation to judge which value for \mathcal{S}_{min} is most suitable for their data set. For the default value of $\mathcal{S}_{\text{min}} = 5$, Gaussian fits or signal peaks spanning 4 or 9 spectral channels would require $\langle \text{S/N} \rangle$ values across the feature of 2.5 and ~ 1.7 , respectively. See App. A.3.3 for a discussion about the effects a variation of the S/N_{min} and \mathcal{S} parameters has on the decomposition results.

2.4.1.4 Mean position outside channel range or signal intervals

All Gaussian components whose mean positions μ_i are outside the channel range $[0, N_{\text{chan}}]$ are automatically discarded from the fit. If the mean position of a fit component is located outside the estimated signal intervals (Sect. 2.3.2), we check the significance value of the fitted data peak $\mathcal{S}_{\text{data}}$ (Sect. 2.4.1.3). We discard the corresponding fit component, if $\mathcal{S}_{\text{data}}$ is smaller than the user-defined threshold for the significance \mathcal{S}_{min} .

2.4.1.5 Estimation of the goodness of fit

When we fit a model to data whose errors are Gaussian distributed and homoscedastic, we can arrive at a good fit solution by minimising the chi-squared (χ^2), which is defined as the weighted sum of the squared residuals:

$$\chi^2 = \sum_{i=1}^N \frac{(y_i - Y_i)^2}{\sigma_{\text{rms}}^2}, \quad (2.6)$$

with y_i and Y_i denoting the data and fit value at channel position i , respectively. The reduced chi-square (χ_{red}^2) value is often used as an estimate for the goodness of fit, since it also takes the sample size (in our case the number of spectral channels) and number of fit parameters into account. χ_{red}^2 is defined as the chi-squared per degrees of freedom:

$$\chi_{\text{red}}^2 = \frac{\chi^2}{N - k'}, \quad (2.7)$$

with N being the sample size (in our case this corresponds to the number of considered spectral channels) and k denoting the degrees of freedom, which in the case of a Gaussian decomposition would be three times the number of fitted Gaussian components. It thus may seem straightforward to use the χ_{red}^2 value to judge whether



all signal peaks in a spectrum were fitted, as one would expect $\chi_{\text{red}}^2 \sim 1$ in this case. However, as [Andrae et al. \(2010\)](#) pointed out, in case of non-linear models such as a combination of Gaussian functions, the exact value for k cannot be reliably determined and can vary between 0 and $N - 1$ and need not even stay constant during the fit. The χ_{red}^2 estimate is thus not the best metric to decide between different fit solutions for a spectrum⁶.

A more suited criterion for model selection is the Akaike information criterion (AIC; [Akaike, 1973](#)), which aims for a compromise between the goodness of fit of a model and its simplicity, by penalising the use of a large number of fit components that do not contribute to a significant increase in the fit quality. The AIC is defined as

$$\text{AIC} = 2k - 2 \ln(\hat{L}), \quad (2.8)$$

with \hat{L} being the maximum value of the likelihood function for the model. If the parameters of a model are estimated using the least squares statistic—as in our case—the AIC is given as⁷

$$\text{AIC} = N \cdot \ln \left(\frac{\sum_{i=1}^N (y_i - Y_i)^2}{N} \right) + 2k. \quad (2.9)$$

For small sample sizes, the AIC tends to select models that have too many parameters, meaning that it will overfit the data. Therefore a correction to the AIC was introduced for small sample sizes⁸ – the corrected Akaike information criterion (AICc; [Hurvich & Tsai, 1989](#)) defined as

$$\text{AICc} = \text{AIC} + \frac{2k^2 + 2k}{N - k - 1}. \quad (2.10)$$

We employ the AICc as our model selection criterion to decide between different fit solutions. The AICc value is meaningful only in relative terms, that is if the AICc values for two different fit solutions are compared with each other. In such a comparison, the fit solution with the lower AICc value is preferred as it incorporates a better trade-off between the used number of components and the goodness of fit of the model.

As an alternative to goodness of fit determinations based on the χ_{red}^2 value, [Andrae et al. \(2010\)](#) suggest to check whether the normalised residuals show a Gaussian distribution. We implement this additional goodness of fit criterion in GAUSSPY+ by subjecting the normalised residuals to two different normality tests: the `SCIPY.STATS.KSTEST`, which is a two-sided Kolmogorov-Smirnov test ([Kolmogorov, 1933](#); [Smirnov, 1939](#)); and the `SCIPY.STATS.NORMALTEST`, which is based on [D’Agostino \(1971\)](#) and [D’Agostino & Pearson \(1973\)](#) and analyses the skew and kurtosis of the data points. Both of these normality tests examine the null hypothesis that the residual resembles a normal distribution, as would be expected if we are only left with Gaussian noise after we subtract the fit solution from the data. If the p -value from one of these tests is less than a user-defined threshold (default: 1%),

⁶ We thus use maps of the determined χ_{red}^2 values only for qualitative comparisons in Sect. 2.7.3.

⁷ For a derivation of Eq. 2.9 see e.g. [Banks & Joyner \(2017\)](#).

⁸ [Burnham & Anderson \(1998\)](#) recommend to use the corrected AIC instead of the AIC if $N/k < 40$. If the sample size $N \rightarrow \infty$, the corrected AIC value converges to the AIC value.



we reject the null hypothesis and will try to refit the spectrum. We found that the combined results of these two hypothesis tests allows a robust conclusion of whether the residual is consistent with Gaussian noise (see App. A.4 for more details).

2.4.2 Optional quality control

The automated checks described in the previous section should already help to reject many fit components that are not satisfying our quality requirements. However, depending on the data set, the user might want to flag and refit the decomposition based on more criteria, which we outline in this section.⁹ The quality criteria discussed in this section are used to flag and refit spectra in the improved fitting and spatially coherent refitting routines discussed in Sect. 2.4.3 and Sect. 2.5, respectively¹⁰. See App. A.3.4 for a discussion about the performance of the optional quality controls on the fitting results of the synthetic spectra (Sect. 2.6) and the GRS test field (Sect. 2.7).

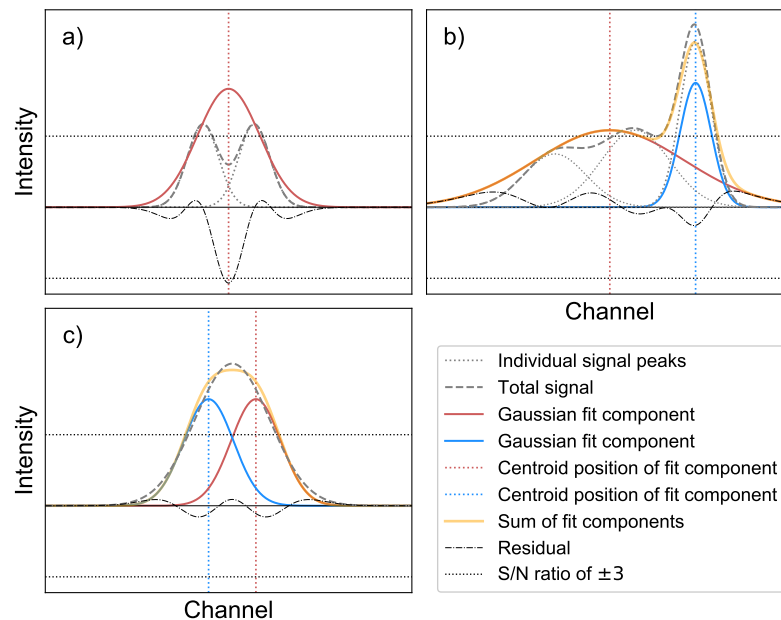


FIGURE 2.5: Optional criteria used to flag fits in the improved fitting routine and in the spatially coherent refitting stage: a) negative residual features introduced by the fit, b) broad components, and c) blended components.

2.4.2.1 Negative peaks in the residual

The first quality check examines negative peaks in the residual, since these can indicate a poor fit. Panel (a) in Fig. 2.5 presents a scenario in which a double peaked profile (shown in dashed grey lines) is fit with a single Gaussian component (red

⁹ All quality checks or flags in this section can be selected or deselected by the user.
¹⁰ The criterion comparing the number of fit components between neighbouring spectra (Sect. 2.4.2.5) is only used in the spatially coherent refitting routines.



line), leading to a significant negative peak in the residual (dash-dotted black line) at the position between the two data peaks. The search for negative peaks in the residual can be controlled by the user with the $S/N_{\min, \text{neg}}$ parameter, which defines the minimum S/N ratio that the negative peak has to have (in the default settings $S/N_{\min, \text{neg}} = S/N_{\min}$). To be flagged as a negative residual feature, a negative peak has to satisfy $|y_i - Y_i| \geq S/N_{\min, \text{neg}} \times \sigma_{\text{rms}}$, with y_i and Y_i denoting the data and corresponding fit value at channel position i . This requirement takes into account that negative peaks could have already been present in the original spectrum and requires that a significant part of the negative peak was introduced by the fit.

2.4.2.2 Gaussian components with a broad FWHM

It can occur that a single, broad Gaussian component is fit over multiple peaks in the spectrum, which can be an undesired property. A broad feature can be caused by peaks being close to the noise limit, multiple blended components, or issues in the data reduction, for instance, insufficient baseline corrections or unsubtracted continuum emission. Panel (b) in Fig. 2.5 shows an example of a broad component that was incorrectly fit over multiple data peaks without introducing significant residual features as in panel (a). This would lead to wrong estimates of the total number of components present in this spectrum, a severe overestimate of the linewidth for the two smaller peaks incorrectly fit with one component, and an underestimate of the amplitude of the rightmost component. The example presented in panel (b) also highlights why it can be beneficial to set the required minimum S/N threshold for fitted component $S/N_{\min, \text{fit}}$ to lower values than the S/N threshold for data peaks S/N_{\min} (see Sect. 2.4.1.2). If $S/N_{\min, \text{fit}}$ were set equal to S/N_{\min} , the fit component for the leftmost peak in panel (b) will get discarded, forcing the fit of a broad component over the two leftmost peaks to minimise the residual.

Unfortunately, it can be difficult to set a maximum allowed FWHM value for the Gaussian components, as the range of expected values in the data may not be known. Setting a strict limit for the maximum FWHM value might also lead to a large number of components which have their linewidth equal to the limiting value. To prevent such an undesired effect, we flag a component as broad if it is broader by a user-defined factor $f_{\ominus, \text{max}}$ (default value: 2) than the second broadest fit component. This obviously does not work for spectra with only one Gaussian component fit, but this case is taken into account during the spatially coherent refitting (Sect. 2.5.1).

Another physical cause for the broadening of the lines could be opacity broadening, which is especially relevant for optically thick emission lines such as the ^{12}CO (1–0) rotational transition (Hacar et al., 2016). In case the user expects opacity broadening for a significant number of spectra in the data set, we recommend to not flag or refit broad fit components.

2.4.2.3 Blended Gaussian components

We define a Gaussian component i as blended with a neighbouring component j , if the distance between their mean positions μ_i and μ_j is less than the minimum required separation μ_{sep} . This minimum required separation is determined by mul-



tipling the lower FWHM value of the two components with a user-defined factor f_{sep} :

$$\mu_{\text{sep}} = f_{\text{sep}} \times \min(\Theta_i, \Theta_j). \quad (2.11)$$

The default value of f_{sep} is $1/\sqrt{2\ln 2}$. This value was chosen so that the required separation between two identical Gaussian components defaults to two times their standard deviation. If two identical Gaussian fit components are separated by a distance larger than two times their standard deviation, their combined signal would have a local minimum between the two peak positions, which we define as a requirement for well resolved Gaussian fit components. Panel (c) in Fig. 2.5 shows a case in which the minimum separation between the peak positions of the two identical Gaussian fit components is not reached. The combined signal of the fit components (shown in orange) shows no local minimum between the peak positions and a single Gaussian component that corresponds to the sum of the two individual components would thus be evaluated as a better fit.

Without additional information from neighbouring spectra it can be very difficult to reliably conclude whether a two-component fit is a better choice than the fit of a single component. If this quality criterion is selected by the user we will therefore always try to replace two blended components with a single bigger component in the improved fitting routine (Sect. 2.4.3), where each spectrum is still treated independently.

2.4.2.4 *Residuals not normally distributed*

This flag checks whether the normalised residuals show a Gaussian distribution. We subject the normalised residual to two different tests for normality (see Sect. 2.4.1.5 for more details), with the null hypothesis that the residual values are normally distributed. We reject this null hypothesis if the p -value of at least one of the normality tests is less than a user-defined threshold (default: 1%), in which case the spectrum gets flagged.

2.4.2.5 *Different number of components compared to neighbouring spectra*

This quality criterion compares the number of fitted Gaussian components of a spectrum with its immediate neighbouring spectra. We include the fit solutions of all neighbouring spectra in this comparison, irrespective of whether they were already flagged by another optional quality criterion. There are two conditions for which a spectrum can be flagged by this check:

- The number of components N_{comp} in the spectrum is different by more than a user defined value ΔN_{max} (default value: 1) from the weighted median number of components determined from all its immediate neighbours. For a sequence of n ordered elements x_1, x_2, \dots, x_n with corresponding positive weights w_1, w_2, \dots, w_n that sum up to w_{tot} , the weighted median is defined as the element x_k for which $\sum_{i=0}^{k-1} w_i < 0.5 \times w_{\text{tot}}$ and $\sum_{i=k+1}^n w_i < 0.5 \times w_{\text{tot}}$. Panel (a) in Fig. 2.6 shows the weights we apply to the immediate neighbours, which are inversely proportional to their distance to the central spectrum.



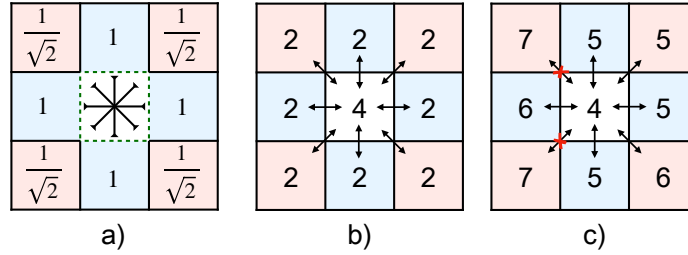


FIGURE 2.6: Illustration of the flagging of spectra based on their number of components with the default settings of our algorithm. Each 3×3 square shows the central spectrum (in white) and the surrounding immediate neighbours coloured according to their weights. *Panel a*: Weights applied to each neighbouring fit solution to calculate their weighted median. *Panels b and c*: Two cases where the fitted number of components of the central spectrum would be flagged as incompatible with the fitted number of components of their neighbours. See Sect. 2.4.2.5 for more details.

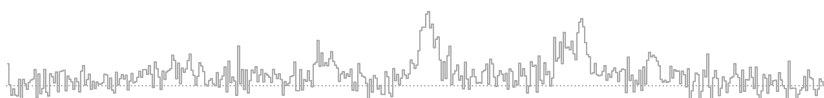
- The spectrum shows differences in N_{comp} towards individual neighbours that exceed a user defined value ΔN_{jump} (default value: 2). We flag a spectrum if these differences occur towards more than N_{jump} (default value: 1) of its neighbouring spectra.

We illustrate this criterion in Fig. 2.6 for two cases and the default settings of GAUSSPY+. Panel (b) shows an instance where the fit solution of the central spectrum shows no component jumps > 2 to any of its neighbours. However, we would still flag the central spectrum for its number of fitted components, since it differs by more than ΔN_{max} to the weighted median number of components as inferred from the neighbouring fit solutions (2 components). Panel (c) shows the opposite case, where the median number of components of 5 is still compatible with the actual number of components but the fit solution of the central spectrum would be flagged as inconsistent with its neighbours as it shows two component jumps > 2 with two of its neighbours.

2.4.3 Improved fitting routine

The improved fitting routine in GAUSSPY+ aims to improve the fitting results of the original GAUSSPY algorithm via the use of the quality controls described in Sect. 2.4.1 and 2.4.2. The original version of GAUSSPY hands over its initial guesses to a least squares minimisation routine without restricting the fitting parameters, apart from a requirement of positive amplitude values. This means that the individual Gaussian components are allowed to freely vary their FWHM and mean positions. Moreover, the number of Gaussian components is set and fixed by the initial guesses, so if GAUSSPY determined that the fit should contain a certain number of Gaussian components, it will try to fit all those components even if one of them does not contribute to improving the fit or is making the fit worse. This unrestricted fitting can lead to unphysical results or conflicting fit solutions between neighbouring spectra (see the quality flags discussed in Sect. 2.4.2).

The general idea of our routine is to try to improve the fit based on the residual and optional user-selected quality criteria (Sect. 2.4.2.1–2.4.2.3). This improved fitting



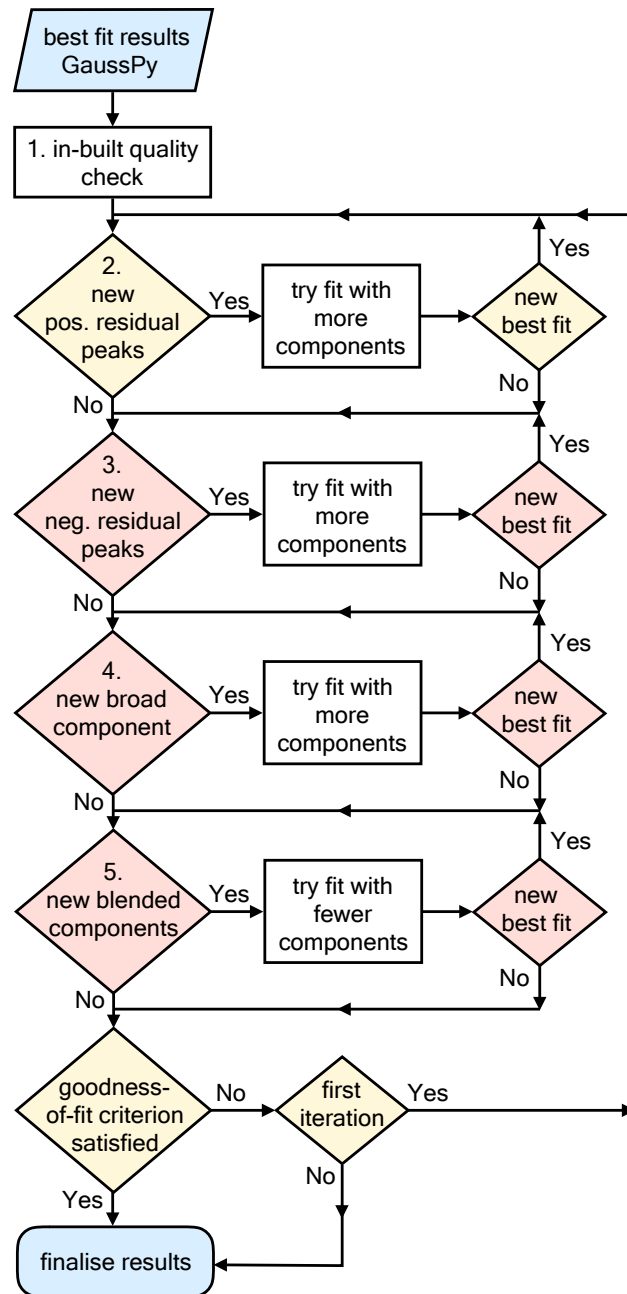


FIGURE 2.7: Flowchart outlining basic steps of our improved fitting routine. The conditional stages in red correspond to optional stages that can be selected by the user. See Sect. 2.4.3 for more details.



phase is applied to every spectrum. The steps of this routine proceed as follows (see also Fig. 2.7):

1. Check the best fit result of GAUSSPY with the quality criteria outlined in Sect. 2.4.1.1–2.4.1.4 (see Fig. 2.3). All Gaussian components not satisfying any of these criteria are removed from the best fit solution of GAUSSPY and the spectrum is refit with the remaining fit components; this procedure gets repeated until all of the leftover fit components satisfy all quality criteria.
2. Try to iteratively improve the fit by adding new Gaussian components based on positive peaks in the residual of the best fit solution. Requirements for the acceptance of residual peaks as additional Gaussian component candidates are that: i) the maximum value of the residual peak is higher than S/N_{\min} ; ii) the consecutive positive spectral channels of the residual peak satisfy the significance criterion $\mathcal{S}_{\text{data}} \geq \mathcal{S}_{\min}$ outlined in Sect. 2.4.1.3. If one or multiple peaks are found in the residual that satisfy these requirements for being new Gaussian component candidates, a refit of the spectrum is performed by adding all of these new candidates. For the refit, the initial Gaussian parameter guesses for the accepted residual peaks are set to: the maximum positive value of the residual peak for the amplitude; the spectral channel containing the maximum positive value of the residual peak for the mean position; the number of consecutive positive channels of the residual peak for the FWHM parameter. After a successful pass of all quality criteria, we adopt the new fit as the new best fit if its AICc value is lower than the AICc value of the previous best fit solution. If a new best fit was chosen, a new iteration with a search for peaks in the residual of the new best fit solution continues. We proceed to the next step if no new positive peaks are found in the residual or no new best fit could be assigned.
3. Optional: Check whether a negative residual feature (Sect. 2.4.2.1) was introduced by the fit components. This check is only performed if it is the first pass through the main loop or a new best fit was assigned. Negative residual features can be indicative of a poor fit with multiple signal peaks fit by a single broad component. In case such a feature is present, we try to replace the broadest Gaussian component at the place of the residual feature with two narrower components. The initial guesses for the two new narrow components are estimated from the residual obtained if the broad component is removed, which proceeds in a similar way as in the previous step. If the new fit with the two narrow components passes all quality requirements and its AICc value is lower than the AICc value of the current best fit, we will assign it as the new best fit and repeat the search for negative residual peaks. In case multiple negative residual features are present in a spectrum, we deal with the features in order of increasing negative residual values, that is we will first try to replace the Gaussian component causing the residual feature that contains the most negative value. We proceed to the next step if no new negative peaks are found in the residual or no new best fit could be assigned.



4. Optional: Check for broad components (Sect. 2.4.2.2). If a broad Gaussian component is present we will try to replace it in this step with multiple narrower components. The number of narrow components and their initial parameter guesses are estimated from the residual we get if the broadest component is removed from the fit. If this results in a new best fit we will repeat this procedure with the resulting next broadest component. We proceed to the next step if no excessively broad component is identified anymore, or no new best fit could be assigned.
5. Optional: Check for blended components (Sect. 2.4.2.3). If this is the case we will try to refit the spectrum by in turn omitting one of the blended components and checking whether the AICc value of the resulting best fit is better than the AICc value of the current best fit. Blended components are omitted in order of increasing amplitude value, that is we will first try to refit the spectrum by excluding the blended component with the lowest amplitude value. If no new best fit is assigned or no blended components are present in the spectrum we exit the improved fitting procedure and finalise the fitting results if the normalised residuals of the best fit solution show a normal distribution, which we verify with two different normality tests (Sect. 2.4.1.5). If this is not the case, we repeat the whole improved fitting procedure beginning with step 2, the search for positive peaks in the residual.

We tested the performance of our improved fitting routine on synthetic spectra and found that it yields a significant improvement in the decomposition compared to the original `GAUSSPY` algorithm. In Sect. 2.6 and App. A.2.6 we give a detailed discussion about the decomposition results for the synthetic spectra.

2.5 SPATIALLY COHERENT REFITTING

So far all steps of the fitting routine treated each spectrum separately and independently from its neighbours. Here we describe a new routine that aims to also incorporate the information from neighbouring spectra and tries to refit spectra according to this information. Our routine proceeds iteratively and starts from the fitting results obtained with the method outlined in the previous section (Sect. 2.4.3). This is different to algorithms such as `SCOUSEPY`, which first start with an averaged spectrum and use its decomposition result to fit the individual spectra. We proceed in a reverse manner: we first produce a sample of high quality fits for each spectrum without regarding their neighbours and then refit them, if it is deemed to be necessary, using the fit solutions of the immediate neighbouring spectra.¹¹

The spatial refitting proceeds in two phases. In phase 1, we try to improve the fit solutions based on a flagging system, for which the fitting results from the previous stage are checked and flagged according to user-selected criteria. We subsequently try to refit each flagged spectrum with the fit solutions from its neighbours and thereby already introduce a limited form of local spatial coherence. In phase 2, we

¹¹ In the current implementation of `GAUSSPY+` we only consider directly neighbouring spectra, whereas algorithms such as `SCOUSEPY` allow the user to also include information from larger spatial areas.



use a weighting system to try to enforce spatial coherence more globally. We check for the entire data set if the Gaussian components of each spectrum are spatially consistent with the neighbouring spectra, by comparing the centroid positions of the Gaussian components. We then try to refit spectra whose Gaussian components show centroid velocity values that are inconsistent with the fit solutions from neighbouring spectra.

2.5.1 Phase 1: Refitting of the flagged fits

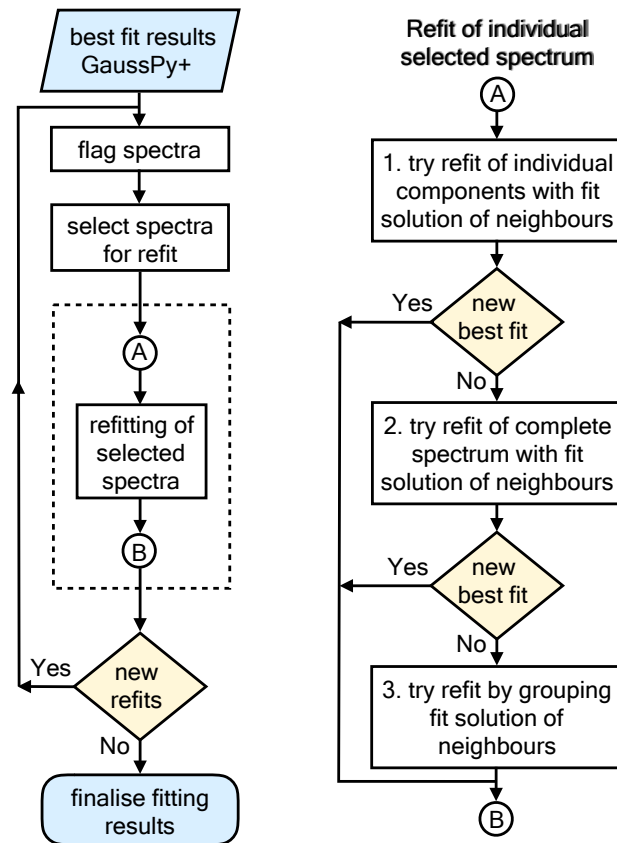


FIGURE 2.8: Flowchart outlining the steps of the first phase of our spatially coherent refitting routine. See Sect. 2.5.1 for more details.

The steps of the first phase of the spatially coherent refitting method are outlined in Fig. 2.8. The idea here is to determine which of the spectra need to be refit based on flags set by the user. We try to refit all spectra that show features that do not satisfy the quality requirements imposed on the fits (these are also retained as flags indicating bad quality fits in case the spectrum cannot be successfully refit). Depending on the data set, the user might not always want to flag or refit spectra that show one or more of these features. Therefore, all of the following flags can be chosen as required by the user. In the current version of GAUSSPY+ the following features can be flagged by the user:

- (i) $\mathcal{F}_{\text{neg. res. peak}}$: The presence of negative peaks in the residual (Sect. 2.4.2.1).



- (ii) \mathcal{F}_Θ : Gaussian components with a broad FWHM value (Sect. 2.4.2.2). For the spatial refitting we additionally flag a component as broad if it is broader by a user-defined factor ($f_{\Theta, \max}$) than the broadest component in more than half of its neighbours.
- (iii) $\mathcal{F}_{\text{blended}}$: The presence of blended Gaussian components in the fit (Sect. 2.4.2.3).
- (iv) $\mathcal{F}_{\text{residual}}$: Fits whose normalised residual values do not pass the tests for normality (Sect. 2.4.2.4).
- (v) $\mathcal{F}_{N_{\text{comp}}}$: The number of components N_{comp} differs significantly from its neighbours (see Sect. 2.4.2.5).

Flags (i)–(v) are recomputed in each new iteration. We then try to refit each flagged spectrum with the help of one or all of the best fit solutions of its neighbouring unflagged spectra. At maximum, this provides eight new different fit solutions for the flagged spectrum (if all of its eight neighbouring spectra are unflagged). If there are multiple unflagged neighbours, they get ranked according to their χ_{red}^2 values, and the neighbouring fit solution with the lowest χ_{red}^2 value is used first.

It is also possible to only flag fit solutions without refitting them, though this has to be selected by the user. This might be useful, for instance, if users want to exclude neighbouring fit solutions whose normalised residuals did not satisfy the normality tests as templates for the refit but do not want to refit these spectra themselves.

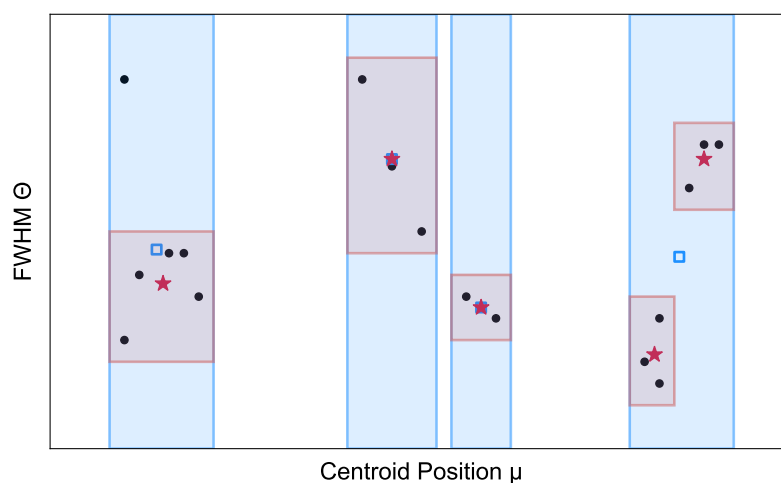
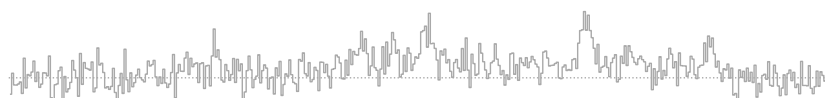


FIGURE 2.9: Illustration of the grouping routine. Black points indicate centroid (μ) and FWHM (Θ) values of Gaussian components from the best fit solutions of unflagged neighbouring spectra. Blue shaded areas indicate the results of the first grouping, in which data points are only separated according to their μ values. Red shaded areas mark the results of the second grouping in which data points are additionally separated according to their Θ values. Blue squares and red stars indicate the initial guesses for the refitting with the first and second grouping approach, respectively.

The refitting of an individual flagged spectrum proceeds in the following way (see right part of Fig. 2.8):



1. Use the fit solutions of unflagged neighbouring spectra to refit individual components of the flagged spectrum. Spectra that are flagged as having negative residual features, broad, or blended components might show a good fit solution apart from the flagged features. Therefore we first try to replace the Gaussian components of such flagged features by using the Gaussian components of neighbouring unflagged fit solutions that cover the same region in the spectrum as new input guesses. The refit attempt is then performed for the entire spectrum by combining these new initial guesses from a neighbouring fit solution with the remaining fit components of the old fit solution of the spectrum that were not affected by the flagged feature. If multiple regions of a spectrum are flagged with different flags we will try to refit the flagged features in the order of: negative residual feature, broad component, blended components. As soon as a flagged feature is successfully refit we stop the refitting iteration, even if other flagged features should still be present in the spectrum. We impose no selection criteria on the neighbouring Gaussian components, that is we will in turn use all unflagged neighbouring fit solutions as new initial guesses, starting with the fit solution that has the lowest χ_{red}^2 value. If one of the input guesses of the unflagged neighbours leads to a new improved fit the refitting of the flagged spectrum is successfully terminated, otherwise we proceed with the next step.
2. Use the fit solutions of unflagged neighbouring spectra to refit the complete flagged spectrum. In this step all fit components of a neighbouring spectrum are used as new input guesses for refitting the entire spectrum. We again loop through all unflagged neighbouring fit solutions, starting with the one that has the lowest χ_{red}^2 value. The refitting of the flagged spectrum is successfully terminated as soon as one of the neighbouring fit solutions leads to a new improved fit, otherwise we continue with the next step.
3. Obtain a new set of fit parameters from the fit solutions of all unflagged neighbouring spectra, by grouping and averaging the parameters of all their Gaussian components in a parameter space spanned by the fitted velocity centroid and FWHM values. Figure 2.9 illustrates how the grouping proceeds. First, the grouping is only performed for the μ values (blue shaded areas). The requirement for group membership is that data points are at maximum located at a distance of $\Delta\mu_{\text{max}}$ (default value: 2 channels) from any other point of this group. We require a minimum group membership of two points, which means that single points that do not belong to any group are treated as outliers. The blue points and shaded areas show the new fitting constraints used for the refitting. As initial guesses for the amplitude, FWHM value and centroid position we use the corresponding average values of all the data points belonging to a group. The fitting constraints for the centroid positions are based on the extent of the groups along the μ axis. For each amplitude value we require that it has a positive value and set its maximum limit to the maximum data point in the original spectrum that occurs in the range that encompasses all μ values of this group multiplied by a user-defined factor f_a . FWHM values are not allowed to be smaller than the user-defined parameter Θ_{min} but there



is no upper constraint for their values. If this first grouping approach does not lead to a successful refit, we use a second grouping approach that additionally groups the data points according to their FWHM values (red shaded areas in Fig. 2.9). A group membership for a data point is established if its μ and Θ values are at maximum located at a distance of $\Delta\mu_{\max}$ (default value: 2 channels) and $\Delta\Theta_{\max}$ (default value: 4 channels), respectively, from any other point of this group. The points in each group are then averaged in a similar way as for the first grouping approach and supplied as new fit parameters for the refitting.

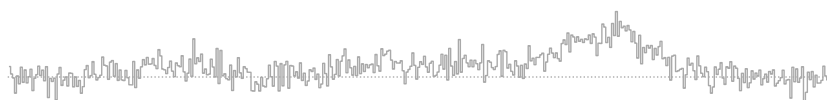
Grouping only by the centroid values has the advantage that it will try to fit the spectrum with the least amount of components inferred from its neighbours. A disadvantage is that outliers in the FWHM regime can negatively influence the initial fit values. The second grouping approach should be able to deal better with the fidelity of the data even though some of the initial guesses for Gaussian fits could overlap strongly.

For the decision of whether to accept a refit as the new fit solution we define a total flag value \mathcal{F}_{tot} that increases by one for each of the user-selected flags the fit solution does not satisfy. For the proposed new fit solutions, the total flag value increases in addition by one for each flagged criterion that got worse than in the current best fit solution, that is for an increase in the number of blended components or negative residual features, broad components that got broader, smaller p -values for the null hypothesis testing for normally-distributed residuals, and a greater difference in the number of components compared to the neighbouring fit solutions.

In the stage where all spectra were treated independently (Sect. 2.4.3), the decision to accept a fit model was made via the AICc. In the spatial refitting phase this decision is mainly guided by the comparison of the total flag value of the new fit solution ($\mathcal{F}_{\text{tot}}^{\text{new}}$) with the old best fit solution ($\mathcal{F}_{\text{tot}}^{\text{old}}$). There are three possible scenarios:

- $\mathcal{F}_{\text{tot}}^{\text{new}} > \mathcal{F}_{\text{tot}}^{\text{old}}$. In this case the new fit solution is rejected.
- $\mathcal{F}_{\text{tot}}^{\text{new}} = \mathcal{F}_{\text{tot}}^{\text{old}}$. The new fit solution is accepted if its AICc value is smaller than the AICc value for the best fit solution we started out with.
- $\mathcal{F}_{\text{tot}}^{\text{new}} < \mathcal{F}_{\text{tot}}^{\text{old}}$. The new fit solution is accepted if the data points of the normalised residual pass the normality tests.

In the last case we have to test whether new fit solutions incorrectly decreased $\mathcal{F}_{\text{tot}}^{\text{new}}$ by removing valid fit components. For example, both $\mathcal{F}_{\text{blended}}$ and \mathcal{F}_{Θ} could be reduced by one if a broad component is deleted. To prevent such incorrect fit solutions we require that the normalised residual resembles a Gaussian distribution, which we check with two different normality tests (see Sect. 2.4.1.5). The null hypothesis of normally distributed residual values gets rejected if the p -value is less than a user-defined threshold (default: 1%), in which case we do not accept the new fit solution.



2.5.2 Phase 2: Refitting of the spatially incoherent fits

In the second phase of the spatially coherent refitting, we check for coherence of the centroid positions of the fitted Gaussian components for all spectra. The motivation for this step is that we would expect coherence in the centroid positions of the fitted Gaussian components for resolved extended objects, especially for oversampled observations where the size of a pixel is smaller than the beam size or resolution element.

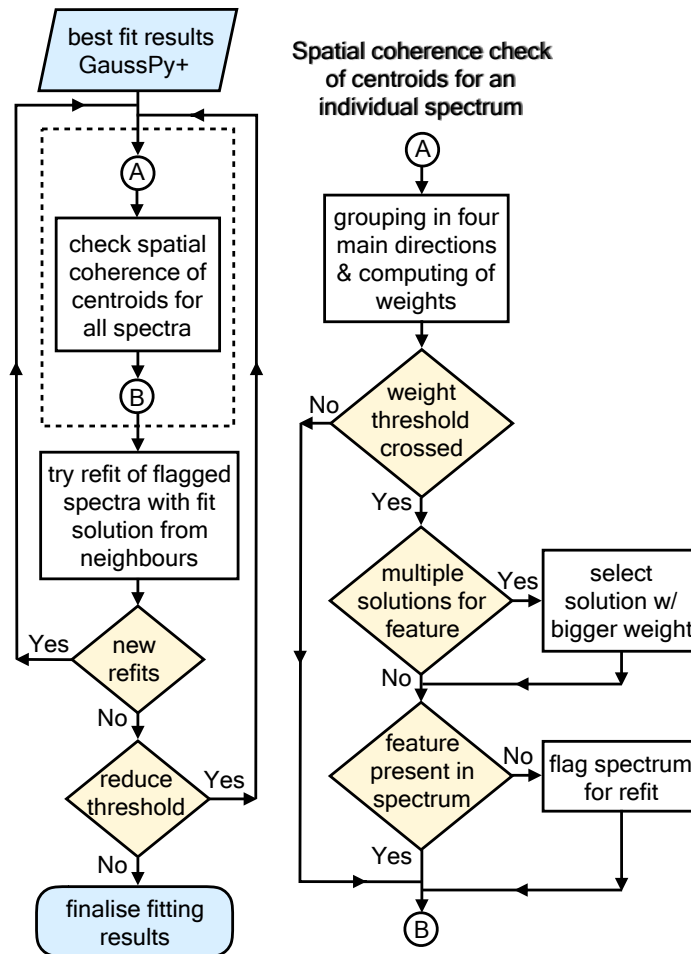


FIGURE 2.10: Flowchart outlining the basic steps of the second phase of the spatial refitting routine. See Sect. 2.5.2 for more details.

The spatial consistency check, in which we determine whether a spectrum should contain Gaussian components in specific spectral ranges based on the fitting results from neighbouring spectra, proceeds in an iterative way. For that, we use 16 neighbours along the 4 main directions (see panel a in Fig. 2.11)¹². For simplicity we do not consider the off-diagonal pixels.

¹² This number is reduced accordingly in case neighbouring spectra are masked out or the central spectrum happens to be close to or at the border of the image.



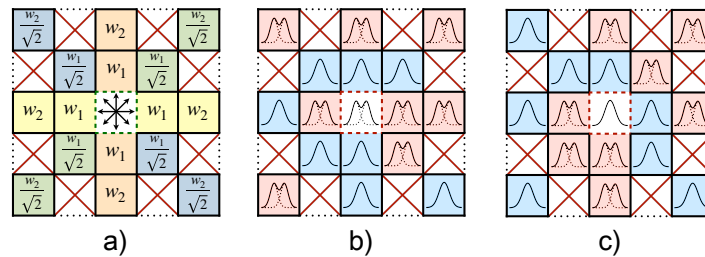
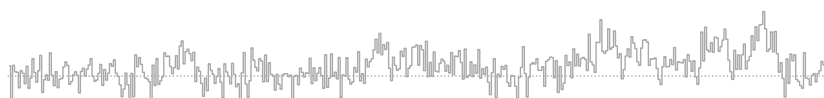


FIGURE 2.11: Illustration of phase two of the spatial refitting routine of GAUSSPY+. Each 5×5 square shows a central spectrum (in white) and its surrounding neighbours. White squares that are crossed out are not considered. The left panel shows the principal directions for which we check for consistency of the centroid positions and shows the applied weights w_1 and w_2 attached to the neighbouring spectra. The middle and right panels show two different example cases with simple fits of one and two Gaussian components shaded in blue and red, respectively. Based on the fits of the neighbouring spectra we would try to refit the central spectrum in the first case (*panel b*) with one Gaussian component, whereas the central spectrum in the second case (*panel c*) is already consistent with what we would expect from our spatial consistency check of the centroid positions. See Sect. 2.5.2 for more details.

Users can specify the ratio of the weight of the closest neighbour (w_1) to the weight of the neighbour located one pixel farther away (w_2) with the parameter $f_w = w_1/w_2$ (default value: 2). In the default settings the contribution of the neighbours is inversely proportional to their distance to the central spectrum (see left panel of Fig. 2.11). The weights w_1 and w_2 are normalised so that $2w_1 + 2w_2 = 1$, which means that along the horizontal and vertical direction the weights sum up to a value of 1. Setting the parameter f_w to higher values than the default value has the effect of decreasing the contribution of neighbours that are located at a distance of two pixels and thus puts even more emphasis on the closest neighbours. In case the central spectrum has Gaussian components whose centroid positions do not match with what would be expected from the fit results of its neighbouring spectra, we try to refit the spectrum with a better-matching fit solution from one of its neighbours.

In the following, we outline the spatial consistency check of the centroid positions in more detail (see also Fig. 2.10):

1. Check for a consistent feature in the neighbouring spectra along any of the main directions indicated in the left panel of Fig. 2.11. For each of the four directions, we group the centroid positions of the fitted Gaussian components as described in Sect. 2.5.1 and shown schematically in Fig. 2.9 (blue shaded areas). We perform the grouping in each direction rather than globally to simplify the grouping, which might get too confused if all 16 neighbours are considered together.
2. Compute the total weight \mathcal{W}_{tot} for each group of centroid position data points by summing up the weights of the neighbouring spectra that contributed data points to the group and check if it exceeds a predefined weight threshold \mathcal{W} .
3. Check whether the central spectrum has Gaussian components compatible with the required Gaussian components inferred from its neighbours (i.e. all centroid position groups that reached the required weight threshold \mathcal{W}). We try to refit



the central spectrum with the fit solution from individual neighbours if its Gaussian components are incompatible with the inferred required components.

In the default settings of GAUSSPY+, the first set of iterations use a weight threshold of $\mathcal{W} = 1 - w_2$; this threshold can only be reached in the horizontal or vertical direction if two immediate spectra and an additional spectrum further out contributed data points to the group, that is show a common feature. The threshold of $\mathcal{W} = 1 - w_2$ is used as long as it leads to new successful refits of spectra. In case no new refits were possible, \mathcal{W} is reduced again by a value of w_2 so that the new threshold is $\mathcal{W} = 1 - 2 \cdot w_2$. This iterative procedure continues until \mathcal{W} gets below a user defined minimum threshold \mathcal{W}_{\min} (default value: 0.5).

We only start the refitting procedure after we looped through all spectra of the data set and determined the spatial consistency of the centroid position values for all of them. This means that the fit solutions are not dynamically updated or propagating outwards during an iteration. New fit solutions are accepted based on the flagging system introduced in the previous section. We add a new flag in this phase that increases the total flag value \mathcal{F}_{tot} by a value of 2 if the fit solution is inconsistent with the required centroid positions inferred from the spatial consistency check.

Panels (b) and (c) of Fig. 2.11 show example cases for the spatial consistency check of centroid values for the case of a simple emission line feature. Based on the fit solutions in the neighbouring spectra we want to establish whether a one- or two-component fit should be used for the central spectrum. For this example we use the default settings of the algorithm, that is $\mathcal{W}_{\min} = 0.5$ and $f_w = 2$, which sets $w_1 = 1/3$ and $w_2 = 1/6$.

For the case depicted in panel (b) the required weight threshold for the first set of iterations is $\mathcal{W} = 1 - w_1 = 5/6$. The \mathcal{W}_{tot} value for the vertical and horizontal direction would reach this threshold, giving us two conflicting fit solutions for the central spectrum. In such a case, we recompute \mathcal{W}_{tot} for the fit solutions by grouping the eight immediate surrounding neighbouring spectra together and choose the fit solution with the higher \mathcal{W}_{tot} value. For the setup depicted in panel (b) the fit solution with one Gaussian component would be selected, as the immediate surrounding neighbours with this fit solution have a bigger total weight of $\mathcal{W}_{\text{tot}} = 2w_1 + 3w_1/\sqrt{2}$ (compared to $\mathcal{W}_{\text{tot}} = 2w_1 + w_1/\sqrt{2}$ for the two-component fit solution).¹³ We would thus try to refit the central spectrum with a fit solution that uses only one Gaussian component. However, the fit solution for the central spectrum is only updated if the total flag value for the fit solution using one component is lower or equal than the total flag value for the fit solution using two components in addition to the requirements that the distribution of the residual data points resembles a normal distribution (see Sect. 2.5.1).

For the example case depicted in panel (c) of Fig. 2.11 none of the four main directions would contain fit solutions that pass a weight threshold of $\mathcal{W} = 5/6$. However, both the vertical and the diagonal direction from upper left to lower right would reach a weight threshold of $\mathcal{W} = 4/6$, which is used in the second round of

¹³ In case both fit solutions have the same total weight as calculated from its immediate surrounding neighbours and this way to decide on the fit solutions thus should be inconclusive, we repeat this total weight calculation for all 16 considered neighbours (coloured squares in panel (a) of Fig. 2.11). If this is also inconclusive we choose the fit solution that uses fewer Gaussian components.

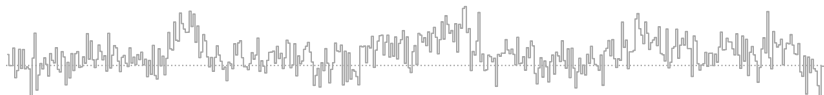


TABLE 2.1: Percentage of correctly and incorrectly identified mean positions of Gaussian components for decomposition runs on samples of synthetic spectra.

Sample	GAUSSPY		GAUSSPY+	
	correct ^a	incorrect ^b	correct ^a	incorrect ^b
A	–	2.8%	–	0.0%
B	78.0%	3.9%	93.7%	1.6%
C	72.6%	3.7%	93.4%	1.8%
D	29.4%	6.5%	81.7%	4.5%

Notes. ^(a) We define the mean position of a Gaussian component as correctly identified if it is within ± 2 spectral channels of the true value.

^(b) We define the fraction of incorrect identifications for sample A as all spectra for which noise features were fitted. The percentage of incorrect identifications for sample B–D refers to the fraction of fitted Gaussian components whose mean position was located at a distance of more than 4 spectral channels to the true value.

iterations. The total weight for the single component fit solution in the diagonal direction ($\mathcal{W}_{\text{tot}} = 2 \cdot w_1 / \sqrt{2} + 2 \cdot w_2 / \sqrt{2} \approx 0.7$) is bigger than the total weight for the two component fit solution in the vertical direction ($\mathcal{W}_{\text{tot}} = w_1 + 2 \cdot w_2 = 2/3$) and thus gets selected. Since the central spectrum already has a single component fit we would not try to refit it.

2.6 PERFORMANCE OF GAUSSPY+ ON SAMPLES OF SYNTHETIC SPECTRA

In this section we compare the decomposition results of the improved fitting routine of GAUSSPY+ (Sect. 2.4.3) with the original GAUSSPY algorithm. We applied both algorithms on samples of synthetic spectra containing: white noise (A); white noise and signal (B); white noise, signal, and negative noise spikes (C); white noise, weak signal, and negative noise spikes (D). We then determine how well the two algorithms were able to recover the mean position, amplitudes, and FWHM values of the Gaussian components used to create the synthetic spectra. For more details about the synthetic spectra see App. A.2.1.

To facilitate the comparison, we supplied the results from the noise calculation of GAUSSPY+ (Sect. 2.3.1) also to the decomposition with the original GAUSSPY algorithm. We also use the same S/N thresholds for the original spectrum ($\text{SNR}_1 = 3$) and the second derivative of the smoothed spectrum ($\text{SNR}_2 = 3$) for the decompositions with GAUSSPY and GAUSSPY+. We use the smoothing parameters α_1 and α_2 we obtained from the training sets decomposed with the method outlined in Sect. 2.3.4¹⁴ (see App. A.2.5 for more details). We left all additional parameters of GAUSSPY+ at their default settings.

Table 2.1 presents quality metrics of the results of the decomposition runs with GAUSSPY and GAUSSPY+ for the four samples of synthetic spectra. The percentage of correct detections refers to the number of Gaussian components that were fitted

¹⁴ For sample A we use the same smoothing parameters as for sample D.



within ± 2 spectral channels of the true position. For a correct identification of a peak position we do not consider whether the amplitude and FWHM values of the Gaussian component were fitted correctly. The fraction of incorrect detections refers either to all spectra for which at least one noise feature was fitted (in case of sample A) or the percentage of Gaussian fit components that were placed at a distance of more than 4 spectral channels away from the true position.

Table 2.1 demonstrates that GAUSSPY+ manages to fit significantly more Gaussian components at the correct positions in the spectrum than GAUSSPY, while decreasing the fraction of incorrect identifications¹⁵. This improvement is especially striking for weak signal peaks (sample D), where the number of correctly placed Gaussian fit components increased by more than a factor of 2.7 in the GAUSSPY+ decomposition. The performance of the GAUSSPY+ decomposition is also not affected by the presence of negative noise spikes in the spectrum (sample C), whereas this has a more significant impact on the performance of GAUSSPY. Moreover, GAUSSPY+ did not incorrectly fit any Gaussian components in sample A, whereas GAUSSPY mistook noise features as signal peaks for 2.8% of the spectra.

Figure 2.12 compares the fitted Gaussian parameters to the true values used to create the synthetic spectra. The GAUSSPY+ decomposition results for sample B, C, and D are shown in blue, red, and orange, respectively and the corresponding GAUSSPY results are indicated with the black line. The left column of panels shows the distribution of fitted mean positions from which the true mean position was subtracted. As already demonstrated in Table 2.1, the vast majority of components were fitted close to the true mean position. There were fewer detected peaks in sample D because the signal in these spectra was constructed to be close to or below the detection limit.

The middle and right column of panels in Fig. 2.12 show the distribution of amplitude and FWHM values, respectively, both normalised by the corresponding true parameter values. In these distributions we only included those fitted Gaussian components whose mean position was less than two channels away from the true mean position of the corresponding Gaussian component in the synthetic spectrum (corresponding to the percentages of correctly identified components in Table 2.1). For all three samples of synthetic spectra the vast majority of fitted parameters are within $\pm 10\%$ of the true values for both decompositions, but due to the higher amount of correctly identified peak positions, GAUSSPY+ manages to fit many more components correctly. Moreover, for sample D the median values of the distribution are closer to the true values for the GAUSSPY+ decomposition results. In contrast, GAUSSPY tends to fit the spectra of sample D with components that have too large amplitude values and too narrow linewidths, as demonstrated from the shape of the distributions and their median values.

We also found that the decomposition performance of GAUSSPY+ shows much less dependence on the number of signal peaks, their S/N ratio, their linewidth, or their closest distance to a neighbouring signal peak than the decomposition with GAUSSPY. See App. A.2.6 for a discussion about these comparisons.

¹⁵ A limiting factor for the performance of GAUSSPY+ was that the synthetic spectra were not set up to show spatial coherence. Thus, the algorithm will have had difficulty in the decomposition of some spectra to correctly decide whether a structure might be blended and better fit by multiple peaks.



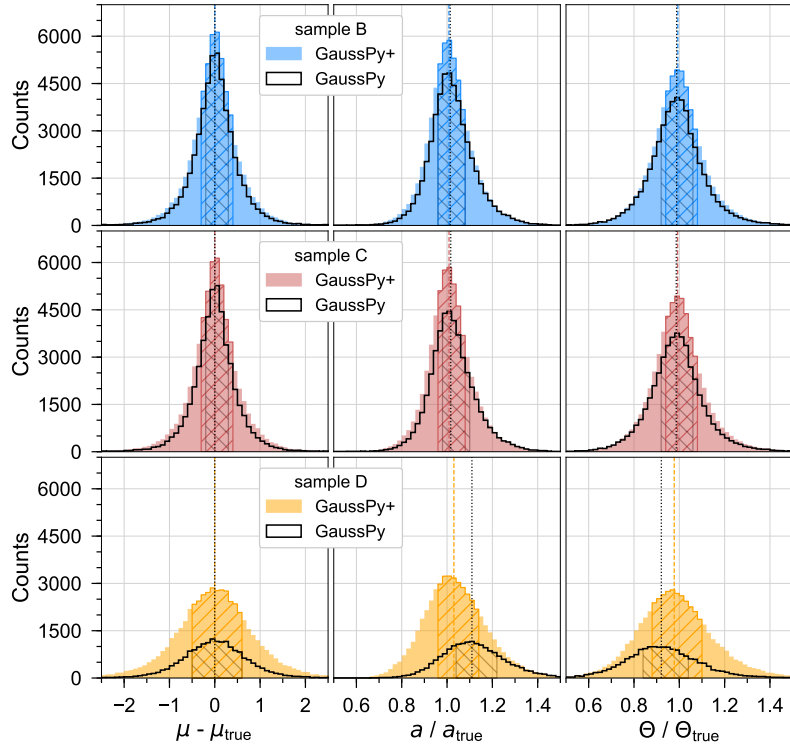


FIGURE 2.12: Comparison of the performance results of decompositions with GAUSSPY+ and GAUSSPY for different samples of synthetic spectra. The distribution shows how the fitted parameter values (mean position μ , amplitude a , and FWHM Θ from left to right, respectively) compare to the true parameter values used to create the synthetic spectra. The unfilled and coloured histograms show the distribution of fit components obtained with GAUSSPY and GAUSSPY+, respectively. Hatched areas correspond to the interquartile ranges and the vertical lines indicate the median value of the distribution (coloured and black for the GAUSSPY+ and GAUSSPY results, respectively). The improved fitting routine of GAUSSPY+ leads to a significant increase of correctly fitted parameters (see also Table 2.1 and Sect. 2.6 for more details).

2.7 PERFORMANCE OF GAUSSPY+ ON A GRS TEST FIELD

In this section we focus on ^{13}CO (1–0) emission line spectra from a sub-region of the GRS data set and perform a detailed analysis and discussion of the decomposition results with GAUSSPY+ to showcase its performance. The test field we chose is a $0.43^\circ \times 0.37^\circ$ region located towards the outer part of the GRS coverage at Galactic coordinates of $l = 55.48^\circ$ and $b = 0.19^\circ$. This GRS region contains 4200 spectra with 424 spectral channels that cover v_{LSR} values of -5 to 85 km s^{-1} . The chosen region contains three molecular clouds (G055.64+00.14, G055.39+00.14, G055.34+00.19) and 19 clumps as identified by Rathborne et al. (2009).

In the following sections we first describe the best way to compare flux between the original data set and the decomposition and show the improvements we gain by using the noise estimation technique built into GAUSSPY+. We then make a detailed comparison between the decomposition results of GAUSSPY and GAUSSPY+. Details



about the execution time for the entire decomposition and the performance of the spatially coherent refitting can be found in App. A.3.2 and App. A.3.5, respectively.

2.7.1 Optimal flux estimate for fair comparisons between the data set and decomposition results

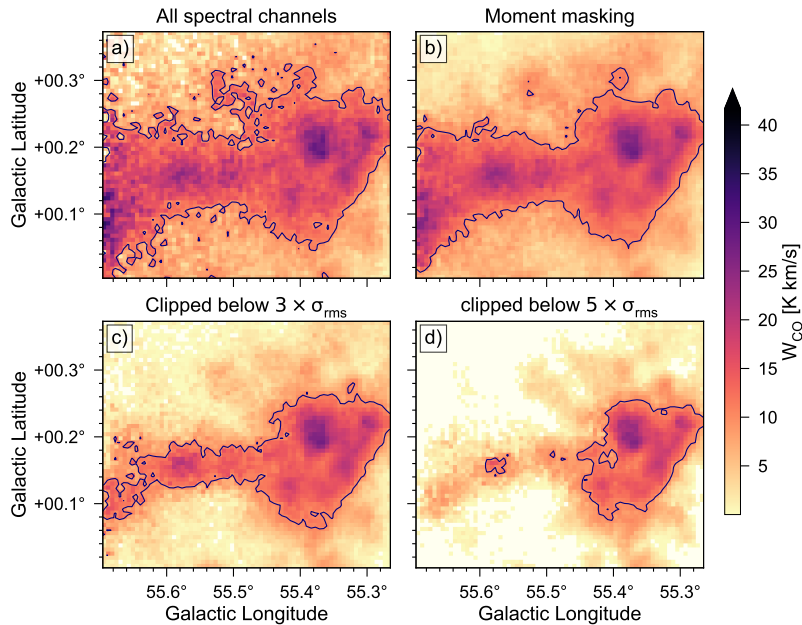
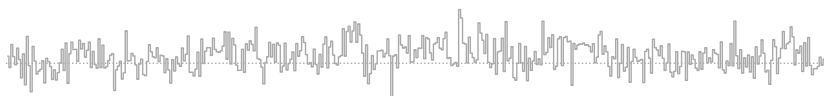


FIGURE 2.13: Zeroth moment maps for a region in the outer parts of the GRS. *Panels a–d:* Results obtained by summing up all spectral channels, applying a moment masking technique (see Sect. 2.7.1 for details), and clipping all spectral channels with values below $3 \times \sigma_{\text{rms}}$ and $5 \times \sigma_{\text{rms}}$, respectively. The contour indicates a W_{CO} level of 5 K km s^{-1} .

One measure of the quality of the decomposition results is the fraction of recovered flux from the comparison of zeroth moment maps; we aim at inspecting this fraction in Section 2.7.3. However, imperfect baseline corrections and noise spikes can lead to wrong flux estimates if all spectral channels are integrated along the spectral axis. It is therefore recommended to mask out all spectral channels that do not contain signal.

For our comparisons of the recovered flux in the decomposition (Sect. 2.7.3) we opted to use the moment masking technique outlined in Dame (2011). The basic idea of moment masking is to mask out spectral channels based on S/N cuts on a spatially and spectrally smoothed version of the original data set. For the smoothed data cube, Dame (2011) suggests to degrade the spatial resolution by a factor of 2 and degrade the spectral resolution to the width of the narrowest spectral lines contained in the data set. Dame (2011) found that a threshold of $5 \times \sigma_{\text{rms,smoothed}}$ gives the best results, where $\sigma_{\text{rms,smoothed}}$ refers to the rms-noise of the smoothed spectra. If a spectral channel in the smoothed cube exceeds this S/N threshold, we unmask this channel and all channels that were within the spatial and spectral smoothing kernels in the original data cube. Moment masking thus allows us to also include spectral



channels whose value has low S/N levels and would be masked out if we based the clipping of spectral channels on a S/N threshold of the original data set. Moreover, the high S/N requirement for spectral channels of the smoothed data set guarantees that most of the channels containing noise are masked out.

For the moment masking of the GRS test field, we created a smoothed version of the data cube by smoothing the original data set spatially with a Gaussian kernel with a FWHM value of $92''$ (corresponding to twice the beam size); spectrally, we smoothed the data set with a Gaussian kernel with a FWHM value of 0.42 km s^{-1} , which corresponds to twice the spectral resolution or 2 spectral channels. We then masked out all spectral channels whose value in the smoothed data cube was below a S/N threshold of 5.

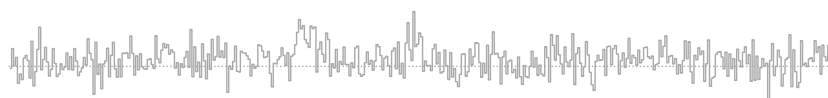
Figure 2.13 shows zeroth moment maps of our test region obtained by: summing up all spectral channels (panel a); using the moment masking technique described above (panel b); masking out all spectral channels with S/N values below 3 and 5 (panel c and d, respectively). The contour in the panels marks a value of $W_{\text{CO}} = 5 \text{ K km s}^{-1}$, with W_{CO} being the integrated CO intensity along the spectral axis. By summing up all intensity values along the spectral axis we also include a significant contribution from noise, which is clearly visible in the fraying of the contour line in panel (a) of Fig. 2.13. If we mask out all spectral channels with S/N values lower than 3 or 5 times the σ_{rms} (panels c and d), we also cut away a significant fraction of real signal, leading to a severe underestimate of the total flux contained in the region. Conversely, the zeroth moment map constructed with the moment masking technique (panel b in Fig. 2.13) replicates the flux distribution of panel (a) well, and excludes most of the noise contributions.

We quantify the recovered flux by summing up all intensity values above a value of 5 K km s^{-1} (contours in Fig. 2.13). The summed up value inside the contour of the map obtained with the moment masking technique is only 8% smaller than the corresponding value of the map in which we sum up all spectral channels. This small difference is likely due to contributions of spectral channels containing only noise that are also included in the zeroth moment map shown in panel (a) in Fig. 2.13. In contrast, the summed up value inside the contours of panels (c) and (d) of Fig. 2.13 is smaller by 33% and 56%, respectively, than the summed up value for the corresponding contour in panel (a).

We conclude that by summing up all spectral channels or masking out spectral channels via a S/N threshold based on the original data set we would either slightly overestimate or severely underestimate the flux contained in the data set, respectively. On the other hand, the moment masking technique gives a good estimate of the total flux contained in a data set and we therefore use it in comparisons of the flux between the decomposition results and the original data set. We assume here implicitly that noise contributions in the remaining spectral channels average out when the intensity values are integrated.

2.7.2 Noise map

A good estimate of the noise is crucial for obtaining good fitting results if parameters of the decomposition technique are based on S/N thresholds (see Sect. 2.3.1). Fig-



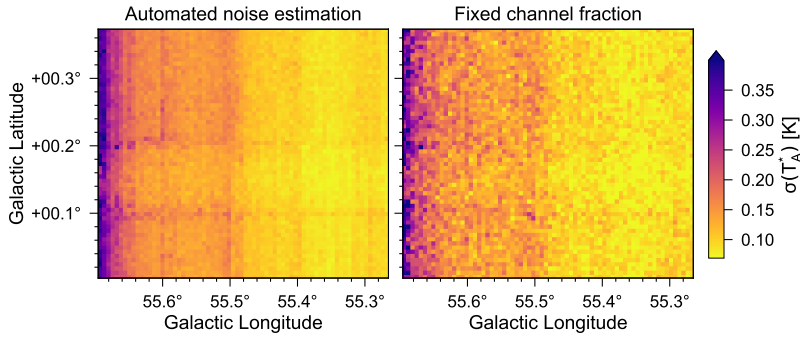


FIGURE 2.14: Noise maps for the region in Fig. 2.13. *Left*: Results from the automated noise estimation technique discussed in Sect. 2.3.1. *Right*: Results from using a fixed amount of spectral channels for the noise calculation.

Figure 2.14 shows noise maps for the region depicted in Fig. 2.13 that were obtained with the noise estimation routine of GAUSSPY+ (panel a) and a much simpler approach that uses a fixed number of channels to calculate the σ_{rms} value (panel b). For the latter approach we used 24 spectral channels from 80 – 85 km s^{-1} (corresponding to $\sim 6\%$ of all available spectral channels), similar as it was done in Jackson et al. (2006) for this region. For the GRS data set, the fixed channel approach can be problematic, since there is not really a channel interval that is guaranteed to be emission-free over the entire survey region. It can be clearly seen that the GAUSSPY+ noise estimation routine gives a much better estimate of the σ_{rms} values, as artefacts from the map-making procedures become more pronounced. There is also a clear gradient in the $\sigma(T_A^*)$ values in this region, which makes the GAUSSPY+ decomposition challenging, since it uses the same decomposition parameters throughout the whole region. We would thus expect to have more difficulty in the decomposition of spectra with high $\sigma(T_A^*)$ values, leading to small S/N values of the signal peaks in these spectra.

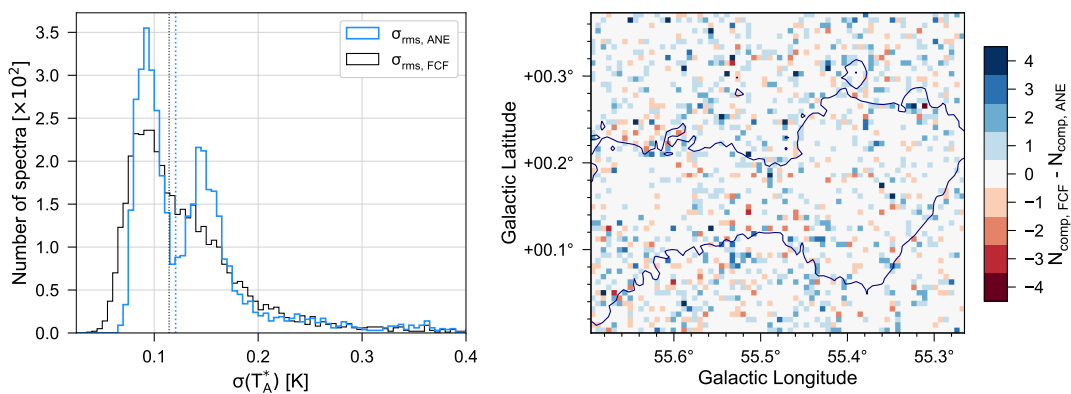
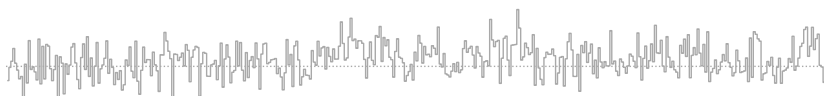


FIGURE 2.15: (*Left*: Histogram of the σ_{rms} values shown in Fig. 2.14 for the automated noise estimation of GAUSSPY+ (ANE, blue) and the fixed channel fraction approach (FCF, black). The dotted vertical lines show the corresponding median values of the two distributions. *Right*: Map showing the difference in the number of fitted components for the automated noise estimation ($N_{\text{comp, ANE}}$) and the fixed channel fraction approach ($N_{\text{comp, FCF}}$).



Panel (a) in Fig. 2.15 displays histograms of the noise maps of Fig. 2.14; the automated noise estimate shows a clear bimodal distribution, whereas the fixed channel fraction approach is more influenced by random fluctuations of the noise in the limited fixed number of channels used for the noise calculation. The median $\sigma(T_A^*)$ value of our automated noise estimation is only $\sim 6\%$ higher than the median value obtained via the fixed channel approach, so globally the two methods give similar results. However, Fig. 2.14 shows that there are considerable differences on the individual line of sight scale, which will lead to large differences in the decomposition.

To quantify the impact of the estimated noise on the fitting results, we performed two decomposition runs with the improved fitting routine of GAUSSPY+ (Sect. 2.4.3) with identical settings but different noise estimates corresponding to the maps of Fig. 2.14. Panel (b) in Fig. 2.15 shows the difference between the number of fitted Gaussian components for the noise estimate using a fixed fraction of channels and the automated routine of GAUSSPY+. About 26% of the spectra in the test field get fitted with a different number of Gaussian components and the total number of fitted components increases by $\sim 9\%$ for the fixed channel fraction approach. Applying the flagging procedure of GAUSSPY+ with its default settings (described in Sect. 2.5.1) to the two decompositions, we get that 43.8% and 51.2% of the fitted spectra would be selected for refitting if the automated noise estimate and fixed channel approach are used, respectively. Compared to the GAUSSPY+ decomposition with the automated noise estimate, in the fixed channel approach the number of spectra flagged as having a number of components incompatible with their neighbours increase from 1.5% to 6.1% and the number of spectra having normalised residual values not matching a Gaussian distribution increases from 20.0% to 25.1%. Both of these increased numbers of flagged spectra are a good indication that the noise estimate using the fixed fraction of channels is yielding poorer decomposition results than the automated noise estimation routine incorporated in GAUSSPY+.

2.7.3 Comparison between the decomposition runs with GaussPy and GaussPy+

In this section we present decomposition runs of the GRS test field obtained with the original GAUSSPY algorithm and GAUSSPY+. The different GAUSSPY+ runs represent results after different stages of the algorithm (improved fitting routine, phase 1 and 2 of the spatially coherent refitting, referred to as Stage 1, 2, and 3, respectively) to better illustrate the changes and improvements obtained in each individual stage.

We decomposed 250 randomly chosen spectra of the test field with the method outlined in Sect. 2.3.4 to create the training set needed to infer optimal smoothing parameters for GAUSSPY. Lindner et al. (2015) found that having two different smoothing parameters—one parameter with a smaller value that accentuates the narrower peaks and another parameter with a higher value that is more suitable for broader peaks—leads to huge improvements in the decomposition of H I spectra. We also found that a two-phase decomposition approach using two different smoothing parameters α_1 and α_2 yields better decomposition results for the CO emission line spectra of the GRS data set. For the same training set, the F_1 score (see Sect. 2.1)



for the one-phase and two-phase decomposition approaches was 67.5% and 74.7%, respectively. We therefore used the smoothing parameters inferred from the two-phase decomposition of the training set, which yielded values of $\alpha_1 = 2.89$ and $\alpha_2 = 6.65$. For the GAUSSPY decomposition we set $\text{SNR}_1 = \text{SNR}_2 = 3$. We left all GAUSSPY+ parameters at their default settings, with the exception of setting $\Delta\mu_{\max} = 4$ for Stage 3.

Panels (a–d) in Fig. 2.16 show zeroth moment maps of the decomposition runs with the original GAUSSPY algorithm supplied with the improved noise estimation (panel a of Fig. 2.14), and GAUSSPY+ after the improved fitting stage (panel b; Sect. 2.4.3), and after phase 1 (panel c; Sect. 2.5.1) and phase 2 (panel d; Sect. 2.5.2) of the spatially coherent refitting. The zeroth moment maps were obtained by masking the same spectral channels as for the moment masked data in panel (b) of Fig. 2.13.

Panels (e–h) in Fig. 2.16 show the corresponding zeroth moment maps of the residual. In all three stages of GAUSSPY+ the performance in terms of the recovered flux is much better for the regions with lower S/N emission than the GAUSSPY decomposition, which was already noticeable in the case of synthetic spectra (Sect. 2.6, App. A.2.6, and App. A.2.7). For regions with high S/N, GAUSSPY and all stages of GAUSSPY+ perform very well.¹⁶

The maps in panels (i–l) of Fig. 2.13 show the χ_{red}^2 values for the fits, with the goodness of fit calculation restricted to the channels estimated to contain signal (see Sect. 2.3.2). We can see a clear improvement towards χ_{red}^2 values closer to 1 for the GAUSSPY+ decompositions compared to the GAUSSPY run. In App. A.5 we demonstrate the importance of restricting the calculation of the χ_{red}^2 values to regions in the spectrum that contain signal for the GRS test field.

The performance in recovered flux does not significantly change in the spatially coherent refitting phases of GAUSSPY+, since the focus in these phases is shifted to reducing flagged features and making the fit results compatible with the neighbours instead of minimising the residual. Therefore the zeroth moment, residual, and χ_{red}^2 maps that show the quality of the fit results in terms of recovered flux do not change significantly between Stage 1 and Stage 3 of the GAUSSPY+ decomposition.

We can see more variation between panels (m–p) in Fig. 2.16, which show maps of the number of fitted Gaussian components per spectrum for each decomposition run. In the GAUSSPY+ decompositions the number of fitted components increases compared to the GAUSSPY run, which is due to the fitting of weaker emission lines in spectra containing increased noise levels (see panels e–h) and the segmentation of very broad components into individual peaks. There is also a clear progression towards more spatial coherence from panel (m) to panel (p).

Figure 2.17 further demonstrates this transition towards spatial coherence by comparing the fitting results of GAUSSPY and Stage 1–3 of GAUSSPY+ for nine neighbouring spectra from the GRS test field. The signal peaks in these spectra show only moderate S/N ratios and GAUSSPY therefore tends to fit broad Gaussian components over most of the signal peaks. Stage 1 of GAUSSPY+ already manages to improve upon these fitting results by separating the emission into more indi-

¹⁶ We caution that while the recovered flux is an essential criterion for the performance of the fit it may not give a good handle on the quality of the fits themselves. For example, the spectra might not be spatially coherent and might use many blended and broad components to fit the spectrum.



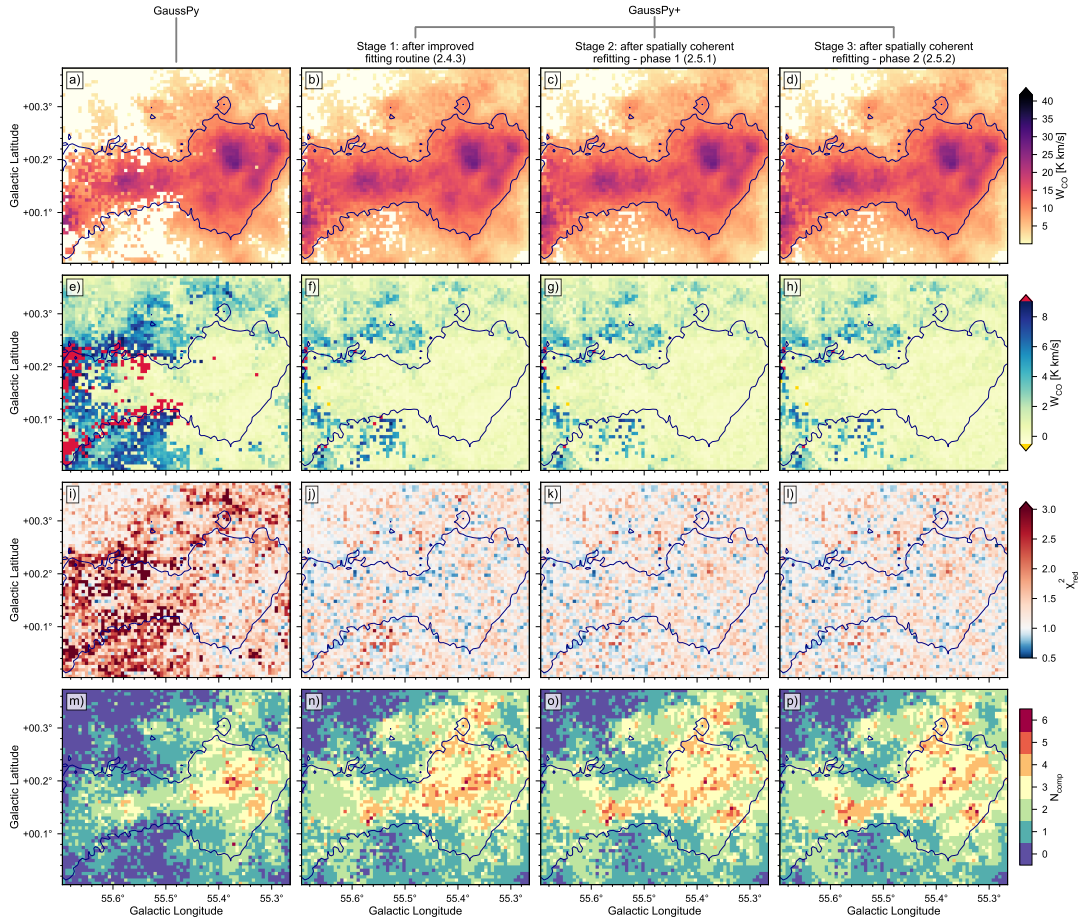


FIGURE 2.16: (From left to right: Decomposition results for the original GAUSSPY algorithm and three stages of GAUSSPY+ (improved fitting routine, phase 1 and 2 of the spatially coherent refitting). From top to bottom: Zeroth moment maps of the decomposition results; residual maps obtained by comparing the zeroth moment maps of the decomposition with panel (b) in Fig. 2.13; maps showing the χ^2_{red} values for the fit, with the goodness of fit calculation restricted to the channels estimated to contain signal (see Sect. 2.3.2); and maps of the number of Gaussian fit components per spectrum. All panels are overplotted with the contour from panel (b) in Fig. 2.13. The GAUSSPY+ decompositions show a clear trend towards more spatial coherence and an improvement in the quality of the fits for the regions with lower emission or higher noise levels.



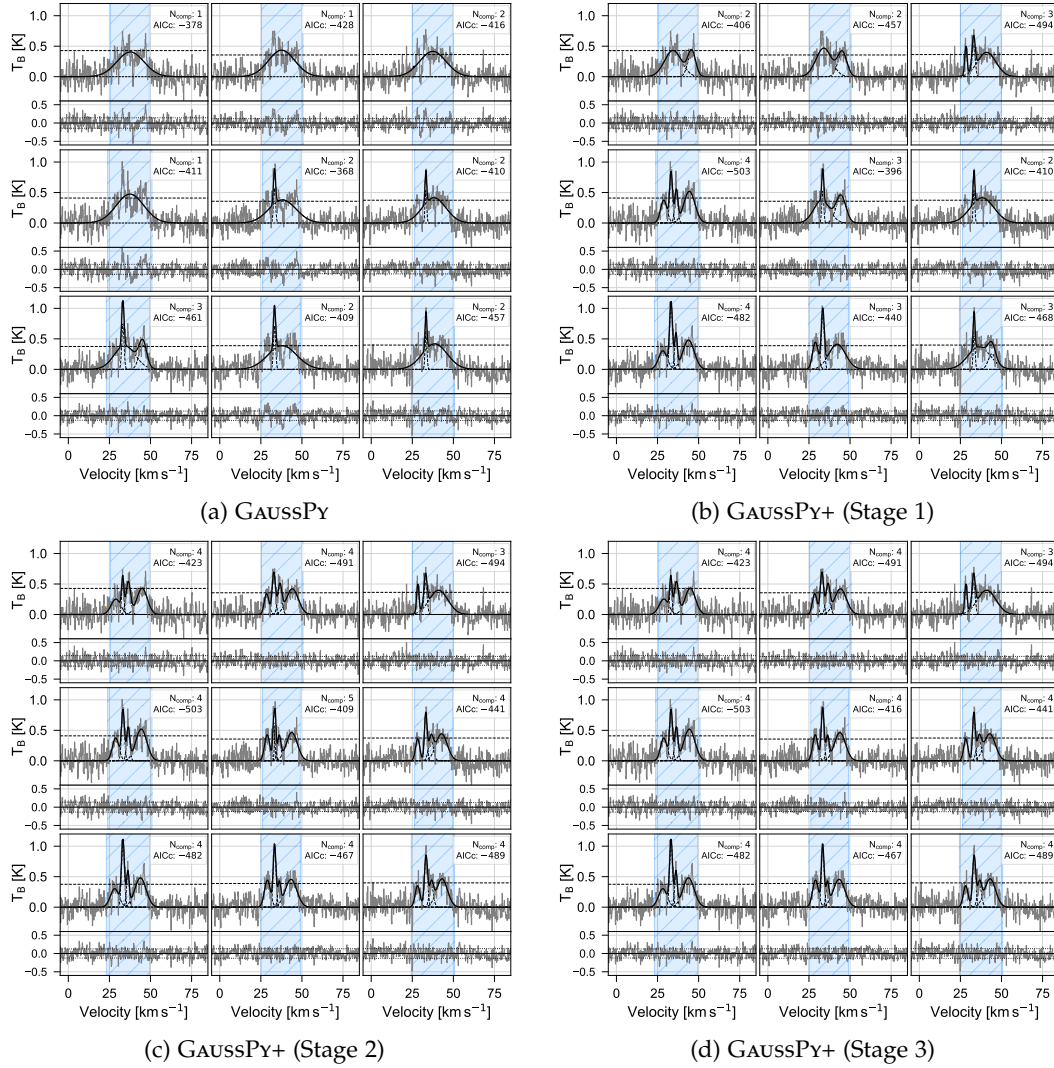


FIGURE 2.17: Fitting results of nine neighbouring spectra in the GRS test field for the decomposition with GAUSSPY (a) and after Stage 1–3 of GAUSSPY+ (b–d, respectively). Individual fit components and their combination are shown in dashed and solid black lines, respectively. Horizontal dashed black lines mark a S/N threshold of 3 and blue shaded areas indicate the identified signal intervals. The number of used fit components N_{comp} and the resulting AICc values are noted in the upper right corner of the main panel. The smaller subpanels show the residual with the horizontal dotted black lines marking values of $\pm\sigma_{\text{rms}}$.



TABLE 2.2: Comparison of parameters and flagged spectra for the decomposition runs with GAUSSPY and GAUSSPY+.

	GAUSSPY	GAUSSPY+ (Stage 1)	GAUSSPY+ (Stage 2)	GAUSSPY+ (Stage 3)
$W_{\text{CO,all}}$	73.0%	88.9%	89.6%	89.8%
$W_{\text{CO,contour}}$	84.0%	95.5%	95.6%	95.7%
$\chi_{\text{red,med}}^2$	1.436	1.123	1.121	1.113
\mathcal{F}_{tot}	59.2%	43.8%	35.5%	38.0%
$\mathcal{F}_{\text{blended}}$	5.8%	7.5%	2.9%	3.2%
$\mathcal{F}_{\text{neg. res. peak}}$	2.6%	0.1%	0.0%	0.1%
\mathcal{F}_{\ominus}	24.0%	22.7%	19.1%	21.6%
$\mathcal{F}_{\ominus > 50}$	10.6%	11.2%	9.6%	9.4%
$\mathcal{F}_{\text{residual}}$	37.1%	20.0%	16.3%	16.5%
$\mathcal{F}_{N_{\text{comp}}}$	0.3%	1.5%	1.1%	1.0%

vidual peaks; this improvement of the decomposition results can also be seen in the decreased residuals shown in the smaller panels. Stage 2 of GAUSSPY+, which uses the information of already well-fit neighbouring spectra as input guesses for flagged spectra, can even further improve upon these results by creating more spatial coherence between the spectra. Finally, Stage 3 of GAUSSPY+, which tries to enforce spatial coherence between the centroid values of the fit components, improves the decomposition results once more, by getting rid of a fit component for the central spectrum that was inconsistent with the neighbouring fit solutions.

In Table 2.2 we compare parameters and the percentage of flagged spectra for the decomposition results for GAUSSPY and the three stages of GAUSSPY+ depicted in Fig. 2.16. The $W_{\text{CO,all}}$ and $W_{\text{CO,contour}}$ parameters give the fraction of recovered intensity values integrated along the spectral axis for the whole test field and inside the contour of 5 K km s^{-1} , respectively. The $W_{\text{CO,all}}$ and $W_{\text{CO,contour}}$ values were determined by comparing the moment maps of the decompositions (panels a–d in Fig. 2.16) to the moment masked zeroth moment map of panel (b) in Fig. 2.13. As already noticeable in Fig. 2.16, the performance of GAUSSPY and GAUSSPY+ is better for spectra containing high S/N emission peaks than for weaker emission lines. With GAUSSPY+ we are able to recover about 90% of the W_{CO} values contained in the entire test field and $\sim 95\%$ of the W_{CO} values contained inside the contour of 5 K km s^{-1} . Compared to the GAUSSPY+ runs, the decomposition with the original GAUSSPY algorithm recovers about 12% less flux inside the contour and 16% less flux in the entire field.

The total number of fitted Gaussian components N_{comp} increases by about half for the GAUSSPY+ decompositions compared to the GAUSSPY run. The median χ_{red}^2 values ($\chi_{\text{red,med}}^2$) of the GAUSSPY+ fitting results are also lower by $\sim 22\%$ than for the GAUSSPY results.



Table 2.2 also shows the fraction of spectra of the GAUSSPY and GAUSSPY+ results that would be flagged as not satisfying the quality criteria used in the first phase of the spatially coherent refitting (Sect. 2.5.2). We use the default flagging criteria of GAUSSPY+, which means that spectra get flagged if they have blended components ($\mathcal{F}_{\text{blended}}$), show negative residual features ($\mathcal{F}_{\text{neg.res.peak}}$), have broad components (\mathcal{F}_{Θ} , determined with $f_{\Theta,\text{max}} = 2$), have residual data values whose distribution does not correspond to what is expected from Gaussian noise ($\mathcal{F}_{\text{residual}}$), or were fitted with a number of components that is not consistent with the number of components used in the fit solutions of neighbouring spectra ($\mathcal{F}_{N_{\text{comp}}}$). The fraction of spectra that contain broad components in relation to neighbouring components is indicated with \mathcal{F}_{Θ} . To better judge how many components with very large absolute FWHM values occur in the decompositions, we also list the fraction of spectra that contain components with FWHM values above 50 spectral channels ($\mathcal{F}_{\Theta > 50}$) that would imply very high velocity dispersion values of $\gtrsim 4.3 \text{ km s}^{-1}$. The total flag value \mathcal{F}_{tot} gives the percentage of spectra that were flagged by at least one of the individual flags. For the GAUSSPY decomposition about 59% of the spectra were flagged as not satisfying at least one of the flagging criteria, whereas this reduces to ~ 35 and 38% for Stage 2 and 3 of GAUSSPY+, respectively. The fit results from Stage 2 of GAUSSPY+ show the lowest fraction of flagged spectra, which is expected given that this stage is designed for decreasing the number of flagged spectra. Stage 3 of GAUSSPY+ aims to increase the spatial coherence of the fit components, which is why the percentage of flagged spectra increases slightly again compared to the Stage 2 fitting results. All three stages of GAUSSPY+ perform well in removing negative residual features and reducing fit results that lead to a residual whose distribution is inconsistent with Gaussian noise. The percentage of spectra flagged with $\mathcal{F}_{\text{blended}}$, $\mathcal{F}_{\Theta > 50}$, and $\mathcal{F}_{N_{\text{comp}}}$ flags actually increases for Stage 1 of GAUSSPY+ compared to the results of GAUSSPY, which is likely just an effect of the increased number of fit components used in the GAUSSPY+ results. These flags are however reduced again in the spatially coherent refitting stages.

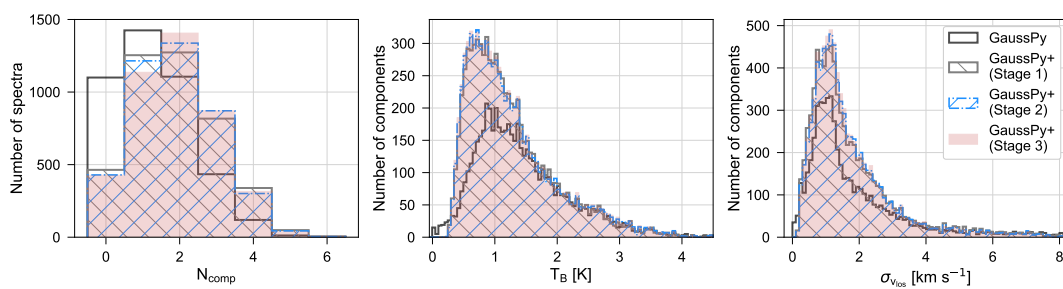
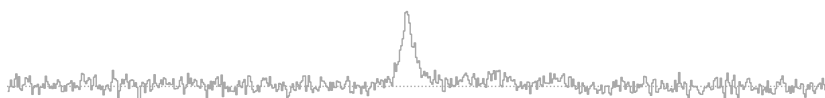


FIGURE 2.18: Distribution of fit parameters for the decomposition results of the GRS test field with GAUSSPY and the three stages of GAUSSPY+. *Left*: Histogram of the number of fitted components per spectrum. *Middle*: Histogram of the amplitude values T_B of all Gaussian fit components. The bin size is 0.05 K. *Right*: Histogram of the velocity dispersion values $\sigma_{v_{\text{los}}}$ of all Gaussian fit components. The bin size is 0.1 km s^{-1} .

Finally, Fig. 2.18 shows distributions of fit parameters for the decomposition results of GAUSSPY and the three stages of GAUSSPY+. The left panel shows histograms of the number of fitted components per spectrum. As was already demonstrated by



panels (m–p) in Fig. 2.16, GAUSSPY+ manages to fit more spectra than GAUSSPY, so that the total number of fitted components increases by about one third for the GAUSSPY+ stages.

The middle panel of Fig. 2.18 shows histograms of the amplitude values of all fit components. Comparing these distributions with the histogram of the estimated noise values shown in the left panel of Fig. 2.15 reveals that GAUSSPY+ manages to fit many more components whose S/N value is only ~ 3 or lower. The median S/N value of fit components decreases from 5.4 for the GAUSSPY decomposition to 4.3 for the GAUSSPY+ fit results.

The histograms of the velocity dispersion values for all fit components are given in the right panel of Fig. 2.15. The long tail towards increased $\sigma_{\text{v}_{\text{los}}}$ values is mostly due to fitted components with low S/N values; about half of the fit components with $\sigma_{\text{v}_{\text{los}}} > 4.3 \text{ km s}^{-1}$ in the GAUSSPY+ decomposition results of Stage 2 and 3 have S/N values < 2 .

2.8 DISCUSSION

In this section we list potential applications as well as limitations of GAUSSPY+. We also give advice on parameter settings to obtain optimal decomposition results.

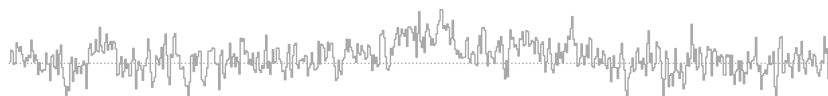
2.8.1 Applications and limitations of GaussPy+

The GAUSSPY+ algorithm should be applicable to any data set that can be well described with Gaussian components; in particular it was designed to decompose large surveys of HI and CO isotopologues. In case the line shape is better matched by a Voigt or Lorentzian profile (e.g. due to effects of pressure broadening) the decomposition with GAUSSPY+ will likely not give satisfactory results. The algorithm can also not fit the hyperfine structure of molecules such as NH₃ or N₂H+ directly.

Many of the individual routines implemented in GAUSSPY+, such as the noise estimation (Sect. 2.3.1), signal identification (Sect. 2.3.2), and masking of noise artefacts (Sect. 2.3.3), can be used as stand-alone applications. For example, the noise estimation can be used in combination with the signal identification to detect baseline shifts, unsubtracted continuum emission, or instrumental artefacts such as increased or amplified noise fluctuations. Phase 1 of the spatially coherent refitting routine (Sect. 2.5.1) can also be used to just flag decomposition results without refitting them.

In its current version, GAUSSPY+ is not designed to deal with spectra that contain both emission and absorption lines. If users would like to use GAUSSPY+ for the decomposition of emission lines that are expected to show strong self-absorption (such as the lowest rotational transitions of the ¹²CO molecule), we recommend to deselect the flagging of negative residual spikes, as in this case one would not want to fit a signal peak that has a dip in its centre with two components.

The GAUSSPY+ algorithm will only perform well on spectra whose baseline is centred on a value of zero. Incomplete continuum subtraction or baseline shifts of the spectrum will lead to wrong noise estimates, which in turn will give insufficient



decomposition results, since core functionalities of GAUSSPY+ depend on the correctness of the estimated noise values.

The GAUSSPY+ algorithm can deal with large variations of the noise (see Sect. 2.7). However, since key steps of the algorithm are based on S/N thresholds, an inhomogeneous noise coverage or variation in the quality of the data will have an impact on the decomposition results.

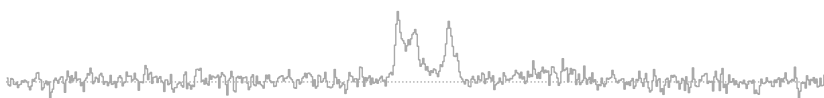
In its current implementation GAUSSPY+ does not explicitly check for spatial coherence of the amplitude and FWHM values. In principle, these values should also become more coherent in the two phases of the spatially coherent refitting (Sect. 2.5), where neighbouring fit solutions are used to improve the fit of a spectrum. We focus on spatial coherence of the centroid positions, since it is a necessary requirement for correct amplitude and FWHM values. If Gaussian fit components are not placed correctly, their amplitude and FWHM values will by default be spatially inconsistent with neighbouring fit solutions. We also have to caution against constraining the FWHM parameters of Gaussian components with too restrictive limits based on fit solutions from neighbours. In tests we performed, such a constraint could lead to Gaussian fit components with FWHM values close to the lower or upper limit of the constraint. This effect caused artefacts in the distribution of all fitted FWHM values, but in case of smaller data sets this might not be easily noticeable. We thus do not enforce limits for the width of the Gaussian fit components in any of the stages of GAUSSPY+, apart from the requirement that the FWHM value has to be larger than the user defined Θ_{\min} parameter, whose value defaults to the channel width of the data set. This fitting without an upper limit and without a more constrained lower limit could allow fluctuations in the FWHM values between the Gaussian components of neighbouring spectra.

Our approach in phase 2 of the spatially coherent refitting will also favour structures with ellipsoid morphologies over possible ring-like structures (see Fig. 2.11). Users thus should be cautious in using the spatially coherent refitting for centroid positions if the structures probed by the observations are not expected to be continuous over multiple neighbouring pixels or the data is not Nyquist sampled.

2.8.2 Recommended settings for GaussPy+

We tested the default settings of GAUSSPY+ on synthetic spectra and line emission data from a ^{13}CO survey and obtained very good decomposition results with them. However, different data sets may require significantly different settings. For example, in H I observations we would expect two distinct populations of narrow and very broad lineshapes corresponding to contributions from the cold and warm neutral medium respectively (e.g. Heiles & Troland, 2003), which is not the case for observations of CO isotopologues. For the H I observations one would thus not flag and refit broad Gaussian components (Sect. 2.4.2.2), whereas this setting can lead to better decomposition results for the CO data sets. Ultimately, it is the responsibility of the user to consider if the decomposition results of GAUSSPY+ are scientifically meaningful for the chosen application.

In our application of GAUSSPY+ on the GRS data set we found it beneficial for the fitting to also retain weak components with amplitudes below a S/N threshold



of 3. Since the decomposition of GAUSSPY+ performs a least squares minimisation of the residual, the fit of higher peaks in a spectrum can be negatively affected if weak components get discarded or neglected. We thus recommend to also accept components with $S/N_{\min, \text{fit}} < 3$ in the decomposition and only later on perform a cut based on their S/N values.

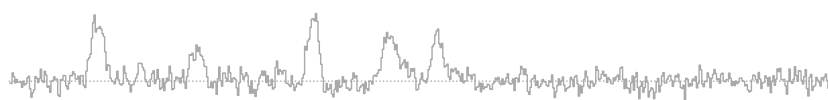
The GAUSSPY+ algorithm is designed to deal with spectra that contain only weak emission lines with S/N values around 3 or even lower. The quality check for the significance of a Gaussian component is specifically designed to help in such cases where GAUSSPY+ operates close to the noise. If the chosen settings for GAUSSPY+ produce too many false positives, users are advised to increase the chosen S/N limit and/or increase the value of the S_{\min} threshold. Conversely, in case the decomposition results of GAUSSPY+ are not including a significant fraction of signal peaks, users should try to decrease one or both of these parameter settings (see App. A.3.3 for how changing both of these parameters affects the decomposition).

We designed GAUSSPY+ to be customisable to different data sets, which means that most of its parameters can be changed and finetuned by the user (see Table A.7). However, the majority of parameters should yield good results for most data sets if left to their default settings. To get first decomposition results only a small number of parameters (listed as *essential parameters*) have to be specified by the user. In case the decomposition does not yield good results we recommend to first change the *essential parameters* before changing the parameters listed under *more advanced settings* in Table A.7.

2.9 SUMMARY

In this chapter we presented and discussed the GAUSSPY+ algorithm, a new fully automated Gaussian fitting package for the decomposition of emission line spectra. The GAUSSPY+ algorithm is built upon GAUSSPY (Lindner et al., 2015), but significantly extends and improves upon its performance by the following added fully automated functionality:

1. Preparatory steps that can also be used as stand-alone applications. This includes methods to accurately estimate the noise (Sect. 2.3.1), identify signal peaks (Sect. 2.3.2), and mask out noise artefacts (Sect. 2.3.3). An additional routine (Sect. 2.3.4) creates suitable training sets for the in-built machine learning process GAUSSPY uses to infer optimal parameter settings for the decomposition of a data set.
2. Quality controls that are highly customisable to different data sets (Sect. 2.4.1). This includes a criterion that takes into account both the S/N values and the number of spectral channels of a signal feature or fitted Gaussian component (Sect. 2.4.1.3) and goodness of fit criteria to aid in the selection of the best fit solution for a spectrum (Sect. 2.4.1.5). Additional optional quality controls (Sect. 2.4.2) allow the user to flag and refit unwanted features in the decomposition such as blended Gaussian components, negative peaks in the residual, very broad Gaussian components, residual data points that are not normally



distributed, or differences in the number of fitted components between neighbouring spectra.

3. An improved fitting routine (Sect. 2.4.3) that is guided by the user-defined optional quality controls.
4. A spatially coherent refitting routine (Sect. 2.5) that tries to refit spectra that do not pass the user-defined quality controls or spectra whose decompositions show spatial incoherence with neighbouring fit solutions.

We thoroughly tested the performance of GAUSSPY+ on synthetic spectra designed to cover a wide range of spectral features expected in observations of emission lines of CO isotopologues. We found that it yields very good decomposition results that significantly outperform the original GAUSSPY algorithm in all tested cases (Sect. 2.6). We also applied GAUSSPY+ to a test field from the GRS (Sect. 2.7) and showed that it can fit the data well, resulting in considerable improvements in the decomposition compared to the original GAUSSPY algorithm.

We conclude that the GAUSSPY+ algorithm is a powerful tool to analyse large Galactic plane surveys, such as GRS or SEDIGISM (Schuller et al., 2017). In the following chapter, we present and discuss its application on the entire GRS data set.



GLOBAL STATISTICS AND PROPERTIES OF THE GRS ^{13}CO EMISSION

*The task is, not so much to see what no one has yet seen;
but to think what nobody has yet thought, about that which everybody sees.*

— Erwin Schrödinger

Based on [Riener et al. \(2020\)](#) published in *Astronomy & Astrophysics* (633, A14).

In Chapter 1 I argued that we need to extend the detailed kinematic studies that have so far been mostly performed for structures in the solar neighbourhood to entire Galactic plane surveys of molecular gas. These large data sets are crucial for our understanding of the dynamics and distribution of molecular gas within our Galaxy, and they provide an essential link between high spatial resolution studies of nearby molecular clouds and nearby galaxies. Since Galactic plane surveys cover a significant area of the Milky Way, they allow us to extend detailed studies about the gas dynamics to much larger regions that sample different environmental conditions, such as spiral arm or interarm regions. A detailed kinematic analysis of the Galactic plane data sets can therefore provide unique knowledge about the gas flow from Galactic to sub-cloud scales and the importance of various physical phenomena—such as gravitational instabilities or turbulence—and Galactic environments in shaping the molecular ISM.

The main aim in this chapter is to present a homogeneous decomposition and analysis of the GRS—a large Galactic plane survey of ^{13}CO (1–0) emission in the first quadrant of the Milky Way—in its full spatial and spectral resolution. In the previous chapter I discussed the spectral decomposition package `GAUSSPY+`, which I developed for the specific aim of analysing large Galactic plane data sets such as the GRS. I already presented a successful decomposition with `GAUSSPY+` of a challenging test field of the GRS in Sect. 2.7. I now extend the `GAUSSPY+` decomposition to the full GRS data set and discuss useful insights that I can gain from an analysis of the resulting global gas emission properties of the entire survey.

The structure of this chapter is as follows. I present the observational data sets used in this chapter in Sect. 3.1. In Sect. 3.2 I give an overview about the `GAUSSPY+` decomposition of the GRS data. I present and discuss statistics of all Gaussian fit parameters in Sect. 3.3. In Sect. 3.4 I discuss the distribution of velocity dispersion values with Galactic coordinates and the complexity of the spectra along the line of sight. In Sect. 3.5 I present how the fitted velocity dispersion values can be useful in disentangling confusion between emission originating from near and far distances to the Sun. In Sect. 3.6 I discuss how a transformation of the data set enabled by the decomposition shows the presence of velocity fluctuations throughout the entire GRS data set. I summarise the contents of this chapter in Sect. 3.7.

3.1 OBSERVATIONAL DATA SETS

3.1.1 *Galactic Ring Survey*

We use data from the Boston University–Five College Radio Astronomy Observatory GRS (Jackson et al. 2006) that we downloaded from the online repository of the Boston University Astronomy Department¹. This survey targeted the lowest rotational transition of the ^{13}CO isotopologue with an angular resolution of $46''$, a pixel sampling of $22''$, and a spectral resolution of 0.21 km s^{-1} . The GRS covers a longitude range of $\ell = 18^\circ - 55.7^\circ$ and a latitude range of $|b| < 1.1^\circ$. The velocity coverage of the survey is -5 to 135 km s^{-1} for $\ell \leq 40^\circ$ and -5 to 85 km s^{-1} for $\ell > 40^\circ$. We also used the additional limited data from $\ell = 14^\circ - 18^\circ$ that does not cover the full latitude range of the rest of the data; the velocity range of this additional data is again -5 to 135 km s^{-1} . In total the GRS consists of about 2.28 million spectra. We used SWARP² (Bertin et al., 2002) to combine the original data cubes of the GRS³ into a single mosaicked cube (see App. B.1.1). The values in the GRS data set are given in terms of antenna temperatures (T_A^*) that we converted to main beam temperatures (T_{MB}) by dividing by the main beam efficiency of $\eta_{\text{mb}} = 0.48$.

3.1.2 *Hi-GAL*

We use maps of mean dust temperatures and H_2 column densities from Marsh et al. (2017)⁴ that are based on dust emission observations from the *Herschel* infrared Galactic Plane Survey (Hi-GAL; Molinari et al., 2016a). The maps from Marsh et al. (2017) combine continuum data spanning a wavelength range of $70 - 500 \mu\text{m}$ at a spatial resolution of $12''$ via the point process mapping (PPMAP) technique outlined in Marsh et al. (2015). We used SWARP² to combine 21 PPMAP fields overlapping with the GRS coverage. We spatially smoothed the mosaicked maps of mean dust temperatures and H_2 column densities to the GRS resolution and regridded the smoothed maps so that the pixels aligned with the GRS mosaic.

3.2 GAUSSIAN DECOMPOSITION OF THE GRS DATA

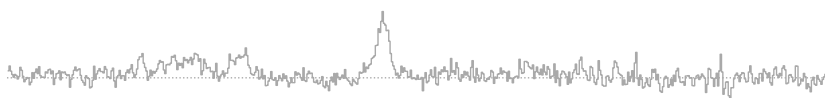
In this section we present results of the Gaussian decomposition with GAUSSPY+ for the entire GRS data set. The appendix contains further, more technical discussions about the decomposition. Details about the data preparation, parameter settings, and decomposition runs can be found in App. B.1; we also present quality assurance metrics for the fit results in App. B.2. Furthermore, we give a detailed discussion about the effects of optical depth on our decomposition in App. B.3. We find that issues due to optical depth only affect the densest regions in the GRS and should not be a problem for the vast majority of the decomposition results presented in this work.

¹ https://www.bu.edu/galacticring/new_data.html

² <http://www.astromatic.net/software/swarp>

³ https://www.bu.edu/galacticring/new_data.html

⁴ <http://www.astro.cardiff.ac.uk/research/ViaLactea/>



The whole GRS data set contains in total 2 283 920 spectra. Of these, we excluded 1188 spectra (0.05%) that showed extremely high noise values (see Sect. B.2.1). In the data preparation step (see App. B.1), GAUSSPY+ identified signal peaks in 75.3% of all spectra; $\sim 96\%$ of these were fitted with one or multiple components in the decomposition.

We use the same parameter settings in GAUSSPY+ throughout the entire survey region to guarantee a comparable analysis of the data set. This means that we do not finetune our settings to individual regions and the decomposition results with GAUSSPY+ thus might show differences in their performance, given the non-uniform noise coverage of the GRS that can show significant variation (see Fig. B.1). The variations in the noise values between different regions of the survey means that the S/N based thresholds of GAUSSPY+ could extract more signal peaks in the spectra that showed reduced noise values. Some of the emission peaks may also have a non-Gaussian shape due to, for example, line blending or optical depth effects and will thus likely not be well fit by GAUSSPY+ (see App. B.3 for a discussion about the impact of optical depth on our fitting results).

The final decomposition contains 4 648 985 fitted Gaussian components. The best fit solutions include fit components with S/N ratios as low as 1.5 (as argued in Sect. 2.4.1.2 it is beneficial to allow fit components with amplitudes below $S/N < 3$). We highlight the $\sim 75\%$ of the fit components with S/N ratios > 3 in our discussion of the fit parameter statistics in Sects. 3.3.1 – 3.3.4, since the components with lower S/N ratios can already be severely affected by the noise. Depending on what the decomposition results are used for, it may thus be beneficial to only select more reliable fit components with S/N ratios > 3 or amplitude values above a specific T_{MB} threshold.

3.2.1 Catalogue description

In this section we describe the entries of a catalogue of our decomposition results, which include quality flags that can be useful in identifying fit solutions that might have problems or are inconsistent with neighbouring decomposition results.

We show a subset of the decomposition results in Table 3.1. Each row corresponds to a single Gaussian fit component; a spectrum fitted with eight Gaussian components thus occupies eight consecutive rows in the table.

Columns (1) and (2) show the pixel position of the spectrum in the mosaicked cube of the GRS with the corresponding Galactic coordinate values given in columns (3) and (4). The next columns list the parameters and associated errors of the Gaussian fit parameters: peak main beam brightness temperature or amplitude value T_{MB} (5) and its error ΔT_{MB} (6); mean position v_{LSR} (7) and its error Δv_{LSR} (8); and line of sight velocity dispersion σ_v (9) and its error $\Delta \sigma_v$ (10). Column (11) gives the root-mean-square value of the estimated noise of the spectrum σ_{rms} given in T_{MB} values. The remaining columns list quality metrics that can indicate problems with the fit solutions, such as inconsistencies with neighbouring fit results. Column (12) gives the resulting p -value of a normality test for normally distributed residual values (see App. B.2.2 for more details); column (13) shows the value of the corrected Akaike information criterion (AICc; Akaike, 1973) for the best fit solution; and column (14)



TABLE 3.1: Decomposition results.

x_{pos}	y_{pos}	ℓ	b	T_{MB}	ΔT_{MB}	v_{LSR}	Δv_{LSR}	σ_v	$\Delta\sigma_v$	σ_{rms}	p	AICc	χ_{red}^2	N_{comp}	N_{med}	N_{jump}	F ₁	F ₂	F ₃	F ₄
(1)	(2)	(3)	(4)	(5)	(6)	(7)	(8)	(9)	(10)	(11)	(12)	(13)	(14)	(15)	(16)	(17)	(18)	(19)	(20)	(21)
286	2	54.241	-1.088	2.26	0.39	24.81	0.04	0.21	0.04	0.41	5.9	-419.4	1.21	2	1	0	0	0	0	0
286	2	54.241	-1.088	1.52	0.25	45.19	0.10	0.50	0.10	0.41	5.9	-419.4	1.21	2	1	0	0	0	0	0
287	2	54.235	-1.088	1.51	0.24	24.85	0.08	0.46	0.08	0.38	1.1	-465.7	0.96	2	1	0	0	0	0	0
287	2	54.235	-1.088	1.43	0.26	44.96	0.08	0.39	0.08	0.38	1.1	-465.7	0.96	2	1	0	0	0	0	0
288	2	54.229	-1.088	2.09	0.34	24.88	0.04	0.20	0.04	0.36	0.8	-367.3	1.09	1	1	0	0	0	0	0
290	2	54.217	-1.088	1.32	0.26	24.84	0.13	0.60	0.13	0.47	19.2	-337.7	1.00	1	0	0	0	0	0	0
291	2	54.210	-1.088	2.28	0.36	24.76	0.04	0.20	0.04	0.37	30.5	-356.9	0.97	1	1	0	0	0	0	0
292	2	54.204	-1.088	2.16	0.34	24.84	0.06	0.34	0.06	0.48	47.5	-326.4	0.88	1	1	0	0	0	0	0
294	2	54.192	-1.088	1.04	0.20	24.79	0.15	0.69	0.15	0.38	55.3	-369.4	1.15	1	1	0	0	0	0	0
295	2	54.186	-1.088	2.26	0.26	24.86	0.06	0.43	0.06	0.41	8.2	-351.1	1.17	1	1	0	0	0	0	0
296	2	54.180	-1.088	1.84	0.24	24.72	0.08	0.54	0.08	0.42	10.6	-450.0	1.02	1	1	0	0	0	0	0

Notes. This table is available in its entirety in electronic form at the CDS via anonymous ftp to cdsarc.u-strasbg.fr (130.79.128.5) or via <http://cdsweb.u-strasbg.fr/cgi-bin/qcat?J/A+A/>. A portion is shown here for guidance regarding its form and content.

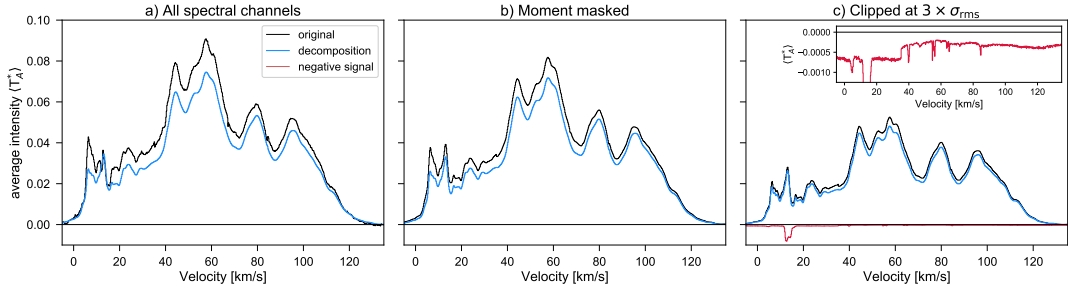


FIGURE 3.1: Average spectra of the full GRS data set (grey lines) and our final Gaussian decomposition results (blue lines). The three panels show different ways the average spectra were created: in *a*) we use all voxels, in *b*) we use only the voxels retained from moment masking, and in *c*) we use only voxels whose intensity value is above a S/N threshold of 3. The red line in *panel c* shows an average of high negative values throughout the GRS data set that was obtained by using only voxels with a value below $-3 \times \sigma_{\text{rms}}$. The inset in the right panel shows a zoom-in of the red line to better display the individual smaller negative peaks. See Sect. 3.2.2 for more details.

gives the reduced chi-squared (χ_{red}^2) values (see App. B.2.2 for more details). The next three columns can be used to identify fit solutions whose number of fit components is inconsistent with neighbouring fit solutions. Columns (15), (16), and (17) give the number of fit components N_{comp} , the weighted median number of fit components N_{med} determined from the fit solutions of the direct neighbours, and the number of component jumps $N_{\text{jump}} > 2$ towards directly neighbouring fit solutions (see Sect. 2.4.2.5). Finally, the last four columns indicate whether the fit component was flagged with one of the remaining optional quality criteria described in Sect. 2.4.2, with ‘1’ indicating that the component was flagged with the respective criterion. The flagging criteria are as follows: F_1 (18) indicates whether the fit component was strongly blended with another component; F_2 (19) indicates whether the fit component caused a negative feature in the residual; F_3 (20) indicates whether the fit component was flagged as comparatively broad; and F_4 (21) indicates whether the fit component was part of a region in the spectrum, which was flagged in phase 2 of the spatially coherent refitting routine in GAUSSPY+, which aims at identifying inconsistencies between the centroid values of the fit components of neighbouring fit solutions (see Sect. 2.5.2 for more details).

The criteria for the quality flags are very strict in the default settings of GAUSSPY+. To catch the majority of potential problems with the fit solutions, these criteria were designed to be biased towards producing false positives rather than false negatives. It is thus likely that a significant fraction of flagged components, in particular those flagged as blended (F_1) or broad (F_3), are good fit solutions.

3.2.2 Flux recovery

In this section we discuss the quality of our decomposition results in terms of recovered flux. We start by comparing the average spectrum of the original GRS data set to that of the decomposition. Figure 3.1 shows this comparison for spectra obtained using three different averaging methods. In Fig. 3.1 (a), we use all available



voxels; in Fig. 3.1 (b), we use the moment masking technique as outlined in Dame (2011); and in Fig. 3.1 (c), we only use voxels that have a value above $3 \times \sigma_{\text{rms}}$. By comparing the average spectra of the original data and the decomposition, we can estimate the recovered flux in our decomposition, which is 84.3%, 87.5%, and 92.1% for the three respective cases. The moment masking technique provides the most accurate comparison, as it recovers most of the emission, while still being relatively unaffected by noise contributions (see Sect. 2.7.1).

We can partly understand the missing flux by the fact that the moment masking technique recovers flux that is buried deep within the noise and is thus likely not recovered in our decomposition. The clipped average spectra in Fig. 3.1 (c) neglect all of the smaller intensity contributions below a S/N threshold of 3. As expected, the fraction of recovered flux in our decomposition is higher for these high S/N regions. A comparison of Fig. 3.1 (b) with Fig. 3.1 (c) shows that about a third of the total flux is coming from voxels with amplitude values below a S/N threshold of 3.

Next, we discuss the average spectrum of negative values to show that the GRS data set contains significant negative spectral features. The red line in Fig. 3.1 (c) shows an average spectrum of all voxels from the original data set with values smaller than $-3 \times \sigma_{\text{rms}}$. The inset in Fig. 3.1 (c) shows a zoomed-in version of the average spectrum of negative values. Most values of this average negative spectrum are due to random noise fluctuations that exceed a threshold of $-3 \times \sigma_{\text{rms}}$ and cause the general offset (the jump occurring at $v_{\text{LSR}} \sim 35 \text{ km s}^{-1}$ is due to a change in the observing mode that resulted in lower noise values; see Jackson et al. 2006). However, on top of this general offset are also many individual negative spikes located at specific v_{LSR} values. The most prominent negative peak is situated at a velocity range of $v_{\text{LSR}} = 11 - 17 \text{ km s}^{-1}$ and reaches its lowest value at $v_{\text{LSR}} \sim 12.5 \text{ km s}^{-1}$. This artefact is due to the presence of ^{13}CO emission in one of the ‘off’ positions used in the subtraction of sky emission (Jackson et al., 2006). The negative spikes at this position affect a significant number of spectra. We suspect that the remaining smaller negative spikes are likely also due to contaminating ^{13}CO emission in other off positions used in the sky subtraction.

In the default settings of GAUSSPY+, all negative peaks smaller than $-5 \times \sigma_{\text{rms}}$ are automatically masked for the decomposition, which led to the identification and masking of negative spectral features for about 1.6% of all spectra from the GRS data set. The vast majority of identified negative spikes are located in the region within $32.8^\circ \leq \ell \leq 38.1^\circ$ and $-0.7^\circ \leq b \leq 1.1^\circ$. Another region containing many negative spikes is located at $32.2^\circ \leq \ell \leq 32.7^\circ$ and $-1.1^\circ \leq b \leq -0.7^\circ$. Not excluding these negative spikes leads to incorrect comparisons if all spectral channels are summed up, since the average spectrum from the original data set is substantially reduced at the spectral range where the largest negative peaks are located (see Fig. 3.1 a).

We now shift our comparison to the examination of the spatial distribution of the integrated intensity, that means the zeroth moment maps of the data and decomposition results (Fig. 3.2). These maps were obtained with the moment masking technique outlined in Dame (2011), that means for the decomposition results we used the same unmasked spectral channels that were also used for the original data set. The similarity of the two maps gives us already a qualitative confirmation that the decomposition manages to reproduce the data set well. We provide a normalised



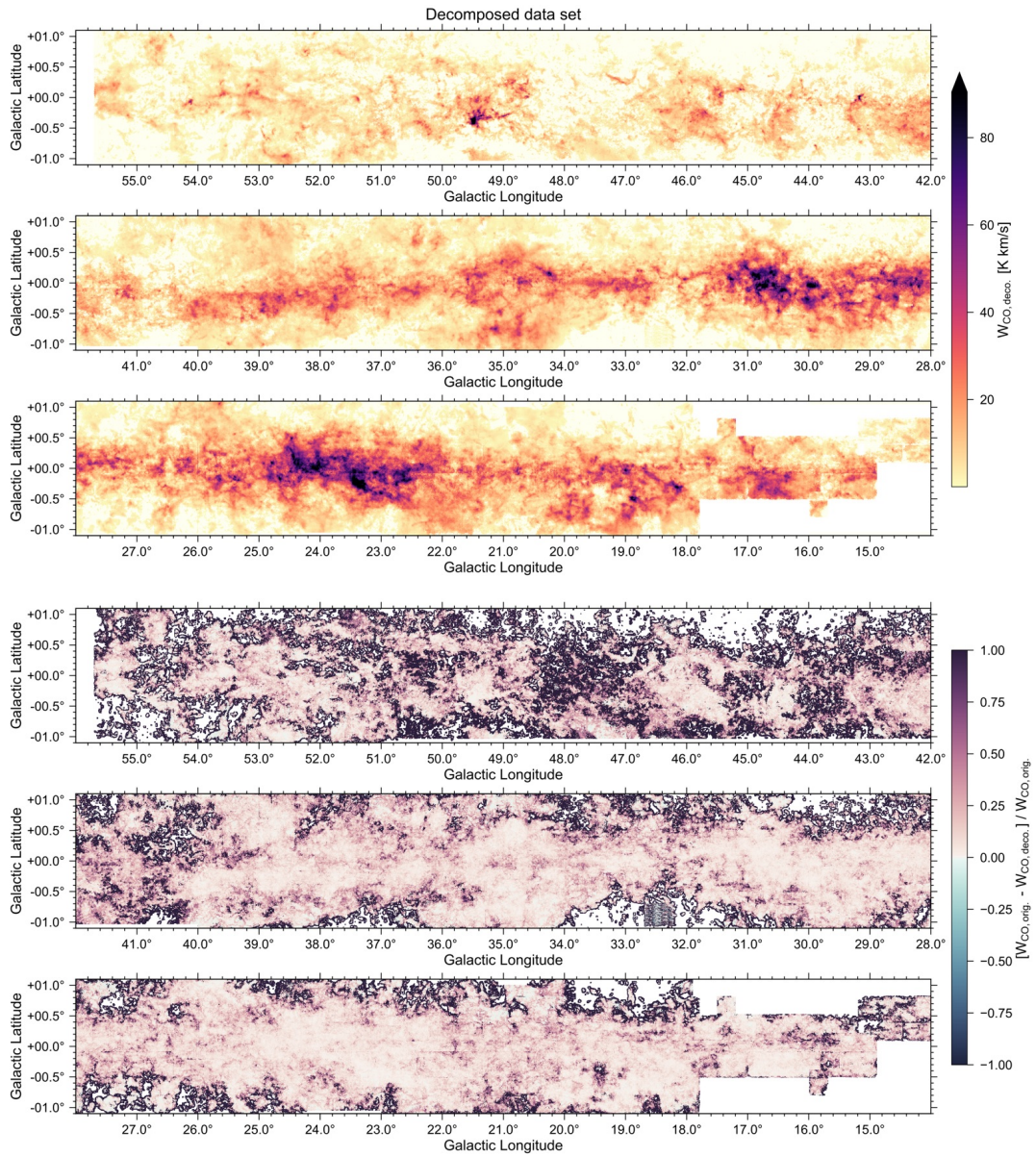
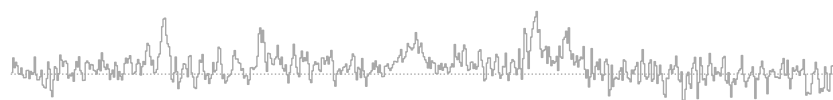


FIGURE 3.2: *Top*: Zeroth moment map of the GRS data set recreated from the Gaussian fit components and integrated over the entire velocity range ($-5 \lesssim v_{\text{LSR}} \lesssim 135 \text{ km s}^{-1}$). When displayed in Adobe Acrobat, it is possible to switch to the map of the [original data set](#). *Bottom*: Map of the normalised residual values.



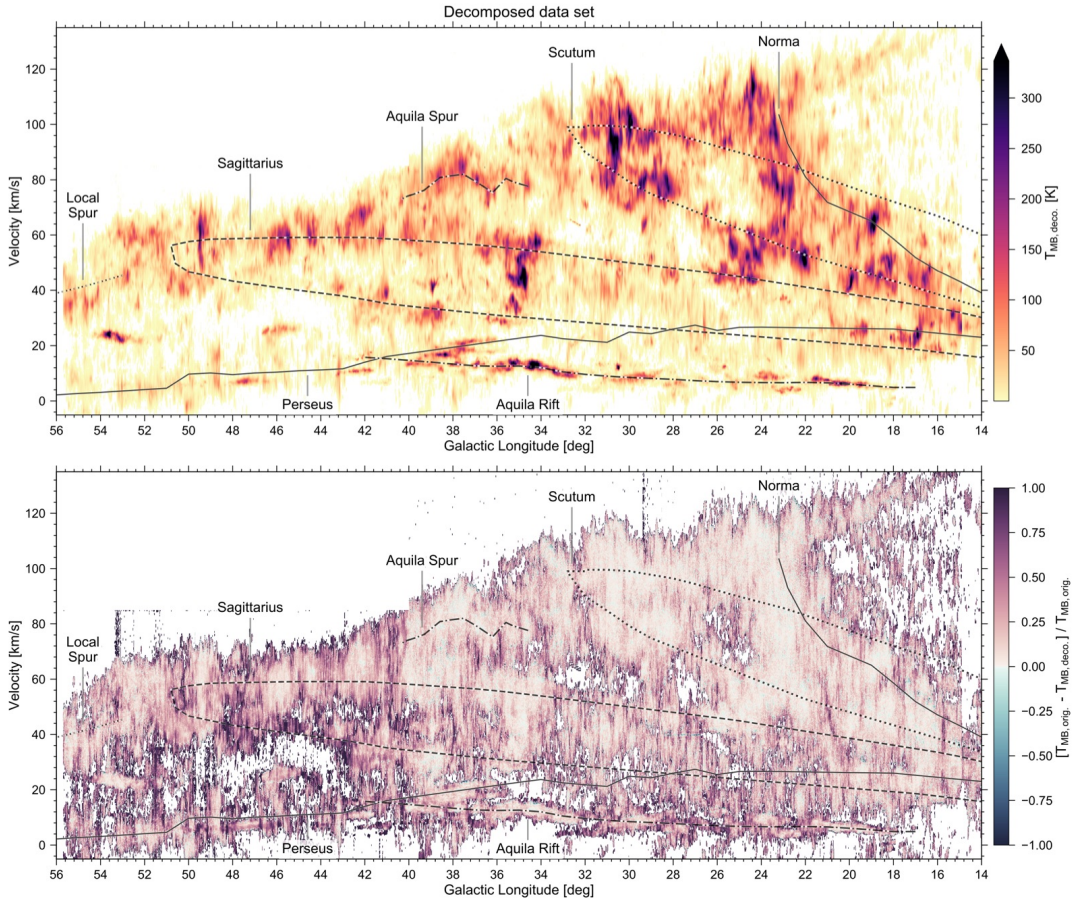


FIGURE 3.3: *Top*: PV map of the decomposed GRS data set. The emission was integrated over the full Galactic latitude range ($\pm 1.1^\circ$). When displayed in Adobe Acrobat, it is possible to switch to the map of the [original data set](#). *Bottom*: Map of the normalised residual values. Overplotted on both panels are positions of spiral arms, spurs, and local Galactic features from Reid et al. (2016).

residual map to better quantify this similarity (*bottom* part of Fig. 3.2). Positive and negative values can indicate spectra for which emission features were left unfit and spectra for which the final fit solution might fit a single component over multiple emission peaks, respectively. The empty spaces correspond to unobserved regions and regions where the moment masking technique identified no signal. The positions of high positive values in the normalised residual map are predominantly associated with diffuse emission in the original data set. This diffuse emission was likely too buried within the noise to be identified in the decomposition. More quantitatively, the 19.4% of the spectra with normalised residual values of one are responsible for 21% of the residual emission but only account for 2.6% of the total flux in the zeroth moment map of the original data set. For 4.1% of the spectra, the value in the zeroth moment map of the decomposed data set is higher than for the original data set; this could indicate that noise was fitted or that a single component was incorrectly fitted over multiple signal peaks. However, since for these spectra the emission from the decomposed data set is on average only higher by about 1% than the emission in the original data set, we conclude that this is only a minor issue.



Features of high values in the normalised residual map can also be traced back to elevated noise levels (see Fig. B.1). This correlation is expected, given that we use the same S/N thresholds over the entire survey region and the noise properties do vary significantly throughout the map. We try to quantify this correlation by splitting the data set in two parts, using the median of the noise distribution ($\sigma(T_{\text{MB}}) = 0.25$ K) as the threshold. We find that the 50% of spectra with noise values > 0.25 K contribute 62.8% to the residual, confirming that the regions with higher noise are indeed correlated with higher residual values.

Next, we discuss the recovered flux in terms of the PV map of the GRS (Fig. 3.3). We obtained these PV maps by integrating the moment masked data over the full Galactic latitude range. The positions of spiral arms, spurs, and local Galactic features from Reid et al. (2016) are also shown. The GRS covers both the near and far sides of the Scutum and Sagittarius spiral arms, which is why they make a turn in the PV map with the near sides having the lower velocity values.

The similarity of the PV maps of the original and decomposed data sets is another reassurance that our fits managed to reproduce all main features of the GRS data set, which is also confirmed in the normalised residuals (*bottom* part of Fig. 3.3). More quantitatively, the 12.5% of the data points in the normalised residual map with positive values of one—so the positions where none of the features of the original PV map could be recreated in the decomposed version—are responsible for 17.9% of the residual flux but are associated with positions in the PV map that account for only 3.5% of the total emission in the GRS. These percentages again confirm that positions with the highest normalised residual values are correlated with weak or diffuse emission in the original data set that was difficult to fit.

3.3 STATISTICS OF THE GAUSSIAN COMPONENTS

In this section we present the distributions of the Gaussian fit parameters, namely the amplitude or intensity T_{MB} , velocity dispersion σ_v , and mean position v_{LSR} . We also examine the relationships between the fit parameters and discuss some general properties of the GRS emission line data.

3.3.1 Number of fitted components

The number of fitted Gaussian components per spectrum (N_{comp}) is an interesting quantity because it is a measure for the complexity of the CO emission along the line of sight. For most of the GRS, we can assume that emission peaks in a spectrum that are well separated in v_{LSR} are associated with different Galactic orbits and thus originate from different structures along the line of sight. Figure 3.4, which shows the N_{comp} values for the entire GRS coverage, is then a proxy for how many structures there are along the line of sight. Especially near the Galactic midplane, multiple Gaussian components are required to fit the spectra.

We show a histogram of the number of fitted Gaussian components for the entire decomposition in Fig. 3.5. For about 27.3% of the spectra, we could fit no Gaussian components and for about 24.7% of the spectra, only one Gaussian component was



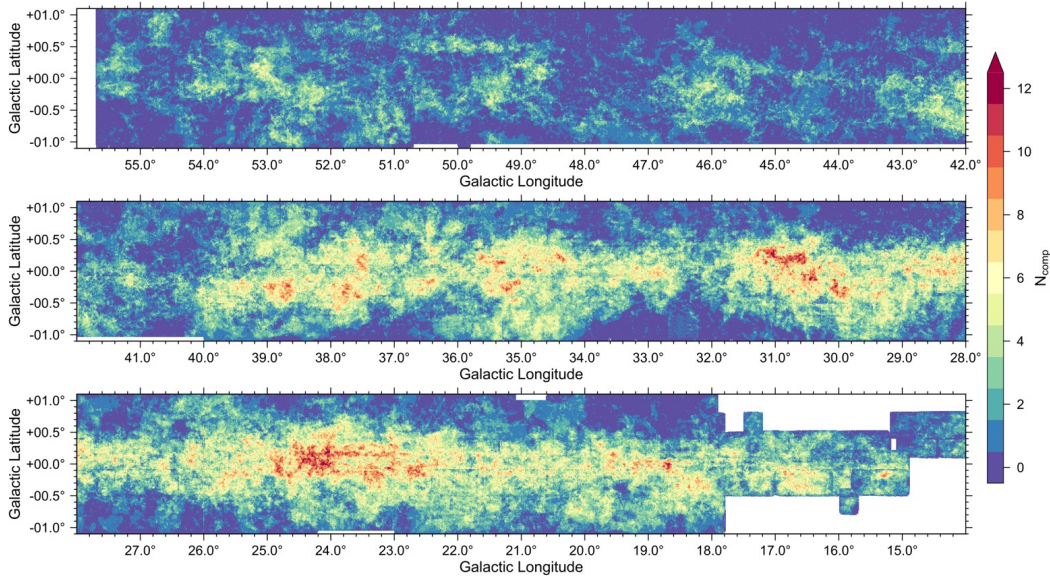


FIGURE 3.4: Map of the number of fitted Gaussian components per spectrum.

fitted. The percentage of GRS spectra that have at least one or more fit components (72.7%) is close to the percentage of spectra for which `GAUSSPY+` identified signal peaks (75.3%). If we assume all signal peaks identified by `GAUSSPY+` are correct, we get that for 2.6% of the spectra from the GRS data set we do not fit valid signal peaks in our decomposition. Most of these unfit signal peaks likely did not satisfy the minimum requirements for fit components in the `GAUSSPY+` decomposition run.

We considered whether the $\sim 0.1\%$ of GRS spectra with best-fit solutions that use a high number of components ($N_{\text{comp}} > 10$) are indeed connected with very complex lines of sight or whether they result from artefacts or problems in the decomposition. Most of the spectra that were fitted with a large number of components do occur in groups near the mid-plane, where complex spectra are expected (see Fig. 3.4). We can use the information contained in Table 3.1 to gauge to first order whether these complex fit solutions are significantly different from their neighbours. We can use the number of component jumps N_{jump} and the difference between N_{comp} and N_{med} (with N_{med} being the weighted median number of components calculated from the immediate neighbours) as good first indicators for whether the fit solution is similar to its neighbours. In the default settings of `GAUSSPY+`, spectra get flagged if $N_{\text{jump}} > 1$ or $\Delta N_{\text{max}} = |N_{\text{comp}} - N_{\text{med}}| > 1$. With these criteria $\sim 71\%$ of the 4884 fit solutions using more than 10 components get flagged. Relaxing the criteria to $\Delta N_{\text{max}} > 2$ and $N_{\text{jump}} > 2$, to factor in uncertainties in the neighbouring fit solutions, and requiring that both of these criteria are fulfilled reduces the percentage of flagged fit solutions to $\sim 31\%$. Based on this analysis, we conclude that for about a third, but possibly the majority of the spectra with high number of components ($N_{\text{comp}} > 10$), the fit solutions could be (partly) inconsistent with their neighbouring fit solutions.

There are multiple possible explanations for these inconsistencies, for example: *i)* spectra that show instrumental artefacts (e.g. regions of the spectrum that fluctuate



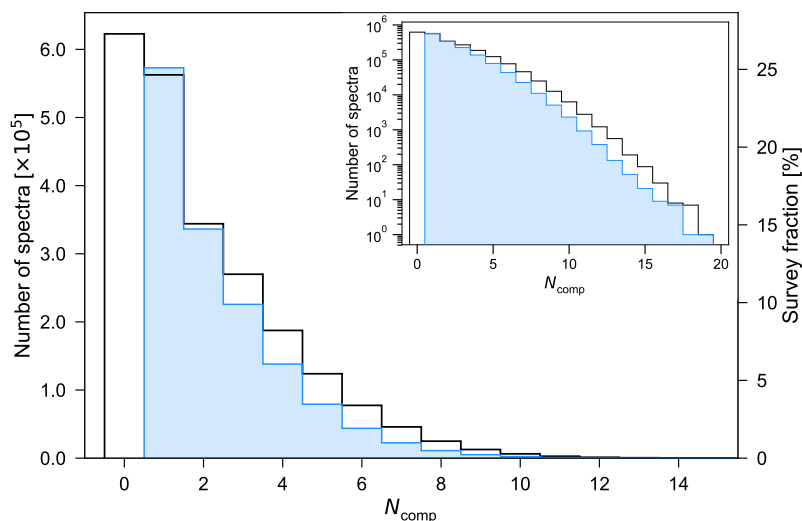


FIGURE 3.5: Histogram of the number of fitted Gaussian components per spectrum across the whole GRS data set for the full decomposition results (black line) and the fit components with S/N ratio > 3 (blue). The inset shows the same distribution on a logarithmic scale.

to very high and low values causing the decomposition algorithm to fit many of the high positive peaks), *ii*) spectra for which the estimated noise value was too low, causing the decomposition algorithm to mistake noise peaks for signal peaks with high S/N, *iii*) spectra that show leftover continuum emission that was fitted with many individual components, or *iv*) spectra that contained emission features deviating from a Gaussian shape that could not be fitted well with Gaussian components. We return to the question of complexity along the line of sight in Sect. 3.4.2, where we compare the number of fit components with the integrated CO emission and molecular gas surface densities derived from dust emission.

3.3.2 Intensity values

The distribution of the fitted amplitude values for the entire GRS data set (Fig. 3.6) peaks at about $T_{\text{MB}} = 0.68$ K and the interquartile range (IQR) is 0.71 – 1.71 K. For the subset of components with S/N > 3 , the distribution peaks at a value of about 0.88 K and the IQR is 0.95 – 1.98 K. The dashed vertical line at $T_{\text{MB}} = 0.6$ K shows the typical sensitivity limit of $3 \times S/N$ based on the peak value from the noise distribution shown in Fig. B.2 ($\sigma(T_{\text{MB}}) = 0.2$ K), which is very close to the peak value of the distribution of intensity values. The drop in the intensity distribution below the indicated sensitivity limit is thus likely not a physical effect but a result of the noise properties preventing the extraction of weaker signal peaks. When viewed logarithmically, the distribution shows an almost linear decrease between $T_{\text{MB}} \sim 1 - 6$ K, after which it flattens. We checked the spatial distribution of the fit components with high amplitude values of $T_{\text{MB}} > 6$ K. The vast majority of these components form separate connected structures on scales of individual molecular clouds, with T_{MB} values $\gtrsim 10$ K concentrated at their centres. We thus conclude that



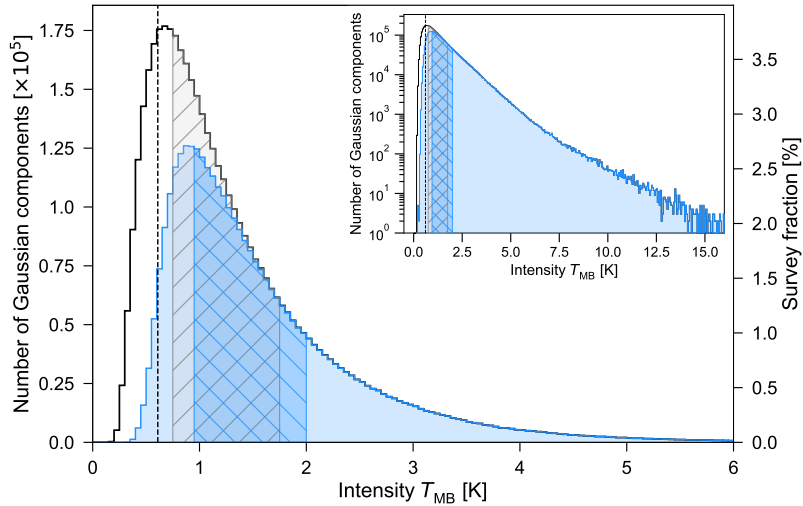


FIGURE 3.6: Histogram of intensity values for all fit components (black line) and fit components with S/N ratios > 3 (blue). The inset shows the same distribution on a logarithmic scale. The dotted vertical line shows the $3 \times \text{S/N}$ limit for the peak value of the noise distribution (shown in Fig. B.2). The hatched areas mark the IQRs of the two distributions. The bin width is 0.05 K.

most of the components with high T_{MB} values are not due to instrumental artefacts, but come from high column density regions.

3.3.3 Centroid velocity values

The distribution of the v_{LSR} positions of the Gaussian fit parameters (Fig. 3.7) shows that we do fit components across the entire velocity range (-5 to 135 km s^{-1}) spanned by the GRS. Some of the peaks in the distribution can be attributed to inferred positions of spiral arms, spurs, or local Galactic features (see the PV map in Fig. 3.3), for example, the Aquila Rift cloud at centroid velocities of about 10 km s^{-1} and the far and near portion of the Sagittarius and Scutum spiral arm, respectively, at around 60 km s^{-1} . As expected, the shape of the distribution is very similar to the average spectra from Fig. 3.1. A comparison between those two figures shows that even though the number of fit components with v_{LSR} values of $0 - 20 \text{ km s}^{-1}$ is high, their average intensity values are much lower than for the v_{LSR} range between $\sim 40 - 70 \text{ km s}^{-1}$. This is likely due to a larger contribution of diffuse, faint emission from local gas at low v_{LSR} values. For regions close to the Sun that are spatially well resolved, we can have only diffuse emission in the beam, which causes comparatively weak emission lines. At larger distances, where much larger physical areas are covered in the beam, this diffuse emission will likely be diluted and merged with stronger emission peaks, so that diffuse and strong emission is detected simultaneously in the beam. Moreover, the moderate spatial resolution of the GRS can cause stronger emission lines for molecular clouds observed at larger distances (if the beam filling factor is still approximately unity).



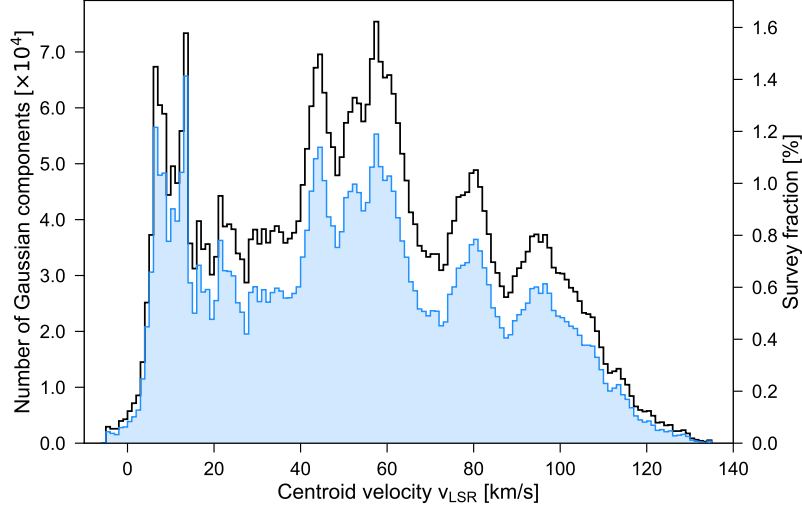


FIGURE 3.7: Histogram of centroid velocity values for all fit components (black) and fit components with S/N ratios > 3 (blue). The bin width is 1 km s^{-1} .

3.3.4 Velocity dispersion values

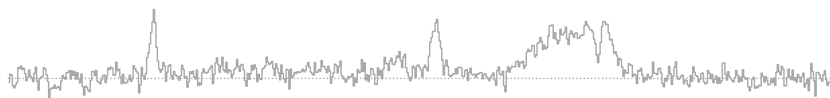
The distribution of the σ_v values of the Gaussian fit components (Fig. 3.8) is interesting, as it allows us to already estimate to first order upper limits for the turbulent Mach number associated with the emission lines. The peak for the distribution of σ_v values for all fit components is at $\sigma_v \sim 0.6 \text{ km s}^{-1}$ and the IQR is $0.68 < \sigma_v < 1.89 \text{ km s}^{-1}$. For the subset of fit components with S/N ratios > 3 , the peak is shifted towards a lower value of 0.45 km s^{-1} and the IQR is $0.59 - 1.58 \text{ km s}^{-1}$. About 0.6% of all fitted components have a velocity dispersion value below the resolution limit. In the default settings of GAUSSPY+, the minimum allowed value for the FWHM is set to the width of a single spectral channel, which yields σ_v values below the resolution limit.

When plotted logarithmically, the distribution has a linear dropoff from about $1 - 4 \text{ km s}^{-1}$, after which it flattens and has a shallower decline; it also shows that most of the fit components with very broad FWHM values have S/N ratios < 3 . It is likely that most of these broad components were fit over multiple low S/N peaks that could not be correctly deblended. A visual inspection of some of the GRS spectra showed that a small fraction also suffers from what seems to be an incorrect or insufficient baseline subtraction, which could lead to broad spectral features with low S/N ratios.

We can get upper limits for the turbulent Mach number $\mathcal{M}_{\sigma_{v_{\text{los}}}, 3\text{D}}$ by assuming that all non-thermal contributions to the velocity dispersion σ_v are due to turbulence:

$$\mathcal{M}_{\sigma_{v_{\text{los}}}, 3\text{D}} \approx \sqrt{3} \frac{\sigma_{v_{\text{turb}, 1\text{D}}}}{c_s} = \sqrt{3} \left[\left(\frac{\sigma_v}{c_s} \right)^2 - \left(\frac{\bar{\mu}_p}{\mu_{\text{obs}}} \right) \right]^{1/2}, \quad (3.1)$$

where σ_v is the velocity dispersion along the line of sight, c_s is the isothermal sound speed, $\bar{\mu}_p$ is the mean molecular mass ($\bar{\mu}_p = 2.33 \text{ amu}$), and μ_{obs} is the molecular



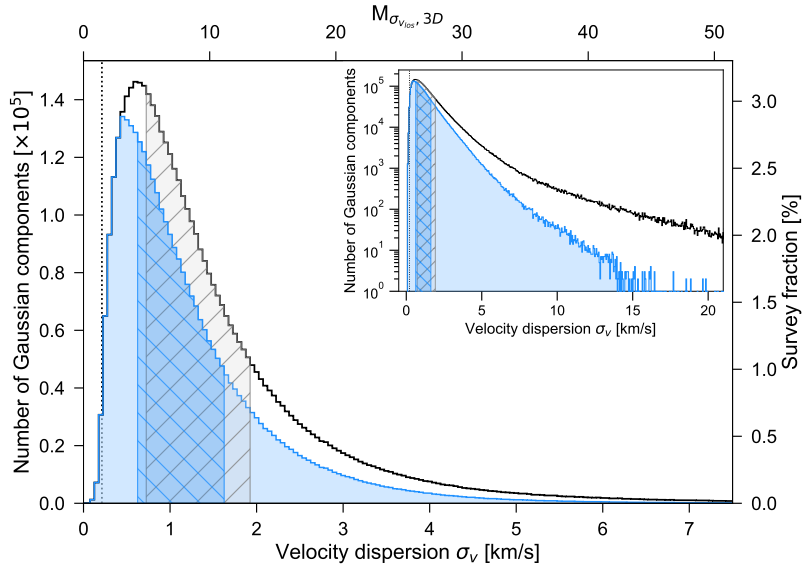


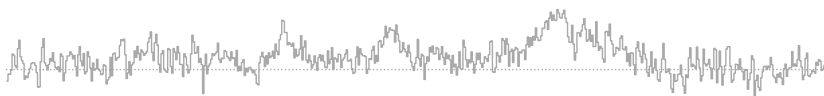
FIGURE 3.8: Histogram of velocity dispersion values for all fit components (black) and fit components with S/N ratios > 3 (blue). The upper abscissa indicates corresponding upper limits for turbulent Mach number values. The inset shows the same distribution on a logarithmic scale. The dotted vertical line indicates the velocity resolution of 0.21 km s^{-1} . The hatched areas mark the IQRs of the two distributions. The bin width is 0.05 km s^{-1} .

mass of the observed molecule (29 amu for ^{13}CO). We estimate the isothermal sound speed c_s with

$$c_s = \sqrt{\frac{k_B T_k}{\bar{\mu}_p m_H}}, \quad (3.2)$$

where T_k is the kinetic temperature of the gas, k_B is the Boltzmann constant, and m_H is the mass of atomic hydrogen. For T_k , we assume a uniform value of 18 K throughout the survey, which corresponds to the average of the mean line of sight dust temperature values for the Hi-GAL data overlapping with the GRS as estimated by [Marsh et al. \(2017\)](#).

The upper abscissa in Fig. 3.8 shows the resulting Mach number axis. The peak of the distribution corresponds to a Mach number of about 4. About 36.7% of all fit components and 28.6% of the fit components with S/N ratio > 3 are associated with turbulent Mach number values > 10 . About 3% of the fit components have σ_v values $> 5 \text{ km s}^{-1}$, resulting in associated high Mach numbers that are greater than 34. To put these large σ_v values into perspective, we can compare them to typical linewidth values found on cloud scales. For their catalogue of molecular clouds in the GRS, [Rathborne et al. \(2009\)](#) found average and maximum values for the of 3.6 and 9.8 km s^{-1} , which translate to σ_v values of 1.5 and 4.2 km s^{-1} , respectively. Given these values, it seems unlikely that the fit components with large σ_v values trace regions of extreme turbulence; it seems more likely they are: *i*) due to non-random ordered motion, for example, velocity gradients along the line of sight; *ii*) incorrect fits of multiple signal peaks with a single component; *iii*) fits of artefacts in the spectrum, introduced, for example, by insufficient or incorrect baseline subtraction;



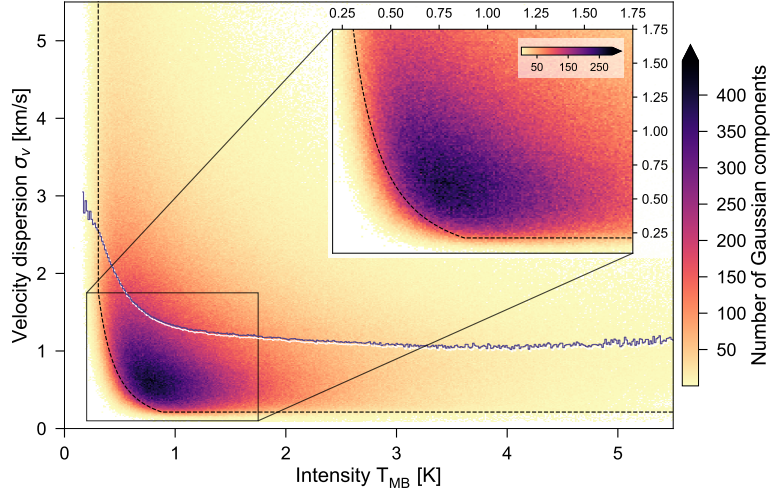


FIGURE 3.9: 2D histogram of intensity and velocity dispersion values for all fit components. The dashed line shows the lower limit for a chosen significance value of $\mathcal{S}_{\min} = 5$ and a velocity dispersion value corresponding to the spectral resolution limit of the survey (0.21 km s^{-1}). The blue line shows the mean σ_v value per intensity bin. The number of bins in either direction is 400. The inset is a zoom-in of the most dense region of the distribution and uses a finer grid with 175 bins in either direction.

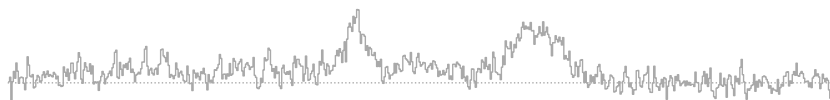
iv) associated with warmer gas temperatures (that increase the thermal linewidth and decrease the non-thermal contribution).

3.3.5 Relationships between the parameters

In this section we describe the relationships between the fit parameters using two-dimensional (2D) histograms. This allows us to better characterise our population of fit components, for example, the typical shape of the fitted lines. We also look at trends of T_{MB} and σ_v values with v_{LSR} position, which we can use to infer to first order properties of the gas emission at different Galactic distances.

Figure 3.9 shows the 2D distribution of the intensity and velocity dispersion values of all Gaussian fit components. The majority of components show both moderate intensity and velocity dispersion values ($0.5 \lesssim T_{\text{MB}} \lesssim 1.5 \text{ K}$, $0.25 \lesssim \sigma_v \lesssim 1.5 \text{ km s}^{-1}$). Beyond this concentration of most data points, the distribution shows a bifurcation, with the components having either high intensity and small velocity dispersion values or low intensity and high velocity dispersion values. That components with high σ_v values are predominantly connected with low T_{MB} values is an indication that these are likely fits to artefacts in the spectrum, as discussed in Sect. 3.3.4.

The absence of components with both low intensity and low velocity dispersion values is due to a selection effect in our decomposition. We only retain Gaussian components above a chosen significance value \mathcal{S}_{\min} (see Sect. 2.4.1.3), which excludes components with low intensity and low velocity dispersion values, because they are indistinguishable from individual random noise peaks. In Fig. 3.9, we indicate the expected lower limit for a significance value of $\mathcal{S}_{\min} = 5$, the spectral resolution limit



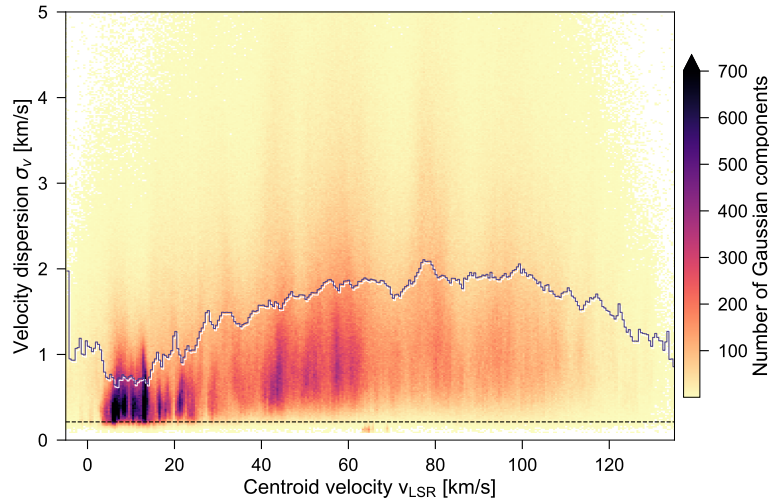


FIGURE 3.10: 2D histogram of centroid velocity and velocity dispersion values for all fit components. The dashed horizontal line indicates the velocity resolution of 0.21 km s^{-1} . The blue line shows the mean σ_v value per centroid velocity bin. The number of bins in either direction is 300. The data points with very low σ_v values located at $\sim 63 < v_{\text{LSR}} < 66 \text{ km s}^{-1}$ are due to an instrumental artefact.

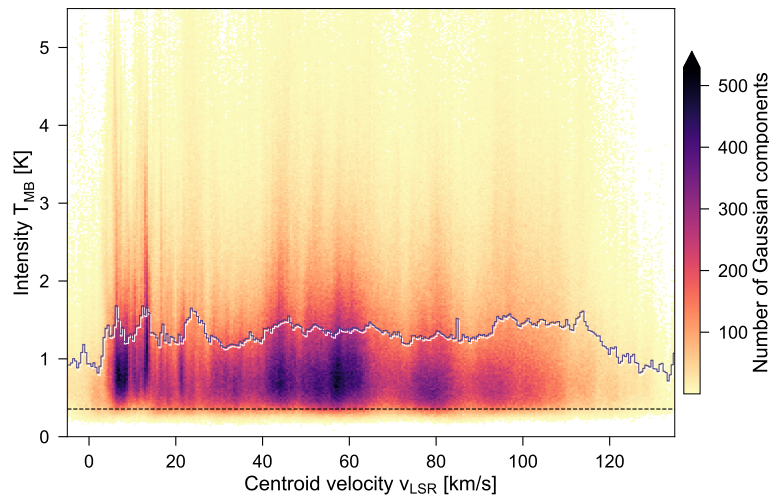


FIGURE 3.11: 2D histogram of centroid velocity and intensity values for all fit components. The dashed horizontal line indicates a S/N limit of 3 for $\sigma(T_{\text{MB}}) = 0.12 \text{ K}$, which corresponds to the 0.1st percentile of the noise distribution shown in Fig. B.2. The blue line shows the mean intensity value per centroid velocity bin. The number of bins in either direction is 300.



of the GRS (0.21 km s^{-1}), and a typical noise value of $\sigma(T_{\text{MB}}) = 0.2 \text{ K}$ (corresponding to the peak of the noise distribution shown in Fig. B.2). This lower limit corresponds very well to the shape of the distribution, with velocity dispersion values being clearly limited by the spectral resolution. Thus, Fig. 3.9 also serves as a good indicator of the sensitivity limit of our decomposition.

Only about 4% of all fit components have both high values of T_{MB} ($> 2 \text{ K}$) and σ_v ($> 2 \text{ km s}^{-1}$). Moreover, the IQR of the v_{LSR} values of these strong fit components stretches from 57.3 to 94.5 km s^{-1} and is thus clearly shifted towards higher values compared to the IQR of the full distribution (30.5 to 78.1 km s^{-1}).

We can see a similar trend of increasing linewidths at higher v_{LSR} values in the relation between the fitted v_{LSR} and σ_v values (Fig. 3.10). In contrast, the distribution of fitted intensity values with v_{LSR} position (Fig. 3.11) is on average very constant at a value of about 1.5 K , which is expected from the distance-independence of the surface brightness. However, Fig. 3.11 also shows very bright intensity peaks, in particular from components located at velocities of $\sim 10 \text{ km s}^{-1}$, most of which also have narrow linewidths (Fig. 3.10). This emission at velocities of $\sim 10 \text{ km s}^{-1}$ predominantly originates from the very nearby Aquila Rift cloud and is thus spatially and spectrally well resolved in the GRS observations, which explains the narrow and bright emission peaks. For regions farther away, beam averaging effects will cause broader emission lines, which will be reflected in the shape of the fit components. We discuss these trends further in Sect. 3.5, where we put them into the context of a size-linewidth relationship.

3.4 GLOBAL PROPERTIES OF THE GAS EMISSION

In this section we focus on the global properties of our decomposition. We first look at the distribution of the velocity dispersion values with Galactic coordinates and then use the number of fit components per spectrum to gauge the complexity of the gas emission along the line of sight.

3.4.1 *Distribution of velocity dispersion values as a function of Galactic coordinates*

Here we examine how the velocity dispersion values of the fit components are distributed as a function of the Galactic coordinates. We search for global trends and outlying regions, such as regions with above-average non-thermal motion, within the Galactic disk. We focus on fit components with S/N ratios > 3 in this analysis, since the line shape of components with a lower S/N ratio could be significantly impacted by noise. We again use the σ_v values to estimate upper limits for the turbulent Mach numbers assuming isothermal gas temperatures of 18 K (see Sect. 3.3.4).

We first focus on the distribution of the σ_v values as a function of Galactic latitude (Fig. 3.12). The number of high velocity dispersions (and Mach numbers) increase towards the Galactic midplane, which is likely due to the following three effects. First, most substantial star-forming regions are concentrated in the midplane (e.g. Beuther et al., 2012). These star-forming regions are associated with warmer molecular gas and plenty of high-velocity dispersion events (such as protostellar jets, outflows,



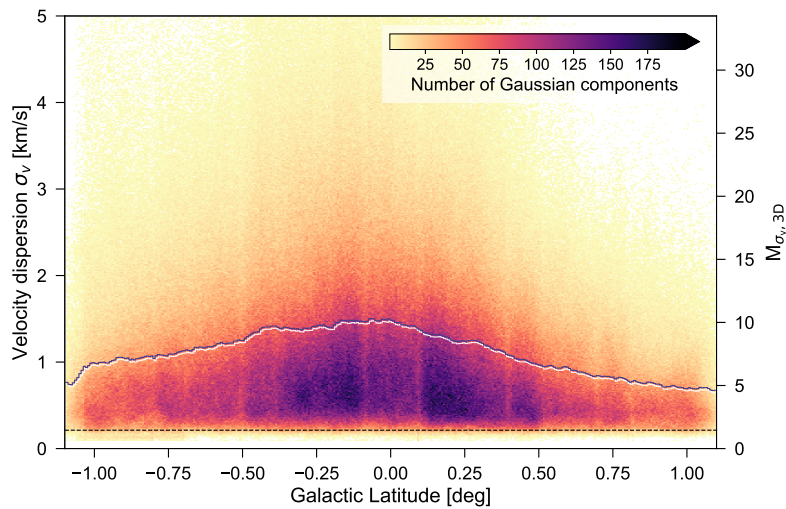
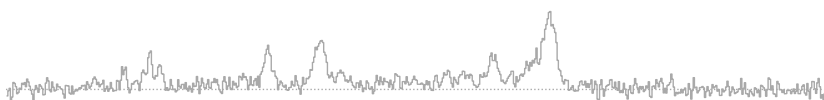


FIGURE 3.12: 2D histogram of the velocity dispersion values against their Galactic latitude positions for all fit components with S/N ratio > 3 . The dashed horizontal line indicates the velocity resolution of 0.21 km s^{-1} . The blue line shows the mean σ_v value per Galactic latitude bin. The number of bins used in either direction is 358.

shells, and supernova remnants), which will cause broader emission lines and higher σ_v values of the associated fit components. Second, we would expect more confusion along the line of sight towards the midplane, where multiple individual velocity components could be blended together and would thus be observed as a single broad component at the moderate resolution of the GRS. Third, to maintain a stable disk, the gas pressure of the Galactic disk must balance the imposed pressure created by the weight of the vertical layers of gas and stars. This pressure will be higher towards the midplane and will accordingly increase the velocity dispersion in the gas.

We also detect a clear asymmetry, with higher mean velocity dispersions at negative Galactic latitude values. This can be partly explained by a vertical offset of the Sun from the physical Galactic midplane (e.g. [Goodman et al., 2014](#), however, see also Sect. 3.5.2).

Next, we look at the distribution of the σ_v values as a function of Galactic longitude (Fig. 3.13). The distribution shows that the number of components with very high σ_v values increases towards the inner Galaxy. The mean of the σ_v distribution shows multiple peaks, some of which are likely associated with large H II region complexes, for example, W51 at $\ell \sim 49.5^\circ$, and W39 at $\ell \sim 19^\circ$. Apart from these individual peaks and even though the velocity coverage is reduced for $\ell > 40^\circ$, the general offset of the mean σ_v curve is remarkably constant at a value of $\sim 1 \text{ km s}^{-1}$ from the outermost coverage in Galactic longitude up until $\ell \sim 32^\circ$. For the GRS coverage with $\ell < 32^\circ$ the offset of the mean σ_v curve is shifted to higher values of ~ 1.2 to 1.3 km s^{-1} , in agreement with recent studies that also found increased molecular gas velocity dispersion towards the inner part of the Milky Way ([Miville-Deschênes et al., 2017](#)). The giant H II region complex W43 is located at a Galactic longitude range of about $30^\circ < \ell < 31.5^\circ$ and is close to the near end of the Galactic bar ([Zhang et al., 2014](#)). Recent simulations of barred galaxies showed that gas



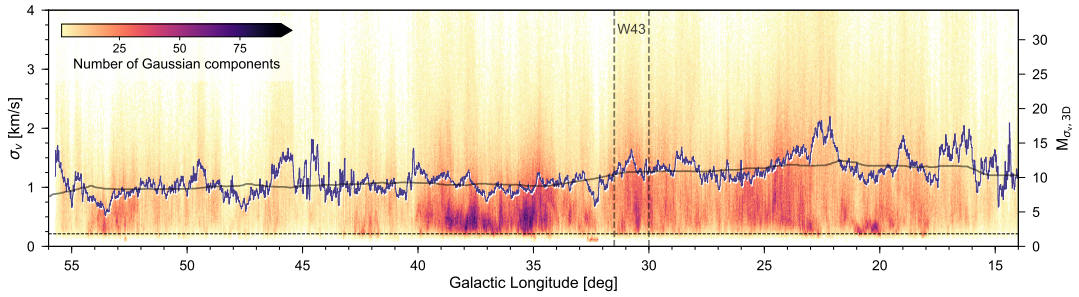


FIGURE 3.13: 2D histogram of velocity dispersion values against their Galactic longitude positions for all fit components with S/N ratio > 3 . The dashed horizontal line indicates the velocity resolution of 0.21 km s^{-1} . In the horizontal and vertical direction we use 3415 and 200 bins, respectively. The blue line indicates the mean velocity dispersion value per Galactic longitude bin. The grey solid line is a smoothed version of the mean σ_v curve using a median filter with a kernel of $\sim 3^\circ$. Dashed vertical lines show the approximate location of the giant HII region complex W43.

within the central regions dominated by the Galactic bar can reach high gas velocity dispersion values (Khoperskov et al., 2018). We thus speculate that the increase in the offset of the mean σ_v curve is at least partly due to increased turbulence introduced by the Galactic bar. Another reason for the increased non-thermal motions could be that there is more feedback from star formation towards the inner part of the Galaxy, as evidenced, for example, by the increased H II region density (see Fig. 3 in Anderson et al. 2017) and an increase in the fraction of clumps that show signs of embedded star formation (Ragan et al., 2018).

3.4.2 Complexity along the line of sight

In this section we discuss the relation between the integrated intensity (W_{CO}) of ^{13}CO emission, H_2 column densities inferred from dust emission, and complexity along the line of sight as measured by the number of fit components. We want to determine if the ^{13}CO emission preferentially originates from a few strong components or a larger number of smaller components, possibly spread wide along the spectrum. We test this by comparing the W_{CO} values of the moment masked GRS data (shown in Fig. 3.2) with the number of fit components per spectrum (Fig. 3.4). We illustrate the results in form of a ridge plot (left panel of Fig. 3.14). In this plot, each row shows the probability distribution functions (PDFs) of W_{CO} values for all spectra fitted with N_{comp} components. For better visibility, we chose upper limits of $W_{\text{CO}} = 85 \text{ K km s}^{-1}$ and $N_{\text{comp}} = 10$. Figure 3.14 shows that the integrated intensity of ^{13}CO correlates with the number of emission peaks. The spread of the distributions increases with the number of components, and the distributions overlap in the W_{CO} range. However, based on Fig. 3.14 we can say that, for example, lines of sight with W_{CO} values of 20 K km s^{-1} are predominantly associated with four to six fit components.

A similar analysis can provide insight into interpreting dust continuum emission features in the Galactic plane; for such data, there is otherwise no straightforward



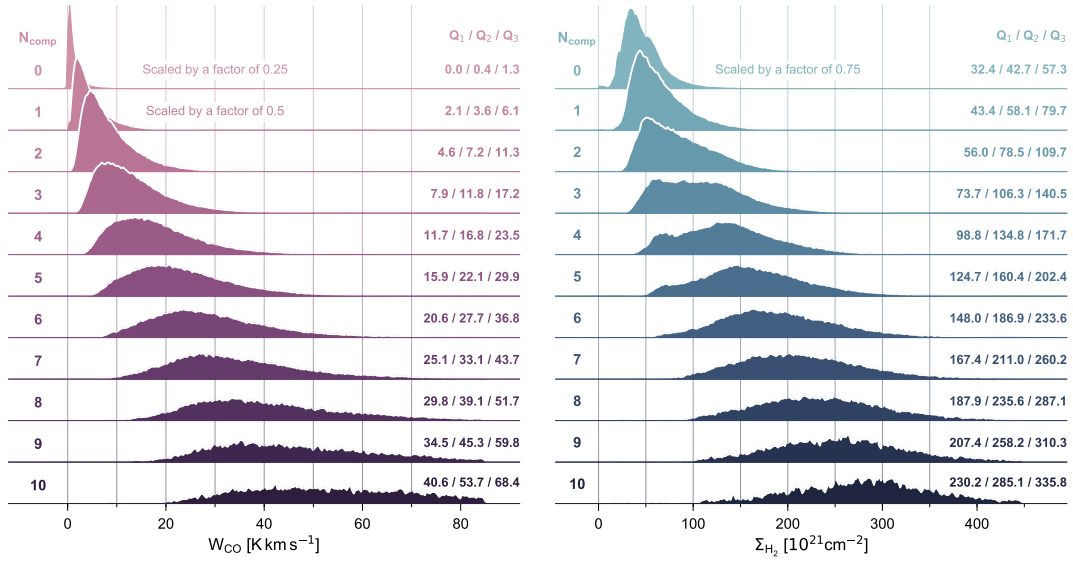
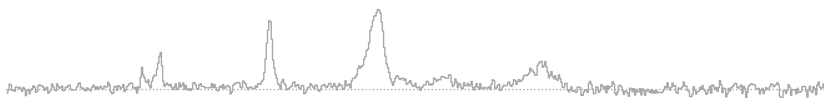


FIGURE 3.14: Ridge plots showing PDFs of integrated ^{13}CO emission (*left panel*) and H_2 surface density values inferred from dust emission (*right panel*). For the *left panel*, each row shows the PDF of the W_{CO} values of all spectra fitted with N_{comp} components (indicated with the number to the left and the colour-shading of the PDF). For the *right panel*, each row shows the PDF of the Σ_{H_2} values associated with ^{13}CO spectra fitted with N_{comp} components (indicated with the number to the left and the colour-shading of the PDF). For better visibility, three of the PDFs have been scaled in size, which is indicated next to the PDFs. The values to the right of the PDFs indicate the first quartile (Q_1), the median (Q_2), and the third quartile (Q_3) of the distribution.

way to estimate how complex a line of sight is. This comparison is interesting, because it immediately shows us how well the gas and dust are mixed. If the dust column density is independent from the number of ^{13}CO fit components, it could indicate differences in the distribution of dust and ^{13}CO gas. The right panel of Fig. 3.14 shows a ridge plot constructed from H_2 column density values derived from dust emission (Sect. 3.1.2). We can see the same trend with dust as with ^{13}CO : the dust-derived column densities correlate with the number of fit components. To first order, this confirms that the ^{13}CO gas and dust are indeed well mixed and thus largely originate from the same structures along the line of sight. Moreover, this analysis indicates that high dust column densities (leading to inferred H_2 column density values $> 200 \times 10^{21} \text{ cm}^{-2}$) arise from a composite of many dust components along the line of sight, rather than a single very dense structure.

Moreover, Fig. 3.14 shows that dust emission is present along lines of sight for which no components could be fit in the ^{13}CO spectra. This implies that the dust emission traces also a more diffuse gas component that shows little to no ^{13}CO emission. This is in agreement with previous studies that have established that ^{13}CO mostly traces the denser parts of molecular clouds, with surface densities exceeding $\sim 25 M_{\odot} \text{ pc}^{-2}$ (e.g. Roman-Duval et al., 2016).



3.5 DISENTANGLING EMISSION FROM THE NEAR AND FAR SIDE OF THE GALAXY

Determining the exact location of molecular gas emission, and hence the Galactic distribution of it, is a major problem for understanding the structure of the Milky Way. The location of the emitting gas is usually determined using the kinematic distance method (Sect. 1.3.3), which yields two distance solutions (near and far) for the lines of sight within the solar orbit. This distance ambiguity can only be resolved with additional information, for example, using H I self-absorption features (e.g. Roman-Duval et al., 2009). In this section we discuss how our decomposition results can be useful in solving the distance ambiguity of features at low v_{LSR} values, specifically between -5 to 20 km s^{-1} . We use the fact that beam averaging effects for regions at larger distances to the Sun will cause broader emission lines and thus higher σ_v values of the fit components. The general principle of using the σ_v value of the fit components to help resolve the kinematic distance ambiguity should also be applicable to other v_{LSR} values, albeit with less accuracy. In Sect. 3.5.1, we first recall the relationship between the Galactic structure and radial velocities of -5 to 20 km s^{-1} . We then discuss the expected location and width of the physical midplane for this v_{LSR} regime (Sect. 3.5.2) and how we would expect the linewidths to differ between emission coming from nearby and far away regions (Sect. 3.5.3). We then use these three discussions in Sect. 3.5.4 to argue how our decomposition results can give useful prior information in solving kinematic distance ambiguities.

3.5.1 Considerations based on Galactic kinematics

The observed line of sight radial velocity v_{LSR} of a point along Galactic longitude ℓ can be calculated as

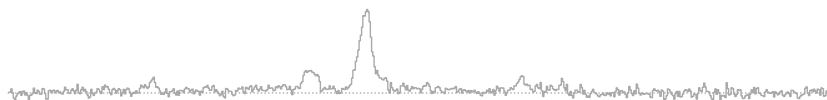
$$v_{\text{LSR}} = R_0 \sin \ell \left(\frac{\Theta(R_{\text{gal}})}{R_{\text{gal}}} - \frac{\Theta_0}{R_0} \right), \quad (3.3)$$

where R_{gal} is the Galactocentric radius to the point along the line of sight, $\Theta(R_{\text{gal}})$ is the value of the rotation curve for R_{gal} , and R_0 and Θ_0 are the radius of the solar circle and the corresponding rotational speed of that orbit. We use values of $R_0 = 8.15 \text{ kpc}$ and $\Theta_0 = 236 \text{ km s}^{-1}$ as estimated by Reid et al. (2019). For simplicity, we assume a flat rotation curve (i.e. $\Theta(R_{\text{gal}}) = \text{const.}$) and we do not correct for effects of non-circular motions towards the Galactic centre or the direction of Galactic rotation. We also do not correct for solar peculiar motions used by the telescope. For a given value of v_{LSR} , Eq. 3.3 can be solved for R_{gal} and rewritten as a function of ℓ . We can then use the relation

$$R_{\text{gal}} = \sqrt{R_0^2 + d_{\odot}^2 - 2 R_0 d_{\odot} \cos \ell} \quad (3.4)$$

to solve for d_{\odot} , the distance to the point along the line of sight associated with the v_{LSR} value:

$$d_{\odot} = R_0 \cos \ell \pm \sqrt{R_{\text{gal}}^2 - (R_0 \sin \ell)^2}. \quad (3.5)$$



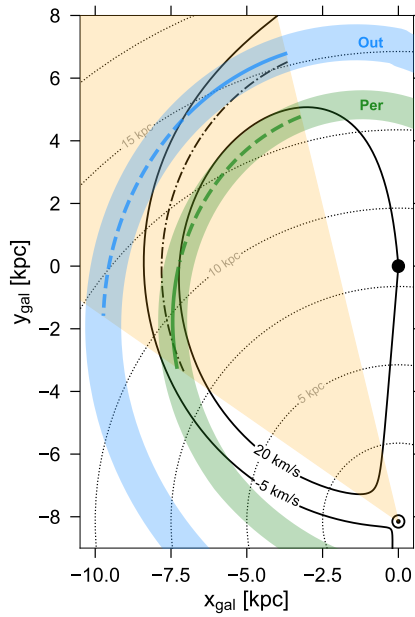


FIGURE 3.15: Face-on view of the Galactic plane. The black solid lines show constant projected v_{LSR} values of -5 and 20 km s^{-1} . The orange-shaded area indicates the coverage of the GRS. Inferred positions and estimated widths for the Perseus and Outer spiral arm from Reid et al. (2019) are shown with the shaded green and blue areas, respectively. The central positions of the spiral arms are marked with solid and dashed lines depending on whether the majority of the arm is visible in the selected velocity range of $-5 < v_{\text{LSR}} < 20 \text{ km s}^{-1}$. The position of the Galactic centre and the Sun are indicated with a black dot and the Sun symbol, respectively. Dotted grey lines indicate distances to the Sun in 2.5 kpc intervals. The black dash-dotted line shows the distances used to estimate the FWHM extent of the molecular gas disk. See Sects. 3.5.1 and 3.5.2 for more details.

For lines of sight inside the solar orbit, Eq. C.7 always yields two distance solutions, corresponding to points on the near and far side of the Galaxy that would be observed as having the same v_{LSR} value.

In Fig. 3.15 we show estimated lines of constant projected v_{LSR} values of -5 and 20 km s^{-1} in a face-on view of the first quadrant of the Milky Way. Given the assumptions listed above, emission peaks observed in GRS with $-5 < v_{\text{LSR}} < 20 \text{ km s}^{-1}$ are thus expected to come from regions between those two curves of constant v_{LSR} . On the near side, this corresponds to the regions in the GRS that are located closest to the Sun, with distances mostly $\lesssim 1 \text{ kpc}$. On the far side, this area overlaps with the inferred locations of the Perseus and Outer spiral arms (Reid et al., 2019), with emission at lower longitude values expected to come from regions that can be located up to $\sim 15 \text{ kpc}$ away.

3.5.2 Expected location and extent of the Galactic disk

Recent studies by Anderson et al. (2019) and Reid et al. (2019) found a good correspondence of the vertical position of the Sun with the IAU definition of the Galactic midplane, which is in contrast to past studies that determined vertical offset posi-



TABLE 3.2: Expected velocity dispersion values based on a size-linewidth relationship for different physical extents of the beam size at different distances.

d_{\odot} [kpc]	d_{beam} [pc]	σ_v^{exp} [km s ⁻¹]
0.25	0.06 pc	0.2
0.5	0.11 pc	0.2
1.0	0.22 pc	0.3
8.5	1.90 pc	1.0
15.0	3.35 pc	1.3

tions of $z_0 = 25 \pm 5$ pc (Bland-Hawthorn & Gerhard, 2016). Even a larger offset of $z_0 = 25$ pc would only have strong implications for the most nearby emission from the Galactic midplane, which would be shifted towards negative Galactic latitudes. We would nevertheless expect the midplane to be centred at about $b = -0.1^\circ$ to 0° for GRS emission with v_{LSR} values of -5 to 20 km s⁻¹ originating from the far side of the Galaxy. However, previous studies of the Milky Way H I and molecular gas disk showed that the first quadrant of the Galactic disk is warped towards positive Galactic latitude values at the larger distances ($\gtrsim 8$ kpc) probed by the GRS (e.g. Kalberla & Kerp, 2009; Roman-Duval et al., 2016; Miville-Deschênes et al., 2017). Assuming a moderate warp of the Galactic midplane of 50 to 100 pc at a distance of about 10 kpc would translate to positive shifts in Galactic latitude of ~ 0.3 to 0.6° . Factoring in a warp of the Galactic disk, we would thus expect the physical midplane to be shifted towards positive Galactic latitude values. The FWHM extent of the molecular gas disk in the outer Galaxy ($R_{\text{gal}} \gtrsim 8.5$ kpc) is on average about 200 pc (Roman-Duval et al., 2016), which at distances of 8 and 15 kpc (the typical distances of GRS emission with $-5 < v_{\text{LSR}} < 20$ km s⁻¹ at the far side of the disk) corresponds to a range in Galactic latitude of about 0.7° and 0.4° , respectively.

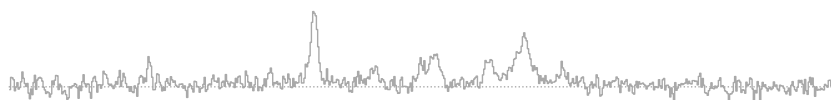
3.5.3 Expected velocity dispersion values

The physical beam size (d_{beam}) of the GRS varies significantly for distances to gas emission on the near and far side of our Galaxy: d_{beam} is about 0.06 pc at the distance of 250 pc and 3.35 pc at 15 kpc (Table 3.2). The larger beam for regions farther away can be argued to result in broader linewidths; the widths of emission lines have been shown to exhibit scale dependency (Solomon et al., 1987)⁵:

$$\sigma \text{ (km s}^{-1}\text{)} = 0.7 \cdot \left(\frac{L}{1 \text{ pc}} \right)^{0.5}. \quad (3.6)$$

Table 3.2 shows the linewidths predicted by this scaling. For the scales probed by the GRS data at near distances (~ 250 to 500 pc), the size-linewidth relation predicts

⁵ The normalisation factor of 0.7 corrects for the different distance to the Galactic centre of $R_0 = 10$ kpc used by Solomon et al. (1987).



narrow velocity dispersions of about 0.2 km s^{-1} . For distances beyond 8.5 kpc, the relation predicts velocity dispersions $> 1 \text{ km s}^{-1}$.

3.5.4 Information contained in the velocity dispersion values

In Sects. 3.5.1 to 3.5.3 we discussed what we would expect for the origin, extent, and shape of velocity components with v_{LSR} values of -5 to 20 km s^{-1} . Now we demonstrate how this applies to our decomposition results and how the σ_v values of the fit components can give us an indication of whether the emission line originates from regions close to the Sun or farther away.

The upper part of Fig. 3.16 shows the moment masked version of the decomposed GRS data set integrated within a velocity range of $-5 < v_{\text{LSR}} < 20 \text{ km s}^{-1}$ (if fit components extended beyond this range we only included the emission within these limits). As already discussed in the previous sections, this channel map contains a combination of emission features that originate either from regions very close to the Sun or as far away as 15 kpc. We also show the positions of the Perseus and Outer spiral arms as inferred by Reid et al. (2019), which indicates where we would expect emission from the far side of the disk to appear in the channel map. In the Galactic longitude range from about 17 to 43° , Fig. 3.16 is dominated by emission from the Aquila Rift cloud (see Fig. 3.3 and the schematic map in Fig. 9 of Dame & Thaddeus 1985), which is located at a distance to the Sun of about 250 to 500 pc (Straizys et al., 2003; Zucker et al., 2019). Due to this close distance, emission from the Aquila Rift is spread out and extends over the full survey coverage in Galactic latitude.

With the predictions from Sects. 3.5.1 to 3.5.3 in hand, we can now try to understand the spatial distribution of the observed velocity dispersions. The *bottom* part of Fig. 3.16 shows for each line of sight the σ_v values and corresponding upper limits for the turbulent Mach number of the narrowest fit components (with centroid position values within $-5 < v_{\text{LSR}} < 20 \text{ km s}^{-1}$). The region dominated by the Aquila Rift shows overall much lower σ_v values. The distribution of all σ_v values contained in the *bottom* part of Fig. 3.16 peaks at a value of 0.35 km s^{-1} , matching the low σ_v values we would expect for the physical extent of the GRS beam at 250 to 500 pc derived from the size-linewidth relation in Sect. 3.5.3. Towards higher Galactic longitude values ($\ell \gtrsim 40^\circ$), where confusion with emission from the Aquila Rift cloud is expected to be less severe, we can see a strip of increased σ_v values that seems confined in Galactic latitude to $\sim 1^\circ$ in extent. If these velocity components also originate from regions close to the Sun, these must be regions with increased non-thermal motions. However interestingly, fit components with higher σ_v values are less spread out in Galactic latitude than components with lower velocity dispersion values, which agrees with what we would expect from emission lines coming from regions farther away. We thus speculate that this emission with high σ_v values is coming mostly from the Perseus and Outer arm on the far side of the Galactic disk (see Fig. 3.15).

Based on our arguments from a size-linewidth relationship, we expect the emission lines originating from far distances to show increased σ_v values $> 1 \text{ km s}^{-1}$ (see Table 3.2). Using this prediction as a threshold, we fitted a polynomial of the third order to all σ_v values $> 1 \text{ km s}^{-1}$ in the lower part of Fig. 3.16, which is indicated with the dash-dotted black line. For the polynomial fit we first calculated the average



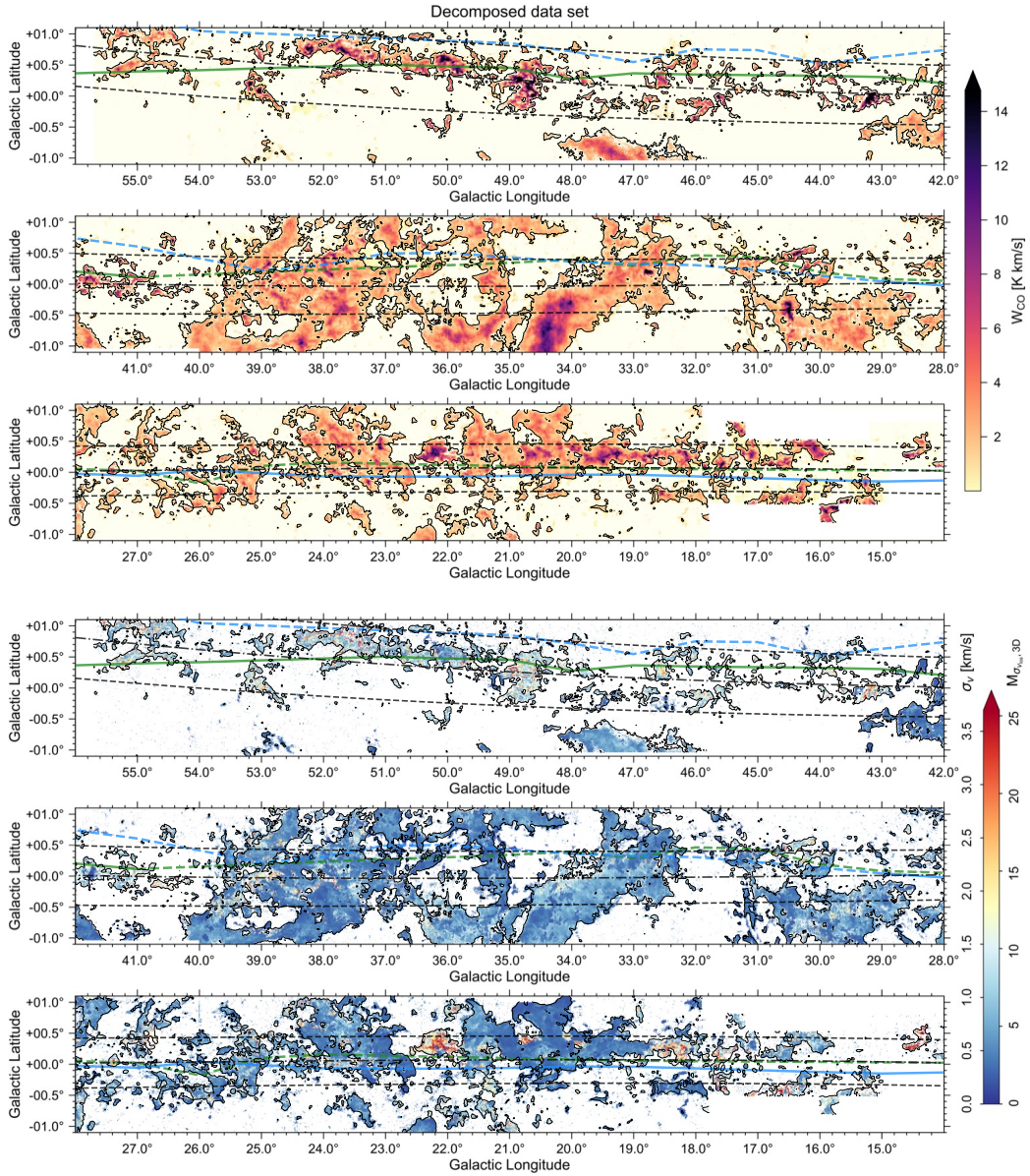


FIGURE 3.16: *Top*: Zeroth moment map of the decomposed data set integrated within $-5 < v_{\text{LSR}} < 20 \text{ km s}^{-1}$. *Bottom*: Velocity dispersion values for the narrowest fit component within the same v_{LSR} range as used in the top panel. The second scaling on the colourbar indicates corresponding estimates for upper limits of the turbulent Mach number. In both panels we show: the position of the Perseus and Outer spiral arms as inferred by Reid et al. (2019) (green and blue lines, respectively, see Fig. 3.15); black contours indicating a W_{CO} value of 0.5 K km s^{-1} ; a fit to the positions with σ_v values $> 1 \text{ km s}^{-1}$ (dash-dotted black line); and the estimated FWHM extent of the molecular gas disk on the far side of the Milky Way (dashed black lines). See Sect. 3.5.4 for more details. When displayed in Adobe Acrobat, it is possible to switch to the channel map of the original data set, show only the positions with σ_v values $> 1 \text{ km s}^{-1}$, hide the contours, hide the fit to the positions with σ_v values $> 1 \text{ km s}^{-1}$ and estimated FWHM extent of the gas disk, and hide the positions of the Perseus arm, and Outer arm.



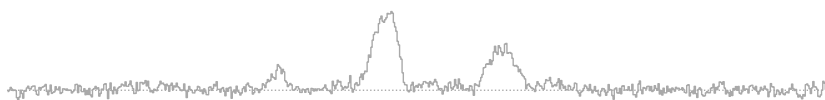
Galactic latitude position per Galactic longitude bin for all σ_v values $> 1 \text{ km s}^{-1}$. We also overplot the expected scale height of the molecular gas disk with dashed black lines, which we calculated for the average distance to emission lines with v_{LSR} values of -5 to 20 km s^{-1} on the far side of the disk (indicated with dashed black lines in Fig. 3.15). This estimated range for the scale height of the molecular gas disk well matches the height of the strip with increased σ_v values. Assuming that the indicated strip of high σ_v values indeed corresponds to the Galactic midplane at the far distance, its position at positive Galactic latitude values would also be consistent with the shift expected from a contribution of the warp of the Galactic disk towards positive heights in the first quadrant (Sect. 3.5.2). If our conjecture is true, this would point to an increase in the warp of the Galactic disk at Galactic longitude values $\gtrsim 42^\circ$ at distances of ~ 10 to 12 kpc (see Fig. 3.15). Moreover, it would suggest that the majority of the increased σ_v values in Fig. 3.16 are caused by effects of resolution, beam averaging, or turbulent motion on the scale of clouds (macroturbulence) rather than being introduced by highly turbulent subregions within nearby local clouds (microturbulence).

The Gaussian decomposition results can thus be useful in disentangling near and far emission for characterising and constraining Galactic structure. In the next chapter we concentrate on establishing distances to the Gaussian fit components, for which the considerations from this section can serve as useful prior information on solving the kinematic distance ambiguity.

3.6 VELOCITY FLUCTUATIONS

With the decomposition results of the GRS data set, we are also able to address the question of how the detailed velocity structure of the molecular gas looks like over a large section of our Galaxy. In the top panel of Fig. 3.18 we again show the classical PV diagram of the entire decomposed GRS data set. Since we integrated along the entire latitude coverage, the resulting map is partly a superposition of physically unrelated structures, but can be useful in determining overdensities that can be indicative of spiral arm structures (see Fig. 3.3).

We also show zoom-ins for two highly elongated molecular clouds—termed giant molecular filaments (GMFs)—that were identified and discussed in Ragan et al. (2014). GMFs are intriguing objects, as they could be connected to or are indicative of larger-scale Galactic structure (Goodman et al., 2014; Zucker et al., 2015). The two GMFs we highlight are located at opposite ends of the GRS longitude coverage and show distinct differences in their physical properties. GMF 20 is located at a distance of $\sim 3.5 \text{ kpc}$, has a total mass of $\sim 2.5 \cdot 10^5 M_\odot$, and a length of $\sim 140 \text{ pc}$ (Zhang et al., 2019); it might still have a physical connection to the Scutum spiral arm, making it a good candidate for a spur (Ragan et al., 2014). GMF 54 is located at a distance of $\sim 2 \text{ kpc}$, has a length of $\sim 40 \text{ pc}$, and has a total mass of $2.5 \cdot 10^4 M_\odot$ (Zhang et al., 2019), thus being about an order of magnitude less massive than GMF 20; it also seems to be a clear interarm structure, as it is located far away from any identified spiral arm features (Ragan et al., 2014). The insets of the two GMFs are only integrated over their respective latitude extent ($-0.32^\circ < b < 0.09^\circ$ for GMF 20 and $-0.19^\circ < b < 0.2^\circ$ for GMF 54).



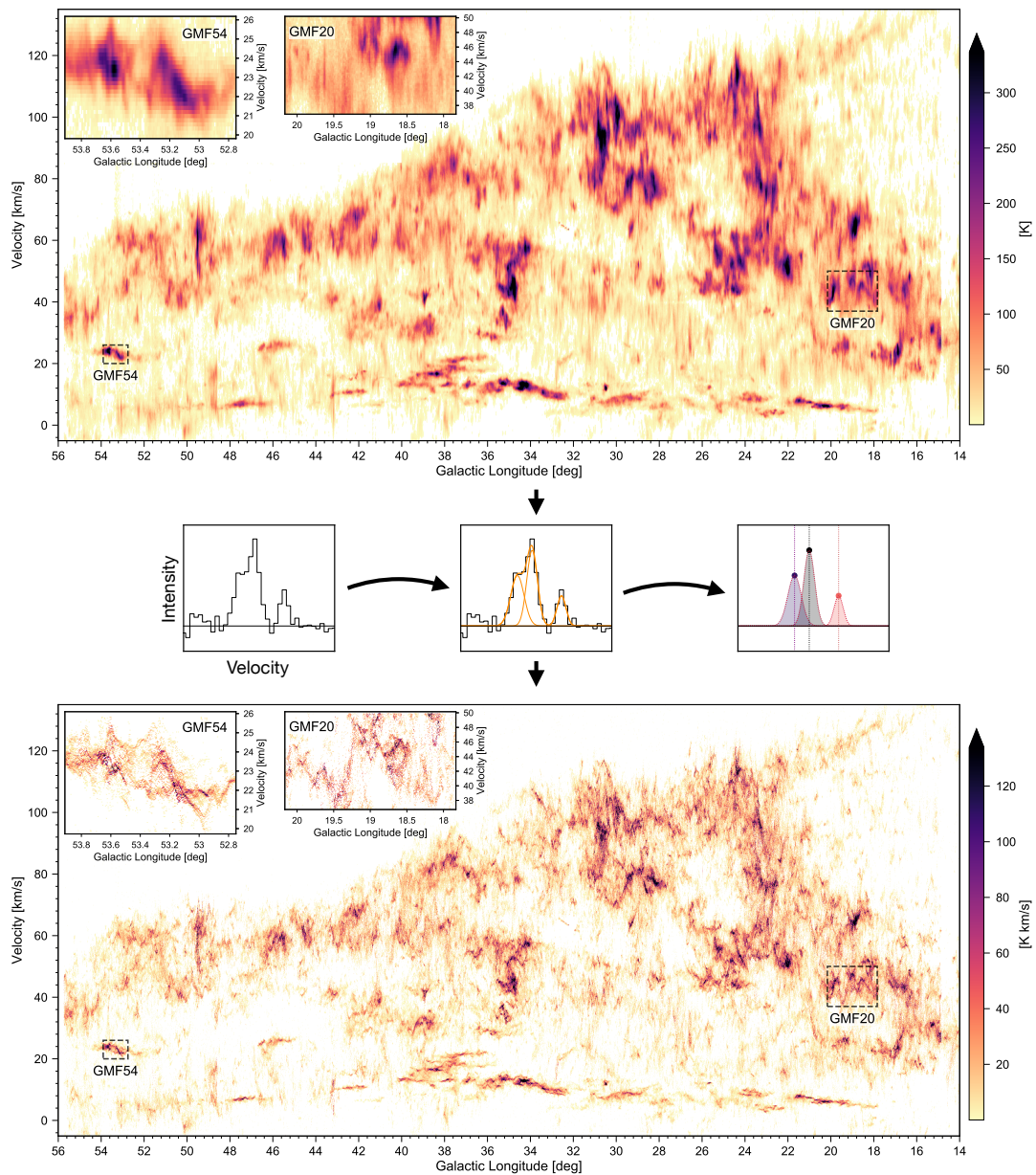
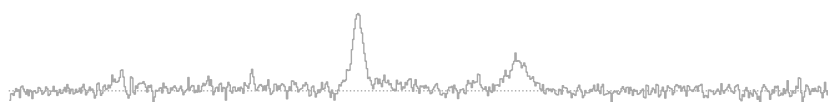


FIGURE 3.17: *Top*: PV diagram of the entire Galactic Ring Survey integrated over the full Galactic latitude coverage. *Middle*: Schematic illustrating the transformation of the data via the Gaussian decomposition, where each resulting data point represents the integrated intensity of a Gaussian fit component concentrated at its centroid position. *Bottom*: PV diagram of the transformed data set. Dashed boxes in the top and bottom panel indicate two giant molecular filaments that are shown in more detail in the insets to highlight the ubiquity of qualitatively similar velocity fluctuations. The inset figures are only integrated along the Galactic latitude range of the respective GMFs.



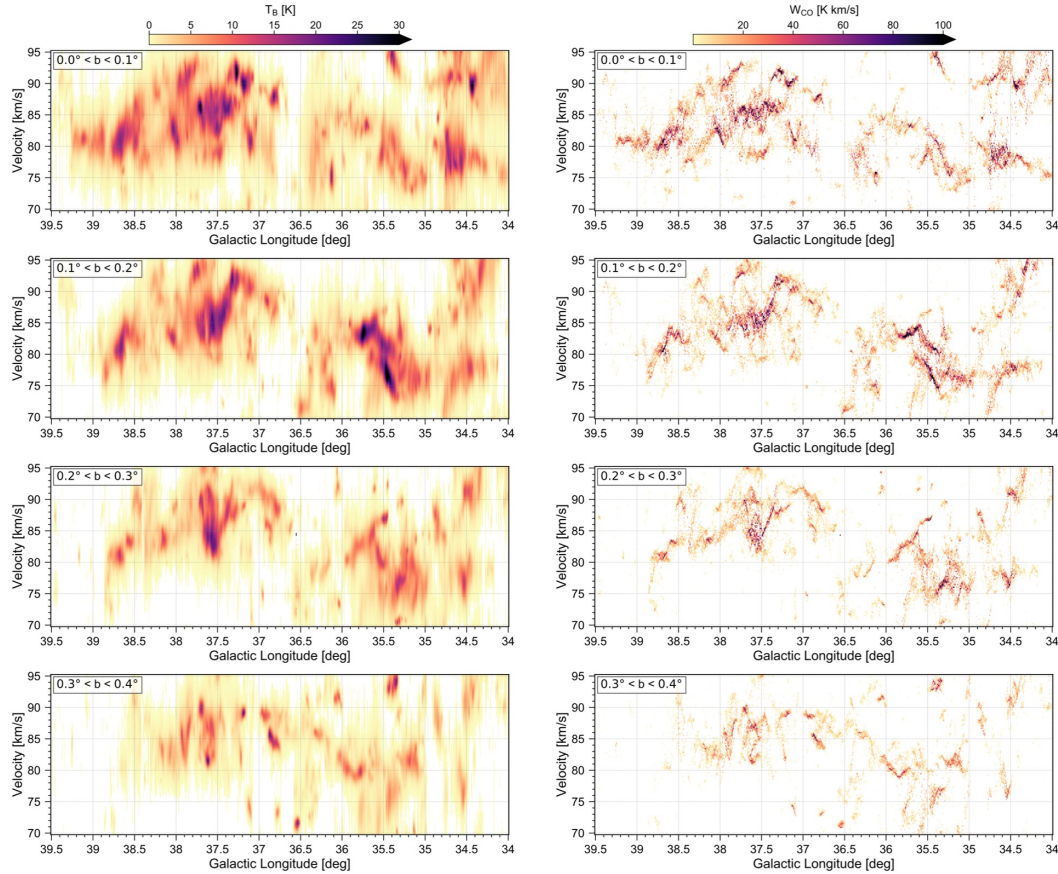
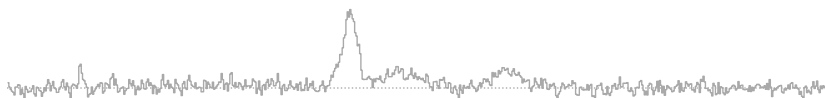


FIGURE 3.18: PV diagrams of the GAUSSPY+ decomposition results for the Aquila Spur region. The left columns show the maps for the recreated data set from the decomposition. The right columns show the same dataset, with the integrated intensity of each Gaussian component concentrated at its centroid velocity. Different rows correspond to integrations for different Galactic latitude ranges indicated in the top left corner of each panel.

The velocity structure in the PV diagrams has a very blurry or washed-out appearance. This is due to the width of the emission lines, which hide how the line centroids change and make it difficult to identify velocity-coherent structures. However, with the help of our decomposition results we can get rid of this blurring effect of the linewidths. We can transform the data set by concentrating the integrated intensity of each fit component at the respective centroid position (see schematic in the middle panel of Fig. 3.17).

The resulting transformed data set (bottom panel of Fig. 3.17) gives a much clearer view of how the line centroids change from position to position, which makes it easier to identify velocity gradients and coherent structures. The change in the appearance of the velocity structure is especially striking for the two GMFs in the insets. The transformed PV diagram shows that the emission line centroids of these two features are characterised by waves and fluctuations, which appear qualitatively similar.

These velocity fluctuations occur throughout the entire GRS dataset and have a similar appearance throughout. Figure 3.18 shows another example for the Aquila



Spur region. The left columns show classical PV diagrams of the decomposition results, for which we integrated the emission along the Galactic latitude axis. The right columns show the same dataset after we performed the additional transformation of concentrating the integrated intensity of each Gaussian fit component at its centroid position. The rows give different integration intervals in Galactic latitude, thus showing the change of the fluctuations over this spatial coordinate. We note again that the wavy appearance of the centroid velocity values in the right panels is completely hidden in the PV diagrams in the left panels.

Similar velocity fluctuations have recently been observed also in other data sets covering different spatial scales and environments (Henshaw et al., 2016b; 2019; Liu et al., 2019; González Lobos & Stutz, 2019). In a collaborative effort (Henshaw et al., in press), we combined the results on the GRS decomposition with additional molecular gas data spanning a wide range of scales and environments, including the nearby galaxy NGC 4321, the central molecular zone (CMZ) of our Galaxy and individual molecular clouds within the Milky Way’s disk and CMZ. We find that all these observations exhibit qualitatively similar fluctuations in their gas velocity structure. These results have led us to conclude that these fluctuations are a universal feature of the molecular ISM. Most importantly, we find evidence that for some of our probed environments peaks in the velocity fluctuations correlate with regular density enhancements, whereas for other environments no such correlations exists. We interpret this as evidence for a highly dynamic ISM, with the kinematic patterns being either consistent with expectations from turbulent motions or convergent motions indicative of accretion flows or large-scale instabilities.

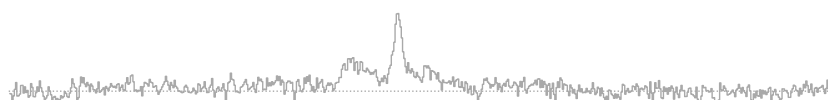
3.7 SUMMARY

In this chapter we presented Gaussian decomposition results for the entire GRS data set at its full spatial and spectral resolution obtained with GAUSSPY+. In total, we fitted ~ 4.6 million Gaussian components to the ~ 2.3 million ^{13}CO emission line spectra of the GRS. Especially spectra from lines of sight near the Galactic midplane showed great complexity, requiring 10 or more fit components for a good decomposition.

The decomposition recovers 87.5% of the flux contained in the GRS (92.1% of emission with a S/N ratio > 3). Most of the non-recovered flux is due to diffuse or weak ^{13}CO emission that could not be identified in the decomposition due to varying noise properties and our use of a single S/N threshold for the entire data set.

Assuming a uniform gas temperature of 18 K, we determined upper limits for the turbulent Mach number. We estimate from the velocity dispersion of our fit components with a S/N ratio > 3 that about 28.6% are associated with turbulent Mach number values > 10 . We see a clear trend of higher velocity dispersion values for fit components with higher v_{LSR} values, which is likely due to the effect of beam averaging of emission lines originating at larger distances to the Sun.

We studied the distribution of velocity dispersion values along the Galactic coordinates and found that velocity dispersions increase towards the Galactic midplane, likely due to the concentration of star forming regions in the Galactic plane. We also

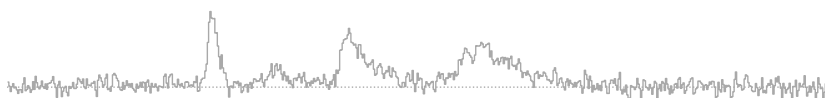


found an increase in the σ_v values towards the inner Galaxy, which we speculate could be due to the influence of the Galactic bar.

The integrated intensities of ^{13}CO correlate with the number of Gaussian fit components along the line of sight, indicating that larger integrated intensity values are associated with more complexity in the spectra. We also compared the number of fitted components to H_2 surface density values inferred from dust emission by [Marsh et al. \(2017\)](#) and find a similar trend of higher Σ_{H_2} values being associated with more fit components in the corresponding ^{13}CO spectra. This indicates that ^{13}CO gas and dust emission is originating from the same structures along the line of sight.

We also demonstrated how the decomposition results can aid in resolving confusion from kinematic distance ambiguities. We used arguments based on Galactic structure and the Galactic rotation curve to disentangle emission from the nearby Aquila Rift molecular cloud and gas emission at distances $\gtrsim 8.5$ kpc that is likely associated with the Perseus and Outer spiral arms. We further explore the usefulness of these fitting results as prior information in determining kinematic distances in the next chapter.

Finally, we showed that the spectral decomposition enables a transformation of the data set that is crucial for identifying trends in the gas kinematics. By concentrating the integrated intensity of each fit component at its centroid position, we obtained a much clearer view of the detailed gas velocity structure. This transformed velocity structure showed the presence of qualitatively similar fluctuations throughout the entire data set. Similar fluctuations have been also observed in data sets covering vastly different scales and environments; we interpret these as evidence for a highly dynamic ISM, which can be indicative of physical phenomena, such as turbulent motions, accretion flows, or large-scale instabilities ([Henshaw et al., in press](#)).



All models are wrong, but some are useful.

— George Box

Based on Riener et al., to be submitted to *Astronomy & Astrophysics*.

In the previous chapter, I presented the fitting results obtained with `GAUSSPY+` for the entire ^{13}CO emission data set of the GRS. The detailed velocity structure obtained via the decomposition has already allowed interesting quantities and intriguing results to be extracted from this large survey. However, as discussed in Chapter 1, the observed emission features in Galactic plane surveys can be a complex superposition of multiple different structures along the line of sight. To disentangle this confused emission and account for the effects of varying spatial resolution we need to determine distances to the emission features.

The main motivation of this chapter is to use the currently most precise model for the structure and rotation curve of the Milky Way from Reid et al. (2019) in conjunction with the Bayesian approach presented in Reid et al. (2016) and Reid et al. (2019) to analyse the distribution of molecular gas within the Galactic disk. In addition, I introduce two new priors: one is based on an extensive compilation of literature distance solutions for molecular clouds and clumps and the other uses the fitted velocity dispersion together with a size-linewidth relationship to separate blended emission from near and far distances (see discussion in Sect. 3.5). With this Bayesian method I derive distance estimates to all ~ 4.6 million Gaussian components fitted to the GRS data, thereby producing the best assessment of the distribution of its ^{13}CO emission.

I discuss the results of two different distance runs that either include or exclude a prior for an assumed model of Galactic features, such as spiral arm and interarm locations. These distance results represent two very useful extremes in the parameter space of the distance estimation. In one case I intentionally bias the emission towards our currently best knowledge of spiral arm features or overdensities of HI and CO , which are expected to also coincide with overdensities in ^{13}CO . In the other case I obtain a picture that is unbiased by an assumed spiral arm model, but is much more dominated by the chosen Galactic rotation curve and suffers more from kinematic distance uncertainties and errors introduced by streaming motions. This approach thus allows me to determine lower and upper limits for the fraction of emission within spiral arm and interarm locations, and enables me to discuss the robustness of the results in terms of how much the gas emission varies with Galactocentric distance and Galactic features.

The structure of this chapter is as follows. In Sect. 4.1 I discuss the Bayesian approach to calculate distances to the fitted emission features, and introduce two additional priors that are based on literature distances and the fitted linewidth. In

Sect. 4.2 I present the results of the two distance runs, discuss the fraction of gas (Sect. 4.2.3) and velocity dispersion (Sect. 4.2.4) in spiral arm and interarm regions, and look at variations of the gas properties with Galactocentric distance (Sect. 4.2.5). I also consider the vertical distribution of the gas (Sect. 4.2.6), discuss potential problems in the distance estimation (Sect. 4.2.7), and compare our distances with previous results (Sect. 4.2.8). I present a summary of this chapter in Sect. 4.3.

4.1 DISTANCE ESTIMATION

In this section we introduce the Bayesian approach for the distance calculation and describe the settings for our two distance runs that either incorporate or neglect a prior based on a model for Galactic structure. We further present how we incorporated additional prior information based on literature KDA information and the fitted linewidths, and discuss how we choose the final distance results.

4.1.1 Bayesian distance calculator

For the distance estimation we used the Bayesian distance calculator (BDC) tool (Reid et al., 2016; 2019) that was designed for the distance calculation of spiral arm sources. For a given $(\ell, b, v_{\text{LSR}})$ coordinate, the BDC calculates a distance PDF based on multiple priors that can be selected by the user. In the current version of the BDC (v2.4, Reid et al. 2019) this includes the following priors:

KD: the kinematic distance;

GL: the Galactic latitude value or displacement from the Galactic midplane;

PS: the proximity to parallax sources; these are high mass star-forming regions, whose trigonometric parallaxes have been determined as part of the Bar and Spiral Structure Legacy (BeSSeL) Survey¹ and the Japanese VLBI Exploration of Radio Astrometry (VERA)²;

SA: the proximity to features from an assumed spiral arm model; these features (such as spiral arms and spurs) have been inferred from combining information from the parallax sources with archival CO and HI Galactic plane surveys;

PM: the proper motion of the source.

The BDC allows users to set weights for these priors ($P_{\text{KD}}, P_{\text{GL}}, P_{\text{PS}}, P_{\text{SA}}, P_{\text{PM}}$) that can range from 0 to 1. If the weight of a prior is set to 0 it is neglected in the distance estimation. In the default settings of the BDC, all prior weights are set to 0.85, with the exception of P_{PS} , which receives a lower weight of 0.15. In addition, users can also supply a prior for the resolution of the KDA, that means they can provide information on whether the source location is expected to be on the near or far side of the Galactic disk. The weight P_{far} for this prior is by default set to 0.5, so that the near and far solutions of the KD prior receive equal weight. In this work we

¹ <http://bessel.vlbi-astrometry.org>

² <http://veraserver.mtk.nao.ac.jp>



TABLE 4.1: Galactic rotation curve parameters used in the BDC runs.

Parameter	Value	Parameter	Value
R_0 [kpc]	8.15 ± 0.15	U_\odot [km s^{-1}]	10.6
Θ_0 (a_1) [km s^{-1}]	236 ± 7	V_\odot [km s^{-1}]	10.7
a_2	0.96	W_\odot [km s^{-1}]	7.6
a_3	1.62		

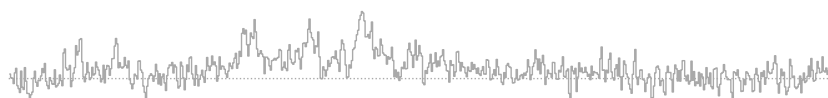
introduce two additional priors based on literature solutions of the KDA (Sect. 4.1.3) and a size-linewidth relationship (Sect. 4.1.4) that inform the P_{far} value for individual sources.

Since the BDC was designed as a distance estimator for spiral arm sources, its default settings have an inherent bias of associating $(\ell, b, v_{\text{LSR}})$ coordinates with the assumed spiral arm model (see Fig. 6 in Reid et al. 2016). To better characterise the impact of this bias, we decided to perform and compare distance calculations with and without the SA prior, which we refer to further on as Run A and Run B, respectively, and describe in more detail in the next section.

4.1.2 Modification of the BDC and setting of prior weights

For the distance calculation we use the most recent version of the BDC tool (Sect. 4.1.1) with the default Galactic rotation curve parameters as determined by Reid et al. (2019); Table 4.1 lists the most important parameters. R_0 denotes the distance to the Galactic centre and Θ_0 (or a_1) is the estimated circular rotation speed at the position of the Sun; both values are in very good agreement with independent observations and measurements (Gravity Collaboration et al., 2019; Kawata et al., 2019). The a_1 , a_2 , and a_3 values are parameters used in the ‘universal’ form of the rotation curve from Persic et al. (1996) that was adopted in the BDC (Reid et al., 2014; 2016; 2019). U_\odot , V_\odot , and W_\odot denote the solar peculiar motions towards the Galactic centre, in the direction of Galactic rotation, and towards the north Galactic pole, respectively.

The BDC results are strongly influenced by the choice of the spiral arm model and the included parallax measurements to maser sources. It is therefore instructive to discuss and illustrate how many spiral arm features and maser sources overlap with the GRS coverage as these will be decisive factors in the distance estimation. The left panel in Fig. 4.1 shows Galactic features, such as spiral arms and spurs, that were inferred from distance measurements to maser parallax sources and archival CO and H I surveys (Reid et al., 2016; 2019) and are used as spiral arm model for the SA prior. The width of the spiral arm features shows the approximate extent for associations of data points with these features. In the right panel we show the position and distance uncertainties of 71 maser sources from Reid et al. (2019) that are overlapping with the spatial and spectral coverage of the GRS. These maser sources all have parallax uncertainties $< 20\%$, which is the BDC default requirement for the inclusion of parallax sources for the PS prior. The PS prior for GRS sources is determined by association with one or more of these parallax sources (see Reid et al.



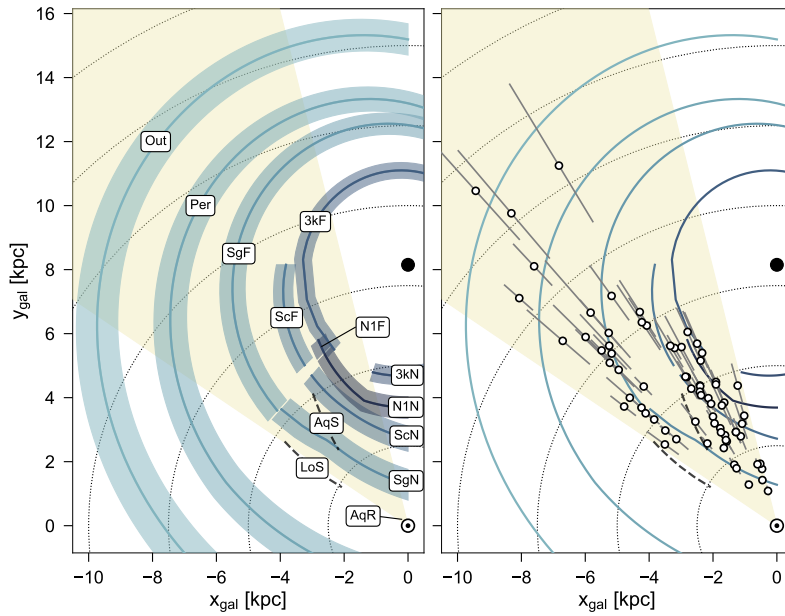


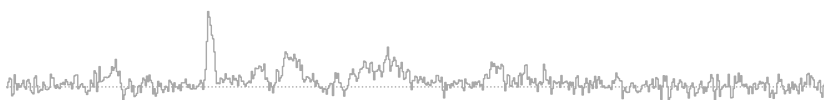
FIGURE 4.1: Face-on view of the 1st Galactic quadrant showing the GRS coverage (beige shaded area), and the positions of the Sun (Sun symbol) and Galactic centre (black dot). Dotted black lines indicate distances to the Sun in 2.5 kpc intervals. *Left panel*: Positions of Galactic features as determined by Reid et al. (2019). Spiral arms are shown with green solid lines and the shaded green areas indicate $\sim 3.3\sigma$ widths of the arms. Spurs are shown with dashed black lines. The features are labelled as follows: 3 kpc far arm (3kF), Aquila Rift (AqR), Aquila Spur (AqS), Local spur (LoS), Norma 1st quadrant near and far portions (N1N, N1F), Outer (Out), Perseus (Per), Scutum near and far portions (ScN, ScF), Sagittarius near and far portions (SgN, SgF). *Right panel*: Position and uncertainties in distance of 71 maser sources overlapping with the GRS coverage. Spiral arm and spur positions are the same as in the *left panel*.

2016 for how this association is performed). Most of the measured maser sources are associated with the Scutum and Sagittarius spiral arms, thus leading to an additional emphasis of these features in the distance determination.

Since we only have access to the radial velocity component of the gas, we do not use the PM prior that would require knowledge about the proper motion of the gas. In the following, we motivate and explain the chosen settings for our two BDC runs:

Run A: For this run we used all priors (KD, GL, PS, SA). We used the default weights for P_{KD} , P_{GL} , and P_{PS} . In test runs of the BDC, we found that the default weight of 0.85 for P_{SA} led to a strong domination of the spiral arm model (see Appendix C.3.2) compared to the remaining priors. We thus opted to reduce P_{SA} to 0.5, which led to a more balanced ratio between the priors in our tests.

Run B: For this run we did not use the priors for the proper motion and the spiral arm model. In the default settings of the BDC, the priors for the spiral arm model and the Galactic latitude are combined, which means that setting $P_{\text{SA}} = 0$ has the effect of also setting $P_{\text{GL}} = 0$. As the Galactic latitude information contains important prior information for the distances, we slightly modified



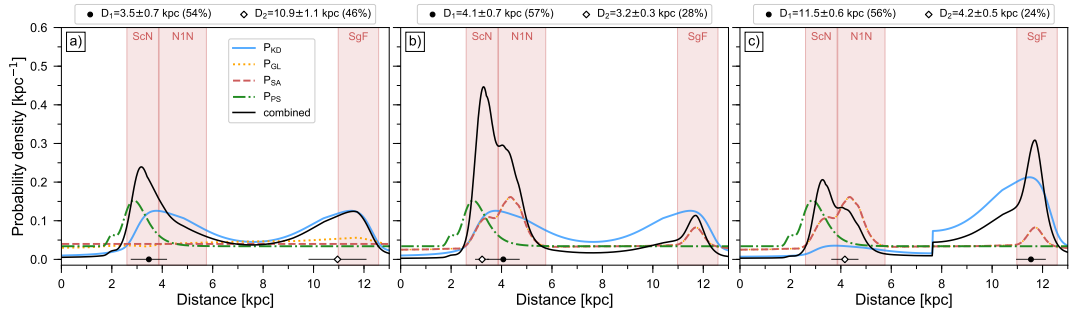


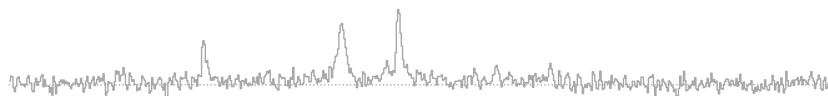
FIGURE 4.2: Effect of BDC priors on the distance estimation. For *panel a* we set $P_{SA} = 0$ and $P_{far} = 0.5$, for *panel b* we set $P_{SA} = 0.5$ and $P_{far} = 0.5$, and for *panel c* we set $P_{SA} = 0.5$ and $P_{far} = 0.875$. Coloured lines show the probabilities of the priors for kinematic distances (blue solid line), latitude probability (orange dotted line), spiral arms (red dashed line), and associations with parallax sources (green dash-dotted line). The black solid line shows the combined distance PDF. The red-shaded areas show the distance ranges for which the source would be associated with individual Galactic features. Black circles and white diamonds indicate the first and second choice for the distance estimates, with the horizontal bars showing their corresponding uncertainties. The boxes above the panels list the resulting distances, their uncertainties, and estimated probabilities.

the BDC source code so that we could use the P_{GL} prior without using the P_{SA} prior. However, we found that in this case the default settings of $P_{GL} = 0.85$ could yield a strong bias towards the far KD solution. To reduce this bias, we opted to decrease P_{GL} to a value of 0.5, which yielded a more balanced ratio between the priors in our tests.

In addition to these settings, we include priors that incorporate literature KDA resolutions and fold in information from the fitted linewidth in both BDC runs. These additional priors are described in more detail in the next two sections.

4.1.3 Prior for the kinematic distance ambiguity

For all sources located within the solar circle the KD prior yields two possible distance solutions (called the *near* and *far* distances). However, over recent years many works have already solved the KDA for many objects such as molecular clouds and clumps that overlap with the GRS coverage. Many of these studies even used the GRS data set directly in their distance estimation. To take advantage of these previous works, we implemented a new scheme that uses these literature KDA solutions to inform the P_{far} prior of the BDC, which results in a preference for the near or far distance solution. In Appendix C.1 we list all literature KDA solutions that we incorporated in our method and describe in detail how we use this information to determine the P_{far} weight for individual sources. In total, this prior was used in the distance estimation of about 30% of the ^{13}CO fit components (see App. C.3.3 for more details). In Appendix C.1 we also discuss the performance of this prior; we found that its inclusion leads to a significant increase in consistency of the BDC distance results with the reported literature distances.



We illustrate the effect of the KDA prior on the distance estimation with an example in Fig. 4.2, which shows the resulting distance PDFs for the individual priors. In panel (a) the spiral arm prior (P_{SA} , in red) was switched off and no KDA prior was supplied (i.e. $P_{\text{far}} = 0.5$), so the only remaining contributions to the combined distance PDF come from the priors for the kinematic distances (P_{KD} , in blue), the association with parallax sources (P_{PS} , in green), and the Galactic latitude (P_{GL} , in orange). Since the source is located close to the centre of the Galaxy, the two peaks of the kinematic distance PDF are not Gaussian-shaped, but were down-weighted to reflect expected large peculiar motions near the Galactic bar (Reid et al., 2019). Distances are estimated by fitting Gaussians to the peaks of the combined distance PDF (in black); the most likely distance value corresponds to the Gaussian component with the highest integrated probability density, so the highest peak of the combined distance PDF need not result in the most likely distance estimate. The distance uncertainty is given by the standard deviation of the Gaussian fit component.

With no associated parallax sources or conclusive latitude information the two distance solutions would have corresponded to the two peaks of the kinematic distance PDF and would have received the same probability (50%). In our case, the prior incorporating the Galactic latitude position favours the far distance, but associated parallax sources shift the balance towards the near kinematic distance solution, yielding a most likely distance value for the source of ~ 3.4 kpc. We note that even though the SA prior is switched off the BDC still gives the information of whether the distance results do overlap with locations of spiral arm and interarm features; the extent for such associations is indicated with the red-shaded areas in Fig. 4.2. For the example depicted in panel (a), D_1 is associated with the near portion of the Scutum spiral arm, whereas D_2 corresponds to an interarm position.

If the spiral arm prior is included (panel b), the most likely distance shifts to a higher value of about 4.2 kpc.³ Also the distance estimate with the second highest probability corresponds to a near distance solution, which illustrates the strength of the spiral arm prior.

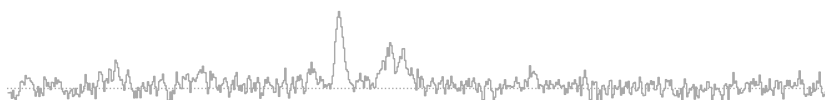
Finally, panel (c) shows the effect of adding a prior for the KDA, which in our case favours the far kinematic distance solution (for this example we assume $P_{\text{far}} = 0.875$; see App. C.1 for how exactly P_{far} is determined from literature KDA solutions). Setting the KDA prior has the effect of rescaling the kinematic distance PDF, which in this example shifts the most likely distance value to a far distance solution.

This example illustrated that the KDA prior can be a decisive factor for the distance estimation. However, while the P_{far} prior can give a strong preference for one of the kinematic distance solutions, we note that the combination with the other priors can still result in a different choice for the most likely distance.

4.1.4 Prior for the fitted linewidth

In our tests of the BDC, we noticed that sources with low v_{LSR} velocities are preferentially placed at larger distances (see Fig. 4.3). This effect is strongest for sources with

³ In this case, the spiral arm and Galactic latitude probabilities are by default combined.



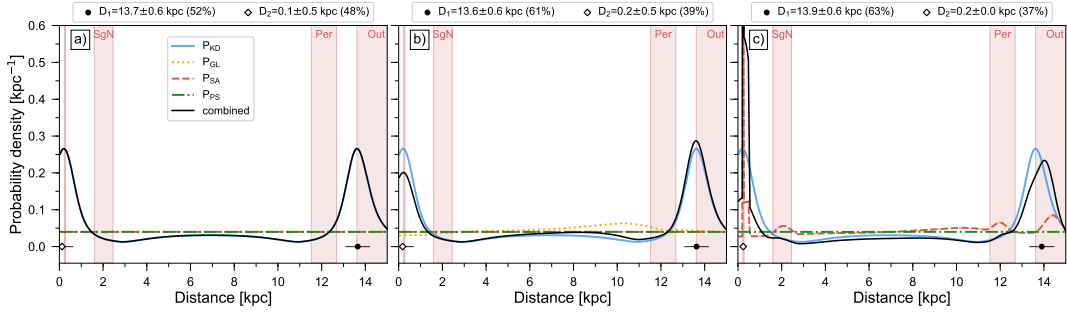
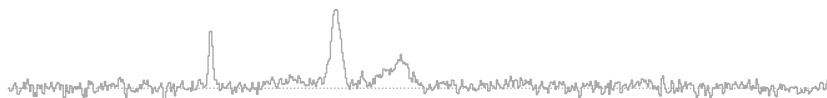


FIGURE 4.3: BDC examples illustrating how sources with low v_{LSR} velocities are biased towards the far distance solution. The panels show BDC results using the KD and PS priors (a), in addition to the GL (b) as well as the SA priors (c). The meaning of the lines and symbols is the same as in Fig. 4.2.

$v_{\text{LSR}} \lesssim 5 \text{ km s}^{-1}$; for sources with $v_{\text{LSR}} \lesssim 0 \text{ km s}^{-1}$ the KD prior permits essentially only the far distance solution. This effect can be mitigated by the inclusion of the SA prior as sources can receive a strong association with the nearby Aquila Rift cloud complex. However, since the association with Aquila Rift is only performed over a very limited distance range, this leads to narrow high peaks in the distance PDF, which in turn yield associated Gaussian fit components with a lower integrated area than for the far distance solution (Fig. 4.3c). This effect thus has a large impact on our distance results, since we expect strong confusion between local emission from the solar neighbourhood and the far side of the Galactic disk at $-5 < v_{\text{LSR}} \lesssim 20 \text{ km s}^{-1}$ (Sect. 3.5).

However, as suggested in Sect. 3.5, we can try to use the velocity dispersion values of the fit components as an additional prior information for the distance calculation. Figure 4.4 recaps the argument put forth in Sect. 3.5: due to averaging of bigger spatial areas at larger distances, we expect broadened lines due to, for example, sub-beam structure and velocity crowding, velocity gradients of the line centroids (either along the line of sight or in the plane of the sky), or fluctuations in the non-thermal contribution to the linewidth (e.g. due to regions with higher turbulence). The example shown in Fig. 4.4 highlights the effect of sub-beam structure and velocity crowding. If a region with two strongly blended velocity components is located at close distances, the individual emission peaks can be well resolved and fitted with two narrow Gaussian components (bottom centre and right panels in Fig. 4.4). However, if the same region is located at far distances, the individual velocity components might not be resolved, leading to a decomposition with a single broad Gaussian component (top centre and right panels in Fig. 4.4).

Given these expected differences due to beam averaging effects, it is unlikely that very narrow fitted linewidths are associated with emission at large distances. For most of the molecular gas in the GRS, the molecular gas temperatures will be about 10 to 20 K, which is the typical temperature of gas at intermediate density ($\sim 10^3 \text{ cm}^{-3}$) in molecular clouds. The thermal broadening of the spectral lines for these temperatures is about 0.2 to 0.3 km s^{-1} , so effectively the spectral resolution of the GRS. The physical extent of the GRS beam is $\sim 0.1 \text{ pc}$ at the distance of the Aquila Rift complex and increases to $\gtrsim 2 \text{ pc}$ at distances beyond the solar radius.



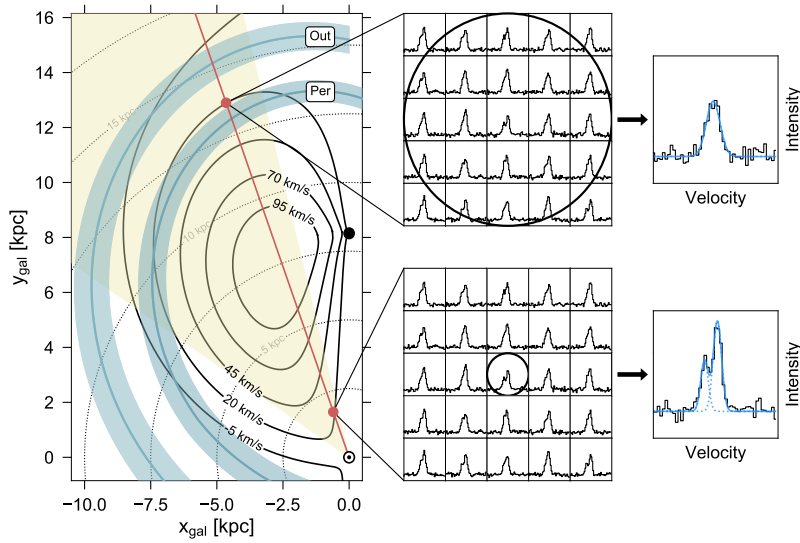
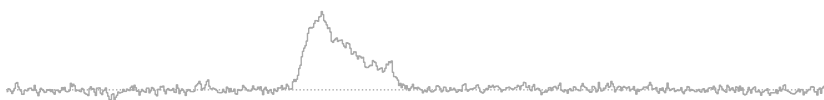


FIGURE 4.4: Illustration of linewidth broadening caused by beam averaging. *Left panel:* Same as the *left panel* of Fig. 4.1, but showing only the positions and estimated widths of the Perseus (Per) and Outer (Out) spiral arms. Black solid lines show curves of constant projected v_{LSR} values. The red line shows a random line of sight with the corresponding intersections with the $v_{\text{LSR}} = 20 \text{ km s}^{-1}$ curve indicated with red dots. The centre panels illustrate the change in spatial extent of the beam (black circle) for a region with two blended velocity components embedded at the near (bottom centre) and far (top centre) distance. The right panels illustrate the resulting observed spectra (black line) and Gaussian fit components (blue lines).

Therefore the physical areas covered by the beam at the nearby distances of the Aquila Rift and the far distances of the Perseus and Outer arm are different by a factor of > 400 . Even in the case of no sub-beam structure and velocity crowding and no significant non-thermal contributions to the linewidth, expected variations in the line centroids across the beam-averaged area are enough to broaden the lines significantly (see Appendix C.2).

The effect of broader linewidths for emission originating at larger heliocentric distances is already noticeable in the fitted linewidths (Fig. 4.5). We would expect fit components in the interval of $-5 < v_{\text{LSR}} < 0 \text{ km s}^{-1}$ (left upper panel of Fig. 4.5) to predominantly originate from large distances and indeed the distribution of σ_v values is shifted towards larger values compared to similar v_{LSR} ranges between 0 and 20 km s^{-1} (remaining panels of Fig. 4.5). The distribution of these other ranges has a strong peak at $\sigma_v < 0.5 \text{ km s}^{-1}$, consistent with the assumption that this corresponds to emission lines originating from nearby spatially resolved regions.

Having established that the fitted velocity dispersion values can contain information about the distance to the gas emission, we will in the following explain how we implement this as prior information for our distance calculation. Similar as in the last chapter, we use the size-linewidth relationship established by Solomon et al. (1987) for molecular clouds in the Galactic disk to inform our decision about whether a fitted σ_v value is more likely associated with a region at near or far distances. This size-linewidth relationship has the form of:



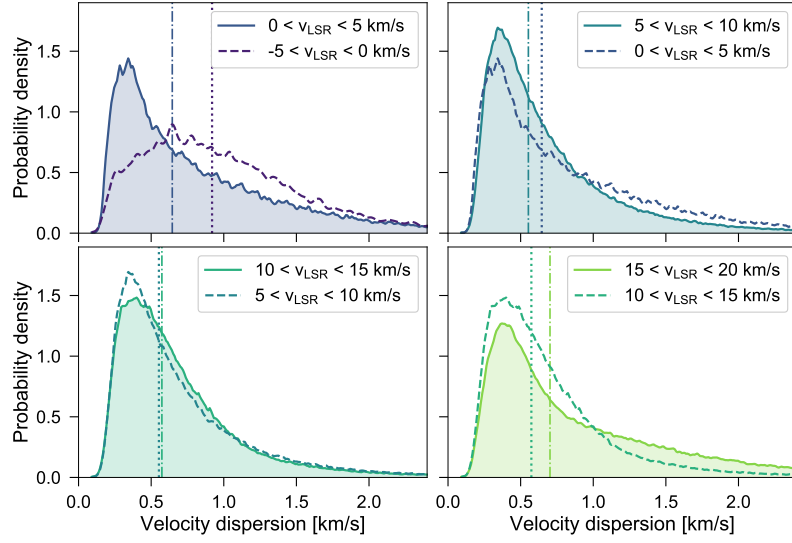


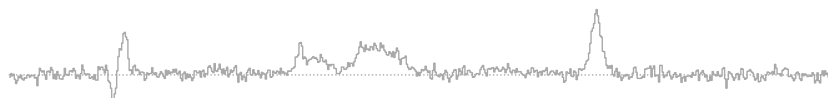
FIGURE 4.5: PDFs of fitted velocity dispersion values in different v_{LSR} ranges. Each panel compares PDFs of two different v_{LSR} ranges; the median values of the PDFs with the solid and dashed lines are indicated with the dash-dotted and dotted vertical lines, respectively.

$$\sigma_v^{\text{exp.}} = \sigma_{v,0} \cdot \left(\frac{L}{1 \text{ pc}} \right)^\gamma, \quad (4.1)$$

with $\gamma = 0.5$ and $\sigma_{v,0} = 0.7$ (corrected for the most recent distance estimates to the Galactic centre; [Gravity Collaboration et al. 2019](#); [Reid et al. 2019](#)). In Fig. 4.6 we show the expected velocity dispersion values based on this relation as a function of physical extents of the beam (d_{beam}) with the solid red line. The shaded red areas indicate $1\tilde{\sigma}$, $2\tilde{\sigma}$, and $3\tilde{\sigma}$ intervals for the size-linewidth relation assuming variations in γ and $\sigma_{v,0}$ of ± 0.1 . The magnitude of these variations was motivated for consistency with results obtained from more local molecular clouds ([Larson, 1981](#); [Shetty et al., 2012](#)).

We use this size-linewidth relationship to inform the KDA prior as follows. We first calculate the physical extent of the beam (d_{beam}) for the two kinematic distance solutions that are always obtained for positive v_{LSR} values in the inner Galaxy. We then use the size-linewidth relationship to calculate the expected velocity dispersions for both d_{beam} values. Subsequently, we compare the actual fitted velocity dispersion with these expected velocity dispersion values to decide whether it is more consistent with the near or far distance value. This decision is driven by how close the fitted σ_v value is to the expected values from the near and far distances. We calculate for both distances the difference between the fitted and expected σ_v values; if the difference is within the $3\tilde{\sigma}$ interval indicated in Fig. 4.6 we give it the corresponding weight from a normalised Gaussian function:

$$w_\sigma = \exp \left(-0.5 \cdot \left(\frac{\sigma_v - \sigma_v^{\text{exp}}}{\tilde{\sigma}} \right)^2 \right), \quad (4.2)$$



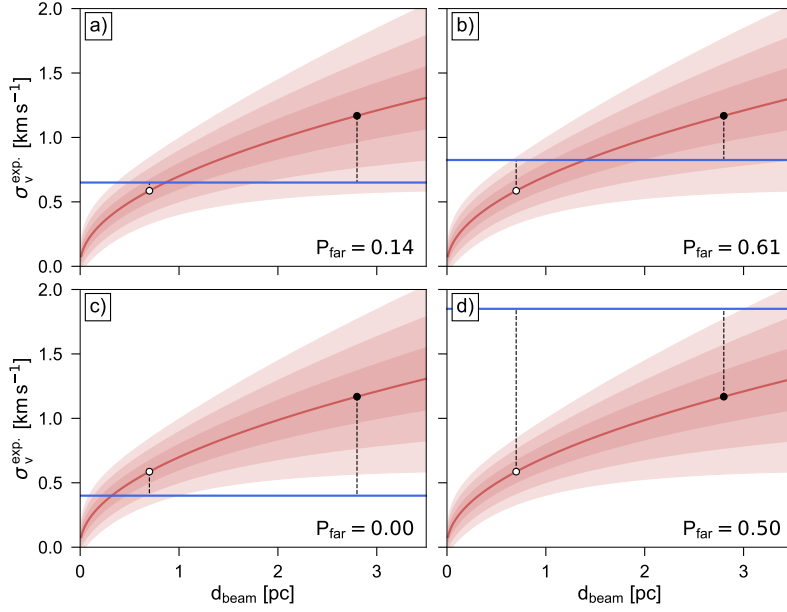


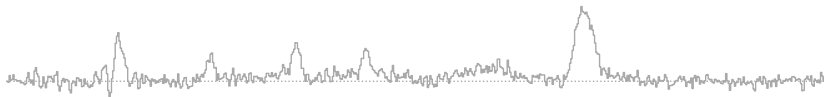
FIGURE 4.6: Illustration of the distance prior based on the fitted linewidth. The red line shows the size-linewidth relation from Solomon et al. (1987) corrected for the most recent distance estimates to the Galactic centre. Red-shaded areas show the $1\tilde{\sigma}$, $2\tilde{\sigma}$, and $3\tilde{\sigma}$ intervals determined from variations of the parameters of the size-linewidth relation. The two dots show expected velocity dispersion values for corresponding physical extents of the beam for the near (white dot) and far (black dot) kinematic distance solutions. Blue horizontal lines show velocity dispersion values of fit components and dashed vertical lines indicate the relevant distances to the expected values, from which the P_{far} prior is determined. See Sect. 4.1.4 for more details.

where $\tilde{\sigma}$ is the standard deviation for σ_v^{exp} . From this we calculate values for the P_{far} prior as:

$$P_{\text{far}} = 1/2 + 1/2 \left(w_{\sigma}^{\text{far}} - w_{\sigma}^{\text{near}} \right), \quad (4.3)$$

with w_{σ}^{near} and w_{σ}^{far} indicating the weights for the near and far distance value. If the fitted σ_v value falls above the $3\tilde{\sigma}$ interval, we set the corresponding weight w_{σ} to zero. If the fitted σ_v value falls below the $3\tilde{\sigma}$ interval for the far distance but is not above the $3\tilde{\sigma}$ interval for the near distance, we automatically assume $P_{\text{far}} = 0$.

We illustrate this procedure for four different cases in Fig. 4.6; for all these cases the kinematic distance solution and the corresponding d_{beam} values are the same but the values of the fitted σ_v values (horizontal blue lines) vary. For the first case (panel a) the σ_v value is more consistent with the near distance; we obtain $w_{\sigma}^{\text{near}} = 0.76$ and $w_{\sigma}^{\text{far}} = 0.04$, yielding $P_{\text{far}} = 0.14$ and thus strongly favouring the near distance. In the second case (panel b) the far distance is favoured, as $w_{\sigma}^{\text{near}} = 0.17$ and $w_{\sigma}^{\text{far}} = 0.24$. In the third case, the fitted σ_v value is much lower than the expected σ_v value and falls below the $3\tilde{\sigma}$ range ($w_{\sigma}^{\text{far}} = 0$); in such cases we always assume $P_{\text{far}} = 0$ unless the σ_v value is above the $3\tilde{\sigma}$ interval for the near distance (in which case P_{far} would be 0.5). Finally, the last case (panel d) yields no P_{far} prior as the fitted σ_v value is much higher than the expected σ_v values for both the near ($w_{\sigma}^{\text{near}} = 0$) and far ($w_{\sigma}^{\text{far}} = 0$)



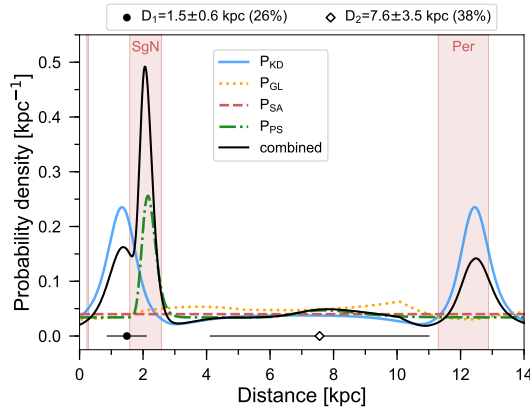


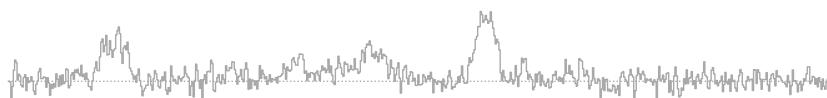
FIGURE 4.7: Example of distance choice in case one of the distance components has a high integrated area but low peak amplitude value. The meaning of the lines and symbols is the same as in Fig. 4.2.

distance. This ensures that we do not exclude the possibility that a source with high σ_v value can come from a nearby region with high non-thermal contributions to the linewidth.

Recent studies have found large dispersions of the size-linewidth relation across the Galactic disk (e.g. [Heyer et al., 2009](#); [Miville-Deschênes et al., 2017](#)) and advocate a scaling relation that also takes the surface density into account. Moreover, especially in the inner part of the Galaxy, linewidths can be systematically higher than predicted by the size-linewidth relation, indicating that σ_v is at least partly set by Galactic environment ([Shetty et al., 2012](#); [Henshaw et al., 2016a](#); [Rice et al., 2016](#); [Henshaw et al., 2019](#)). We want to emphasise here that we do not use the size-linewidth relation to make conclusive decisions about the distance to a gas emission peak, but only use it as additional prior KDA information for sources with $v_{\text{LSR}} < 20 \text{ km s}^{-1}$. For sources with larger v_{LSR} values the difference between the σ_v^{exp} values for the two KD solutions gets smaller and the size-linewidth prior might bias components with narrower fitted linewidths to be preferentially placed at the near distance solution. We also do not use the σ_v prior in case the literature solutions for the KDA (Sect. 4.1.3) already yielded a P_{far} value $\neq 0.5$.

4.1.5 Choice of distance solution

The distance calculation with the BDC yields multiple alternative distance solutions with corresponding estimates of their probability. These probabilities are obtained from Gaussian fits to the combined distance PDF ([Reid et al., 2016](#)). By default, the Gaussian distance component with the highest integrated area is chosen as the most likely distance value. So even if the distance PDF shows a clear peak, this need not correspond to the selected most likely distance value. Our tests showed that this could be problematic, as very broad Gaussian components with low peak values can be selected as the most probable distance component, resulting in unlikely distance solutions (Fig. 4.7). For our BDC runs we found that such broad components with



low peak values would be chosen as the preferred distance value in $\sim 2.5\%$ (Run A) and $\sim 9\%$ (Run B) of the distance assignments.

To avoid the selection of such broad components with low peak values, we adapted the choice for the most likely distance as follows. In case of two reported distance solutions (as is the default in v2.4 of the BDC), we first check whether the peaks of the individual Gaussian fit components exceed a pre-defined limit. We set this limit to 0.12, which corresponds to three times the value of a flat distance PDF⁴. If one of the distance components does not satisfy this criterion, we choose the remaining distance solution, regardless of whether its integrated area was less (see Fig. 4.7). If both of the distance components exceed or fail the amplitude limit, we choose the distance component with the highest assigned probability (i.e. the Gaussian fit component having the highest integrated area). In case both distance components have the same assigned probability, we choose the distance solution with the lower absolute distance error. If both components are also tied in the distance errors (as can happen if the combined distance PDF is dominated strongly by the KD prior), we choose the distance component with the lower distance value. The last two conditions were only used in $\sim 1\%$ of the distance choices for the two BDC runs (see App. C.3.3 for more details).

4.2 GALACTIC DISTRIBUTION OF THE GAS EMISSION

In this section we report the distance results obtained for the BDC runs including (Run A) and excluding (Run B) the prior for the spiral arm model (Sect. 4.1.2). In the subsections discussing the results, we always show and compare both BDC runs; if not indicated otherwise, the left- and right-hand panels depict the results of Run A and B, respectively. We first present an overview of the results and then discuss the differences in terms of the face-on and vertical distribution of the gas emission and its variation with heliocentric and Galactocentric distance. Finally, we discuss problems and biases of the two distance runs and compare our results with previous studies.

4.2.1 Face-on view of the ^{13}CO emission

We show face-on view maps of the integrated ^{13}CO emission, the number of Gaussian fit components, and the median σ_v value in Figs. 4.8-4.10. Comparing the maps of the ^{13}CO emission (Fig. 4.8), we can clearly see the effect of the SA prior in the left panel, which tends to concentrate most of the emission close to the Galactic features as they are defined in the spiral arm model (Fig. 4.1). By neglecting the SA prior we get a distribution of the ^{13}CO emission that is much more spread out and extends over a much larger area in between the arms, which can also be clearly observed in Fig. 4.9. This spreading of the emission to interarm locations is to a large part due to our use of archival KDA solutions to inform the P_{far} prior. We present a comparison of the face-on map of ^{13}CO emission with and without the use of archival KDA

⁴ The distance PDF is evaluated from 0 to 25 kpc. Requiring that the integrated area of a flat distance PDF is equal to unity yields a value of 0.04 for the PDF at all distances.



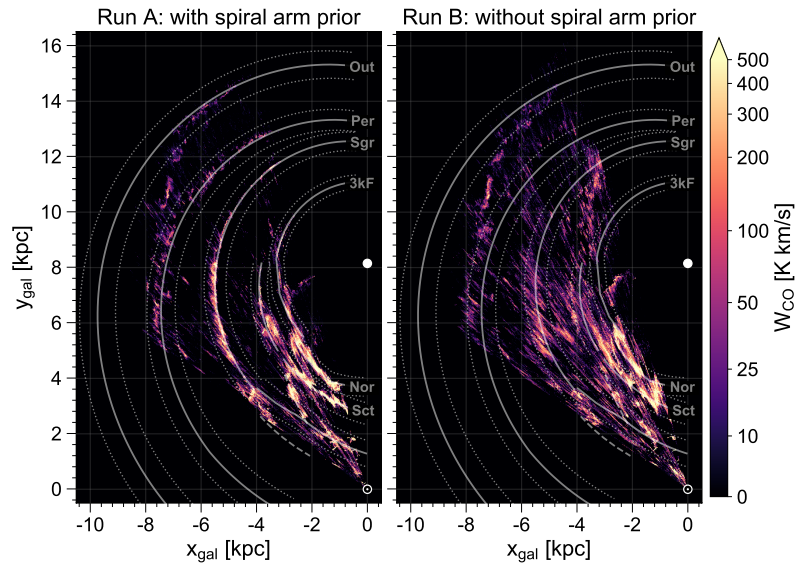


FIGURE 4.8: Face-on view of the integrated ^{13}CO emission for the BDC results obtained with (left) and without (right) the spiral arm prior. The values are binned in 10×10 pc cells and are summed up along the z_{gal} axis. The position of the Sun and Galactic centre are indicated by the Sun symbol and black dot, respectively. When displayed in Adobe Acrobat, it is possible to hide the `spiral arm positions` and the `grid`.

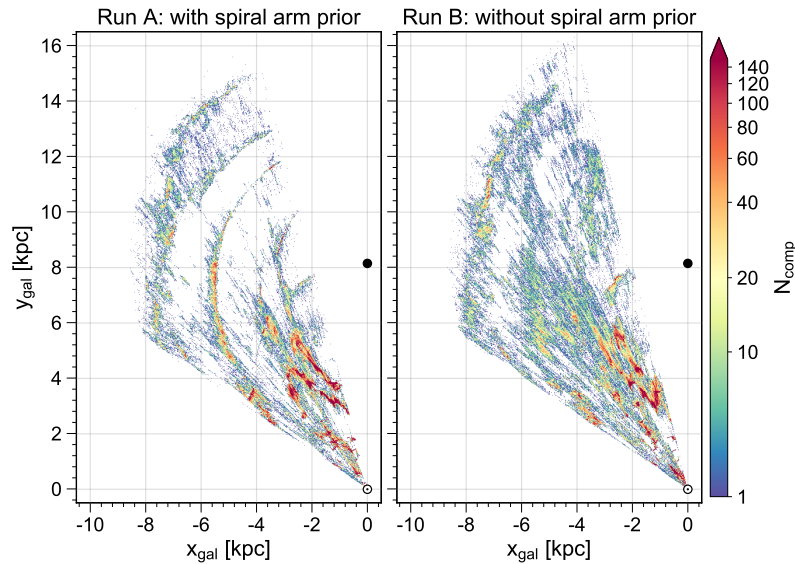


FIGURE 4.9: Face-on view of the number of Gaussian fit components for the BDC results obtained with (left) and without (right) the spiral arm prior. The values are binned in 10×10 pc cells and are summed up along the z_{gal} axis. The position of the Sun and Galactic centre are indicated by the Sun symbol and black dot, respectively. When displayed in Adobe Acrobat, it is possible to show the `spiral arm positions` and hide the `grid`.



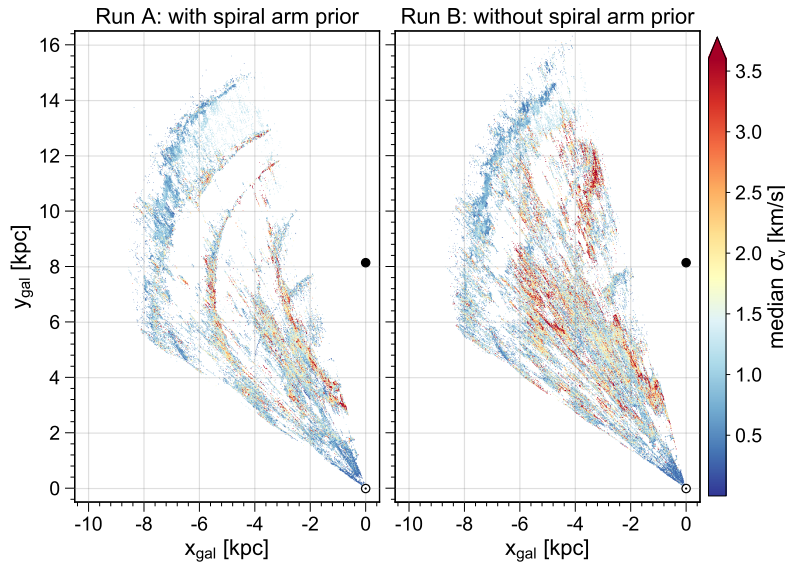
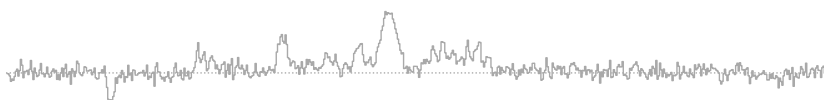


FIGURE 4.10: Face-on view of the median velocity dispersion values of Gaussian fit components for the BDC results obtained with (*left*) and without (*right*) the spiral arm prior. The values are binned in 10×10 pc cells and the median was calculated along the z_{gal} axis. The position of the Sun and Galactic centre are indicated by the Sun symbol and black dot, respectively. When displayed in Adobe Acrobat, it is possible to show the `spiral arm positions` and hide the `grid`.

solutions in Appendix C.3.2. While we find only moderate differences in the fraction of emission assigned to interarm locations, the distribution of the gas emission itself changes significantly.

Even though Run B shows a larger spreading of emission into interarm regions, we can still identify ^{13}CO overdensities at the positions of the Galactic features of the SA model (right panels of Figs. 4.8 and 4.9). This is not surprising, as Run B has still a contribution from the maser parallax sources, which tend to be concentrated at spiral arms and spurs as well (see right panel in Fig. 4.1). Moreover, the Galactic features for the spiral arm model are also based on overdensities in archival H I and ^{12}CO Galactic plane surveys, so we would expect that the ^{13}CO emission is also present at these same locations.

Looking at the maps of the median σ_v values (Fig. 4.10), we qualitatively observe that spiral arm features seem to be associated with ^{13}CO components with larger linewidths. In general, we can see increased median σ_v values within Galactocentric distances $\lesssim 6$ kpc; as already speculated in Sect. 3.4.1, these increasing σ_v values towards the inner Galaxy could be due to the presence of the Galactic bar and the observed overdensity of star-forming regions (Anderson et al., 2017; Ragan et al., 2018), but could also partly result from our inability to correctly decompose strongly blended emission lines. We can further see an increase of the median σ_v values with heliocentric distance; for emission lines with $v_{\text{LSR}} < 20 \text{ km s}^{-1}$ this is partly due to our use of the size-linewidth prior (Sect. 4.1.4). However, this effect is also present if we do not use this prior (see Appendix C.3.2 for a comparison between the maps of median σ_v values obtained with and without the size-linewidth prior).



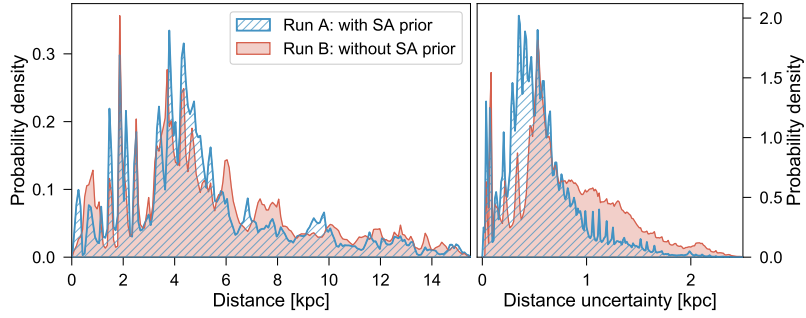


FIGURE 4.11: PDFs for the estimated heliocentric distances (*left*) and corresponding uncertainties (*right*).

Figures 4.8-4.10 also show a persistent feature between the Perseus and Outer arm at a Galactic longitude range of $29^\circ \lesssim \ell \lesssim 38^\circ$. This is very likely emission originating close to the Sun that has been erroneously placed at far distances. We can find evidence for this in Fig. 4.10, where the median σ_v value shows significantly lower values ($\lesssim 0.5 \text{ km s}^{-1}$) at these locations than for most of the other parts of the Perseus arm. This erroneously placed local emission is also clearly identifiable in the offset positions from the Galactic midplane, which we will discuss in Sect. 4.2.6.

4.2.2 Comparison of the distance results

Comparing the resulting distances of the two BDC runs, we find that 68.2% are compatible with each other within their estimated uncertainties.⁵ The distance uncertainties are given by the standard deviation of the chosen Gaussian component fit to the combined distance PDF (see Sect. 4.1.5). In terms of differences in absolute distance uncertainty values, 67.2%, 78.8%, and 83.8% of the distance results are compatible within ± 0.5 , ± 1.0 , and ± 1.5 kpc, respectively. We thus conclude that for the majority of the GRS fit components the two distance runs yielded similar results. We can use the PDFs of the estimated heliocentric distances and corresponding distance uncertainties (Fig. 4.11) to identify where the distance estimates deviated. For example, Run B yielded more distances above 8 kpc (21.2%) but produced fewer distance assignments < 0.5 kpc (1.2%) compared to Run A (17.1% and 2.4%, respectively).

The difference between the BDC runs is even more pronounced in the distance uncertainties. Half of the distance assignments of Run A have distance uncertainties < 0.5 kpc, but only a quarter of the distance assignments for Run B are below this distance uncertainty threshold. This difference is also reflected in the estimated probabilities of the distances: about 44% of the results from Run A have high-confidence probabilities > 0.75 ; for Run B only $\sim 34\%$ of the distance results exceed this probability threshold (see App. C.3.3 for more details). We caution that the estimated uncertainties and probabilities do not allow for a straightforward comparison of the quality of the distance results. Strongly favouring the distance assignments towards a particular prior may yield small uncertainties and high

⁵ We note that each percentage point corresponds to about 46 500 independent distance assignments.



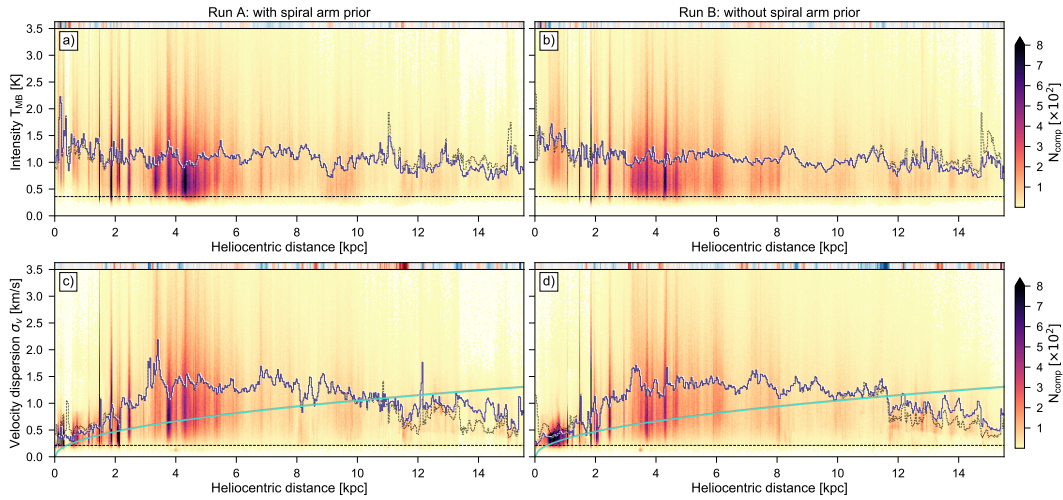


FIGURE 4.12: 2D histograms of estimated distance values and intensity (*top*) and velocity dispersion (*bottom*) values for the BDC run with (*left column*) and without (*right column*) the spiral arm prior. The blue lines show the respective median values per distance bin and dotted black lines give the corresponding values for distances obtained without the size-linewidth prior. The small strips at the top of the individual panels show where the median value is higher (blue) or lower (red) compared to the opposite BDC run, with the strength of the colour corresponding to the magnitude of the difference. The turquoise line in the bottom panels indicates the expected values from the size-linewidth relationship (Eq. 4.1). The dashed horizontal line in the top panels at $T_{\text{MB}} = 0.36$ K corresponds to the $3 \times S/N$ limit for the 0.1st percentile of the GRS noise distribution (see Fig. B.2). The dashed horizontal line in the bottom panels indicates the velocity resolution of the GRS (0.21 km s^{-1}).

probabilities but the prior itself may lead to biased distance results. We discuss these issues further in Sect. 4.2.7.

In the top panels of Fig. 4.12 we show how the intensity and velocity dispersion values of the Gaussian fit components vary with heliocentric distance for both BDC runs. While the intensity values cover a large range, their median values stay flat over all considered distances.

The bottom panels in Fig. 4.12 show how the σ_v values of the fit components vary with their estimated distances. We can see a clear increase in the median σ_v values up until heliocentric distances of about 3.5 kpc, after which it stays at increased values of $> 1 \text{ km s}^{-1}$, until it drops again at distances $\gtrsim 11.5$ kpc. This drop at the largest distances is due to a bias in the distance calculation that erroneously puts emission from nearby regions at large distances from the Sun (see Sect. 4.2.1). We also show the median σ_v values we would have gotten if we had not used the size-linewidth prior (Sect. 4.1.4), which shows an even bigger drop at these large distances. However, for $d < 4$ kpc we recover a similar trend of increased linewidths with larger heliocentric distances, indicating that beam averaging effects play a crucial role in producing these increased linewidths. Another explanation could be a larger non-thermal contribution to the linewidth for emission located in the inner part of the Galaxy. The comparison of the median σ_v curve with the size-linewidth relationship from Eq. 4.1 shows that most of the fit components have linewidths

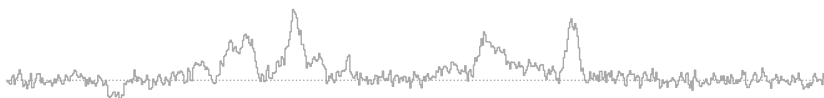


TABLE 4.2: Distance results for the two BDC runs.

Feature ^a	Run A: with SA prior			Run B: without SA prior		
	W _{CO} [%]	N _{comp} [%]	$\sigma_{v,med.}^b$ [km s ⁻¹]	W _{CO} [%]	N _{comp} [%]	$\sigma_{v,med.}^b$ [km s ⁻¹]
3kF	2.6	2.4	1.4 $^{0.9}_{2.2}$	1.4	1.6	1.3 $^{0.8}_{2.0}$
AqR ^c	1.1	2.8	0.4 $^{0.3}_{0.5}$	1.0	2.5	0.4 $^{0.3}_{0.6}$
AqS	7.0	7.2	1.4 $^{0.9}_{2.2}$	4.3	4.5	1.3 $^{0.8}_{2.1}$
LoS	1.8	2.5	1.0 $^{0.7}_{1.6}$	1.5	2.1	1.0 $^{0.7}_{1.5}$
N1F	1.3	1.0	1.3 $^{0.9}_{2.0}$	3.2	2.3	1.5 $^{1.0}_{2.3}$
N1N	20.6	14.9	1.5 $^{1.0}_{2.5}$	16.8	11.7	1.5 $^{1.0}_{2.5}$
Out ^c	0.6	1.3	0.7 $^{0.5}_{1.0}$	0.6	1.4	0.7 $^{0.5}_{1.0}$
Per ^c	3.9	6.0	0.9 $^{0.6}_{1.4}$	4.0	6.0	1.0 $^{0.6}_{1.5}$
ScF	5.7	4.3	1.4 $^{0.9}_{2.2}$	6.2	5.1	1.4 $^{0.9}_{2.2}$
ScN	24.6	20.1	1.4 $^{0.9}_{2.3}$	23.6	19.2	1.4 $^{0.9}_{2.3}$
SgF	12.2	10.3	1.4 $^{0.9}_{2.1}$	11.9	9.7	1.4 $^{0.9}_{2.3}$
SgN	12.1	15.8	0.8 $^{0.5}_{1.4}$	8.0	9.4	1.0 $^{0.6}_{1.5}$
N/A	6.5	11.2	0.7 $^{0.5}_{1.1}$	17.5	24.5	0.8 $^{0.5}_{1.4}$
Spiral arms	83.6	76.2	1.2 $^{0.8}_{2.0}$	75.6	66.3	1.3 $^{0.8}_{2.1}$
Interarm	16.4	23.8	0.8 $^{0.5}_{1.4}$	24.4	33.7	0.8 $^{0.5}_{1.4}$

Notes. ^(a) 3 kpc far arm (3kF), Aquila Rift (AqR), Aquila Spur (AqS), Local spur (LoS), Norma 1st quadrant near and far portions (N1N, N1F), Outer (Out), Perseus (Per), Scutum near and far portions (ScN, ScF), Sagittarius near and far portions (SgN, SgF), unassociated (N/A).

^(b) The two values in the brackets give the corresponding IQR.

^(c) Values are likely severely impacted by confusion between emission from the solar neighbourhood and far distances; see Sects. 4.2.6 and 4.2.7.

that are significantly larger than those expected values. This implies that we need to exercise caution in the use of the size-linewidth prior; however the distributions in Fig. 4.12 show that its restricted use for v_{LSR} values $< 20 \text{ km s}^{-1}$ led to significant improvements.

4.2.3 Gas fraction in spiral arm and interarm regions

In this section we discuss the fraction of ¹³CO residing in spiral arm and interarm environments, which also serves to give a more quantitative overview of the distance results. In Table 4.2 we split our distance results into different subsamples that correspond to the determined association with Galactic features (*left panel* in Fig. 4.1) by the BDC. This association is based on the $(\ell, b, v_{\text{LSR}})$ coordinates and the position and extents of the spiral arm and interarm features (see Sect. 2.1 in Reid et al. 2016 for more details about this association). For each subsample we report the fraction



of the total integrated ^{13}CO intensity (W_{CO}), the fraction of the total number of fit components (N_{comp}), and the median velocity dispersion value ($\sigma_{v,\text{med.}}$) with the corresponding IQR in brackets. We also list the combined values for all spiral arm (3kF, N1F, N1N, Out, Per, ScF, ScN, SgF, and SgN) and interarm (AqR, AqS, LoS, N/A) features as *Spiral arm* and *Interarm*, respectively.

In the two BDC runs, about 76 – 84% of the integrated ^{13}CO emission and 66 – 76% of the ^{13}CO fit components were associated with spiral arm features, mostly with the Norma, Scutum, and Sagittarius arms. Run B placed significantly more ^{13}CO emission in interarm regions not associated with any of the Galactic features shown in Fig. 4.1. To put these numbers into perspective and check whether also the gas distribution in Run B shows a significant concentration towards spiral arm features, we determined the fraction of ^{13}CO gas in spiral arms based on only kinematic distances. We calculate the kinematic distances using methods contained in the BDC v2.4 and solve for the KDA by using the Monte Carlo approach outlined in Sect. 3.1 of Roman-Duval et al. (2016), assuming a Gaussian vertical density profile of the molecular gas with a FWHM of 110 pc as was done in that study. For these pure kinematic distance solutions we find that $\sim 58\%$ of the integrated ^{13}CO emission and $\sim 52\%$ of the fit components overlap with the positions of spiral arms from our assumed model. These results demonstrate that compared to pure kinematic distances both our BDC runs contain a significant enhancement of ^{13}CO emission at the position of spiral arm features.

To further check the robustness of our results we also looked at the distance results of only the $\sim 75\%$ of fit components that had a S/N ratio > 3 . We do not find significant deviations from the trends presented in Table 4.2. In particular, we recover the same difference in $\sigma_{v,\text{med.}}$ between the Galactic features, which we discuss in the next section.

4.2.4 Velocity dispersion in spiral arm and interarm regions

One interesting exercise is to look for possible variations of the gas velocity dispersion between spiral arm and interarm regions, which has been observed for the nearby spiral galaxy M51 (Colombo et al., 2014). To split our data points into spiral arm and interarm features, we again use the BDC assignment with Galactic features from the previous section. Figure 4.13 shows σ_v -PDFs for these Galactic features and Table 4.2 gives the corresponding median values and interquartile ranges for these distributions. Generally speaking, spiral arm structures are associated with larger σ_v values than interarm structures, with the spiral arm PDF peaking at larger σ_v values. We note that the PDF labelled *Interarm* contains also associations with the spur features (AqS, LoS) and the nearby Aquila Rift complex (AqR). To check how this might skew the results, we also show PDFs for interarm emission not associated with any of the Galactic features from the SA model (labelled *Interarm (N/A)*) and emission only associated with spur features (*Spurs*). Interestingly, the PDF for the spurs is almost indistinguishable from the PDF of the spiral arms.

We make a more detailed comparison between emission associated with spiral arm and spur structures in Fig. 4.13c–f. The emission associated with the two major spiral structures covered by the GRS, the Scutum and Sagittarius arms, essentially has



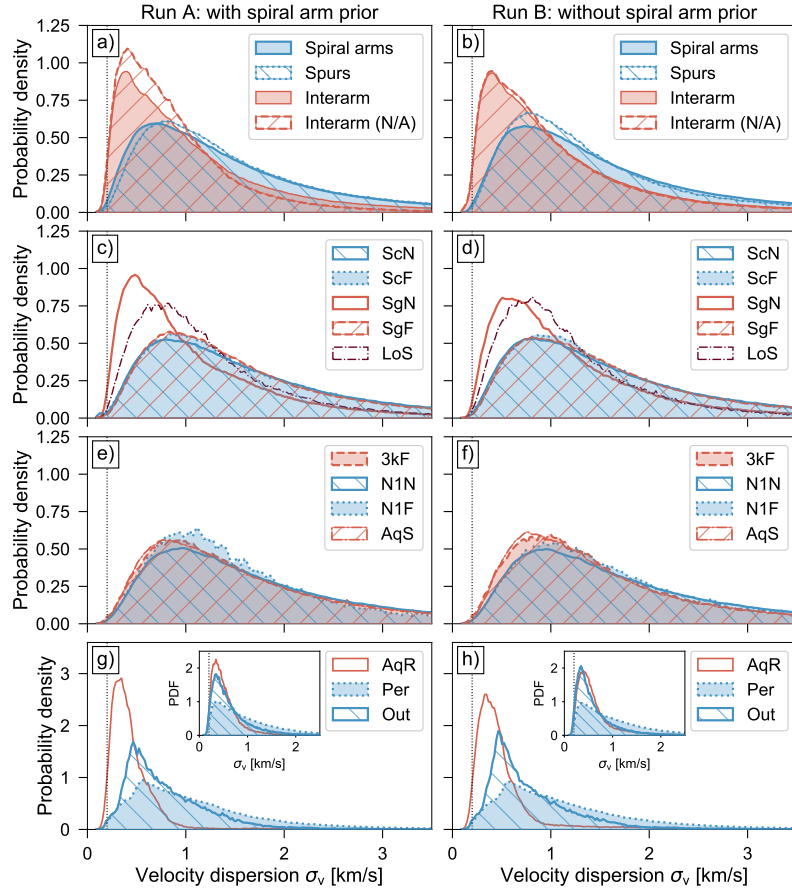


FIGURE 4.13: PDFs of velocity dispersion values associated with Galactic features for the distance results with (*left columns*) and without (*right columns*) the SA prior. The dotted vertical line indicates the GRS velocity resolution (0.21 km s^{-1}). The insets in the bottom panels show the corresponding PDFs without the use of the size-linewidth prior.

identical σ_v -PDFs apart from the near portion of the Sagittarius arm (SgN), whose distribution peaks at much lower σ_v values and is more similar to the PDF of the Local Spur (LoS) and the interarm PDFs in panel (a) and (b). Other structures in the inner Galaxy—the Norma arm (N1N, N1F), the far portion of the 3-kpc-arm (3kF), and the Aquila spur (AqS)—all show a very similar σ_v distribution that is essentially identical to the PDFs of the Scutum arm and the far portion of the Sagittarius arm. Since the near portion of the Sagittarius arm and the Local Spur are located at the highest longitude ranges covered by the GRS, this might point to real differences in terms of the linewidth distribution in the innermost and more outer parts of the GRS coverage. However, since parts of the SgN are also located close to the Sun ($d_\odot < 3 \text{ kpc}$), its emission lines might simply be better resolved spatially, leading to narrower linewidths (see also discussion in Sect. 4.1.4). The difference in the σ_v -PDFs might also be explained by difficulties in the decomposition of strongly blended emission lines in the inner Galaxy, which could have led to higher fitted σ_v values.

The bottom panels (g, h) show PDFs for the Aquila Rift (AqR) complex and the Perseus (Per) and Outer (Out) arms. As already mentioned, we are not able to fully separate the near and far contribution of this emission with low v_{LSR} values. This



problem is reflected in the shape of the PDFs, which are moreover impacted by our use of the size-linewidth prior. For comparison, we also show how the PDFs would look like if we did not use the size-linewidth prior (small insets in panels g and h). In this case their σ_v -PDFs become more similar, which is in contrast to expectations based on beam averaging effects (see Sect. 4.1.4 and Appendix C.2) and the other spiral arm PDFs, which show much higher σ_v values. We currently also have no reason to suspect that the Perseus and Outer arms should be peculiar in terms of their linewidth distribution compared to other spiral arms.

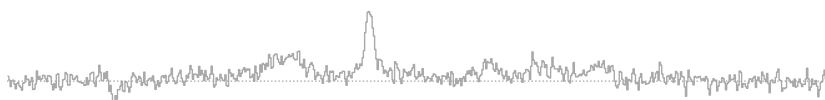
To further check the significance of the difference in the σ_v -PDFs of spiral arm and interarm structures, we looked at the σ_v -PDFs in 2 kpc heliocentric bins (Fig. 4.14). About one third of the fit components associated with interarm structures have distances < 2 kpc (panels a, b), compared to a much lower fraction of fit components associated with spiral arms in this distance range. This difference seems to be the major cause for the difference in the total σ_v -PDFs in Fig. 4.13 (a) and (b). The remaining interarm distributions in Fig. 4.14 show much closer resemblance to the spiral arm PDFs, and indicate no consistent or considerable trend towards lower linewidths.

Figure 4.14 once more highlights the problem of confusion between emission originating from the near and far side of the Galactic disk. For most of the PDFs in Fig. 4.14 (a)–(j) we do see a shift towards higher linewidths with increasing distance ranges, which would match our expectations based on beam averaging effects. The interarm PDFs in panels (g) and (i) show a deviation from this trend, which could be indicative of an increased confusion between near and far emission at these distance bins. The second bump at low σ_v values ($< 0.2 \text{ km s}^{-1}$) in panel (d) is due to an instrumental artefact in the GRS data set that led to the fitting of very narrow components (see Appendix B.1.4).

The strong confusion for emission at low v_{LSR} values ($< 20 \text{ km s}^{-1}$) also becomes apparent again in panels (a), (b), and (k–p) of Fig. 4.14, which also highlight the effect of the size-linewidth prior. While we do find artefacts induced by the prior in these σ_v -PDFs, the distributions are nonetheless more consistent with the trend of higher σ_v values with increasing heliocentric distance. So even though Figs. 4.13 and 4.14 show that we need to be careful in interpreting the distance results for the emission features with low v_{LSR} values, we conclude that the use of the size-linewidth prior was justified and successful in disentangling part of the confusion between near and far emission.

4.2.5 Galactocentric variation of the gas properties

We now focus on the distribution of intensity and velocity dispersion values of the ^{13}CO fit components with Galactocentric distance (Fig. 4.15). These distributions also reveal some intriguing differences between the BDC runs. For example, for Run A we can identify an accumulation of data points at the approximate R_{gal} extent of the far portion of the 3-kpc arm (3kF), which however is almost entirely missing in Run B. Indeed, a comparison with Fig. 4.8 confirms that Run B puts significantly less emission at the location of the 3kF arm than Run A. This is most likely due to large uncertainties around the tangent point that is due to increased uncertainties in



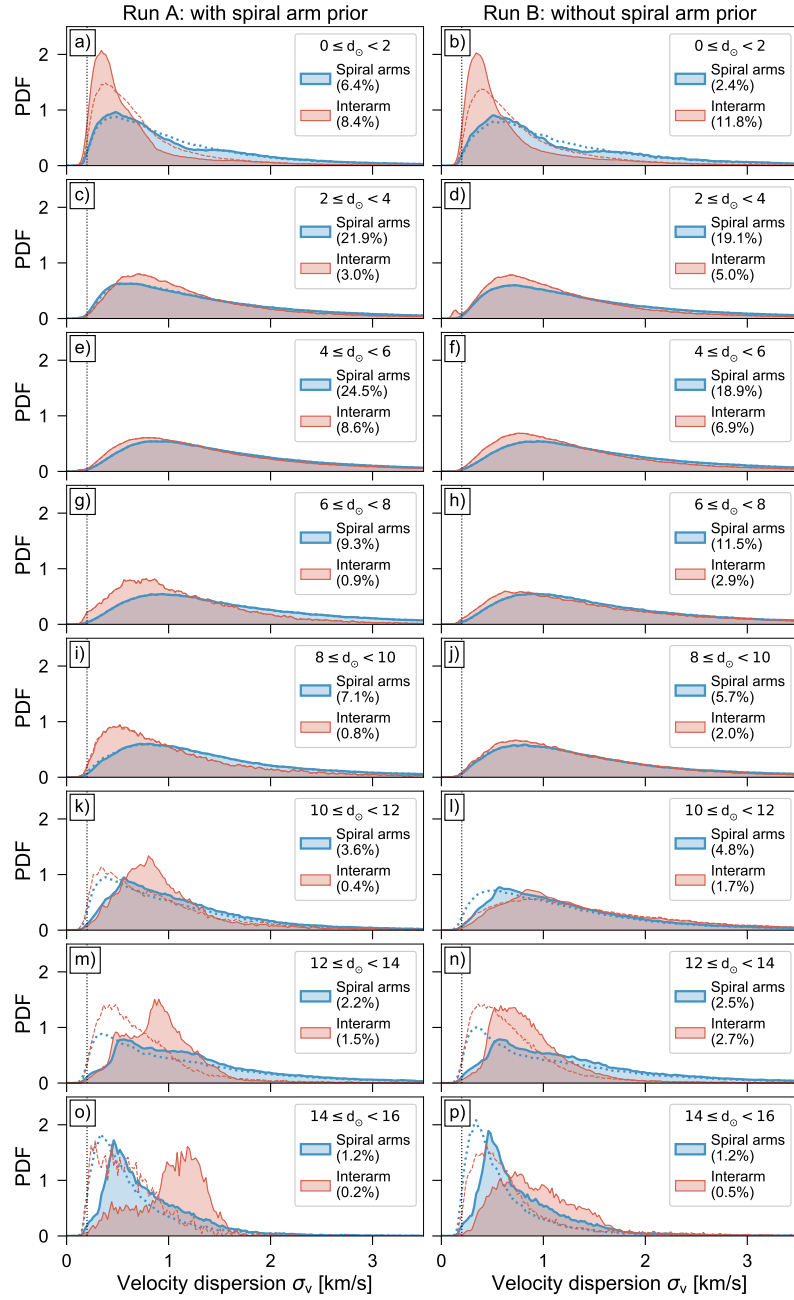
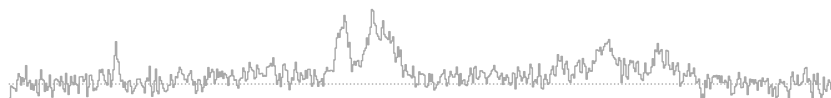


FIGURE 4.14: PDFs of velocity dispersion values for 2 kpc heliocentric distance bins for the distance results with (*left columns*) and without (*right columns*) the SA prior. The dotted vertical line indicates the GRS velocity resolution (0.21 km s^{-1}). Dotted and dashed histograms show the distribution for distance results obtained without the size-linewidth prior. Percentages in the legend indicate the respective fraction of Gaussian fit components associated with spiral arm and interarm structures.



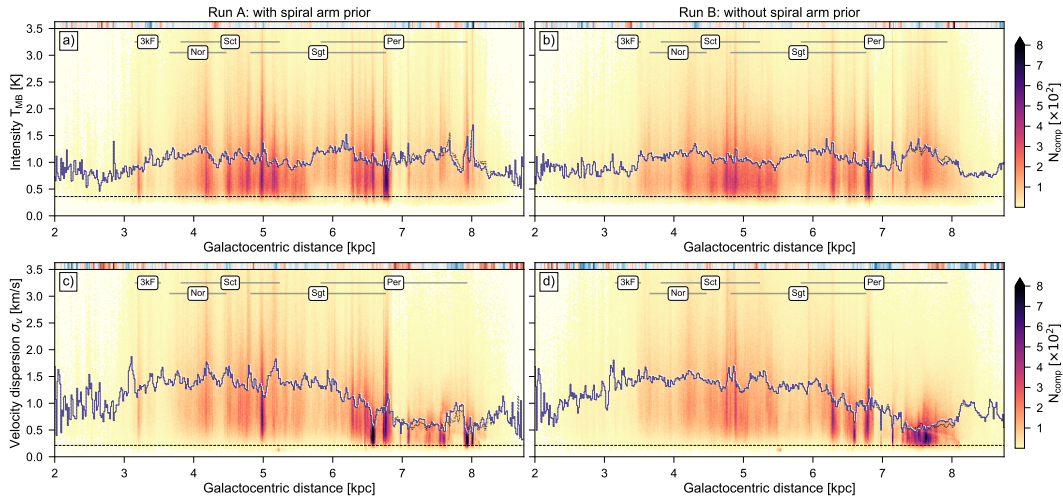
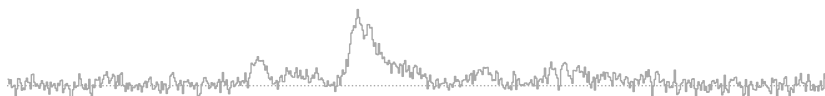


FIGURE 4.15: 2D histograms of estimated Galactocentric distance values and intensity (*top*) and velocity dispersion (*bottom*) values for the BDC run with (*left column*) and without (*right column*) the spiral arm prior. The blue lines show the respective median values per distance bin and dotted black lines give the corresponding values for distances obtained without the size-linewidth prior. The small strips at the top of the individual panels show where the median value is higher (blue) or lower (red) compared to the opposite BDC run, with the strength of the colour corresponding to the magnitude of the difference. The grey horizontal lines in all panels show the approximate R_{gal} extent of five spiral arms overlapping with the GRS coverage. The dashed horizontal line in the top panels at $T_{\text{MB}} = 0.36$ K corresponds to the $3 \times S/N$ limit for the 0.1st percentile of the GRS noise distribution (see Fig. B.2). The dashed horizontal line in the bottom panels indicates the velocity resolution of the GRS (0.21 km s^{-1}).

the KD method (which is also downweighted at smaller R_{gal} values) and increased difficulties in resolving the KDA. Another striking difference occurs at an R_{gal} value of ~ 8 kpc, where Run A shows large peaks that are missing in Run B. This emission corresponds to the position of the nearby Aquila Rift complex, but in Run B most of its emission is allocated to R_{gal} distances of ~ 7.5 kpc. We can confirm this in the top panels, where the accumulation of data points < 0.5 kpc for Run A is shifted to higher distances (between 0.5 and 1 kpc) in Run B.

The intensity distribution (top panels) shows large variation but an almost constant median value with no significant trends, similar to Fig. 4.12. The σ_v distributions (bottom panels) show a more interesting behaviour; the median σ_v value stays at a large value of $\sim 1.5 \text{ km s}^{-1}$ from $3 \lesssim R_{\text{gal}} \lesssim 6$ kpc, after which it drops significantly to a value of $\sim 0.5 \text{ km s}^{-1}$. As mentioned before, this could indicate that in the inner Galaxy the ^{13}CO components have higher non-thermal contributions or that there are increased problems in the decomposition of strongly blended emission in the inner parts of the GRS. We can however also interpret this trend as yet another indication that most of the emission at $R_{\text{gal}} \gtrsim 6.5$ kpc is associated with regions close to the Sun and thus has better resolved emission lines (Sect. 4.1.4).



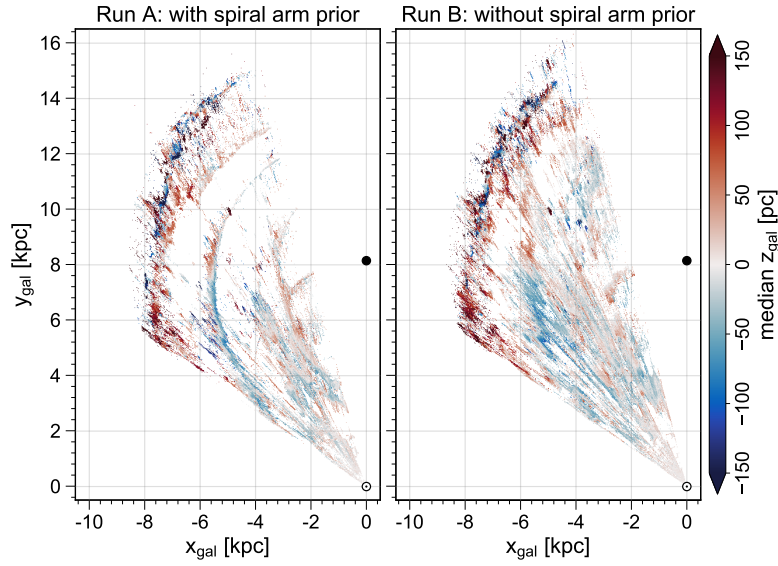


FIGURE 4.16: Face-on view of the median z_{gal} values from the BDC results obtained with (*left*) and without (*right*) the spiral arm prior. The values are binned in 10×10 pc cells and the median was calculated along the z_{gal} axis. The position of the Sun and Galactic centre are indicated by the Sun symbol and black dot, respectively. When displayed in Adobe Acrobat, it is possible to show only the negative median z_{gal} positions, show the spiral arm positions and hide the grid.

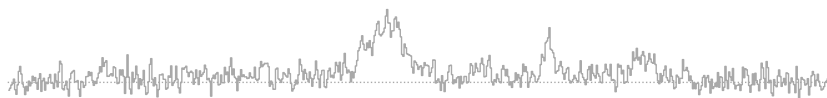
4.2.6 Vertical distribution of the ^{13}CO emission

The Galactic plane has long been known to show a warp towards positive z_{gal} values in the first quadrant at Galactocentric distances $R_{\text{gal}} \gtrsim 7$ kpc (Gum et al., 1960)⁶. In Fig. 4.16 we show a face-on view of the median z_{gal} values of our estimated distances, which clearly shows this warp of the molecular gas disk at $R_{\text{gal}} \gtrsim 7$ kpc. However, we can also see patches of negative z_{gal} values (< -100 pc) for regions that coincide with the Perseus and Outer arms. A comparison with Fig. 4.10 shows that these patches also correspond to the anomalously low σ_v values we already pointed out in Sect. 4.2.1. This confirms our suspicion that these patches most likely correspond to gas emission that originates from very nearby regions that were erroneously assigned to large distances.⁷

Another conspicuous feature is the presence of substantial negative z_{gal} values at the location of the Sagittarius arm at Galactic longitude values of $35^\circ \lesssim \ell \lesssim 50^\circ$ and $5 \text{ kpc} \lesssim R_{\text{gal}} \lesssim 7 \text{ kpc}$. This bend of the Galactic disk towards negative z_{gal} values at this longitude range is already clearly visible in the zeroth moment maps of the GRS data set (see Fig. 3.2) and has also been observed in the *Herschel* Hi-GAL survey (Molinari et al., 2016b). Since this distortion seems to be mainly present in the diffuse ISM component of the Milky Way, Molinari et al. (2016b) speculated that it might be

⁶ The BDC takes into account the effects of this warping in its calculation for the GL prior.

⁷ We note that the presence of these incorrect distance assignments do not change our general conclusion about the warp of the Galactic disk towards positive z_{gal} values.



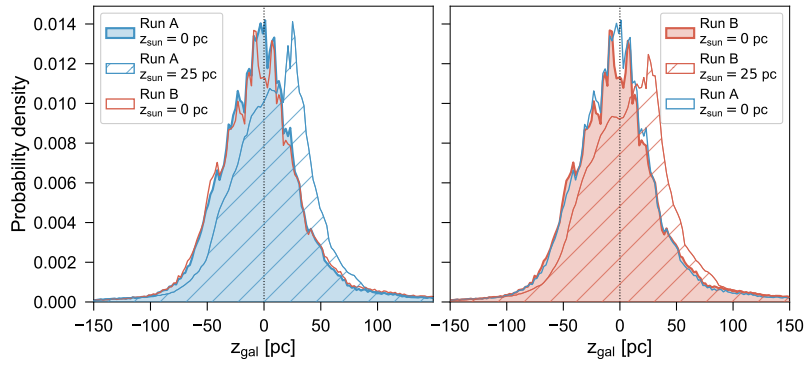


FIGURE 4.17: PDFs of the vertical distribution of the ^{13}CO emission. Shaded PDFs are for the BDC runs with (*left*) and without (*right*) the SA prior, and unfilled PDFs show the distribution of the opposite panel for reference. Hatched PDFs show the z_{gal} distribution assuming an offset of the Sun above the midplane of $z_{\text{offset}} = 25$ pc.

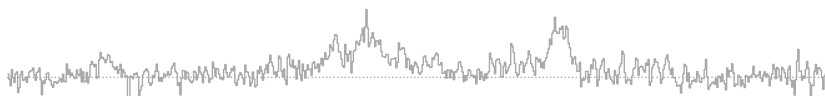
due to interaction with gas flows that originate from the Galactic halo or the Galactic fountain.

In Fig. 4.17 we present PDFs for the estimated z_{gal} values, which have very similar shapes in both BDC runs. The most notable difference is that Run A shows a higher concentration at $z_{\text{gal}} = 0$, whereas Run B shows a dip at this position. This difference is mostly due to the association of sources with the Aquila Rift complex in Run A.

In our calculations we assumed that the Sun is located in the Galactic midplane, which is consistent with results from the most recent studies (Anderson et al., 2019; Reid et al., 2019). However, previous studies and observations found that the Sun has a vertical offset of $z_{\text{offset}} \sim 25$ pc from the IAU definition of the Galactic midplane (Goodman et al., 2014; Bland-Hawthorn & Gerhard, 2016). Figure 4.17 shows how the PDFs would change if we correct for this assumed vertical offset of the Sun using Eq. C3 from Ellsworth-Bowers et al. (2013). Accounting for such an offset leads to a shift of the distribution towards positive z_{gal} values, with an asymmetric peak at $z_{\text{gal}} \sim 25$ pc introduced by emission originating close to the Sun ($\lesssim 1$ kpc).

A Gaussian fit to the PDFs in Fig. 4.17 yields FWHM values of 72 and 77 pc with corresponding mean positions at $z_{\text{gal}} = -5$ and -6 pc for Run A and B, respectively. If a z_{offset} value of 25 pc is factored in, the FWHM values increase slightly to values of 78 and 83 pc and the centroid position changes to $z_{\text{gal}} = 10$ and 8 pc, respectively. Our FWHM estimate is lower by about one third than the value of 110 pc Roman-Duval et al. (2016) found for the dense gas (corresponding to H_2 surface densities $\gtrsim 25 M_{\odot} \text{pc}^{-2}$) in the inner Milky Way. To check whether our results are impacted by the inclusion of both near and far emission, we also estimated the FWHM estimates for individual 1 kpc bins in the R_{gal} range of 3 – 6 kpc. We find a maximum FWHM extent of ~ 90 pc for $5 < R_{\text{gal}} < 6$ kpc and FWHM values of 70 – 75 pc at lower R_{gal} bins.

Figure 4.18 shows the distribution of σ_v values with vertical height z_{gal} . For both distance results we can see a clear concentration of data points towards the midplane. The decrease in the median σ_v value around a z_{gal} value of 0 is due to very nearby emission located < 1 kpc from the Sun, which has very narrow linewidths. We also



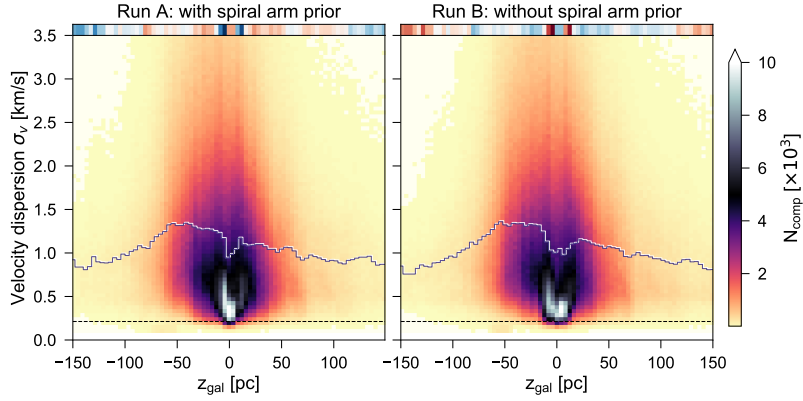


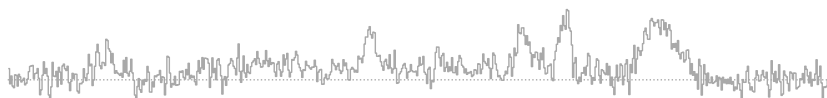
FIGURE 4.18: 2D histograms of velocity dispersion and estimated vertical distances z_{gal} for the BDC run with (*left*) and without (*right*) the spiral arm prior. The blue line shows the median σ_v value per z_{gal} bin. The small strips at the top of the individual panels show where the median value is higher (blue) or lower (red) compared to the opposite BDC run, with the strength of the colour corresponding to the magnitude of the difference. The dashed horizontal line indicates the GRS velocity resolution (0.21 km s^{-1}).

note the presence of an asymmetry, especially striking in the curve of median values, with a larger fraction of components with broader linewidths located at negative z_{gal} values. We already found a similar asymmetry in the distribution of σ_v values with Galactic latitude (see Fig. 3.12). As argued in Sect. 3.4.1, such an asymmetry could be explained by an offset position of the Sun above the Galactic midplane. However, as mentioned, recent results have found that the vertical position of the Sun agrees well with the location of the Galactic midplane (Anderson et al., 2019; Reid et al., 2019).

4.2.7 Potential problems, artefacts, and biases

The BDC tool was designed to estimate distances for spiral arm sources, which means that its default settings have an inherent bias of associating sources with Galactic features from its spiral arm model. Since we use the BDC in assigning distances to the gas emission of an entire Galactic plane survey, we need to be careful in interpreting its results and should be aware of the biases present in the distance calculation.

It is a priori not clear which of our BDC runs yields more trustworthy or better distance solutions. Run A has the obvious problem that the gas emission will be preferentially located closer to the Galactic features included in the spiral arm model. For this run we expect biased results in terms of the distribution of emission in spiral arm and interarm regions, with the latter likely severely underestimated. Run B gives more unbiased results with regards to the allocation of the gas to arm and interarm regions. However, we note that for the distance results from Run B an association with maser parallax sources can be a decisive factor for the choice of the most likely distance (see left panel of Fig. 4.2). Since these maser sources do mostly overlap with the Galactic features of the spiral arm model (Fig. 4.1), the distance results thus still contain an implicit, albeit moderate, association with these Galactic features.



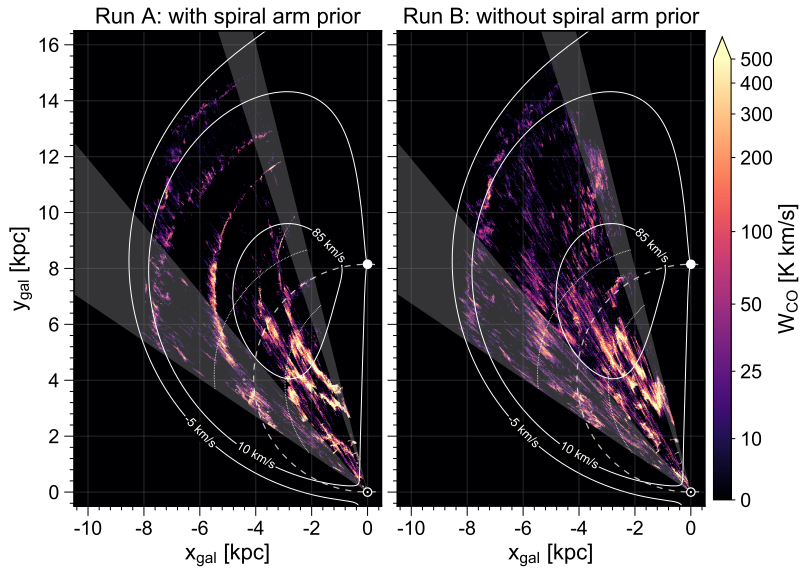


FIGURE 4.19: Same as Fig. 4.8, but overplotted with diagnostics to illustrate potential issues in the distance assignment. The position of the Sun and the Galactic centre are indicated with a Sun symbol and a white dot, respectively. Solid white curves show constant projected v_{LSR} velocities. The dashed white curve marks the locus of tangent points and dotted lines indicate the area where v_{LSR} values are within 10 km s^{-1} of the tangent point velocity. Shaded areas show GRS regions that either had limited latitude or velocity coverage.

Moreover, since Run B is dominated by the KD prior, it is also more strongly affected by the ambiguities and uncertainties of the KD method.

We can identify an accumulation of emission features around the locus of tangent points for both distance estimates. Confusion between the two KD solutions is strongest around this tangent point locus, as the two distance solutions result in more similar values the closer the v_{LSR} value gets to the tangent point velocity. Thus often a threshold is used for the tangent point distance allocation, where for example all sources with v_{LSR} values within 10 km s^{-1} of the tangent point velocity are assigned the tangent point distance (e.g. [Urquhart et al., 2018](#)). We indicate the corresponding region where v_{LSR} values are within 10 km s^{-1} of the tangent point velocity in Fig. 4.19. This threshold of 10 km s^{-1} corresponds to expected velocity deviations introduced by streaming motions (e.g. [Burton, 1971](#); [Ramón-Fox & Bonnell, 2018](#)). We can indeed identify conspicuous empty voids within this region, which might be at least partly due to this confusion around the tangent point velocity. However, a comparison with the default BDC runs (Fig. C.6) shows that our use of literature distance solutions helped to substantially decrease artefacts around the locus of tangent points.

Figure 4.20 shows a comparison of the median associated v_{LSR} values for the distance results. We overplot this figure with curves of constant projected v_{LSR} values that were calculated with the methods included in the BDC. In general, the BDC runs produced distance results that are well in agreement with the assumed Galactic rotation curve model. This good correspondence is not surprising, given that the KD solutions are calculated using the rotation curve model. However, an anticipated



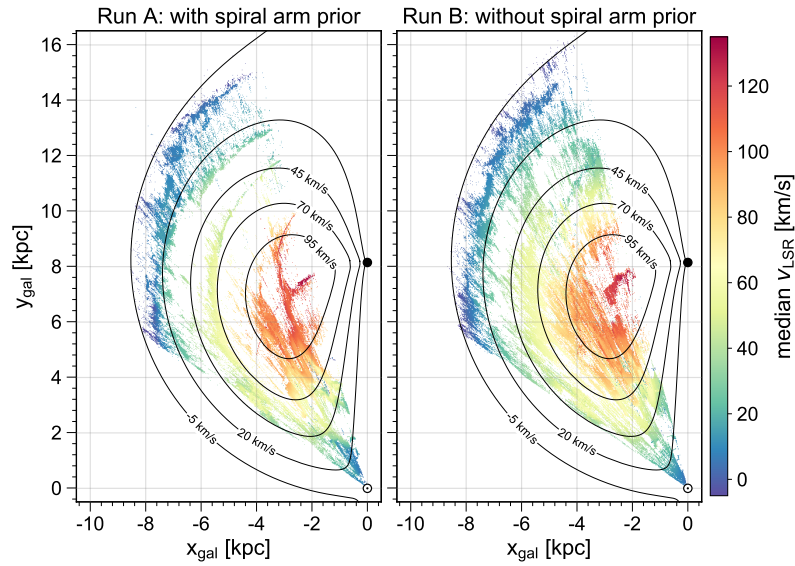


FIGURE 4.20: Face-on view of the median v_{LSR} values from the BDC results obtained with (left) and without (right) the spiral arm prior. The values are binned in 10×10 pc cells and the median was calculated along the z_{gal} axis. The position of the Sun and Galactic centre are indicated by the Sun symbol and black dot, respectively. When displayed in Adobe Acrobat, it is possible to show the `spiral arm positions`, hide the `curves of constant projected v_{LSR}` , and hide the `grid`.

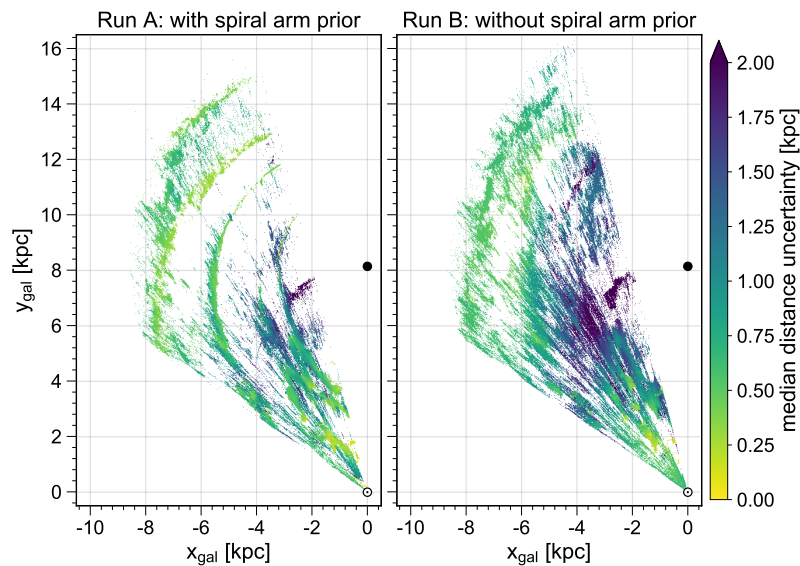
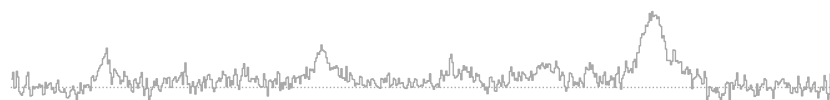


FIGURE 4.21: Face-on view of the median distance uncertainty for the BDC results obtained with (left) and without (right) the spiral arm prior. The values are binned in 10×10 pc cells and are summed up along the z_{gal} axis. The position of the Sun and Galactic centre are indicated by the Sun symbol and black dot, respectively. When displayed in Adobe Acrobat, it is possible to show the `spiral arm positions` and hide the `grid`.



problem is that peculiar gas motions, for example introduced by streaming motions within spiral arms, might cause a significant deviation from the expected v_{LSR} velocities of the assumed rotation curve model (e.g. Ramón-Fox & Bonnell, 2018). This strongly affects regions with R_{gal} values $\lesssim 5$ kpc, for which we expect large peculiar motions due to the influence of the Galactic bar (Reid et al., 2019). The BDC takes this into account by down-weighting the KD prior for regions closer to the Galactic centre (see Fig. 4.2); this however has a significant impact on the estimated distance uncertainties, which show a substantial increase with decreasing R_{gal} values (Fig. 4.21). As already noticed in Fig. 4.11, this effect is much stronger for Run B, since in this case the combined PDF shows broader peaks and corresponding Gaussian fits to these peaks result in higher estimated distance uncertainties. We give a more detailed discussion about the deviations from the rotation curve velocities and the regions where they occur in Appendix C.3.4. We also note that the v_{LSR} uncertainties of the fit components can have a large impact on the distance calculation routine, as larger uncertainty values can lead to an association with more parallax sources or Galactic features. We illustrate and discuss this effect with an example in Appendix C.3.1.

Since in this work we do not explicitly correlate the distance results of neighbouring lines of sight, it is possible that assigned distance values can show strong variation between neighbouring lines of sight. We can see this effect as emission features that are spread out along the line of sight (reminiscent of the ‘Fingers of God effect’; see e.g. the right panel of Fig. 4.19).

The limited spatial and spectral coverage of the GRS also introduces some artefacts in the distance estimation (Fig. 4.19). The limited latitude coverage from $14^\circ \lesssim \ell \lesssim 18^\circ$ results in missing patches of CO emission at this longitude range. Moreover, the face-on view is restricted by the lower limit of the velocity coverage ($v_{\text{LSR}} = -5 \text{ km s}^{-1}$) and thus contains no emission past $d \sim 13$ kpc at $\ell > 40^\circ$. However, the reduced velocity coverage of $-5 \lesssim v_{\text{LSR}} \lesssim 85 \text{ km s}^{-1}$ for $40^\circ \lesssim \ell \lesssim 56^\circ$ should not impact our distance results as we would not expect emission peaks with $v_{\text{LSR}} > 85 \text{ km s}^{-1}$ at these larger longitude values, as demonstrated in Fig. 4.19.

We note that the GRS decomposition also has uncertainties that might cause problems for the distance estimation. Especially in the inner part of the Galaxy emission lines can be strongly blended, which could have led to difficulties in the decomposition (see the discussion about flagged components in Sect. 3.2.1). We tried to fold these considerations into the uncertainties of the v_{LSR} position supplied to the BDC (see discussion in Appendix C.3.1). Moreover, we tested the effects of a quality cut based on the S/N ratio of the fit components and found that this does not change our overall conclusions (see Sect. 4.2.3).

As already mentioned in previous sections, the feature between the location of the Perseus and Outer arm corresponding to emission with v_{LSR} values around 10 km s^{-1} (see Fig. 4.19) is most likely an artefact introduced by the KD prior. As discussed in Sect. 3.5 and Sect. 4.1.4, for this v_{LSR} regime there is strong confusion between emission from the solar neighbourhood and the far disk. Moreover, the BDC biases emission lines with $v_{\text{LSR}} \lesssim 5 \text{ km s}^{-1}$ towards far distances (see Fig. 4.3). We can estimate the magnitude of this error by counting all components with an unlikely combination of distance, z_{gal} , and σ_v values. Choosing $d > 8$ kpc, $z_{\text{gal}} < -50$ pc,



and $\sigma_v < 0.5 \text{ km s}^{-1}$ as unlikely combination of parameters, we find that for both distance results about 0.3% of the fit components satisfy these parameters⁸. Since the W_{CO} values of these components account for only about 0.1% of the total emission, we conclude that this problem has a very minor impact on our overall conclusions concerning the fraction of emission located in arm and interarm regions. However, this issue has strong impacts on our conclusions about the σ_v distribution in the Perseus and Outer arm (see Sect. 4.2.4).

4.2.8 Comparison with previous results

The BDC has already been used in the distance estimation to clouds and clumps extracted from other Galactic plane surveys (Urquhart et al., 2018; Rigby et al., 2019). However, since these works used an older version of the BDC (v1.0), it is not straightforward to compare their distance results with the distances obtained in this work. Moreover, our distance estimations are not independent from these previous results, since we use them as input for our KDA prior. Notwithstanding these issues, in Appendix C.1.4 we discuss how well we are able to match these previous distance results and conclude that we recover the vast majority of literature distance results within the degree of expected uncertainties introduced by the updated rotation curve parameters from BDC v1 to v2.4.

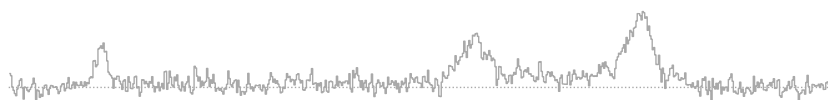
Unfortunately, it is also extremely challenging to compare our results in terms of the spiral arm to interarm fraction and variation of physical properties with previous studies, given that other works used a combination of different tracers, different spiral arm models, or different assumptions about the Galactic rotation curve and the distance to the Galactic centre. It would be necessary to homogenise all data sets before any attempted comparison, which potentially requires recalculating and updating the literature distance results with our assumed Galactic parameters. Since such a homogenisation exceeds the scope of this work, we decided on a strictly qualitative comparison with some of the previous results and do not attempt to account for any of these systematic differences.

Previous works analysing the GRS found a similar overdensity of ^{13}CO with spiral arm features. Roman-Duval et al. (2009) found for their sample of GRS molecular clouds that the ^{13}CO surface brightness is strongly enhanced at the location of spiral arms from the model of Vallee (1995). Sawada et al. (2012) also found that the GRS emission shows bright and compact concentrations along spiral arm features, whereas more diffuse and extended emission dominates the interarm regions.

However, recent results from other Galactic plane surveys in the first quadrant found a weaker correspondence of molecular clouds with spiral arms. Colombo et al. (2019) analysed a large ^{12}CO (3–2) survey overlapping with the GRS and could only attribute about 35% of the flux to molecular clouds associated with spiral arms⁹. Colombo et al. (2019) attribute this low fraction of flux in spiral arm clouds to

⁸ If we had not used the size-linewidth prior this fraction would increase to about 0.6 and 0.9% of the fit components for the runs with and without the SA prior, respectively.

⁹ Colombo et al. (2019) used the spiral arm model by Vallée (2017) as a comparison, in which positions for the Scutum and Sagittarius arms deviate by up to $\sim 1 \text{ kpc}$ compared to the corresponding arms defined by Reid et al. (2019)



difficulties in the distance assignments and optical depth effects of the ^{12}CO (3–2) emission.

Recently, [Rigby et al. \(2019\)](#) found that clumps from a distance limited ($6 < d_{\odot} < 9$ kpc) sample associated with spiral arms have significantly higher σ_v values than clumps at the same distances that are located in interarm regions. They further note that this difference in linewidth is comparable to what has been found in extragalactic work ([Colombo et al., 2014](#)) and smoothed particle-hydrodynamics simulations ([Duarte-Cabral & Dobbs, 2016](#)). We do find a trend for lower σ_v values at around the same distances for interarm regions for Run A, but not for Run B (Fig. 4.12). This is somewhat surprising, given that [Rigby et al. \(2019\)](#) used the BDC without the SA prior for their distance calculation, which should have yielded a better agreement with our Run B. However, we note that [Rigby et al. \(2019\)](#) used a higher-density tracer (^{13}CO (3–2)) and v1 of the BDC¹⁰, which could both account for any differences compared to our results.

4.3 SUMMARY

In this chapter we presented distance estimates for the Gaussian decomposition results of the Galactic Ring Survey discussed in the previous chapter. Using the most recent version of the Bayesian Distance Calculator tool ([Reid et al., 2016; 2019](#)), we perform two separate distance calculations for the ~ 4.6 million individual Gaussian fit components, for which we vary the settings so as to either incorporate or neglect a prior for an association with spiral arm structure (labelled Run A and Run B, respectively). In addition, we include literature distance information of objects overlapping with the GRS coverage as prior information for solving the kinematic distance ambiguity. We also incorporate a size-linewidth prior to solve for the confusion between emission from the solar neighbourhood and the far Galactic disk for emission peaks with line centroids of $v_{\text{LSR}} < 20 \text{ km s}^{-1}$.

We find that most of the distance results of the two BDC runs are consistent with each other within their uncertainties, with most of the differences either due to the strong influence of the spiral arm prior for Run A or larger uncertainties introduced by the stronger effect of the kinematic distance prior for Run B. The two distance runs complement each other and show opposing strengths and weaknesses, thus suggesting that the true distribution of the gas emission is closer to a combination of the two results than to each of the individual distance runs. Our main findings based on these two distance results are as follows:

1. The majority of the ^{13}CO emission is associated with spiral arm features as defined in the model by [Reid et al. \(2019\)](#). The fraction of ^{13}CO emission located in interarm regions changes from 16% to 24% in terms of the total ^{13}CO integrated emission and 24% to 34% in terms of the total number of ^{13}CO velocity components.

¹⁰ BDC v2.4 includes new maser parallax sources, updated models for the Galactic rotation curve and spiral arm features, and contains significant changes in the distance estimation, such as a down-weighting of the KD prior in the inner Galaxy to accommodate expected large streaming motions introduced by the Galactic bar. See [Reid et al. \(2019\)](#) for more information.



2. The vertical distribution of the gas emission has a FWHM extent of ~ 75 pc. We recover a significant warp of the molecular disk towards positive z_{gal} values of more than 100 pc for the far side of the disk at $R_{\text{gal}} > 7$ kpc. The gas disk shows a significant bend towards negative z_{gal} values at the position of the far portion of the Sagittarius arm.
3. We find a trend of higher velocity dispersion values with increasing heliocentric distance, which we attribute mostly to beam averaging effects. Most of the velocity dispersion values also significantly exceed expected values based on an assumed size-linewidth relationship.
4. The ^{13}CO emission associated with spiral arms and spur features has a similar distribution of velocity dispersion values, which is shifted to higher values compared to the distribution of velocity dispersion values in interarm structures. However, we find that most of this difference is due to the location of a significant fraction of interarm gas at close distances to the Sun, which resulted in spatially better resolved lines and narrower linewidths. While we cannot exclude variations in the linewidth between spiral arm and interarm gas, we conclude that our present results do not support strong differences in σ_v between these environments.
5. There is strong confusion between ^{13}CO emission coming from the local solar neighbourhood and regions associated with the Perseus and Outer arm. By using the velocity dispersion values of the fit components as an additional prior we could significantly reduce the confusion between near and far emission for low v_{LSR} velocities ($-5 < v_{\text{LSR}} < 20 \text{ km s}^{-1}$).

While we use the currently best knowledge about the structure of our Galaxy for our distance results, we anticipate that these will be subject to change, in particular due to updates on the BDC method, the Galactic rotation model, and the position of Galactic features, with additional and more precise maser parallax measurements, and new KDA solutions for sources overlapping with the GRS coverage. The BDC tool and its enhancements discussed in this work are designed to be versatile enough to incorporate these changes. We thus conclude that the approach presented herein should be a helpful contribution to the problem of estimating distances to gas emission features in Galactic plane surveys.



CONCLUSIONS & OUTLOOK

Life is the art of drawing sufficient conclusions from insufficient premises.

— Samuel Butler

In this thesis I studied the detailed velocity structure and distribution of molecular gas in the inner part of the Milky Way. I exploited and analysed the kinematic information contained in the GRS (Jackson et al., 2006), a large ^{13}CO (1–0) survey of the Galactic plane in the first quadrant of the Milky Way consisting of ~ 2.3 million spectra. In Chapter 1 I introduced and motivated the importance of such Galactic plane surveys for understanding the dynamics and distribution of molecular gas within the Milky Way. These surveys also provide a crucial link between high-resolution observations of molecular clouds in the solar neighbourhood and the large statistical studies enabled by interferometric observations of nearby galaxies. Moreover, I highlighted the usefulness of ^{13}CO observations and illustrated how we can use those data sets to extract information about the kinematics and location of the molecular gas within the Milky Way, which is crucial for our understanding of the formation and evolution of dense structures in the ISM.

Common analysis approaches based on segmenting the gas emission into molecular clouds or clumps are not sensitive to and average over the gas kinematics in between and within the extracted objects. I thus advocated spectral decomposition as a favourable alternative method for studying the detailed kinematics of Galactic plane surveys and developed GAUSSPY+ as a suitable new analysis tool (Chapter 2, published in Riener et al. 2019). GAUSSPY+ is a fully automated Gaussian decomposition package that can be applied to emission line data sets, especially large surveys of HI and isotopologues of CO. The GAUSSPY+ package is built upon the existing GAUSSPY algorithm (Lindner et al., 2015), but contains physically-motivated developments that are specifically designed for analysing the dynamics of the ISM and significantly improve its performance for noisy data. New functionalities of GAUSSPY+ include: i) automated preparatory steps, such as an accurate noise estimation which can also be used for stand-alone applications; ii) an improved fitting routine; and iii) an automated spatial refitting routine that can add spatial coherence to the decomposition results by refitting spectra based on neighbouring fit solutions. I thoroughly tested the performance of GAUSSPY+ on synthetic spectra and a challenging test field of the GRS data set, for which it performed well in terms of recovered flux and spatial coherence of the fit results. Moreover, I found that the algorithm can deal with cases of complex emission and even low to moderate signal-to-noise values. I thus concluded that GAUSSPY+ provides a significant leap forward in the automated fitting of large emission line data sets and is a valuable tool for analysing the kinematics of gas structures.

With this new analysis tool tested and benchmarked, I set out in Chapter 3 (published in Riener et al. 2020) to address the question of how the detailed velocity

structure of molecular gas looks like over a large section of our Galaxy and what we can infer from this new knowledge about the properties and kinematics of the molecular gas. I used GAUSSPY+ to autonomously fit all spectra of the GRS, which resulted in ~ 4.6 million individual fit components. These decomposition results provide a wealth of data that enable novel, unexplored ways to interpret the gas velocity structure, which complement and go beyond existing studies of the full GRS data set (e.g. Roman-Duval et al., 2010; Sawada et al., 2012; Roman-Duval et al., 2016). Focussing on the global gas emission properties, I found that the turbulent energy of the gas correlates with Galactic latitude and is higher towards the Galactic centre, most likely due to the concentration of star-forming regions in the Galactic midplane and the impact of the Galactic bar, respectively. I also established that the complexity of the CO spectra correlates with their integrated intensity, which helps to understand the nature of CO emission in data in which the velocity structure is not resolved (e.g. in extragalactic observations). By comparing the decomposition results with H₂ surface densities inferred from *Herschel* dust emission observations, I found that gas and dust are well mixed along the line of sight but that dust emission traces also lower H₂ surface densities for which no ¹³CO gas is detected. This comparison thus showcased the potential of synergies between the extracted detailed gas kinematics and complementary ISM tracers, such as dust extinction and dust emission data sets. Taking further advantage of the decomposition results, I found evidence from the GRS data for sub-cloud scale velocity fluctuations present throughout the entire gas disk of the Milky Way. Together with other recent works (Henshaw et al., 2016b; 2019; Liu et al., 2019; González Lobos & Stutz, 2019) this presents evidence for a highly dynamic ISM, and statistical analysis of these fluctuations further demonstrates that they can be linked to turbulent motions or convergent motions indicative of accretion flows or large-scale instabilities (Henshaw et al., in press). Shifting the focus on the distribution of the gas within the Milky Way, I showed how we can use beam averaging effects to our advantage in characterising Galactic structure. Based on considerations of a size-linewidth relationship, I argued that the fitted velocity dispersions can be indicative of whether the emitting region is located on the near or far side of the Galactic disk, which is useful prior information for solving ambiguities that complicate distance estimations to the gas emission features.

As outlined in the introduction, the precise location of the molecular gas within the Milky Way is one of the outstanding issues in Galactic ISM studies. Knowledge about the gas distribution is crucial to study variation of the gas emission as a function of Galactic location and to correct for differences in spatial resolution introduced by our location inside the Galactic disk. Given this significance, I used the kinematic information from the decomposition results to obtain the current best assessment of the Galactic distribution of ¹³CO gas from the GRS data (Chapter 4, to be submitted to *Astronomy & Astrophysics*). I used a Bayesian approach based on the presently most precise knowledge about the structure and kinematics of the Milky Way (Reid et al., 2016; 2019) to determine distances to the ~ 4.6 million Gaussian fit components obtained from the spectral decomposition presented in Chapter 3. To characterise the impact and effect of priors on the Bayesian distance calculation and establish limits for the fraction of ¹³CO emission in spiral arm and interarm regions, I performed two different distance estimates that either included or excluded a prior for a model



of Galactic features, such as spiral arms or spurs. I further included priors to resolve the kinematic distance ambiguity based on an extensive compilation of literature distances and considerations based on an assumed size-linewidth relationship. I found that the fraction of ^{13}CO emission associated with spiral arm features varies between 76% to 84% in the two distance runs and that the vertical distribution of the gas is concentrated around the Galactic midplane with FWHM values of ~ 75 pc. While these results show qualitative agreement with previous studies of the GRS (e.g. [Roman-Duval et al., 2009](#); [Sawada et al., 2012](#); [Roman-Duval et al., 2016](#)), they allow for a more quantitative and precise analysis of the data set, as for instance blended emission features can be better separated via the spectral decomposition. Studying possible variations with Galactic location, I did not find any significant difference between gas emission properties associated with spiral arm and interarm features. However, there is a trend of higher velocity dispersion values with increasing heliocentric distance, which I attributed to beam averaging effects caused by differences in spatial resolution. Even though the majority of the distance results of the two runs are consistent with each other, they show differences due to the domination of the prior for Galactic features and large uncertainties in the kinematic distances, respectively. I argued that the true distribution of the gas emission is likely more similar to a combination of the two discussed distance results, and highlighted the importance of using complementary distance estimations to safeguard against the pitfalls of any single approach. I concluded that the methodology presented in this work is therefore a well-suited approach for distance determinations of gas emission features in Galactic plane surveys.

To summarise, in this thesis I showed that new spectral decomposition methods, such as GAUSSPY+, allow for an efficient extraction of the detailed kinematic information contained within large Galactic plane surveys of molecular gas emission. I demonstrated that this detailed gas velocity structure enables novel analysis approaches that complement and go beyond commonly used cloud segmentation methods and analysis approaches. I also highlighted how a synergy with complementary ISM tracers allows a characterisation of the complexity along the line of sight. Moreover, I showed that the extracted velocity structure can be combined with new distance analysis methods to determine the distribution of the gas emission and discussed variation of its properties with Galactic environment.

I conclude that the methodology presented in this work is a well-suited approach to uncover and exploit the detailed velocity structure hidden within the complex data sets of large Galactic plane surveys. The work presented herein also demonstrates that the analysis of the velocity structure from Galactic down to sub-cloud scales has enormous potential for furthering our knowledge about the molecular ISM.

OUTLOOK

The next crucial steps following the work presented in this thesis are to utilise the detailed kinematic information extracted from the large Galactic plane surveys to further improve our knowledge about the molecular gas within the Milky Way, in particular its distribution, its connection with interstellar dust, and the importance of its dynamics on the star formation process. In the following, I outline three potential



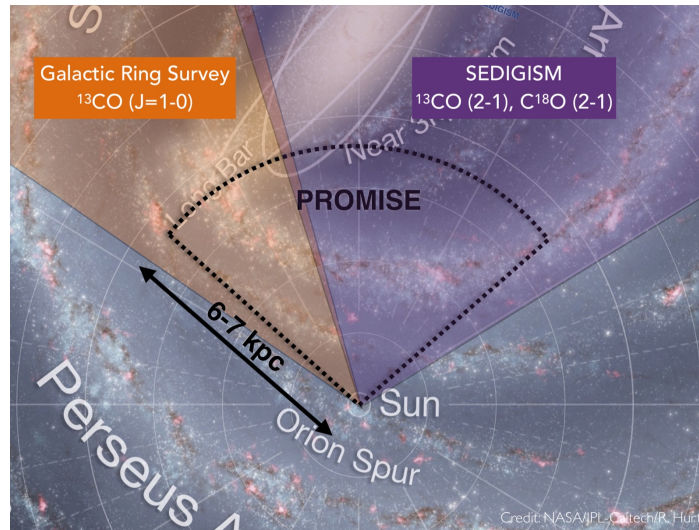
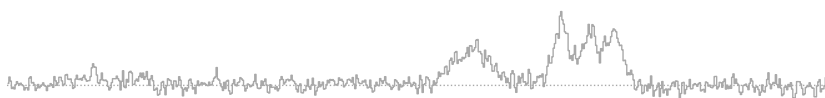


FIGURE 5.1: Schematic indication of the coverage of two Galactic plane emission line surveys (GRS and SEDIGISM) and a new dust extinction map of the inner Galactic plane (PROMISE). Background image credit: NASA/JPL-Caltech/R. Hurt (SSC/Caltech).

avenues for research that directly build upon the analysis tools and scientific results presented in this thesis.

Investigating the distribution and kinematics of ^{13}CO in the entire inner Galactic plane

To better characterise the properties of molecular gas on Galactic environment, it is necessary to homogeneously study the distribution and velocity structure of ^{13}CO in the entire inner Galactic plane. This requires to extend the work presented herein to the Galactic centre and the fourth quadrant of the Milky Way. These regions are covered by SEDIGISM (Schuller et al., 2017), which is a large Galactic plane survey conducted with the APEX telescope that contains 12.3 million ^{13}CO (2–1) and C^{18}O (2–1) spectra (Fig. 5.1). The SEDIGISM coverage overlaps partly with the GRS, which can be used to determine differences between the ^{13}CO (1–0) and ^{13}CO (2–1) transition, which is essential to benchmark and compare results from the two surveys. A spectral decomposition of SEDIGISM similar to the one presented in this thesis for the GRS would be highly complementary to cloud-scale analysis of the SEDIGISM data (Duarte-Cabral et al., *subm.*) and would yield important information about the detailed state of the gas within and in between these extracted clouds. The spectral decomposition results will also provide a clearer picture of the effects of gas kinematics on the structure and average physical properties of these molecular clouds. Since SEDIGISM covers the centre of our Galaxy, the kinematic analysis will also be extremely helpful for studies of the dynamics of the Central Molecular Zone and regions probing the Galactic bar. The approach of using the fitted linewidth as an additional discriminator for the distance assignment might prove to be extremely valuable in disentangling foreground emission from the very crowded lines of sight towards the Galactic centre.



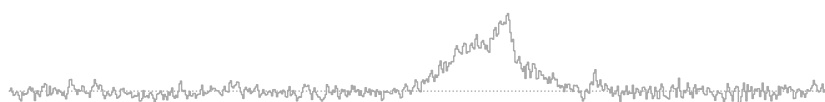
Creating and exploiting synergies between molecular gas and interstellar dust

As demonstrated in Chapter 3, the synergy of the molecular gas observations with complementary ISM tracers has enormous potential in furthering our understanding of the structure, composition, and distribution of the ISM. We need to combine our new knowledge about the velocity structure of molecular gas emission with existing, complementary data sets of ISM tracers, mainly dust emission and extinction, to investigate the large-scale structure and properties of molecular gas and its relation to star formation. The distance results for the gas presented in Chapter 4 can be combined and improved with new 3D dust maps of the Galactic plane that take advantage of *Gaia* and near-infrared observations (Rezaei Kh. et al., 2017; Rezaei Kh. et al., 2018). A particularly promising avenue is to correlate the lines of sight for the gas emission observations in a similar fashion as for these dust maps, which may enable a new mapping of the Galactic structure that is far less dependent on kinematic distances and its large uncertainties. Such an analysis will also immediately indicate interesting Galactic regions where gas and dust show a deviating behaviour in their correlation. In addition, detailed line of sight comparisons between molecular gas and interstellar dust in different Galactic environments (such as the Galactic centre, spiral arm and interarm regions) can establish how the location within the Galaxy impacts the abundance of these tracers, which will yield important information on variations in the CO-to-H₂ conversion factor, Galactocentric gradients of CO isotopologues, and CO depletion effects. For the comparison of gas and dust observations, a new tool such as the Histogram of Oriented Gradients (HOG; Soler et al. 2019) can be used, which is based on machine vision techniques and morphologically matches structures between different data sets to establish their degree of correlation.

The PRobing the Origins of Massive molecular cloud StructureE (PROMISE) project (Kainulainen et al., in prep.) will soon yield a new high-resolution dust extinction map of the inner Galactic plane (Fig. 5.1), which will provide an unprecedented degree of detailed information about the dust in the Galactic plane at spatial resolution scales of 2". Systematic morphological association of PROMISE dust extinction features (such as IRDCs) with molecular gas features will allow to further probe the dependency of a molecular cloud's structure on its kinematics—thereby testing our current paradigm and theories of the turbulence-dominated ISM—and in addition will aid in solving kinematic distance ambiguities.

Probing the impact of gas dynamics on the formation and evolution of ISM structures

Finally, it is crucial to learn more about the formation and evolution of structures in the ISM, in particular in light of our new discovery of the universal fluctuations in the velocity structure of molecular gas (Sect. 3.6; Henshaw et al. in press). Next potential steps could be to extend the analysis of these velocity fluctuations to a sample of 10 to 20 spatially and spectrally well resolved GMFs covered by GRS and SEDIGISM. The analysis of such a GMF sample could address whether their velocity fluctuations are impacted by the presence of spiral arms causing large-scale instabilities—which would be consistent with our findings in extragalactic studies (Henshaw et al., in press)—and to what fraction the velocity fields of these structures are associated with turbulent motions or convergent accretion flows. Such a study



can utilise a clustering technique based on unsupervised machine learning (Henshaw et al., 2019) to extract velocity coherent structures from the decomposed data sets, and employ analysis tools that have been intensively tested and shown to reliably identify periodicity in the velocity fluctuations (Henshaw et al., in press). An analysis on the moderate spatial and spectral scales of GRS and SEDIGISM will be the ideal foundation for proposals of follow-up interferometric observations of objects with intriguing kinematic properties with the Submillimetre Array or the Atacama Large Millimetre/Submillimetre Array.

These three outlined research avenues have the potential to yield important contributions to debates on the distribution of the ISM within our Galaxy, the correlation and complementarity of interstellar gas and dust, and the importance of gas dynamics for the formation and evolution of structures in the ISM, which will have strong implications for ISM and star formation research within the Milky Way and nearby galaxies. I am confident that great progress in studies of the ISM can be achieved by approaching the enormous data sets of Galactic plane surveys with innovative analysis methods and data science tools that go beyond commonly used approaches of cloud segmentation. The work presented in this thesis is a first step towards this goal and the methodology, analysis tools, data products, and scientific outcomes presented herein can serve as the foundation for an even deeper exploration of the information contained in these vast molecular gas observations of the ISM in the Milky Way.



A.1 MARKOV CHAIN

The basic principle or question behind this step is: given a certain peak in the spectrum, what is the probability that this peak was caused by random fluctuations of the noise? This probability depends on the size of the spectrum, as the probability that random noise fluctuations cause a feature resembling a signal peak will increase with the number of spectral channels. The following probabilistic estimation does *not* attempt to quantify the probability of a signal peak being a real feature, but tries to establish the probability of a peak being the result of random noise fluctuations.

To obtain this estimate, we first convert the spectrum into a binary sequence by setting negative channels to a value of 0 and positive channels to a value of 1 (we treat channels that have an exact value of zero as positive channels). Assuming that each channel can be treated independently from each other and is not correlated with its neighbouring channels, this binary sequence is analogous to a sequence of coin tosses, with the number of coin tosses equivalent to the number of spectral channels.

This transformation thus allows us to work out the probability of a sequence of negative or positive channels being due to random noise fluctuations. In case of pure white noise, the probability of a spectral channel having a positive or negative value is $1/2$. To calculate the probability of a sequence of n negative or positive spectral channels we use a one-step Markov chain with state space of $\{1, 2, \dots, n\}$. The $n \times n$ transition matrix $P_{i,j}$ that we use to determine the probability of a sequence of n negative or positive consecutive channels has the following structure:

$$P_{i,j} = \begin{pmatrix} p_{i=1,j=1} & p_{i=1,j=2} & \cdots & p_{i=1,j=n} \\ p_{i=2,j=1} & p_{i=2,j=2} & \cdots & p_{i=2,j=n} \\ \vdots & \vdots & \ddots & \vdots \\ p_{i=n,j=1} & p_{i=n,j=2} & \cdots & p_{i=n,j=n} \end{pmatrix} \quad (\text{A.1})$$

The rows i give the possible states the system can be in (pre-transition states) and the column entries give the probability of transitioning to respective new states. That means that all of the elements in a row have to sum up to a probability of 1 ($\sum_{j=1}^n p_{i,j} = 1$).

The individual entries $p_{i,j}$ of the transition matrix have the following values:

$$p_{i,j} = \begin{cases} 1/2, & \text{for } i = 1, 2, \dots, n-1 \text{ and } j = i+1 \\ 1/2, & \text{for } i = 1, 2, \dots, n-1 \text{ and } j = 1 \\ 1, & \text{for } i = n \text{ and } j = n \\ 0, & \text{otherwise.} \end{cases} \quad (\text{A.2})$$

This allows us to determine the probability of finding a sequence of n consecutive negative or positive channels in a spectrum with N channels. We start in state 1 (the first spectral channel has either a positive or a negative value) and need to determine the probability of being in state n (corresponding to a sequence of n spectral channels with either positive or negative values) after $N - 1$ Markov chain steps. *This probability is given by the $p_{1,n}$ entry of the one-step transition matrix of the form $n \times n$ raised to the power of $N - 1$.* We can thus compute the probability for any sequence of n consecutive positive or negative channels in a spectrum with N_{chan} spectral channels with random values.

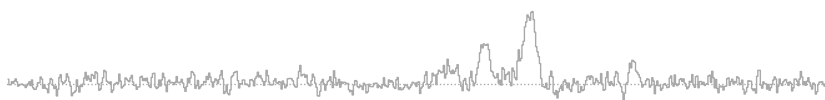
Let us illustrate this with the example of a Markov chain for 4 consecutive negative or positive channels. In this case the Markov chain has a state space of $\{1, 2, 3, 4\}$ and the transition matrix has the following form:

$$P_{i,j} = \begin{pmatrix} 1/2 & 1/2 & 0 & 0 \\ 1/2 & 0 & 1/2 & 0 \\ 1/2 & 0 & 0 & 1/2 \\ 0 & 0 & 0 & 1 \end{pmatrix} \quad (\text{A.3})$$

In state 1 (which corresponds to row $i = 1$ of the transition matrix) we have a sequence of one positive or negative channel and we will always start with this state or revert to this state if the sign between neighbouring channels changes before we reached the full sequence of four consecutive channels. In state 2 (row $i = 2$) and state 3 (row $i = 3$) we have a sequence of two and three positive or negative channels, respectively. State 4 (row $i = 4$) is the absorbing final state, where we reached four consecutive positive or negative channels. The individual column entries of each row then give the probabilities of moving to a new state. In our example, the transition matrix element $p_{1,2}$ gives the probability of moving from state 1 to state 2 ($p_{1,2} = 1/2$), and the element $p_{4,3}$ gives the probability of moving from state 4 to state 3 ($p_{4,3} = 0$).

In our example we always start out with a spectral channel that has either a positive or negative value, so state 1 is just a sequence of 1 positive or negative channel. For state 1, there is a probability of $1/2$ that the system stays in state 1 (if the value of the next channel changes sign) or that it moves to state 2 (row $i = 2$), in which we have two consecutive channels with the same sign. For state 2 and state 3, there is again a probability of $1/2$ that the channel value changes sign and the system moves back to state 1, and a probability of $1/2$ that it moves to state 3 or the absorbing state 4, respectively.

Figure A.1 shows Markov chain results for 4 consecutive positive or negative channels in a sequence of 4 or 10 channels with random values (left and right panel, respectively). These matrices were obtained by raising the one-step transition matrix



0.5	0.25	0.125	0.125	0.291	0.158	0.086	0.465
0.375	0.25	0.125	0.25	0.244	0.133	0.072	0.551
0.25	0.125	0.125	0.5	0.158	0.086	0.047	0.709
0	0	0	1	0	0	0	1
N = 4				N = 10			

FIGURE A.1: One-step Markov chain results for 4 consecutive negative or positive spectral channels in a sequence of 4 (*left*) or 10 (*right*) channels with random values. The value highlighted in blue gives the probability that 4 consecutive channels in the respective sequence are either positive or negative.

given in A.3 to the power of 3 and 9, respectively. The last element in the first row of the matrices (highlighted in blue) gives the respective probabilities to get 4 consecutive positive or negative channels in random sequences of 4 or 10 channels.

Given the random fluctuations of the noise, it becomes clear that the more spectral channels there are, the higher the probability of getting a sequence of n channels with positive or negative value. For example, the probability of having a sequence of ten consecutive positive or negative channels in a spectrum of 100 channels is 0.088. If the number of spectral channels doubles to 200, the probability of getting a sequence of ten consecutive positive or negative channels increases to 0.173.

The noise estimation routine of GAUSSPY+ uses a user-defined probability threshold P_{Limit} (default value: 2%) to decide which features get masked out for the noise calculation in a spectrum with N_{chan} channels. We use an iterative approach to calculate the minimum necessary number of consecutive positive or negative spectral channels n for which $p_{1,n} < P_{\text{Limit}}$. We start by constructing a transition matrix for $n = 2$ and determine the $p_{1,n}$ value of $P^{N_{\text{chan}}-1}$. If $p_{1,n} > P_{\text{Limit}}$ we increase n by one and repeat the calculation. We stop these iterations once $p_{1,n} < P_{\text{Limit}}$ and the final value of n determines the minimum number of consecutive positive or negative channels a feature has to have to get masked out. For example, for a spectrum with 700 spectral channels, features with more than 15 consecutive positive or negative spectral channels have a probability of less than 2% to be caused by random noise fluctuations and will be thus masked out in the noise calculation routine.

A.2 TESTING GAUSSPY+ ON SYNTHETIC SPECTRA

A.2.1 Sample of synthetic spectra

We created four different samples of 10 000 synthetic spectra each, to mimic expected properties of spectra (see Fig. A.2 for examples of each sample):

A: White noise only.



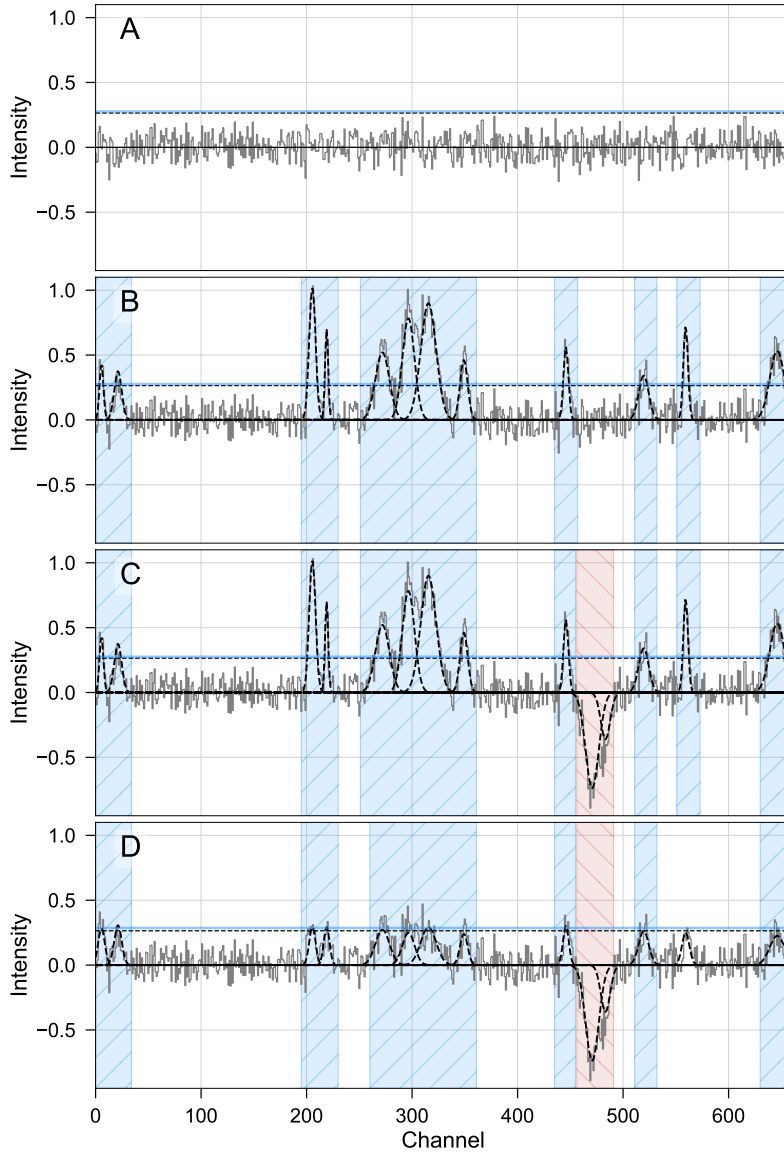


FIGURE A.2: Example spectra from the four samples of synthetic spectra (A–D) used to test the performance of GAUSSPY+. Black dashed lines indicate individual Gaussian components of the signal and negative noise spikes. Shaded areas indicate intervals that GAUSSPY+ classified as signal intervals (blue) and noise spikes (red). The horizontal dashed black and blue solid lines show a S/N threshold of 3 based on the true noise and the estimated noise by GAUSSPY+, respectively. The noise is the same in all four panels.



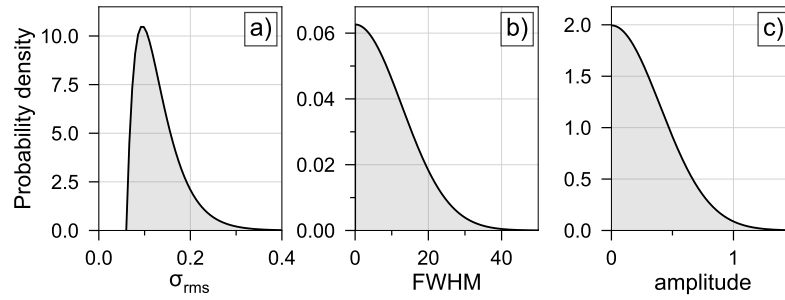


FIGURE A.3: Probability distribution functions for σ_{rms} (left), FWHM (middle), and amplitude values (right). For the synthetic spectra, these distributions were randomly sampled to obtain the noise and Gaussian components of the signal.

- B: White noise and signal. For spectra in this sample up to 12 Gaussian components ('signal') were added to the white noise of the spectra from sample A.
- C: White noise, signal, and negative noise spikes. For spectra in this sample one or two negative Gaussian components ('noise spikes') were added to the spectra from sample B to mimic instrumental artefacts.
- D: White noise, weak signal, and negative noise spikes. For spectra in this sample the positive Gaussian components from sample C had their amplitudes reduced. The signal peaks can thus be hidden in the noise, which makes the decomposition very challenging.

The synthetic spectra were set up to closely mimic spectra from the GRS data set with regards to the number of spectral channels (659), and expected noise and signal properties. The σ_{rms} value used to generate the white noise was randomly sampled from a Gamma distribution of the form

$$p(x) = x^{k-1} \frac{e^{-x/\theta}}{\theta^k \Gamma(k)}, \quad (\text{A.4})$$

with $k = 2$, and $\theta = 0.35$. To closely mimic the noise distribution of the GRS (see Fig. 8 from Jackson et al., 2006) we shifted the distribution by a value of 0.06 and scaled it by a factor of 0.1 (panel a in Fig. A.3). The minimum σ_{rms} value of our sample is 0.06 K and we limited the maximum σ_{rms} value to 0.4 K.

The parameters of the Gaussian components of the signal were randomly sampled from distributions set up to resemble the signal peaks observed in the GRS data set. We sampled the FWHM values from a standard normal distribution scaled by a factor of ~ 13 (panel b in Fig. A.3). We limited the FWHM to a maximum value of 50 spectral channels. We sampled the amplitude values from another standard normal distribution scaled by a factor of 0.4 (panel c in Fig. A.3). We limited the amplitude range to values of $[3.5 \times \sigma_{\text{rms}}, 2.5]$. We sampled the mean values of the Gaussians from a uniform distribution over all 659 spectral channels. For each spectrum, we required for every Gaussian signal component i that: its significance value \mathcal{S} (Sect. 2.4.1.3) had to be > 6 ; its mean position μ_i had to be at a minimum distance of Θ_j to the mean position μ_j of the closest Gaussian signal component j ,



where Θ_j is the FWHM of the Gaussian component j ; its FWHM value Θ_j had to be < 20 channels if its amplitude value a_j was > 1 . The last condition was implemented to exclude components with both high amplitude values and broad linewidths. This exclusion of the strongest components was only done to create a more challenging setup for the decomposition. Data sets with low to moderate spatial resolution such as GRS are likely to contain such strong features that can be caused by the broadening of lines due to the large spatial beam size and large distances to the emitting physical objects. However, these strong emission lines are fitted well with GAUSSPY and GAUSSPY+ in case no strong blending with other lines is present, as is the case for our samples of synthetic spectra.

The parameters for the negative Gaussian components of the noise spikes were randomly sampled in mean position, amplitude, and FWHM from uniform distributions within the limits $[0, 659]$, $[-4 \times \sigma_{\text{rms}}, -1.5]$, and $[1, 20]$, respectively. We required that the noise spikes were placed at least a distance of Θ_j from the closest Gaussian signal component j . The amplitude values of the Gaussian components for sample D were sampled from a uniform distribution with the range $[2.5 \times \sigma_{\text{rms}}, 3.5 \times \sigma_{\text{rms}}]$.

A.2.2 Performance of the automated noise estimation routine

Here we report results of the automated noise estimation of GAUSSPY+ (Sect. 2.3.1) on the synthetic spectra from samples A–D discussed in the last section. We used the default settings for the noise estimation routine ($P_{\text{Limit}} = 2\%$, $N_{\text{pad}} = 5$), which means that sequences above 15 consecutively positive or negative spectral channels get masked out for the noise estimation in addition to peaks that show high amplitude values.

Figure A.4 shows probability density distributions of the relative errors of the σ_{rms} values determined by GAUSSPY+. These relative errors were obtained by comparing the estimated σ_{rms} values to the true noise values ($\sigma_{\text{rms, true}}$) used to generate the white noise for all four samples (A–D). For comparison, we also show the probability distribution obtained if all channels in the spectra of sample A are used for the calculation of the σ_{rms} value (solid black line). This distribution corresponds to the best we could do for the calculation of the σ_{rms} value and its spread around the $\sigma_{\text{rms, true}}$ value reflects inherent random effects of the noise that would be decreased if the number of spectral channels were increased.

For the majority of the synthetic spectra the noise estimation performed very well with the median of the distribution (dotted vertical line) being very close to the $\sigma_{\text{rms, true}}$ value and the interquartile ranges (hatched areas) within relative errors of $\pm 3\%$ and $\pm 4\%$ for samples A–C and sample D, respectively. Since the noise estimation always excludes the spectral channels with the highest negative and positive values (see Sect. 2.3.1), it tends to slightly underestimate the σ_{rms} value for spectra containing only noise (sample A). For sample B (white noise and signal), nearly all estimated σ_{rms} values are within $\pm 10\%$ of $\sigma_{\text{rms, true}}$. For the spectra of sample C the performance of the noise calculation is almost as good, which demonstrates that our method is robust to the presence of negative noise spikes or similar instrumental artefacts. As expected, for sample D (white noise, weak signal, noise spikes) we tend to overestimate the σ_{rms} values. However, given that a fraction



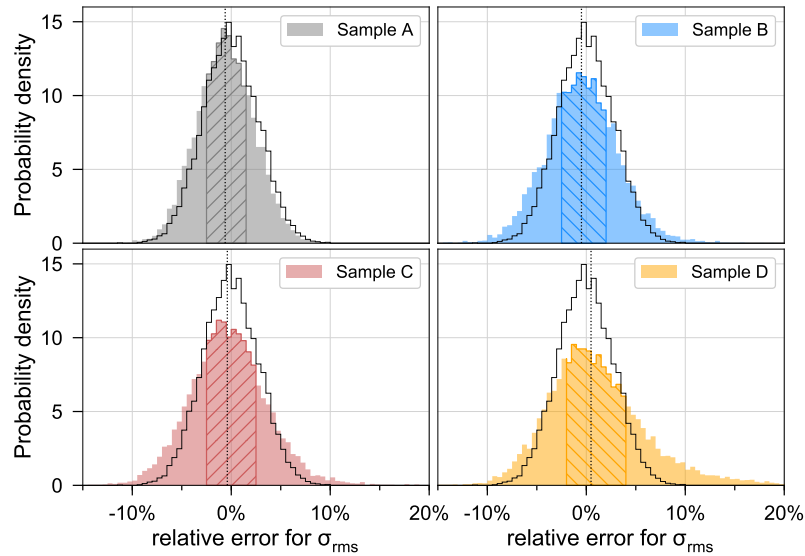


FIGURE A.4: Probability density distributions showing the results of our automated noise estimation for the sample of synthetic spectra containing: only white noise (upper left panel); white noise and signal (upper right panel); white noise, signal, and negative noise spikes (lower left panel); white noise, weak signal, and negative noise spikes (lower right panel). The abscissa shows the determined root-mean-square noise value σ_{rms} normalised by the true root-mean-square noise value $\sigma_{\text{rms,true}}$ that was used to generate the white noise. Hatched areas and vertical dotted lines show the respective interquartile ranges and median value of the respective distributions. The black solid line shows the distribution obtained by using all spectral channels from sample A for the noise calculation. See App. A.2.2 for more details.

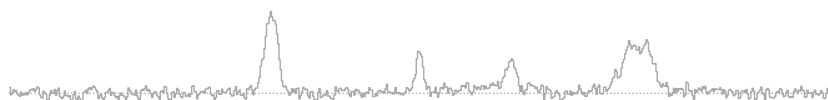
of the signal peaks in these spectra is buried within the noise, the noise calculation still performs very well, with σ_{rms} values within $\pm 10\%$ of $\sigma_{\text{rms,true}}$ for about 93% of the spectra.

A.2.3 Performance of the identification of signal intervals

In this section we report on the results of the automated identification of signal intervals of GAUSSPY+ (Sect. 2.3.2) on our samples of synthetic spectra (App. A.2.1). We used the default settings of GAUSSPY+, with $S/N_{\text{min}} = 3$, $\mathcal{S}_{\text{min}} = 5$, $N_{\text{min}} = 100$, and $N_{\text{pad}} = 5$.

For sample A, whose spectra contain no signal, the signal identification had a false positive rate of 0.01%. That means out of a sample of 10 000 spectra with white noise there was only a single spectrum for which a signal interval was incorrectly identified.

The left panel in Fig. A.5 shows the cumulative percentage of the synthetic spectra as a function of unidentified spectral channels that contain true signal. We define the interval of channels containing true signal as all channels within $\mu_i \pm \Theta_i$ for a true Gaussian signal component i . For $\sim 90\%$ of the spectra in sample B and C, the fraction of unidentified spectral channels containing signal is $< 10\%$. In case of weak signal (sample D), the percentage of unidentified spectral channels with signal is still $< 20\%$ for $\sim 90\%$ of the spectra. This performance is very good, given that many of



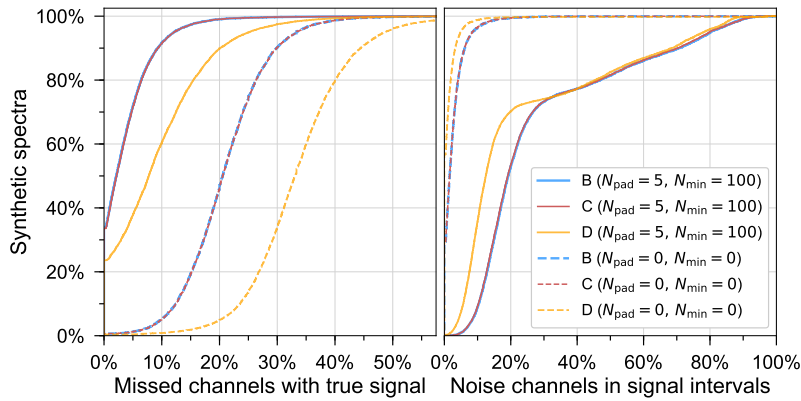


FIGURE A.5: Results of the signal interval identification of GAUSSPY+ for our samples of synthetic spectra. *Left*: Cumulative percentage of the synthetic spectra showing the fraction of unidentified spectral channels containing true signal. *Right*: Cumulative percentage of the synthetic spectra showing the fraction of identified signal interval channels corresponding to noise. See App. A.2.3 for more details.

the signal peaks in sample D are by construction nearly indistinguishable from noise features (with their amplitude values ranging from only $2.5 \times \sigma_{\text{rms}}$ to $3.5 \times \sigma_{\text{rms}}$). The dashed lines indicate runs of the signal interval identification, for which we set the N_{pad} and N_{min} keywords to zero, meaning that there are no channels added on either side of the identified signal intervals. The left panel in Fig. A.5 demonstrates that we would miss a larger fraction of spectral channels containing true signal by setting N_{pad} and N_{min} to zero.

The right panel in Fig. A.5 shows the cumulative percentage of the synthetic spectra as a function of the fraction of noise channels included in the identified signal intervals, again for the two runs in which we vary the N_{pad} and N_{min} values as for the left panel. If N_{pad} and N_{min} are set to zero, only a very small fraction of noise channels is included in the estimated signal intervals. As expected, this fraction increases if we extend the signal intervals on both sides by $N_{\text{pad}} = 5$ and require that the signal intervals contain a minimum number of channels per spectrum of $N_{\text{min}} = 100$. However, this has no negative impact on the decomposition, since the signal intervals are only used in the goodness of fit calculations. It would be more problematic if we set N_{pad} and N_{min} to zero, because in that case we would miss a higher fraction of real signal, which would not be considered in the goodness of fit estimates.

We thus conclude that our method to estimate signal intervals works well. This good performance of the signal interval determination is also illustrated in Fig. 2.17, Fig. A.2, and Fig. A.8, where the estimated signal intervals are indicated with the blue shaded areas.

A.2.4 Performance of the masking of noise artefacts

In this section we report on the performance of GAUSSPY+ in automatically masking negative noise spikes (Sect. 2.3.3) for our samples of synthetic spectra (App. A.2.1).

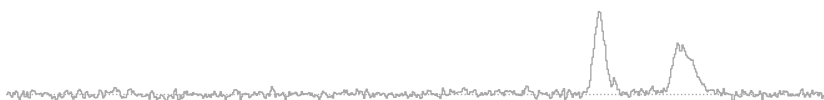


TABLE A.1: Comparison of obtained smoothing parameter values α_1 and α_2 and the corresponding F_1 score for different training sets.

Sample	α_1	α_2	F_1 score [%]
B	2.08	4.91	82.4
B (true)	2.03	4.91	82.7
C	2.11	4.89	79.0
C (true)	2.07	4.87	79.6
D	3.23	4.98	69.0
D (true)	3.44	5.09	71.5

We used the default settings for the S/N_{spike} parameter that masks out all spectral features that contain negative values below $-5 \times \sigma_{\text{rms}}$.

Our routine managed to correctly identify 99.4% and 98.8% of all noise spikes with minimum values $< -5 \times \sigma_{\text{rms, true}}$ in the synthetic spectra of samples C and D, respectively. The small fraction of unidentified noise spikes with S/N ratios $< -5 \times \sigma_{\text{rms, true}}$ was due to overestimates of the σ_{rms} values. The fraction of false positives—that means noise fluctuations that were incorrectly identified as noise spikes—was 0.02% for both samples. The performance of the masking of noise artefacts is also illustrated in Fig. A.2 and Fig. A.8, where the shaded red areas indicate the spectral channels identified as noise spikes.

A.2.5 Performance of the automated decomposition routine for the training set

As discussed in Sect. 2.3.4, GAUSSPY+ can supply a training set for the determination of the best smoothing parameters for a data set. Here we discuss the performance results of the automated decomposition of spectra for the training set. We quantify the performance by comparing the resulting smoothing parameters α_1 and α_2 obtained from the decomposed training set with the smoothing parameters obtained for the same training set if the true known Gaussian parameters are supplied. For the training sets, we randomly selected 250 synthetic spectra from samples B–D (App. A.2.1). We then created two training sets for each sample by: i) decomposing the spectra via the method discussed in Sect. 2.3.4; ii) supplying the true parameters for the Gaussian components of the synthetic spectra.

Table A.1 lists the result of the gradient descent technique applied by GAUSSPY to determine the best smoothing parameters for the training sets. The run in which the true values of the Gaussian components were supplied in the training set is indicated with '(true)'. For all runs the S/N ratio for the spectrum and its second derivative were set to $\text{SNR}_1 = \text{SNR}_2 = 3$.

For sample B and C the runs for both training sets converge to essentially the same smoothing parameters α_1 and α_2 . For sample D, the value for α_1 inferred from the training set decomposed with our routine is slightly smaller than the parameter we get from the true values. We tested the effect of this change by repeating the GAUSSPY decomposition for sample D with the smoothing parameter



values $\alpha_1 = 3.44$ and $\alpha_2 = 5.09$. We then recomputed the percentage of correct identifications (30.4%) and false positives (6.9%) in the same way as for the values inferred from the decomposed training set given in Table 2.1 (29.4% and 6.5% for the correct identifications and false positives, respectively). This shows that the slight difference in the smoothing parameter inferred for sample D has only a limited impact on the GAUSSPY decomposition results.

The comparison in Table A.1 thus demonstrates that the automated method for creating training sets that is implemented in GAUSSPY+ works well. We thus conclude that smoothing parameters close to the optimal value can be obtained via this method.

A.2.6 Performance of the Gaussian decomposition

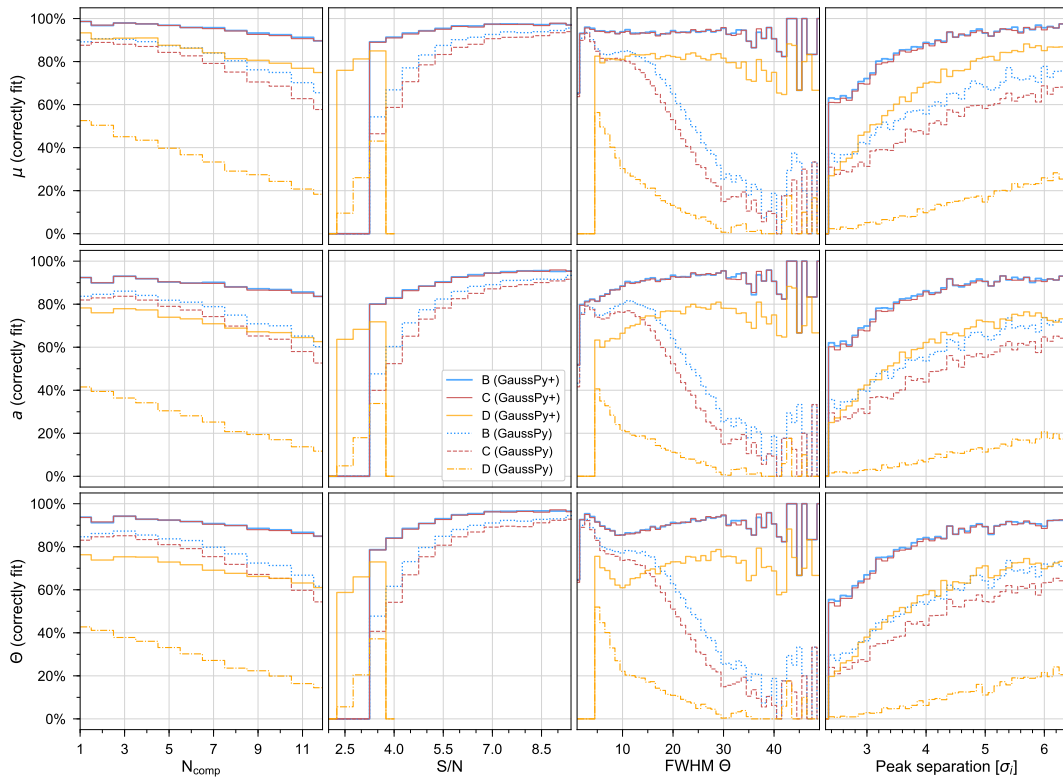


FIGURE A.6: Performance of the GAUSSPY and GAUSSPY+ decomposition runs for samples of synthetic spectra. The ordinate in the upper, middle, and lower panels show the fraction of correctly fit Gaussian mean positions, amplitude values, and FWHM values, respectively, plotted against the number of true Gaussian components, the S/N ratio, the true FWHM values, and the peak separation in the *left*, *centre left*, *centre right*, and *right* panels, respectively. See App. A.2.6 for more details.

Here we compare the performance of the decomposition of the original GAUSSPY algorithm and the improved fitting routine of GAUSSPY+ (Sect. 2.4.3) on our samples of synthetic spectra (App. A.2.1). First, we explore how the performance of the decomposition results of GAUSSPY and GAUSSPY+ for samples B–D of the synthetic spectra varies with the number of components in the spectrum, the S/N ratio, the



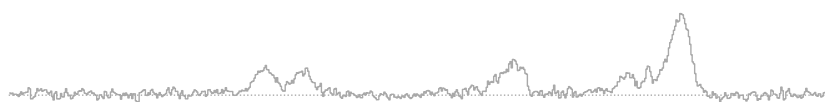
width of the signal peaks, and the separation between signal peaks. We counted the mean position of fitted Gaussian components as correct if their values were within ± 2 channels of the peak positions of the true underlying signal peak. We counted amplitude and FWHM parameters as correctly fit if their values were within $\pm 20\%$ of the true value in addition to the requirement that the fitted mean position is within ± 2 channels of the true position of the component. Since for narrow signal peaks 20% of the FWHM can amount to only a fraction of a channel we additionally count a FWHM parameter as correctly fit if its absolute error is within ± 2 spectral channels of the correct FWHM value.

The left panels in Fig. A.6 show the percentage of correctly identified Gaussian fit parameters (mean position, amplitude and FWHM value from top to bottom, respectively) as a function of the number of components in the spectrum. The GAUSSPY+ decomposition shows a very stable performance that is not much affected by a higher number of components or the existence of noise spikes. Even in the case of signal peaks very close to the detection threshold (sample D) it still yields a good performance. In contrast, the ability of the original GAUSSPY algorithm to correctly decompose the components deteriorates by about 10 – 20% for the synthetic spectra of sample B and C, and up to 30% for sample D the more complex the spectra are.

The centre left panels in Fig. A.6 show the number of correctly determined Gaussian fit parameters as a function of the S/N ratio. As expected, the performance results strongly depend on the S/N ratio. However, compared to the results of the original GAUSSPY algorithm, the GAUSSPY+ decomposition gives a significantly better performance, especially in determining correct fit parameters for signal peaks with S/N values ≤ 3 , which can be heavily affected by the noise.

The centre right panels in Fig. A.6 show the number of correctly determined Gaussian fit parameters as a function of the FWHM values of the true signal peaks. In contrast to the GAUSSPY fit results, the performance of the GAUSSPY+ decomposition does not deteriorate with increasing width of the signal peaks, which means that both narrow and broad components are well fitted. The decomposition with the original GAUSSPY algorithm shows a much stronger dependence on the linewidth, and has difficulties in correctly decomposing broader components.

Finally, the right panels in Fig. A.6 show the percentage of correctly determined Gaussian fit parameters of signal component i as a function of peak separation to its closest neighbouring signal component j . This peak separation is given as multiples of the standard deviation σ_i of component i . As expected, the performance of the decomposition with GAUSSPY+ decreases the closer two components are placed to each other as it gets exceedingly more difficult to correctly deblend them. Nonetheless, the decomposition with GAUSSPY+ manages to fit about $\sim 60\%$ of even the most heavily blended components in sample B and C correctly, which exceeds the performance of GAUSSPY by more than 20%. For the challenging weak signal peaks of sample D, the fraction of correctly decomposed components that were blended the most was lower ($\sim 20\text{--}30\%$). However, the percentage of correct fits increases already significantly for moderate peak separations of $\sim 3\text{--}4 \times \sigma_i$ and reaches a stable high performance for even larger peak separations. We test the performance of GAUSSPY+ for blended components in more detail in App. A.2.7.



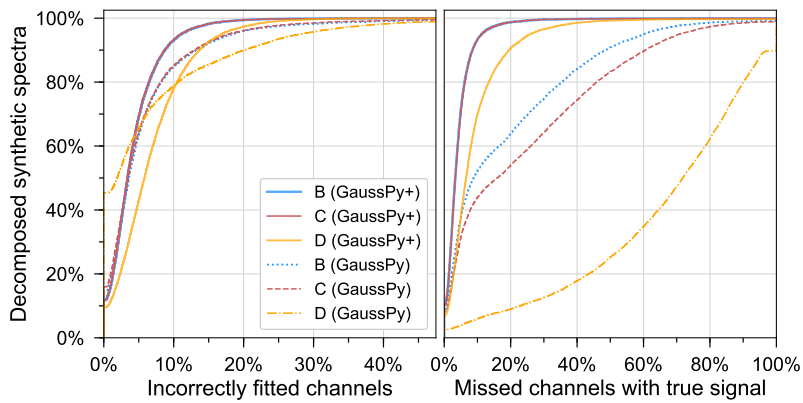


FIGURE A.7: Comparison of the decomposition results obtained with GAUSSPY and GAUSSPY+ for our samples of synthetic spectra. *Left*: Cumulative percentage of decomposed spectra showing the fraction of spectral channels that were incorrectly fit. *Right*: Cumulative percentage of decomposed spectra showing the fraction of spectral channels containing true signal that were not fit. See App. A.2.6 for more details.

We also note that the GAUSSPY decomposition results deteriorate in case of the presence of negative noise spikes. However, the performance of GAUSSPY+ is unaffected by these negative noise spikes, as can be seen by the almost overlapping blue and red solid lines in all panels shown in Fig. A.6.

We tried to choose fair criteria for the definition of when we count components in Fig. A.6 as correctly fit. Given that many of our signal peaks show only low to moderate S/N values, noise properties might already severely affect their lineshapes, so stricter criteria would not accept decomposition results that a human would likely classify as correctly fit. Conversely, more relaxed criteria could allow too large absolute deviations from the correct parameter values. However, we repeated the analysis of Fig. A.6 for both stricter and more relaxed criteria and we do recover the same general trends: performance results that exceed the decomposition of GAUSSPY and are almost unaffected by the number of components in the spectrum, the FWHM value or the presence of noise spikes, and increase with higher S/N values or larger peak separations.

Next, we compare the number of fitted spectral channels with the channels containing true signal for the GAUSSPY and GAUSSPY+ decompositions. We define the interval of fitted channels or channels containing true signal as all channels within $\mu_i \pm \Theta_i$ for a fitted or true Gaussian component i . The left panel in Fig. A.7 shows the cumulative percentage of decomposed synthetic spectra as a function of the percentage of incorrectly fitted spectral channels. Both GAUSSPY and GAUSSPY+ show a very good performance with a low fraction of false positives. The improved results of GAUSSPY+ are due to its ability to more correctly identify individual signal peaks where GAUSSPY fits a single component over multiple peaks.

The right panel in Fig. A.7 shows the cumulative percentage of decomposed synthetic spectra as a function of spectral channels containing true signal that were not fit by Gaussian components. For all three samples of synthetic spectra GAUSSPY+ significantly improves the decomposition results of GAUSSPY by fitting



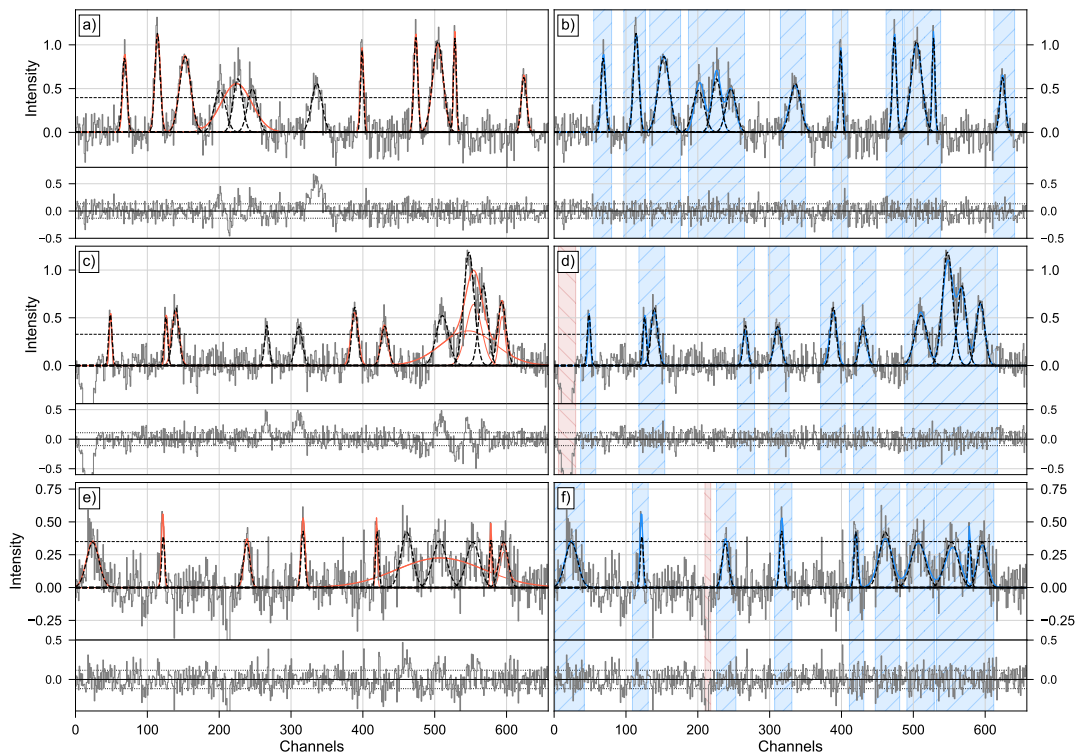


FIGURE A.8: Example spectra illustrating the better performance of the improved fitting routine of GAUSSPY+ (Sect. 2.4.3) compared to the original GAUSSPY algorithm. The upper (*a*, *b*), middle (*c*, *d*), and lower (*e*, *f*) panels show synthetic spectra from samples B, C, and D, respectively. The panels on the left (*a*, *c*, *e*) show the decomposition results obtained with the original GAUSSPY algorithm and panels on the right (*b*, *d*, *f*) show the corresponding decomposition results from the improved fitting routine of GAUSSPY+. The correct individual Gaussian components are indicated in dashed black lines; individual Gaussian components and their combined intensity from the decomposition run with GAUSSPY and GAUSSPY+ are indicated in solid red and blue lines, respectively. The smaller panels below the spectrum show the corresponding residual with the dotted black lines indicating values of $\pm\sigma_{\text{rms}}$. Dashed black horizontal lines indicate a S/N ratio of 3. Blue and red shaded areas show the automatically identified signal and noise spike intervals, respectively.

more components at their correct positions. The improvement is especially striking in case of the spectra from sample D that contain only weak signal.

Figure A.7 thus illustrates that GAUSSPY+ manages to fit significantly more channels containing true signal than GAUSSPY. Moreover, GAUSSPY+ does not fit too many noise features.

The improved performance of GAUSSPY+ is further illustrated in Fig. A.8, which contrasts decompositions of the original GAUSSPY algorithm (left panels) with decompositions obtained with our improved fitting routine (right panels) for synthetic spectra from samples B–D. Figure A.8 shows that the original GAUSSPY algorithm sometimes has problems in decomposing mildly blended signal peaks and signal peaks at the edge of the spectrum, whereas GAUSSPY+ has no problems in fitting those components correctly. The GAUSSPY+ algorithm also does a good job of identifying signal peaks and noise artefacts.



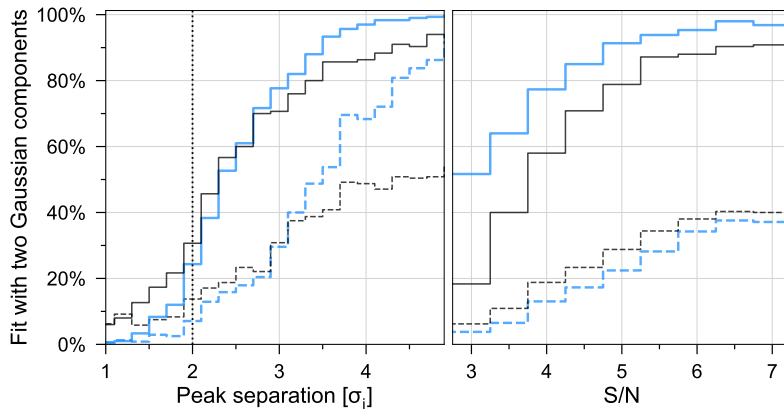


FIGURE A.9: Decomposition results of a sample of synthetic spectra with two identical Gaussian components, whose S/N ratio, peak separation, and FWHM parameter were varied. Blue and black lines indicate the results obtained for the decomposition runs with GAUSSPY+ and GAUSSPY, respectively. *Left*: Percentage of fitted spectra with two Gaussian components as a function of peak separation for S/N ratios < 5 (dashed lines) and ≥ 5 (solid lines). The dotted vertical line indicates the separation threshold for two identical Gaussian components without noise. *Right*: Percentage of fitted spectra with two Gaussian components as a function of their S/N ratio for peak separations of $< 3 \times \sigma_i$ (dashed lines) and $\geq 3 \times \sigma_i$ (solid lines).

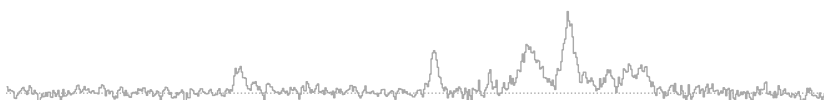
A.2.7 Recovery of identical components with different S/N ratios and degrees of blendedness

Here we quantify how well the improved fitting algorithm of GAUSSPY+ (Sect. 2.4.3) is able to recover blended components. For this, we create a sample of synthetic spectra that contain two identical Gaussian signal peaks. We vary the parameters of the signal peaks between the following values: $[3, 3.5, \dots, 7]$ for the S/N ratio; $[5, 10, \dots, 30]$ spectral channels for the FWHM; and $[1, 1.2, \dots, 5] \times \sigma_i$ for the separation of the mean positions of the signal peaks. We created ten spectra of each possible parameter combination for a total of 11 340 spectra and added different noise sampled from a σ_{rms} value of 0.13 to each spectrum¹.

We constructed a training set by randomly selecting 500 spectra of different parameter combinations and inferred smoothing parameters α_1 and α_2 by supplying the true values of the signal peaks. Since our aim here is to establish the performance of our decomposition given ideal settings, we supplied the true parameter values as solutions instead of decomposing the training set with the method described in Sect. 2.3.4. From this training set we inferred smoothing parameters values of $\alpha_1 = 2.16$ and $\alpha_2 = 6.19$ that led to an F₁ score of 76.8%. We then performed decompositions with the original GAUSSPY algorithm and the improved fitting routine of GAUSSPY+, leaving all the settings at their default values.

Figure A.9 shows the performance results of the two decomposition runs. The left panel shows the percentage of fits using two Gaussian components as a function of peak separation, split into a sample with low to moderate S/N ratios (< 5 , dashed lines) and high S/N ratios (≥ 5 , solid lines). The vertical dotted line indicates the

¹ The number of spectral channels (659) and the σ_{rms} value were again chosen to closely mimic properties of the GRS data set.



separation threshold for two identical Gaussian components in case of no noise (see also Sect. 2.4.2.3). For low to moderate S/N ratios it becomes very difficult to differentiate two similar Gaussian components if their peak positions are separated by less than about 3.5 times their standard deviation. For higher S/N ratios identical signal peaks can be located closer together until they essentially become indistinguishable from a single component. For the decomposition with GAUSSPY+, the signal peaks need to have a distance to each other of more than $\sim 2.5 \times \sigma_i$ until the majority of signal peaks will be fit with two components. The GAUSSPY+ algorithm by design fits preferentially a single instead of two components if the peaks are only separated closely, as in such cases a fit with a single Gaussian component will already be a good match to the combined signal peaks and the simplest fit solution is preferred without additional information (e.g. from neighbouring fit solutions) to inform the fit. For larger peak separations GAUSSPY+ exceeds the performance of GAUSSPY, especially in the case of low to moderate S/N values.

The right panel of Fig. A.9 shows the percentage of decomposition results using two Gaussian fit components, split into two samples with small ($< 3 \times \sigma_i$, dashed lines) and large ($\geq 3 \times \sigma_i$, solid lines) peak separations. For small peak separations, GAUSSPY and GAUSSPY+ will preferentially fit the signal peaks with a single component, even if the S/N ratio is high. For larger peak separations the two-component fit solution is dominant and the percentage of spectra fit with two components increases significantly for high S/N ratios.

Since the decomposition was performed without any additional knowledge about the signal peaks (as could be imposed by neighbouring spectra in spatially coherent decompositions), it can become very challenging to correctly fit signal peaks with low S/N ratios, as random fluctuations of the noise can significantly change their shape. Moreover, the two identical signal peaks we placed in the spectra will combine to a symmetric peak that might be equally well fit by a single or two components if they are heavily blended. Spectral features of two blended components of different shape will cause an asymmetry that can make it easier to decompose them correctly.

A.3 PERFORMANCE DETAILS FOR GAUSSPY+

A.3.1 Performance and execution time for the decomposition of the training set

We compared the decomposition results and runtime of the SLSQPLSQFITTER fitting routine used to create training sets for GAUSSPY (Sect. 2.3.4) with the runtime of the improved fitting routine of GAUSSPY+ (Sect. 2.4.3). We used both fitting techniques to decompose sample B of our synthetic spectra (App. A.2.1). For both algorithms we distributed the decomposition over 50 CPUs.

In terms of performance the decomposition with the SLSQPLSQFITTER could correctly identify 95.4% of the signal components and had a false positive fraction of 1.5%. Both of these values exceed the corresponding numbers for the results of GAUSSPY+ (93.7% and 1.6%, respectively, see Table 2.1), which confirms that our routine for creating training sets produces high quality decompositions.

Table A.2 lists the results of the execution times: t_{real} is the elapsed wall clock time from start to finish of the execution of the decomposition and t_{CPU} is the total

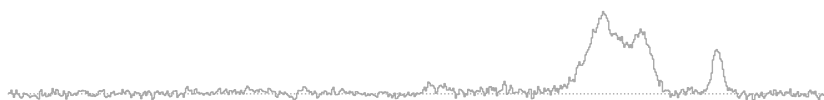


TABLE A.2: Comparison of the execution times for sample B of the synthetic spectra.

	t_{real} [min]	t_{CPU} [min]
SLSQPLSQFITTER	43.06	1868.87
GAUSSPY+	2.59	110.01

TABLE A.3: Comparison of the execution times for the GAUSSPY+ decomposition of the GRS test field.

Method	t_{real} [min]	f_{real} [%]	t_{CPU} [min]	f_{CPU} [%]
Training set creation	0.39	4.5	16.33	21.3
Training	5.61	64.2	20.86	27.2
Preparation	0.08	0.9	0.28	0.4
Decomposition Stage 1	0.32	3.6	9.55	12.4
Decomposition Stage 2	0.44	5.0	8.03	10.5
Decomposition Stage 3	1.91	21.8	16.69	21.8

amount of spent CPU time. These results show that the SLSQPLSQFITTER fitting routine is about an order of magnitude slower than GAUSSPY+, which is why we recommend to use the former routine only for the decomposition of spectra for the training set.

A.3.2 Execution time for the GRS test field

In this section we discuss the execution time of the GAUSSPY+ algorithm for the decomposition of the GRS test field using the default settings of GAUSSPY+ and distributing the computation over 50 CPUs. Table A.3 shows an overview of the execution time for all stages of GAUSSPY+ in terms of wall clock time t_{real} and total CPU time t_{CPU} as well as their respective relative percentages f_{real} and f_{CPU} . The entire GAUSSPY+ decomposition for the GRS test field needed $t_{\text{real}} = 8.74$ min and $t_{\text{CPU}} = 76.74$ min.

Since the total size of the GRS test field (4200 spectra) is relatively small, the creation of the training set and training with GAUSSPY amounted to a significant contribution to f_{real} and f_{CPU} , which would be reduced for larger data sets, where the decomposition steps will need a larger fraction of the total time. We also report the individual times for the execution of the three decomposition stages of GAUSSPY+: the improved fitting routine (Sect. 2.4.3; Stage 1), phase 1 of the spatially coherent refitting (Sect. 2.5.1, Stage 2), and phase 2 of the spatially coherent refitting (Sect. 2.5.2, Stage 3). Execution times for the spatially coherent refitting stages will typically depend on how many criteria are used in the flagging of spectra in Stage 2 and the minimum weight threshold \mathcal{W}_{min} the user selects in Stage 3 (see Fig. A.12).



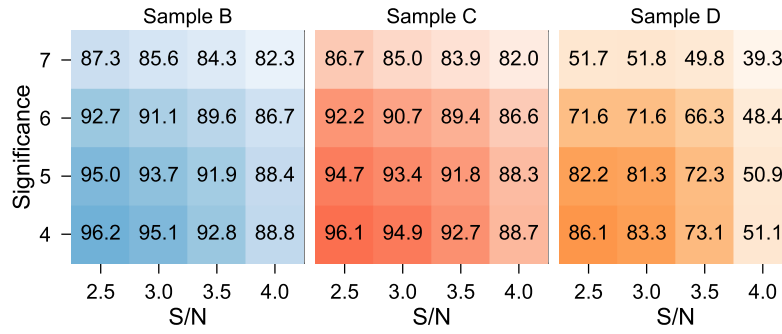


FIGURE A.10: Percentage of correctly identified mean positions of Gaussian components in the decomposition of samples B–D (left to right) with varying values for the minimum S/N ratio and significance parameters.

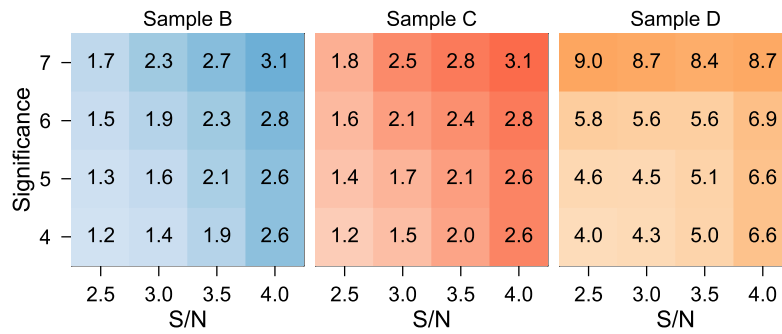


FIGURE A.11: Percentage of incorrectly identified mean positions of Gaussian components in the decomposition of samples B–D (left to right) with varying values for the minimum S/N ratio and significance parameters.

A.3.3 Effect of varying minimum S/N ratio and significance

Here we test how changing the values of the minimum S/N ratio S/N_{\min} and significance parameter \mathcal{S}_{fit} affects the decomposition results for our samples of synthetic spectra (App. A.2.1). We use S/N_{\min} and \mathcal{S}_{fit} values of [2.5, 3, 3.5, 4] and [4, 5, 6, 7] respectively, and perform a decomposition with GAUSSPY+ for every combination of those values (16 in total). For the spectra of sample A that contain only white noise we found that with significance values $\mathcal{S}_{\text{fit}} \geq 5$ no noise features were fitted. For a significance value of $\mathcal{S}_{\text{fit}} = 4$ and S/N_{\min} values of 2.5, 3, 3.5, and 4, GAUSSPY+ incorrectly fitted 38, 31, 21, and 8 noise features, respectively.

For samples B–D we calculated the percentage of correctly and incorrectly fitted mean position values of Gaussian components for each decomposition run, which are shown in Fig. A.10 and Fig. A.11, respectively. We count the mean position of a Gaussian component as correctly detected if it is within ± 2 channels of the true value. If the mean position value of a fitted component was more than 4 channels away from the true mean positions of all signal components in the spectrum we counted it as an incorrect identification. The decomposition with $\mathcal{S}_{\text{fit}} = 5$ and $S/N_{\min} = 3$ corresponds to the GAUSSPY+ run at its default settings we presented in Sect. 2.6. Figure A.10 and Fig. A.11 demonstrate the interdependence between the \mathcal{S}_{fit} and



S/N_{\min} parameters. In general, increasing one of these parameters has adverse effects on the percentage of correct and incorrect detections of Gaussian components in the synthetic spectra of samples B–D. However, this adverse effect can be offset by decreasing the value for the other parameter. The results from Fig. A.11 show that setting the \mathcal{S}_{fit} and S/N_{\min} parameters to higher values can lead to a big increase in incorrectly identified fit components. This increase is due to the large fraction of signal components with low S/N ratios in our synthetic spectra. If we set the S/N_{\min} or \mathcal{S}_{fit} parameters to higher values, those components are either prevented from being fit or are incorrectly fit with one broad component instead of multiple narrower ones.

Figure A.10 and Fig. A.11 also demonstrate that we could have improved the decomposition results reported in Sect. 2.6 by choosing a lower minimum S/N ratio of $S/N_{\min} = 2.5$. In principle we could have even further improved upon that result by also decreasing the required significance value to $\mathcal{S}_{\text{fit}} = 4$, but the results from the decomposition of sample A demonstrate that this setting would already allow the fit of noise features.

Ultimately, the choice for the values of the S/N_{\min} and \mathcal{S}_{fit} parameters needs to be guided by the data set. For the synthetic spectra we used perfect Gaussian noise properties, which will likely not be the case for real observational data. Thus users might want to set higher values for the \mathcal{S}_{fit} parameters to exclude the fitting of noise features, even though it might result in a reduction of fitted weaker signal peaks. We constructed the synthetic spectra of samples B–D to contain a large fraction of signal peaks with amplitudes close to or even below a S/N ratio of 3 to test how well the GAUSSPY+ decomposition with default settings works for weak signal peaks. Decompositions of data sets for which users expect signal peaks with high S/N ratios will thus likely benefit from an increase of the values for the S/N_{\min} and \mathcal{S}_{fit} parameters.

A.3.4 Performance of in-built and optional quality control procedures

Here we discuss the performance of the in-built and optional quality control procedures described in Sect. 2.4.1.1–2.4.1.4 and Sect. 2.4.2.1–2.4.2.3. While we report here only on the performance of the in-built quality criteria for the improved fitting routine, these criteria are also used in all refit attempts in the spatially coherent refitting phases.

For $\sim 34\%$ of the spectra of the GRS test field at least one of the in-built quality control procedures was used to remove one or more components in the decomposition with the improved fitting routine of GAUSSPY+. For sample A–D of the synthetic spectra the percentage of spectra for which components were removed due to failing the in-built quality controls was $\sim 3\%$, 20%, 20% and 22%, respectively. The comparatively larger fraction of spectra with rejected fit components in the decomposition of the GRS test field was mostly due to the presence of low-intensity signal peaks that did not satisfy the criterion for the amplitude value and imperfect noise properties, which led to the fitting of noise peaks that did not satisfy the requirement for the significance value.



TABLE A.4: Number of fit components removed by the in-built quality control procedures for the decomposition of the GRS test field and the synthetic spectra.

	Θ (2.4.1.1) ^a	a (2.4.1.2) ^a	S_{fit} (2.4.1.3) ^a	μ (2.4.1.4) ^a
GRS test field	136	705	1127	16
Sample A	17	7	263	0
Sample B	673	669	836	506
Sample C	690	632	829	492
Sample D	447	585	1975	434

Notes. ^(a) See corresponding section for a description of the parameter.

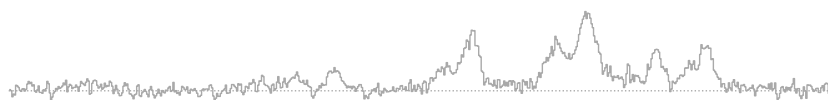
TABLE A.5: Number of new best fit solutions obtained by utilising the optional quality control procedures for the decomposition of the GRS test field and the synthetic spectra.

	neg. res. peak (2.4.2.1) ^a	broad (2.4.2.2) ^a	blended (2.4.2.3) ^a
GRS test field	25	542	14
Sample A	0	0	0
Sample B	133	353	40
Sample C	137	354	49
Sample D	2	683	1

Notes. ^(a) See corresponding section for a description of the parameter.

Table A.4 gives the exact number of fit components that were removed due to the in-built quality controls using the default settings of GAUSSPY+. In general, the significance criterion was most often used and thus is the strictest criterion, followed by the requirement of a minimum S/N value for the fitted amplitude and a minimum value for the fitted FWHM. Since the synthetic spectra were set up to also contain emission in the outermost channels, the criterion checking whether the fitted mean position was within the channel range was also used frequently to correct fit results for these spectra. The sequence of how the in-built quality controls are used matters, as for example a component that already failed the requirements for the amplitude value will not be subjected to the significance criterion anymore (see Fig. 2.3). Thus, had we checked the significance criterion first, it would have been responsible for removing even more components.

Table A.5 lists the number of successful refits based on the optional quality control procedures for refitting negative residual features, broad and blended components for the GRS test field and the four samples of synthetic spectra. The refitting of broad fit components into multiple narrower individual components was the criterion that led to most successful refits, followed by the refitting of components that caused negative residual features. This mostly reflects the generally low S/N values of signal peaks in the spectra, for which GAUSSPY often fits a single broad Gaussian component



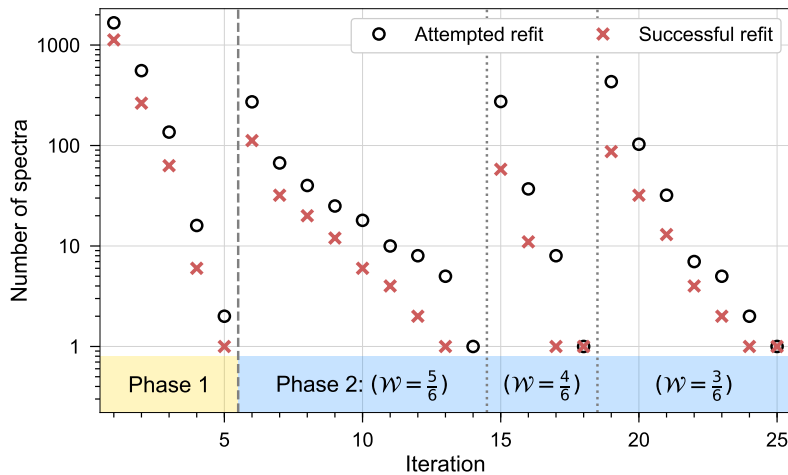


FIGURE A.12: Number of refit attempts and successful refits of spectra of the GRS test field for each iteration in the two phases of the spatially coherent refitting. See App. A.3.5 for more details.

over multiple individual signal peaks (see Fig. A.8). The refitting of features labelled as blended did not yield that many successful refits. The low success rate for refits based on the criterion for blended components is expected for the signal peaks in the synthetic spectra, which were constructed in such a way as to not show heavily blended components. For the GRS test field, deviations of emission lines from a Gaussian shape could have caused the fit of multiple blended components, which resulted in low residuals or AICc values that could not be matched with the fit of a single component.

A.3.5 Refit iterations of the spatially coherent refitting phases

In this section we discuss the performance of the two phases of spatially coherent refitting (Sect. 2.5.1 and 2.5.2). The total number of refit iterations needed in these two phases depends on the size of the spectral cube, the number of flags set in phase 1, and the minimum required weight threshold \mathcal{W} chosen in phase 2.

For the GRS test field, the two spatially coherent refitting phases needed 25 iterations in total to converge to a final fit solution. Figure A.12 shows the number of attempted and successful refits for all iterations. Most of the attempted and successful refits occur in phase 1, which needed 5 iterations. Since in a new iteration we will only refit spectra if they had not been flagged in the previous iteration or at least one of the fit solutions of its neighbours got updated, fewer spectra will be refit in each progressing iteration, which is demonstrated by the steep decrease of refit attempts in Fig. A.12. For example, in the first iteration of phase 1, 1839 out of the 4200 spectra were flagged and selected for refitting. The GAUSSPY+ algorithm tried to refit 1664 of these flagged spectra² with new fit solutions derived from neighbouring spectra, $\sim 68\%$ of which received a new best fit solution. In the second iteration,

² For the remaining 175 flagged spectra no unflagged neighbouring fit solutions were available.



GAUSSPY+ only tried to refit 556 flagged spectra, of which $\sim 47\%$ obtained a new best fit solution.

Figure A.12 further shows the performance of phase 2 of the spatially coherent refitting, which proceeded in three stages, since in the default settings of GAUSSPY+ the minimum required weight threshold \mathcal{W} is reset to a lower value two times. The runtime of phase 2 can therefore be decreased by setting a higher minimum weight threshold (e.g. $\mathcal{W}_{\min} = 4/6$), which should already lead to good spatial coherence between the neighbouring fit solutions.

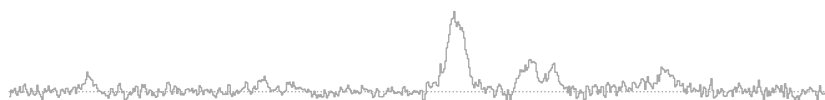
In terms of the total added and subtracted number of components for the decomposition of the GRS test field, phase 1 removed 226 components and added 295, whereas phase 2 subtracted 84 components and added 191 components. About 13% of the added components in phase 2 led to fit solutions being flagged as blended.

A.4 NORMALITY TESTS

As discussed in Sect. 2.4.1.5, as a goodness of fit check we subject the normalised residual to two normality tests to decide whether the data points of the residual are normally distributed and thus consistent with Gaussian noise. We found that a combination of the two-sided Kolmogorov-Smirnov (K-S) test (Kolmogorov, 1933; Smirnov, 1939) and the normality test based on D’Agostino and Pearson (D-P; D’Agostino, 1971; D’Agostino & Pearson, 1973) yielded the most reliable means to detect unfitted signal peaks in the residual.

We tested the performance of each normality test for mock residuals that we created by adding a single Gaussian component to white noise. We used six different combinations of the S/N and significance values for the Gaussian components. We also varied the number of spectral channels between 100–1000 in steps of 100. We produced 1000 spectra for each possible combination of Gaussian signal component and number of spectral channels for a total of 60 000 spectra. We then applied the normality tests to each of these mock residuals to check which test could most reliably identify the leftover signal component by rejecting the null hypothesis of normally distributed residual values.

Figure A.13 shows the performance of the normality tests for the different combinations. On the ordinate we plot the percentage of spectra for which the normality tests yielded p -values below the default threshold in GAUSSPY+ of 1%, which is used as an indication that the residual data points are not normally distributed. The results of the K-S and D-P test are shown in blue and red, respectively. Moreover, we applied both normality tests on the whole residual and only the residual data points within the identified signal ranges, which is indicated by the filled and unfilled symbols, respectively. The black line shows the performance of the null hypothesis testing included in GAUSSPY+, which combines the results of the D-P test applied to the full residual and the results of the D-P and K-S tests applied to only the residual data points within the identified signal intervals. For this combination, we use the smallest p -value resulting from these three normality tests. Figure A.13 demonstrates that this combination results in an increased ability to detect leftover signal peaks in the residual for both narrow and broad components (with low and high significance values, respectively). We are able to identify the majority of residual peaks in every



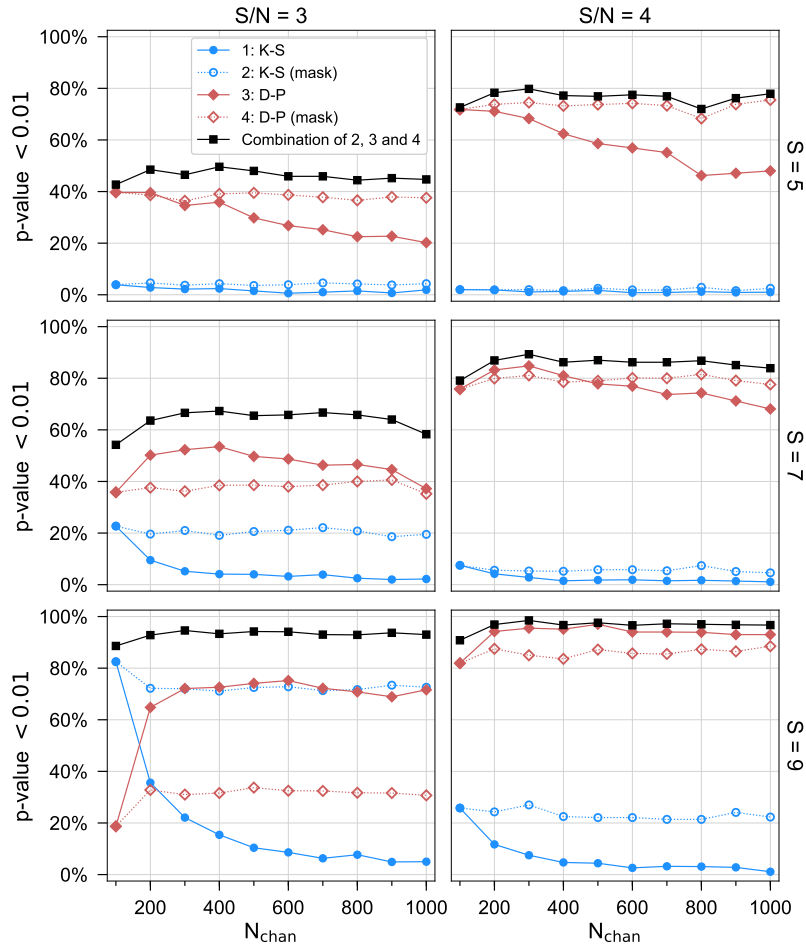


FIGURE A.13: Comparison of the performance of different normality tests for mock residuals as a function of the number of spectral channels. The residuals contain a single Gaussian signal component with a signal-to-noise ratio of 3 or 4 (left and right panels, respectively) and significance values of 5, 7, and 9 (upper, middle, and lower panels, respectively). See App. A.4 for more details.

tested case apart from the one with the weakest component ($S = 5$, $S/N = 3$). The identification fraction reaches nearly 100% for the strongest tested residual peaks ($S = 9$, $S/N = 4$). Moreover, this improved performance is independent of the number of spectral channels. In comparison, the individual results of the K-S and D-P tests show a decreased performance and even a complementary behaviour for broader Gaussian residual peaks with lower S/N values ($S = 9$, $S/N = 3$) and low number of spectral channels (< 300).

To check the fraction of false positives identified by the normality tests, we checked their performance also for Gaussian noise only, for which we removed the signal component from all residuals used in Fig. A.13. We evaluate the spectra again in groups of 1000 spectra and report the median, minimum and maximum false positive rate for all groups as the fraction of spectra for which the hypothesis tests yielded a p -value $< 1\%$ and thus would not pass our criterion for normally distributed residuals.



TABLE A.6: Percentage of false positives identified by the normality tests.

Test	Combination	K-S	D-P
Median	2.2%	5.5%	7.6%
Minimum	1.4%	0.3%	1.1%
Maximum	3.3%	11.5%	13.9%

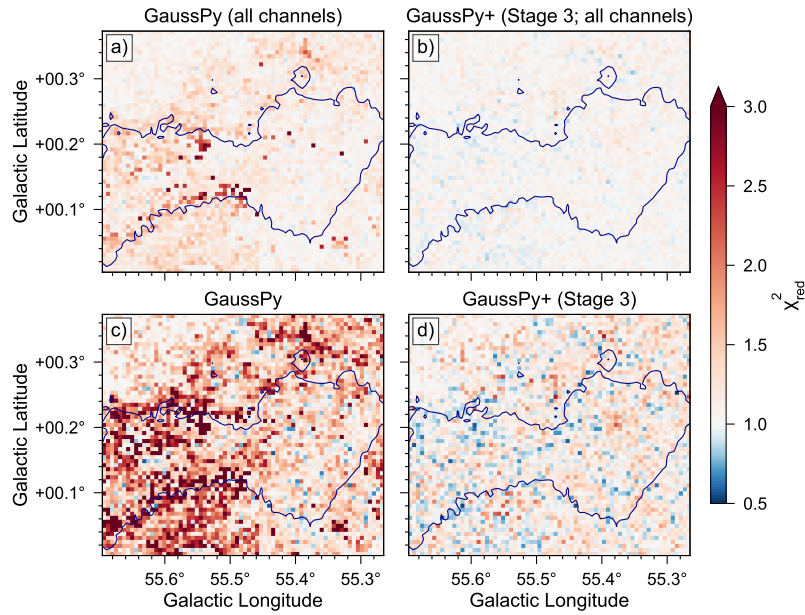


FIGURE A.14: Maps showing the χ_{red}^2 values for the GAUSSPY (left panels) and Stage 3 of the GAUSSPY+ (right panels) decomposition results, calculated by using either all available spectral channels (upper panels) or restricted to the spectral channels estimated to contain signal (lower panels). All panels are overplotted with the contour from panel (b) in Fig. 2.13. Panels (c) and (d) are identical to panels (i) and (l) in Fig. 2.16.

Table A.6 lists the false positive rates. The combination of normality tests as implemented in GAUSSPY+ leads to the best performance over different channel ranges, as evidenced by the reduced median false positive rate compared to the individual normality tests. The K-S and D-P tests produce higher false positive rates with increasing numbers of spectral channels, whereas the combination of the two tests performed best for the highest number of spectral channels we probed.

A.5 χ_{red}^2 CALCULATIONS FOR THE GRS TEST FIELD

A problem in determining the χ_{red}^2 value (Sect. 2.4.1.5) is that it depends on the number of channels in the spectrum. If the spectrum consists of many channels that contain only noise, low χ^2 values and χ_{red}^2 values close to 1 follow even if the performance of the fit is not satisfactory in the part of the spectrum where there is signal.



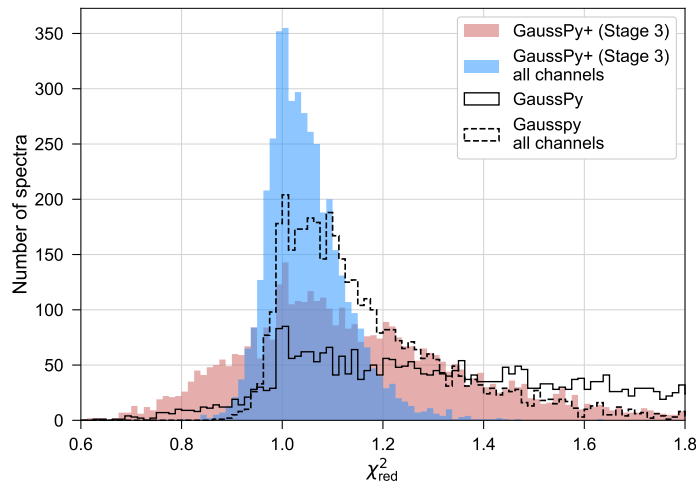


FIGURE A.15: Comparison of the distribution of the χ^2_{red} values for the decomposition results of GAUSSPY and Stage 3 of GAUSSPY+ restricted to spectral channels estimated to contain signal and calculated over the whole spectral range.

To avoid this problem we identify the regions likely to contain signal already in the noise estimation step (see Sect. 2.3.2) and use only these regions for the χ^2_{red} calculations. We also mask negative noise spike features that tend to produce high χ^2_{red} values even for spectra whose signal features were well fit (see Sect. 2.3.3).

To illustrate the importance of restricting the χ^2_{red} calculation to intervals containing signal we recomputed the goodness of fit calculations for the decomposition results of the GRS test field (Sect. 2.7.3) obtained with GAUSSPY and after Stage 3 of GAUSSPY+ by using all available spectral channels. Panels (a) and (b) in Fig. A.14 show the recomputed χ^2_{red} values using all 424 spectral channels. For comparison, we also show the maps of χ^2_{red} values again that were obtained by restricting the goodness of fit calculations to spectral channels estimated to contain signal (panels c and d, which are identical to panels m and p in Fig. 2.16). Figure A.15 gives the corresponding histograms. Both figures clearly illustrate how the goodness of fit values are artificially reduced if most of the spectral channels included in the calculation contain only noise. Using all available spectral channels for the goodness of fit calculations thus makes it more challenging to use the χ^2_{red} values to decide which fit results were not successful.

A.6 GAUSSPY+ KEYWORDS AND DEFAULT VALUES

Table A.7 gives an overview of the parameter settings of GAUSSPY+, listing their corresponding default values and symbols used throughout the text. To get first decomposition results users only need to supply values for the parameters listed under *essential parameters*. In case the decomposition does not yield good results we recommend to first use different values for the *essential parameters*. If this should not improve the results users can vary the parameters listed under *more advanced settings*.

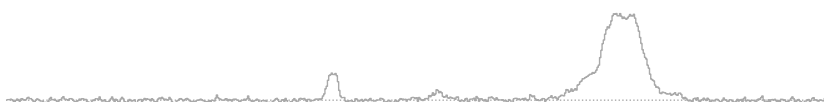


TABLE A.7: GAUSSPY+ keywords mentioned throughout the text.

Symbol	Description	GAUSSPY+ keyword	Default
ESSENTIAL PARAMETERS			
α_1	first smoothing parameter used in GAUSSPY decomposition (Sect. 2.1)	alpha1	None
α_2	second GAUSSPY smoothing parameter; only used in two-phase decomposition (Sect. 2.1)	alpha2	None
S/N_{\min}	minimum S/N ratio for signal peaks in the data (Sect. 2.4.1.2)	snr	3
S_{\min}	Minimum significance value for signal peaks and fitted Gaussian components (Sect. 2.4.1.3)	significance	5
MORE ADVANCED SETTINGS			
$\Delta\mu_{\max}$	maximum difference in offset positions of Gaussian components for grouping (Sect. 2.5.1)	mean_separation	2*
$\Delta\Theta_{\max}$	maximum difference in FWHM values of Gaussian components for grouping (Sect. 2.5.1)	fwhm_separation	4*
Θ_{\min}	minimum value for the FWHM of fitted Gaussian components	min_fwhm	1*
Θ_{\max}	maximum value for the FWHM of fitted Gaussian components	max_fwhm	None*
f_a	multiplication factor to get maximum amplitude limit for fit components	max_amp_factor	1.1
f_{Θ}	factor determining when FWHM of fit components is flagged as broad	fwhm_factor	2
f_{sep}	factor determining the minimum required separation between two fit components (Sect. 2.4.2.3)	separation_factor	$1/\sqrt{2\ln 2}$
f_w	factor that determines the weight given to neighbouring spectra (Sect. 2.5.2)	weight_factor	2
$\mathcal{F}_{\text{neg. res. peak}}$	flag for negative residual features (Sect. 2.4.2.1)	flag_neg_res_peak	True
\mathcal{F}_{Θ}	flag for broad fit components (Sect. 2.4.2.2)	flag_broad	True
$\mathcal{F}_{\text{blended}}$	flag for blended fit components (Sect. 2.4.2.3)	flag_blended	True
$\mathcal{F}_{\text{residual}}$	flag for fit results not passing normality tests (Sect. 2.4.2.4)	flag_residual	True

Table A.7 continued: GAUSSPY+ keywords mentioned throughout the text.

Symbol	Description	GAUSSPY+ keyword	Default
$\mathcal{F}_{N_{\text{comp}}}$	flag for fit results with incompatible number of components w.r.t. neighbours (Sect. 2.4.2.5)	flag_ncomps	True
N_{pad}	number of spectral channels added to the left and right of signal intervals (Sect. 2.3.2)	pad_channels	5*
N_{min}	minimum number of spectral channels the signal intervals in a spectrum must have (Sect. 2.3.2)	min_channels	100*
ΔN_{max}	maximum allowed difference in N_{comp} between fit solution and weighted median number of components determined from all immediate neighbours (Sect. 2.4.2.5)	max_diff_comps	1
ΔN_{jump}	maximum allowed difference in N_{comp} between individual neighbouring spectra (Sect. 2.4.2.5)	max_jump_comps	2
N_{jump}	maximum number of allowed ΔN_{jump} occurrences for a single spectrum (Sect. 2.4.2.5)	n_max_jump_comps	1
P_{Limit}	probability threshold for features of consecutive positive or negative channels to be counted as more likely to be a noise feature (Sect. 2.3.1, App. A.1)	p_limit	0.02
p -value	p -value for the null hypothesis that the residual resembles a normal distribution (Sect. 2.5.1)	min_pvalue	0.01
$S/N_{\text{min,fit}}$	minimum S/N ratio ($= a_i/\sigma_{\text{rms}}$) for fitted Gaussian components (Sect. 2.4.1.2)	snr_fit	None
$S/N_{\text{min,neg}}$	minimum S/N ratio for negative peaks in the spectrum (Sect. 2.4.2.1)	snr_negative	None
S/N_{spike}	S/N threshold for noise spikes (Sect. 2.3.3)	snr_noise_spike	5
SNR_1	S/N threshold used by GAUSSPY for the original spectrum	snr_thresh	None
SNR_2	S/N threshold used by GAUSSPY for the second derivative of the smoothed spectrum	snr2_thresh	None
ζ	minimum number of spectral channels a peak has to contain on either side (Sect. 2.3.4)	order	6*
\mathcal{W}_{min}	minimum weight threshold for termination of phase 2 of spatially coherent refitting (Sect. 2.5.2)	min_weight	0.5

Notes. (*) Have to be specified in channel units.



SUPPLEMENTARY MATERIAL FOR CHAPTER 3

B.1 CHOSEN PARAMETERS, DATA PREPARATION, AND DECOMPOSITION RUNS

In this appendix we describe the settings we used for the decomposition runs with GAUSSPY+. Where not specified otherwise, we used the default settings of GAUSSPY+ as described in App. A.6.

B.1.1 Preparatory steps

The cubes of the original GRS data set¹ are centred on integer Galactic longitude values, with each cube overlapping by one degree with the following cube. For the mosaicking we only used the cubes centred on odd integer values in Galactic longitude. Since the mosaicked cube of the entire GRS data set was too large for a decomposition with GAUSSPY+, we split it again along the Galactic longitude axis into 23 individual, non-overlapping subcubes.² We performed all preparatory and decomposition steps with GAUSSPY+ on these individual subcubes; this also included the spatially coherent refitting phases, which means that the decomposition results might show discontinuities at the borders of the individual subcubes. We checked for such an effect on the map showing the number of fit components (Fig. 3.4) but did not find any obvious problems.

Especially close to the borders of the coverage in Galactic latitude and longitude, the GRS data set contains spectra with instrumental artefacts, such as strongly amplified noise fluctuations. We thus masked out all spectra with extremely high noise values ($\sigma(T_A^*) > 0.75\text{ K}$; see Sect. B.2.1 for more details).

The GAUSSPY+ package includes preparatory steps for the decomposition, such as the identification of regions in the spectrum estimated to contain signal and the automated masking of negative features that are likely noise spikes or artefacts (see Sect. 2.3 for more details). We found that about 1.6% of the spectra from the GRS data set contained significant negative features in the spectrum (see Sect. 3.2.2 for more details).

B.1.2 Choice of the GaussPy smoothing parameters

For the GRS data set, we used the default settings of GAUSSPY+ to create nine different training sets, each containing 500 spectra. The spectra for each training set were randomly sampled from the entire GRS coverage and were then auto-

¹ https://www.bu.edu/galacticring/new_data.html

² This was driven by restrictions in available computing memory. For big spectral cubes we found it beneficial to split the data set into smaller subcubes for the GAUSSPY+ decomposition runs, but this will depend on the computing infrastructure available to the user.

TABLE B.1: Smoothing parameters (in units of spectral channels) obtained for the GAUSSPY+ training sets.

Sample	α_1	α_2	F ₁ score
1	1.75	4.02	74.2%
2	1.89	4.08	75.4%
3	1.95	4.15	76.5%
4	2.01	3.98	76.4%
5	1.97	4.22	73.4%
6	2.1	4.72	74.9%
7	2.12	4.36	72.6%
8	1.77	3.98	74.1%
9	1.98	4.63	74.9%

matically decomposed with GAUSSPY+ (see Sect. 2.3.4 for more details about the decomposition method that is used to create training sets).

In Table B.1 we list the value for the smoothing parameters α_1 and α_2 and the corresponding F₁ score we obtained with the machine learning functionality of GAUSSPY for these nine training sets. In general, the resulting inferred smoothing parameter values are similar and compare well to each other. We expect small to moderate deviations between the samples such as they are present in Table B.1, since we randomly chose the spectra for the training sets from the entire GRS coverage, which contains spectra with significantly different noise values (Fig. B.1). As discussed in App. A.2.5, such small deviations of the smoothing parameters only have a limited impact on the decomposition results. Moreover, with GAUSSPY+ the fitting is not that dependent anymore on the exact values of the smoothing parameters, since it includes an improved fitting routine that aims to improve decompositions obtained with GAUSSPY that did not yield a good fit.

The training set decomposition method in GAUSSPY+ only includes fit solutions that have a χ_{red}^2 value below a chosen threshold (in our case 1.2). As discussed by Andrae et al. (2010), a threshold based on a fixed value of χ_{red}^2 can be problematic, since for non-linear functions, such as Gaussian fit components, the degrees of freedom cannot be exactly determined and may vary substantially. To check whether this χ_{red}^2 threshold might have biased the training samples produced with GAUSSPY+, we also tried a different approach to create training sets by using the semi-automated spectral line fitting package SCOUSEPY (Henshaw et al., 2016a; 2019).

In SCOUSEPY, the data set is first divided into spectral averaging areas (SAAs). All spectra contained in an individual SAA are then averaged and the user manually fits the resulting spectrum by deciding on the number of fit components and their shape. The fit results from the SAA then help to inform the automated decomposition of the individual spectra contained in the SAA, which moreover leads to spatial coherence between the fit results of neighbouring spectra.

To create training sets with SCOUSEPY, we split the mosaicked GRS data set along the Galactic longitude axis into 23 individual subcubes and randomly placed nine



TABLE B.2: Smoothing parameters (in units of spectral channels) obtained for training set decompositions with SCOUSEPY and GAUSSPY+.

Sample	SCOUSEPY			GAUSSPY+		
	α_1	α_2	F ₁ score	α_1	α_2	F ₁ score
1	2.02	4.48	73.9%	2.38	4.28	77.9%
2	2.0	4.08	73.9%	2.12	4.17	75.9%
3	2.14	4.8	73.6%	1.41	4.49	71.4%

spectral averaging areas (SAAs) with 3×3 pixels in each subcube for a total of 207 SAAs and 1863 individual spectra. We then proceeded with the suggested workflow for SCOUSEPY: First we manually fitted the averaged spectrum of each SAA, which informed the automated decomposition step for each individual spectrum contained in the SAA. Then we visually inspected the best fit solutions for all individual spectra and refitted them manually if the best fit results were not satisfactory, that means if they showed unfit peaks, strongly blended components, or fit components with very broad linewidths, or if the fit solution was not spatially coherent with its neighbours.

For the selection of good-quality decompositions for the training set, we checked the final SCOUSEPY best fit results of all 1863 decomposed spectra with their corresponding residuals again by eye, which left us with a working sample of 1639 individual spectra. We then created three training sets, each of which contained 500 randomly chosen spectra and decomposition results from our final selection (we drew the spectra without replacement, which means an individual spectrum could only appear in one training set).

Table B.2 shows the resulting smoothing parameter values for these three training sets as determined by the machine learning routine of GAUSSPY. A comparison with Table B.1 demonstrates that the inferred values for α_1 and α_2 cover the same range of values. Table B.2 also shows the results obtained if we instead used the training set decomposition technique of GAUSSPY+ to produce best fit solutions for GAUSSPY for the same three training sets. The obtained values for the smoothing parameters are again similar to the values obtained with SCOUSEPY and the values obtained for the GAUSSPY+ training sets in Table B.1. The larger spread of the obtained values for α_1 is due to the presence of emission lines with low S/N ratio and non-Gaussian shapes in the random selection of spectra in the SCOUSEPY training sets. Spectra containing such challenging spectral features can lead to increased χ_{red}^2 values for the fit solution, which would usually cause their exclusion from the GAUSSPY+ training set selection. The similarity of the obtained smoothing parameter values is thus a reassuring confirmation that both GAUSSPY+ and SCOUSEPY produce good training set decompositions.

Given this similarity, we thus decided to use the median values for α_1 and α_2 obtained from the nine training sets created with GAUSSPY+ as our chosen parameters for the decomposition of the GRS data set. This yielded values of $\alpha_1 = 1.97$ and $\alpha_2 = 4.15$, which also compare well with the values inferred from the three training sets listed in Table B.2. Given the highly non-uniform noise coverage of the GRS (see



Fig. B.1), it is clear that our chosen values for the smoothing parameters will not be the optimal ones for all regions of the GRS data set. For example, we inferred higher smoothing parameters of $\alpha_1 = 2.89$ and $\alpha_2 = 6.65$ for the small GRS test field that showed a strong noise gradient (Sect. 2.7.3). However, the improved fitting and spatially coherent refitting routines of GAUSSPY+ should be able to salvage or mitigate negative effects introduced by the choice of non-optimal smoothing parameters.

B.1.3 Decomposition parameters and steps

The GAUSSPY+ decomposition proceeds in three stages (see Sect. 2.4.3–2.5.2). In Stage 1, GAUSSPY+ fits each spectrum individually, with the AICc serving as decision criterion between different fit solutions for the same spectrum. In Stage 2, fit solutions from Stage 1 can be flagged based on different user-selected criteria. Neighbouring fit solutions are then used for refitting attempts of the flagged spectra, which already introduces local spatial coherence between the fit solutions. Finally, in Stage 3 all fit solutions are checked for spatial coherence of the centroid position values of the fit components, with the aim of introducing spatial coherence more globally. Neighbouring fit solutions again serve as refit templates for decomposition results that have deviating centroid position values.

By default, GAUSSPY+ does not include flagged spectra as possible refit solutions in Stage 1. This was problematic for the GRS data set, as with our chosen flagging criteria there were regions near the Galactic midplane where almost all spectra were flagged and thus no refit solutions were available. We thus introduced the new parameter `use_all_neighbors` to GAUSSPY+, with which users can allow flagged spectra to serve as templates in case no unflagged spectra are available or refit attempts using only the unflagged spectra were not successful. In case flagged neighbouring spectra are used as refit templates, the flagged spectra are ranked according to their total flag values \mathcal{F}_{tot} and the fit solution with the lowest \mathcal{F}_{tot} value is used first. Otherwise, we used the default settings of GAUSSPY+ as described in App. A.6, with the exception of relaxing the $\Delta\mu_{\text{max}}$ parameter from its default value of 2 to 4 channels in phase 2 of the spatially coherent refitting, as it was done for the decomposition of the GRS test field in Sect. 2.7.3. We also increased the minimum weight threshold \mathcal{W}_{min} from its default value of $3/6$ to $4/6$, which means that in Stage 3 we only had two iterations with subsequent weight thresholds of $\mathcal{W} = 5/6$ and $\mathcal{W} = 4/6$ (see Sect. 2.5.2 for more details). We tested the decomposition for one of the most complex regions in the GRS (with 10 or more emission peaks per spectrum) and found that a \mathcal{W}_{min} value of 0.5 was less beneficial, as it sometimes resulted in overly complex best fit solutions, especially for heavily blended structures.

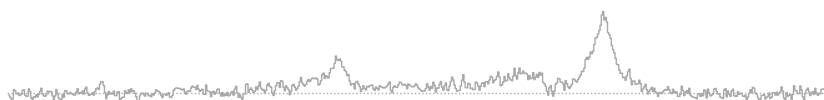
Table B.3 gives an overview of the percentage of spectra refitted in each stage and the percentage of spectra flagged after each stage. The N_{refit} parameter gives the percentage of spectra that obtained a new best fit solution in the spatially coherent refitting phases. In Stage 2, almost 59% of the spectra were successfully refit based on a neighbouring fit solution, whereas in Stage 3 only about 6% of the spectra were refit based on the neighbouring centroid position values. Based on this high fraction of refitted spectra, it is reasonable to assume that Stage 2 of GAUSSPY+



TABLE B.3: Percentages of refitted spectra, added and subtracted fit components, and flagged spectra after each stage of GAUSSPY+. The percentage is calculated relative to the total number of spectra in the GRS.

	Stage 1	Stage 2	Stage 3
N_{refit}	–	58.9%	6.2%
$N_{\text{comp}(+)}$	–	2.9%	1.1%
$N_{\text{comp}(-)}$	–	1.8%	0.6%
\mathcal{F}_{tot}	37.28%	31.67%	32.68%
$\mathcal{F}_{\text{blended}}$	4.12%	1.86%	2.32%
$\mathcal{F}_{\text{neg. res. peak}}$	0.13%	0.09%	0.10%
\mathcal{F}_{Θ}	17.39%	14.98%	15.70%
$\mathcal{F}_{\Theta > 50}$	8.05%	6.95%	7.11%
$\mathcal{F}_{\text{residual}}$	18.65%	15.55%	15.65%
$\mathcal{F}_{N_{\text{comp}}}$	4.73%	3.69%	3.74%

already managed to introduce a large amount of spatial coherence. The $N_{\text{comp}(+)}$ and $N_{\text{comp}(-)}$ parameters give the percentage of added and removed fit components from the total number of fit components used for the entire decomposition in Stages 2 and 3 of GAUSSPY+. Similar as for the decomposition of the GRS test field in Sect. 2.7.3, we find that the spatially coherent refitting stages tend to add more components to the fit solution. This is expected, as the fit solutions in Stage 1 are guided by the AICc, which aims at a good trade-off between the number of fit components and the resulting goodness of fit of the model (see Sect. 2.4.1.5 and 2.4.3 for more information). Stages 2 and 3 are designed to improve the fit solutions of spectra that were flagged by user-selected criteria. For the decomposition of the GRS we use the default flags of GAUSSPY+, which flag spectra with: blended fit components ($\mathcal{F}_{\text{blended}}$); negative residual peaks ($\mathcal{F}_{\text{neg. res. peak}}$); broad fit components (\mathcal{F}_{Θ}); non-normally distributed residual values ($\mathcal{F}_{\text{residual}}$); the number of fit components not compatible with neighbouring fits ($\mathcal{F}_{N_{\text{comp}}}$). The \mathcal{F}_{tot} value gives the percentage of spectra that were flagged by any of these flagging criteria. The \mathcal{F}_{Θ} criterion only flags spectra that contain fit components that are broad compared to other fit components in the spectrum or broad compared to components in the fit solutions of directly neighbouring spectra. However, it is also interesting to see whether the decomposition managed to reduce the fraction of fit components with very high absolute values for the linewidth. We thus also give the percentage of spectra that contain fit components with FWHM values that are higher than 50 spectral channels or about 10.5 km s^{-1} ($\mathcal{F}_{\Theta > 50}$), even though this was not a flagging criterion used in the GAUSSPY+ decomposition. We chose this upper limit for the FWHM as it is close to the maximum linewidths of 9.8 and 8.3 km s^{-1} that Rathborne et al. (2009) found in their catalogue of GRS clouds and clumps, respectively. Table B.3 shows that in Stage 2 we are able to significantly reduce the percentage of flagged spectra for all flagging criteria. Since in Stage 3 we are more concerned with enforcing spatial



coherence based on the centroid velocity values of neighbouring fit components, the number of spectra flagged as having blended and broad fit components increases again slightly.

B.1.4 Additional remarks on the decomposition results

Some of the original GRS subcubes we used to produce a big mosaic of the entire data set (Sect. B.1.1) overlapped with each other. This overlap caused an averaging of the columns at the edges of the respective subcubes at even integer values in Galactic longitude ($\ell = 16, 18, \dots, 54^\circ$). This averaging produced lower noise values and higher S/N ratios of peaks in the spectrum, which led to a large number of fit components. We include these averaged columns in the best fit solutions presented in Tables 3.1 and B.3, but we note that these fit solutions should be treated with caution.

There is an instrumental artefact present at v_{LSR} values of 63.3 to 66.1 km s^{-1} and ranges in Galactic coordinates of $32.2^\circ < \ell < 32.7^\circ$ and $-1.1^\circ < b < -0.7^\circ$, which causes very narrow positive and negative high amplitude spikes, whose effect is especially visible in Figs. 3.3 and 3.10. The final decomposition results still contain the fit components of the positive spikes for this region.

B.2 QUALITY ASSURANCE METRICS

In this appendix we present different quality assurance metrics for our decomposition results. We discuss the distributions of our calculated noise values, goodness of fit values, and measures for the distribution of the residual values.

B.2.1 Noise values

Vital parameters of the GAUSSPY+ algorithm are based on S/N thresholds, which is why a reliable noise estimate is an essential basis for obtaining good decomposition results. Figure B.1 shows the noise map of the entire coverage of the GRS data set that was obtained with the automated noise estimation routine of GAUSSPY+ (see Sect. 2.3.1 for more details on the noise estimation). A comparison with the noise map published in the GRS overview paper (Fig. 7 from Jackson et al. 2006) shows that our noise map reproduces the overall large-scale patterns; however, the individual noise values on a line of sight scale are more accurate and can show significant differences (see Sect. 2.7.2 for more details).

We show a histogram of the σ_{rms} values (given in antenna temperatures) estimated by GAUSSPY+ in Fig. B.2. The noise distribution peaks at a value of $\sigma(T_A^*) = 0.1$ K and shows a clear second bump after the IQR indicated with the hatched grey area. This bimodal noise distribution was already discussed in Jackson et al. (2006) and is explained by different observing modes used for the GRS (see their Fig. 8, but we note that they do not include positions of $\ell < 18^\circ$ and $|b| > 1^\circ$). We decided to mask out 1188 spectra with $\sigma(T_A^*)$ values > 0.75 K, which corresponds to the top 0.05% of the noise distribution. We found that such high $\sigma(T_A^*)$ values can be indicative



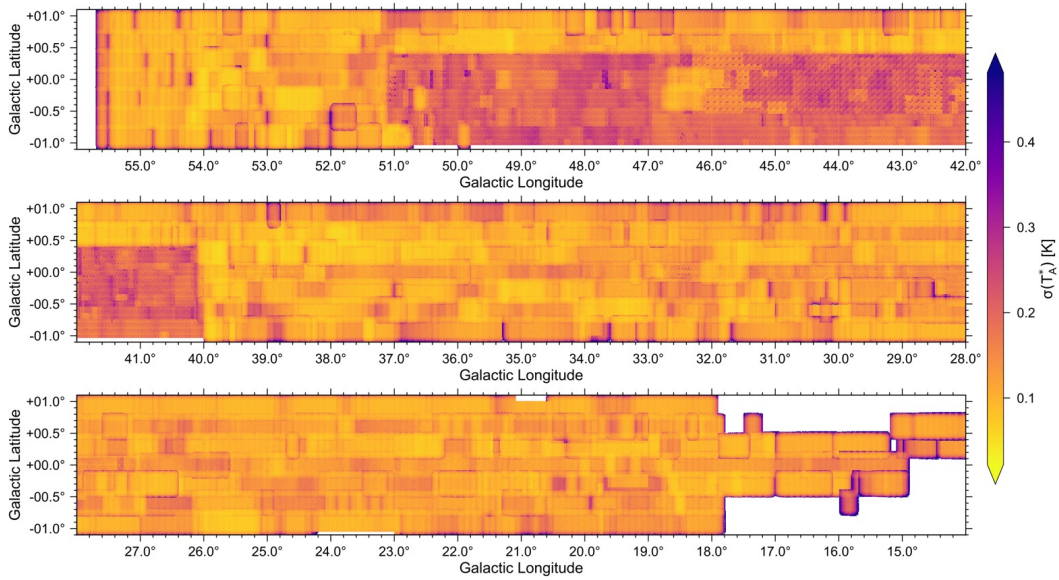


FIGURE B.1: Map of determined rms noise (given in antenna temperature values).

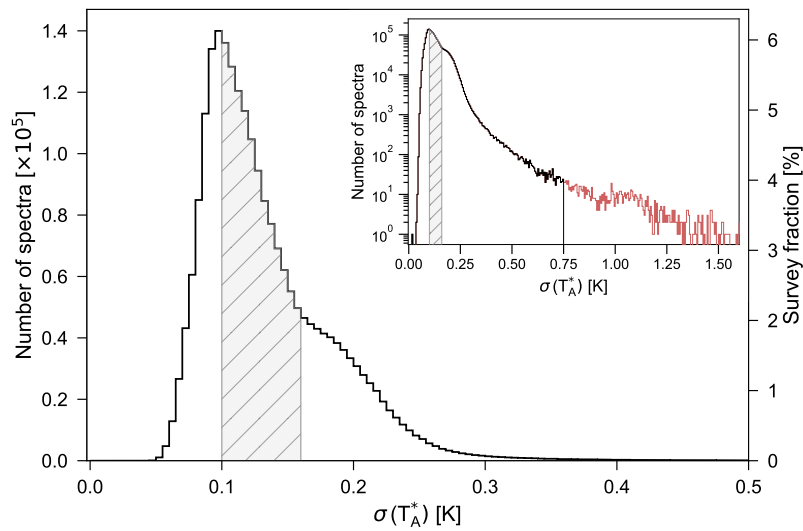
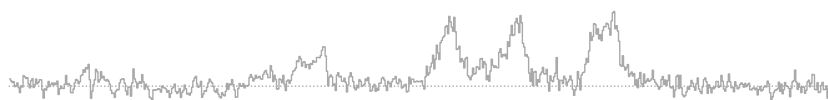


FIGURE B.2: Histogram of determined rms noise (given in antenna temperature values) for all spectra in the GRS. The inset shows the same distribution on a logarithmic scale. The red line in the inset indicates masked out spectra with high noise values. The grey-shaded area marks the IQR, ranging from about 0.1 – 0.16 K. The bin width is 0.005 K.



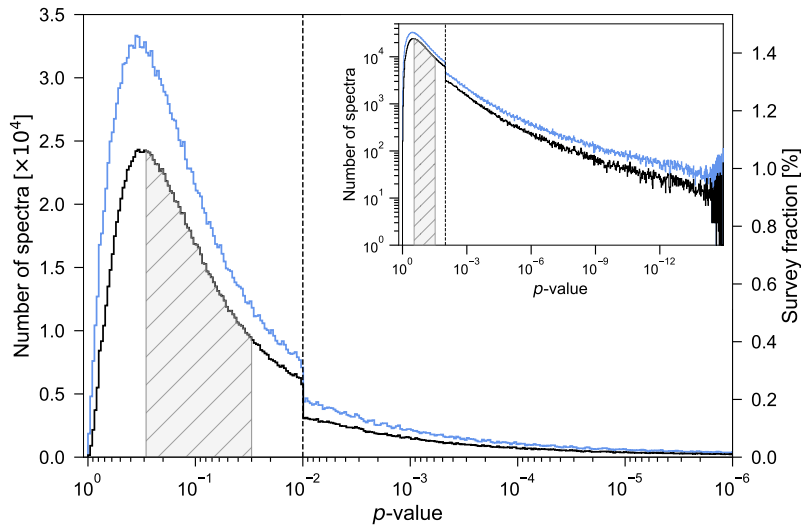


FIGURE B.3: Histogram of p -values from normality tests for the distribution of residual values for all GRS spectra (blue) and GRS spectra that have at least one fit component (black). The inset shows the same distribution on a logarithmic scale. The dashed vertical line marks the default p -value limit, below which GAUSSPY+ tries to refit spectra if possible. The grey-shaded area marks the IQR for the distribution of spectra with fitted components, ranging from about 0.03 – 0.3. The bin width is 0.02 dex.

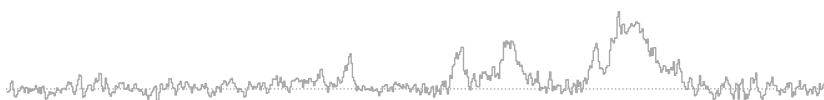
of instrumental artefacts. The inset in Fig. B.2 shows the noise distribution plotted on a logarithmic scale, and the $\sigma(T_A^*)$ values of the masked spectra with high noise values are indicated in red.

B.2.2 Goodness of fit statistics

One of the goodness-of-fit estimates employed by GAUSSPY+ is a check of whether the normalised residuals of the spectra show a normal distribution and are thus consistent with Gaussian or white noise (see Sect. 2.4.2.4 for more details). This check yields a p -value for the null hypothesis that the residuals are consistent with white noise. Figure B.3 shows the distribution of p -values for all spectra (blue line) and spectra that were fit by at least one component in the final decomposition results (black line). The inset gives the same distribution for a logarithmically scaled ordinate. In the default settings of GAUSSPY+, a p -value of $< 1\%$ serves as an indication that the residual contains features inconsistent with Gaussian noise, which is used to initiate refit attempts or decide between alternative fit solutions. This threshold for the p -value is indicated with the vertical dashed line and we can see a clear jump in the distribution at this value.

Another goodness-of-fit statistic that is often used to report the quality of fit results is the χ_{red}^2 value that is defined as

$$\chi_{\text{red}}^2 = \frac{1}{N - k} \sum_{i=1}^N \frac{(y_i - Y_i)^2}{\sigma_{\text{rms}}^2}, \quad (\text{B.1})$$



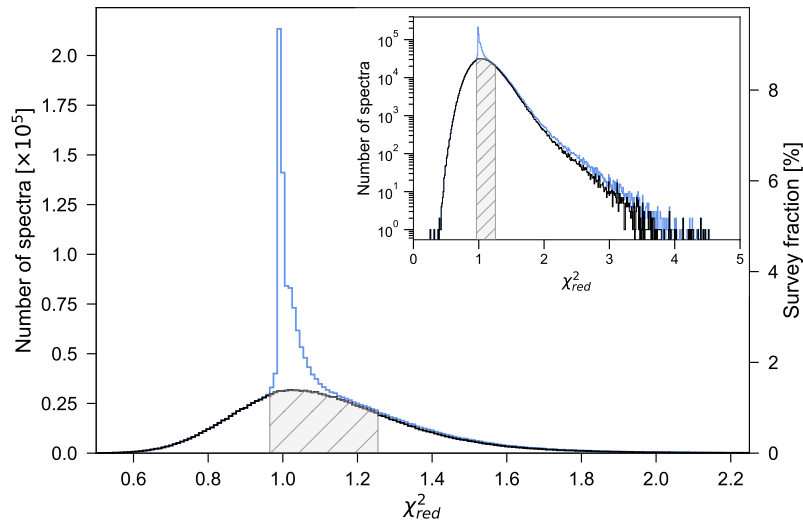
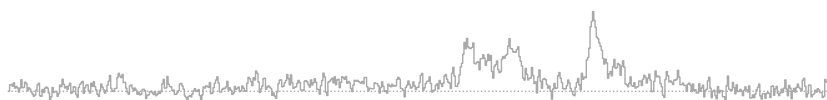


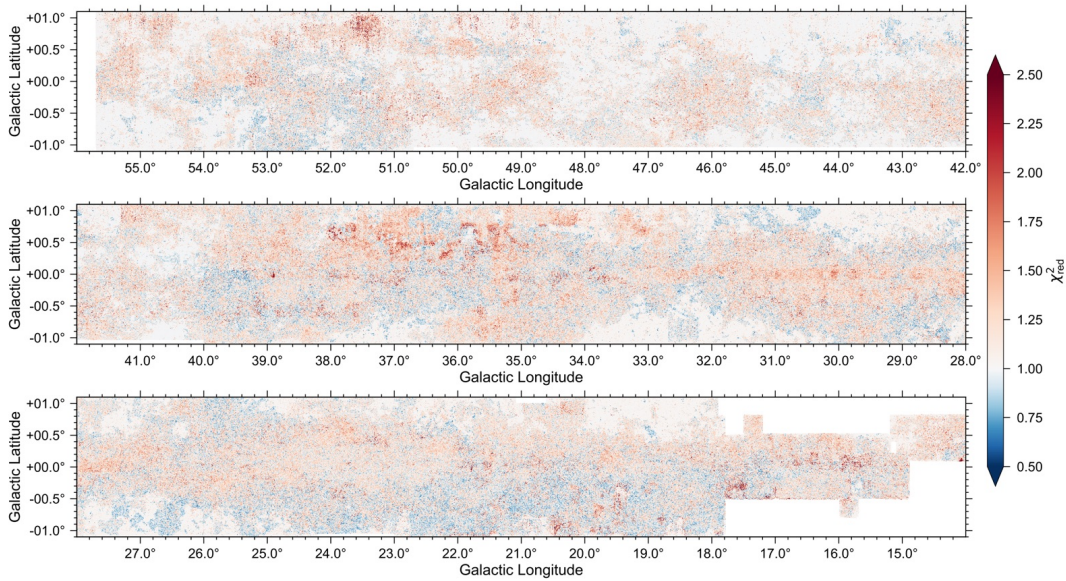
FIGURE B.4: Histogram of χ_{red}^2 values for all GRS spectra (blue) and GRS spectra with at least one fit component (black). The inset shows the same distribution on a logarithmic scale. The grey-shaded area marks the IQR for the distribution of spectra with fitted components, ranging from about 0.96 – 1.25. The bin width is 0.01.

where in the case of the Gaussian decomposition N corresponds to the number of spectral channels, k corresponds to the number of free parameters used in the fit solution, and y_i and Y_i are the data and fit value at channel position i . Since for non-linear models the χ_{red}^2 estimate can suffer from large uncertainties (Andrae et al., 2010), it is not the best goodness-of-fit metric for the Gaussian decomposition results. As discussed in App. A.5, another problem of χ_{red}^2 estimates is that the inclusion of a large number of spectral channels containing only noise can mask bad fit results. Given these caveats, our reported χ_{red}^2 values for our fit results should be taken with caution. If GAUSSPY+ identified signal intervals in a spectrum, we only include the spectral channels from those identified intervals for the χ_{red}^2 estimate, which increases its ability to identify potentially incorrect or insufficient fit results.

The distribution of the χ_{red}^2 values for the spectra from the GRS is shown in Fig. B.4. The distribution marked with the blue line contains all spectra of the GRS data set, irrespective of whether they were fitted in the decomposition. The black line shows the distribution of the χ_{red}^2 values for spectra that have at least one fitted Gaussian component. Both of the distributions peak at a value of 1. Spectra with no fitted Gaussian components are expected to have a χ_{red}^2 value close to 1 if they only contain noise and the σ_{rms} value was estimated correctly. Increased χ_{red}^2 values for these unfitted spectra can thus indicate spectra with valid signal that could not be fit, an incorrect noise estimation, or artefacts in the spectrum such as insufficient baseline subtraction.

About 35% of the spectra with fitted Gaussian components have χ_{red}^2 values below 1; about 0.4% of the spectra with fitted Gaussian components have χ_{red}^2 values above 2. Since we aimed to mostly include channels that contain signal in the calculation of the goodness of fit criterion, for most of the spectra low χ_{red}^2 values do very likely



FIGURE B.5: Map of χ_{red}^2 values.

not indicate an overfitting of the data, but rather reflect a smaller amount of spectral channels that were used for the χ_{red}^2 calculation.

Figure B.5 shows a map of the χ_{red}^2 values for the entire GRS data set. This map does not show any obvious correlations with the maps showing the normalised residuals (Fig. 3.2), noise values (Fig. B.1), and number of fit components (Fig. 3.4). However, we can see regions of increased χ_{red}^2 values (e.g. around $\ell \sim 51.5^\circ$ and $b \sim 1^\circ$), which could indicate problems with the decomposition, such as missed or incorrectly fitted signal peaks, or problems in the original data, such as insufficient baseline corrections.

B.3 EFFECTS OF OPTICAL DEPTH ON THE DECOMPOSITION RESULTS

Interpretation of the Gaussian decomposition data can potentially be affected by optical depth effects; we examine in this section how severe such effects may be. Moderate optical depth effects can lead to a broadening of the emission lines, which affects the linewidths (and further, estimated Mach numbers; e.g. [Hacar et al. 2016](#)). Increased optical depth effects can cause flat-topped or self-absorbed emission lines, which can yield two-component fits that are unphysical. The version of GAUSSPY+ used in this work does not account for any possible optical depth effects. If an emission line is affected by self-absorption, GAUSSPY+ will likely fit it with multiple Gaussian components. Our aim here is to establish in which regions, or for which spectra in the GRS, optical depth effects may impact the decomposition results. We start by recalling previous results about optical depth effects, depletion, and freeze out on the ^{13}CO isotopologue. We then present two methods of calculating the optical depth τ_0^{13} for ^{13}CO (1–0). Subsequently, we apply these methods to observations from the MWISP survey of a dense molecular cloud, to establish how severe the optical depth effects are and how we can apply these results to the GRS decomposition.



B.3.1 Depletion, freeze-out, and self-absorption of ^{13}CO

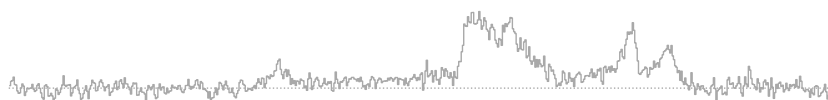
Evidence for depletion or freeze-out of CO isotopologues is already well-documented for IRDCs and clumps contained in the GRS data set (e.g. [Hernandez et al., 2011](#); [Pitann et al., 2013](#); [Giannetti et al., 2014](#); [Pon et al., 2016](#); [Barnes et al., 2018](#)), albeit for observations at spatial and spectral resolutions that are typically at least a factor of two better than for the GRS. For clumps, the depletions are usually most severe for their densest and coldest parts ([Hernandez et al., 2011](#); [Giannetti et al., 2014](#)). In the GRS data set, such small regions are only resolved for gas emission that is located within ~ 3 kpc of the sun, which is only a small fraction of the emission contained in the GRS. We thus conclude that freeze-out and depletion effects will not be a problem at the scales probed by the GRS.

Optical depth values have already been calculated for the GRS, albeit only on scales of molecular clouds and for spatially and spectrally smoothed versions of the data set. For their catalogue of molecular clouds in the GRS, [Rathborne et al. \(2009\)](#) found the ^{13}CO emission to be optically thin with average and maximum τ_0^{13} values of 0.13 and 0.5, respectively. [Roman-Duval et al. \(2010\)](#) repeated the τ_0^{13} estimation for 583 molecular clouds from [Rathborne et al. \(2009\)](#), but performed the calculation on a voxel-by-voxel basis first before averaging; this resulted in a higher mean optical depth value of 1.46, indicating that the GRS data set includes optically thick emission. [Rigby et al. \(2016\)](#) also found indications for self-absorption in the GRS data set, by comparing it to ^{13}CO (3–2) and C^{18}O (3–2) transitions of the CHIMPS survey (that has a spatial resolution about 3 times better than GRS).

However, there are also counterexamples that indicate that ^{13}CO (1–0) stays mostly optically thin even in dense regions. For example, [Beuther & Sridharan \(2007\)](#) studied a sample of 43 IRDCs and found that the peaks in ^{13}CO (1–0) correspond very well with peaks of the high density tracer H^{13}CO^+ (1–0), even for regions in the spectrum where ^{12}CO (2–1) seems to get optically thick. Since these were IRAM-30m observations at about half the spatial resolution of GRS, one would conclude that for a larger physical beam such effects should be even more reduced due to beam averaging.

B.3.2 Calculation of optical depth values

Here we review two common ways of estimating the optical depth of ^{13}CO , which we later apply in Sect. [B.3.3](#) to assess the importance of optical depth effects on the decomposition results. The first method for calculating τ_0^{13} requires information about the excitation temperature T_{ex} , obtained from ^{12}CO (1–0) emission that is assumed to be optically thick. The second method for calculating τ_0^{13} is based on the relative abundance of ^{13}CO to another isotopologue that traces higher column densities and is assumed to be optically thin; in our case this is the C^{18}O (1–0) emission line. This method is thus best applicable to dense regions of molecular clouds, such as IRDCs, filaments, clumps, and cores.



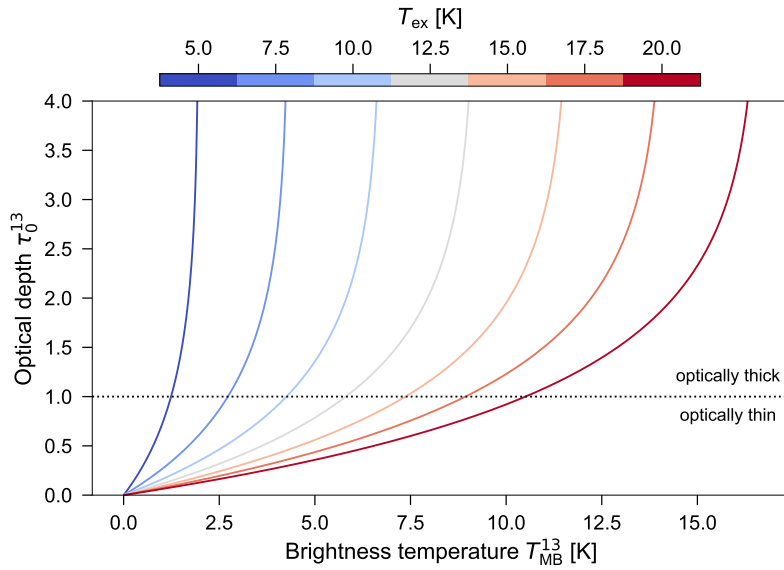


FIGURE B.6: Optical depth of ^{13}CO as a function of main beam brightness temperature for different excitation temperature (T_{ex}) values. The dotted horizontal line marks the threshold between the regimes where ^{13}CO is optically thin or thick.

B.3.2.1 Method 1: Estimating τ_0^{13} with additional ^{12}CO (1–0) observations

Under the condition of local thermodynamic equilibrium and the assumption that the ^{12}CO (1–0) line is optically thick, the excitation temperature T_{ex} can be determined as (Wilson et al., 2014):

$$T_{\text{ex}} = T_0^{12} \cdot \left(\ln \left[1 + \frac{T_0^{12}}{T_{\text{MB}}^{12} + 0.82} \right] \right)^{-1}, \quad (\text{B.2})$$

where T_{MB}^{12} is the maximum main beam brightness temperature of the ^{12}CO (1–0) line and $T_0^{12} = h\nu^{12}/k_{\text{B}} \sim 5.5$ K at the rest frequency of ^{12}CO ($\nu^{12} = 115.271$ GHz). Assuming that T_{ex} is the same for the ^{12}CO (1–0) and ^{13}CO (1–0) transitions, the optical depth for the ^{13}CO (1–0) line is then given by (Wilson et al., 2014):

$$\tau_0^{13} = -\ln \left[1 - \frac{T_{\text{MB}}^{13}}{T_0^{13}} \left(\frac{1}{e^{T_0^{13}/T_{\text{ex}}} - 1} - 0.16 \right)^{-1} \right], \quad (\text{B.3})$$

where T_{MB}^{13} is the maximum main beam brightness temperature of the ^{13}CO (1–0) line and $T_0^{13} = h\nu^{13}/k_{\text{B}} \sim 5.3$ K at the rest frequency of ^{13}CO ($\nu^{13} = 110.201$ GHz).

Figure B.6 shows how τ_0^{13} increases as a function of T_{MB}^{13} for different fixed values of T_{ex} . Table B.4 gives the T_{MB}^{13} values for which we expect the ^{13}CO emission to get optically thick for a given T_{ex} value. The table also shows the percentage of fit components from the GRS decomposition that have amplitude values greater than this $T_{\text{MB}, \text{crit}}^{13}$ value. For example, for an assumed fixed value of $T_{\text{ex}} = 10$ K, about 1.8% of all Gaussian fit components in the GRS decomposition would pass the threshold between optically thin and optically thick gas. A comparison with Fig. 3.6 also confirms that optical depth effects get important for our decomposition results if the excitation temperature values are $\lesssim 10$ K.

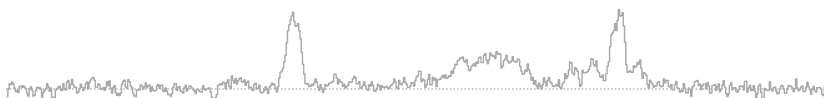


TABLE B.4: Threshold between optically thin and thick emission for given excitation temperature values.

T_{ex} [K]	$T_{\text{MB, crit.}}^{13}$ [K]	$T_{\text{MB, GRS}}^{13} > T_{\text{MB, crit.}}^{13}$
5.0	1.2	41.96%
7.5	2.7	8.55%
10.0	4.3	1.84%
12.5	5.8	0.47%
15.0	7.4	0.16%
17.5	8.9	0.06%
20.0	10.5	0.02%

B.3.2.2 Method 2: Estimating τ_0^{13} with additional $\text{C}^{18}\text{O}(1-0)$ observations

In case additional $\text{C}^{18}\text{O}(1-0)$ observations are available, τ_0^{13} can be determined based on the expected relative abundance of ^{13}CO to C^{18}O . Under the assumption that the C^{18}O emission is optically thin, a comparison of the integrated emission W_{CO} of ^{13}CO and C^{18}O can be put in direct relation to their opacities τ_0 :

$$\frac{W_{^{13}\text{C}^{16}\text{O}}}{W_{^{12}\text{C}^{18}\text{O}}} = \frac{1 - e^{-\tau_0^{13}}}{1 - e^{-\tau_0^{18}}}. \quad (\text{B.4})$$

We can use information about the isotopic ratios of carbon and oxygen to rewrite τ_0^{18} in terms of τ_0^{13} :

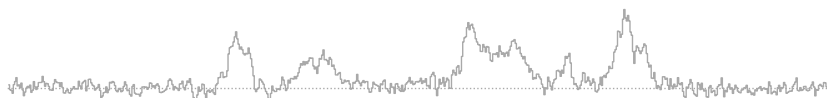
$$\tau_0^{18} = \frac{[^{12}\text{C}]/[^{13}\text{C}]}{[^{16}\text{O}]/[^{18}\text{O}]} \cdot \tau_0^{13}. \quad (\text{B.5})$$

Giannetti et al. (2014) determined that these isotope ratios vary with Galactocentric distance R_{gal} as $[^{12}\text{C}]/[^{13}\text{C}] = 6.1 \times R_{\text{gal}} [\text{kpc}] + 14.3$ and $[^{16}\text{O}]/[^{18}\text{O}] = 58.8 \times R_{\text{gal}} [\text{kpc}] + 37.1$. Substituting Eq. B.5 in Eq. B.4 thus allows to solve for τ_0^{13} .

B.3.3 Optical depth effects in the G24 region

In this section we study the effects of optical depth on the decomposition with the help of a dense, elongated giant molecular cloud. The cloud, G24, has been identified by Wang et al. (2015) from the Hi-GAL and GRS data sets. G24 is located at the Galactic coordinates $\ell = 24^\circ, b = +0.48^\circ$, and spans v_{LSR} values of 93–99 km s^{-1} (Wang et al., 2015). The total mass of G24 has been estimated to be about $10^5 M_\odot$, the length about 100 pc, and the distance about 5.8 kpc (Zucker et al., 2018; Zhang et al., 2019). The cloud is star-forming and its star formation rate and efficiency are typical for similar clouds in the Milky Way (Zhang et al., 2019). G24 overlaps with the molecular cloud GRSMC G024.09+00.44 identified by (Rathborne et al., 2009), whose total mass was estimated to be $2.8 \times 10^5 M_\odot$ (Roman-Duval et al., 2010).

There are two reasons that make G24 a good example to test if optical depth effects impact our decomposition. First, G24 is located in one of the most complex regions



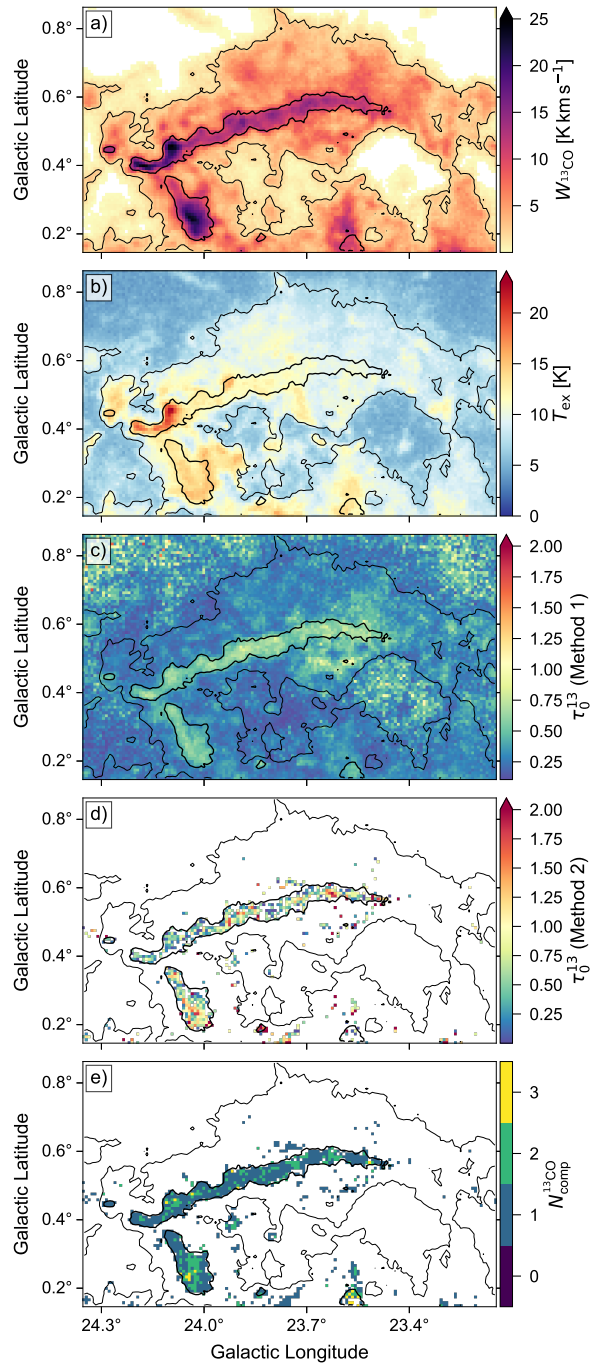


FIGURE B.7: Maps for the region containing the elongated molecular cloud G24. *a*): Zeroth moment map of the ^{13}CO emission. *b*): Map of determined excitation temperature values. *c*): Map of determined τ_0^{13} values using Method 1 (App. B.3.2.1). *d*): Map of determined τ_0^{13} values using Method 2 (App. B.3.2.2). *e*): Map showing the number of ^{13}CO fit components associated with a single C^{18}O fit component. The black contours indicate $W_{^{13}\text{CO}}$ values of 2 K km s^{-1} (thin line) and $W_{\text{C}^{18}\text{O}}$ values of 1 K km s^{-1} (thick line). All maps were obtained from voxels between $93 < v_{\text{LSR}} < 99 \text{ km s}^{-1}$.



TABLE B.5: Smoothing parameters (in units of spectral channels) obtained for decompositions of the GAUSSPY+ training sets for the ^{13}CO and C^{18}O MWISP data sets.

Isotopologue	α_1	α_2	F ₁ score
^{13}CO	2.18	4.94	71.1%
C^{18}O	2.98	5.75	70.2%

of the GRS data set, judging by the number of fitted components along the line of sight (Fig. 3.4). The decomposition is most challenging for such complex lines of sight. Second, G24 is among the most massive structures identified from GRS as distinct clouds, with a gas surface density of $\sim 105 M_{\odot} \text{pc}^{-2}$ (Zhang et al., 2019). As a result, if optical depth effects hamper the GRS decomposition in general, we should definitely see the effects in G24.

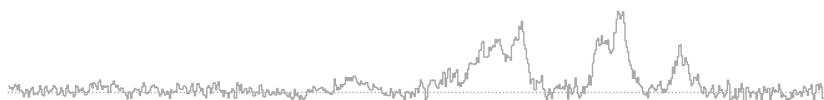
B.3.3.1 Observations

We used data of the G24 region from the MWISP project (Su et al., 2019), which is an ongoing CO survey for the northern Galactic plane ($\ell = -10$ to 250° , $|b| \leq 5.2^{\circ}$) using the PMO-13.7 m single-dish telescope located at Delingha in China. We obtained observations of ^{12}CO (1–0), ^{13}CO (1–0), and C^{18}O (1–0) covering a $2.5^{\circ} \times 1^{\circ}$ field centred at Galactic coordinates $\ell = 23.75^{\circ}$ and $b = 0.5^{\circ}$. The angular resolution of the data is $54.8''$ with a pixel sampling of $30''$. The covered velocity range is from -500 to $+500 \text{ km s}^{-1}$ with a velocity resolution of $\sim 0.16 \text{ km s}^{-1}$ and 0.17 km s^{-1} for the ^{12}CO and $^{13}\text{CO}/\text{C}^{18}\text{O}$ observations, respectively. The data was already supplied in main beam temperatures.

Figure B.7 (a) shows a zeroth moment map for the G24 region, which was obtained from the ^{13}CO MWISP data integrated between $93 < v_{\text{LSR}} < 99 \text{ km s}^{-1}$ using the moment masking technique described in Dame (2011). The very good correspondence of the $W_{\text{C}^{18}\text{O}}$ contour defined on the corresponding C^{18}O data with the zeroth moment map of ^{13}CO confirms that C^{18}O emission is coming from areas with increased ^{13}CO emission and thus increased column density. The $W_{\text{C}^{18}\text{O}}$ contour shown in Fig. B.7 (a) corresponds to a $W_{^{13}\text{CO}}$ contour of $\sim 10 \text{ K km s}^{-1}$.

B.3.3.2 GaussPy+ decomposition

For the decomposition of the MWISP data set we reduced the velocity axis to a range of -50 to $+150 \text{ km s}^{-1}$, which corresponds to 1207 and 1202 spectral channels for ^{13}CO and C^{18}O , respectively. Similar as in App. B.1.2, we used the default settings of GAUSSPY+ to create training sets with 500 decomposed spectra for both isotopologues. In Table B.5, we list the determined smoothing parameters and corresponding F₁ score for both training sets. The C^{18}O data has a much lower S/N ratio and noise properties can thus affect the line shape already significantly, so the data needed to be smoothed more to yield a good decomposition performance. Apart from the different smoothing parameter values, we used the same GAUSSPY+ settings to prepare and decompose the MWISP ^{13}CO and C^{18}O spectra as for the GRS data set (described in App. B.1.1 and App. B.1.3).



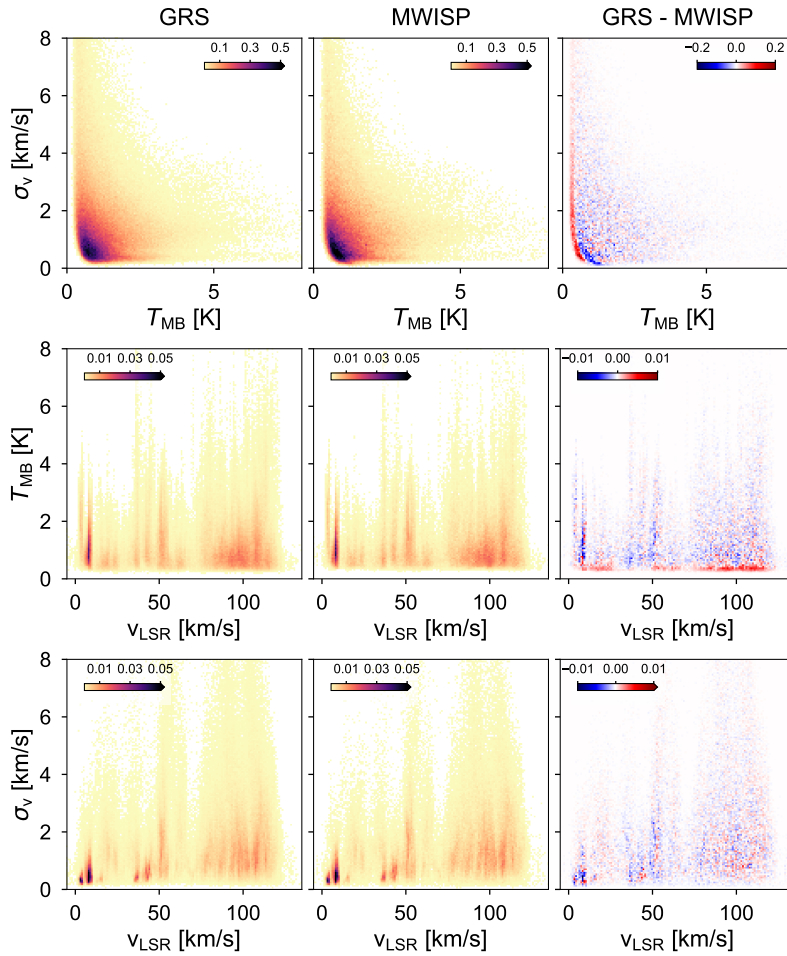


FIGURE B.8: Distributions of fit parameters for the decomposition of the GRS (*left*), MWISP (*middle*), and the difference between the two data sets (*right*). The rows show normalised 2D histograms of: peak main beam brightness temperature and velocity dispersion values (*top*), centroid velocity and peak main beam brightness temperature values (*middle*), centroid velocity and velocity dispersion values (*bottom*). Colourbars in all panels indicate the values of the normalised 2D distributions.

B.3.3.3 Comparison of the decomposition results between the GRS and MWISP

We now compare the GAUSSPY+ decomposition results obtained for the GRS and MWISP data sets. If the fit results for the two data sets are comparable, we can conclude that also our following results about the optical depth effects derived for the MWISP data will apply similarly to the GRS. We cannot perform a straightforward spectrum-per-spectrum comparison, since the spectral channel widths and pixel scales of the data sets are not identical. We thus opted for a simpler approach of comparing the fit parameter statistics.

For this comparison we used all fit components within $22.5^\circ \lesssim \ell \lesssim 25^\circ$, $0^\circ \lesssim b \lesssim 1^\circ$, and $-5 \lesssim v_{\text{LSR}} \lesssim 135 \text{ km s}^{-1}$. Due to the different spatial resolutions and pixel scales this selection included 58 635 spectra with 271 896 fit components in the GRS data set and 32 153 spectra with 144 555 fit components in the MWISP data set. Figure B.8 shows normalised 2D histograms for all possible combinations of the



Gaussian fit parameters for the GRS (*left panels*) and MWISP (*middle panels*) data sets. The shapes of the 2D distributions of the GRS and MWISP match very well, which already demonstrates that the two decompositions yielded similar results. To better quantify how similar the 2D distributions are, we show the difference between their distributions in the *right panels*, where red and blue indicate higher values in the GRS and MWISP distributions, respectively. The GRS data set includes regions with very low σ_{rms} values, which led to fitted components with low T_{MB} values that could not be detected in the MWISP data set. Otherwise these distributions do not show any noticeable biases; there are individual small differences, but these can be explained by the variation in the resolution elements and the noise coverage.

We thus conclude that the GRS and MWISP decomposition results are sufficiently similar. Thus, we expect that the following results about optical depth effects derived from the MWISP data can be applied to the GRS.

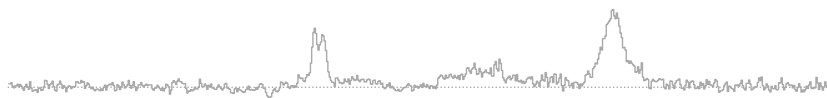
B.3.3.4 Estimated τ_0^{13} values with Method 1

With the ^{12}CO and ^{13}CO MWISP observations of the G24 region and Eqs. B.2 and B.3 we can estimate values for T_{ex} and τ_0^{13} , respectively. For the T_{ex} and τ_0^{13} calculation we only considered data points within $93 < v_{\text{LSR}} < 99 \text{ km s}^{-1}$. We show the resulting maps for T_{ex} and τ_0^{13} in Fig. B.7 (b) and (c), which already shows that the densest part of G24 is associated with higher τ_0^{13} values. To better quantify how the optical depth varies with density and excitation temperature, we show 2D distributions of the T_{ex} and τ_0^{13} values in Fig. B.9. Inside the contour defined by $W_{^{13}\text{CO}} > 2 \text{ K km s}^{-1}$, the T_{ex} values range from about 6 to 23.5 K and the τ_0^{13} values range from 0.12 to 1.04, with a median τ_0^{13} value of 0.32. The area of G24 within a contour of $W_{\text{C}^{18}\text{O}} > 1 \text{ K km s}^{-1}$ is also associated with the highest T_{ex} values (from about 8.5 to 23.5 K), as can be clearly seen in the respective marginal distribution shown in red in Fig. B.9. The corresponding τ_0^{13} values in this area range from 0.3 to 0.92, and the median τ_0^{13} value is 0.54. While the densest regions of G24 definitely show increased values for τ_0^{13} , the ^{13}CO (1–0) transition is for most lines of sight still well below optical depth values of 1. Based on the calculation of τ_0^{13} with Method 1, we conclude that optical depth effects do not play a significant role in the GRS data set.

B.3.3.5 Estimated τ_0^{13} values with Method 2

With the ^{13}CO and C^{18}O MWISP observations of the G24 region and Eq. B.4, we can give an independent estimate for τ_0^{13} . We took values for the integrated intensity from our GAUSSPY+ decomposition of the MWISP ^{13}CO and C^{18}O data sets (App. B.3.3.2)³. We selected all C^{18}O fit components in the region whose centroid positions were within $93 \lesssim v_{\text{LSR}} \lesssim 99 \text{ km s}^{-1}$. For each of these fitted C^{18}O components, we associated ^{13}CO fit components along the same line of sight, whose centroid position was contained within the FWHM interval ($v_{\text{LSR}} \pm \text{FWHM}$) of the C^{18}O fit component. Thus a single C^{18}O fit component could be associated with multiple ^{13}CO fit components.

³ In principle we could use moment analysis to get the integrated intensity, but blending with nearby emission features would make these results more uncertain.



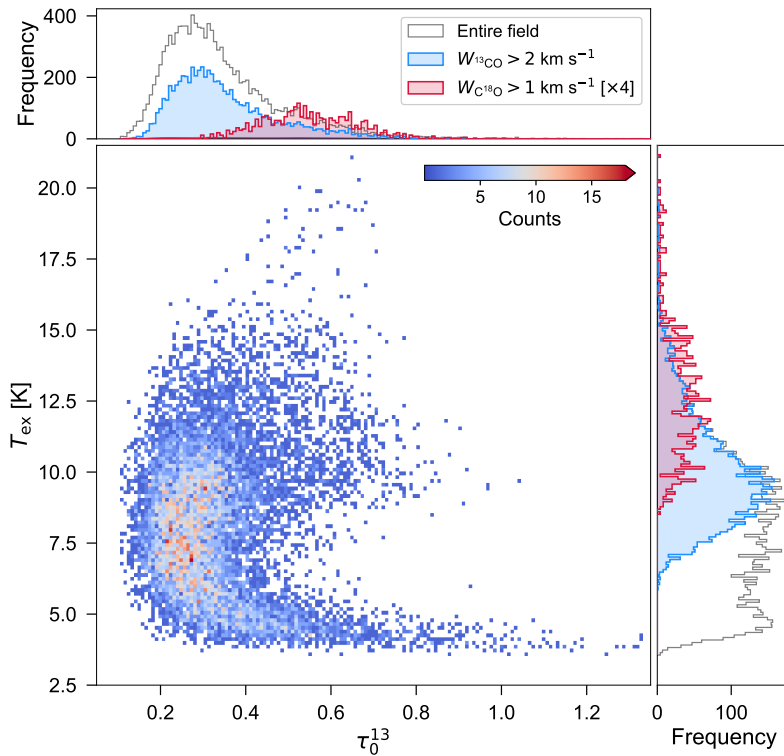


FIGURE B.9: 2D distribution of determined T_{ex} and τ_0^{13} values shown in Fig. B.7 (b) and (c). Marginal distributions on top and to the right are for the entire region shown in Fig. B.7 (unfilled histograms), and subsets of the region within the $W_{13\text{CO}} = 2 \text{ K km s}^{-1}$ contour (blue histograms) and the region within the $W_{\text{C}^{18}\text{O}} = 1 \text{ K km s}^{-1}$ contour (red histograms; the counts are scaled by a factor 4 for better visibility).

For a calculated Galactocentric distance of G24 of about 3.8 kpc we expect isotope ratios of $[^{12}\text{C}]/[^{13}\text{C}] \sim 38$ and $[^{16}\text{O}]/[^{18}\text{O}] \sim 263$ (based on the work of [Giannetti et al., 2014](#)). Using these isotope ratios to rewrite τ_0^{18} in terms of τ_0^{13} together with the integrated emission inferred from the ^{13}CO and C^{18}O fit components, we can solve for τ_0^{13} in Eq. B.4. We show the resulting map of τ_0^{13} values estimated with Method 2 in Fig. B.7 (d). The IQR of the τ_0^{13} values goes from 0.29 to 0.96, with a median value of 0.57. So even though the median τ_0^{13} value is comparable to what was obtained with Method 1 for the same region, individual τ_0^{13} values can be much higher for Method 2. However, the median S/N ratio for the fit components in C^{18}O is only ~ 2.8 , which means that the uncertainty on their fit parameters due to impacts of the noise and thus also the uncertainty on the τ_0^{13} calculation will be increased. These increased uncertainties might also explain the surprising lack of correlation we find between the two independent results for τ_0^{13} obtained for 471 positions with Method 1 and 2 (with a Pearson correlation coefficient of 0.1 and corresponding p -value of 1.2%). Based on the τ_0^{13} calculation with Method 2, we thus conclude that optical depth effects can get important for the densest structures in the GRS, but still seem to not be an overwhelming issue even for these most problematic regions.



B.3.4 Effects on the decomposition

Our main concern is whether τ_0^{13} values are high enough to impact the decomposition, so that the underlying emission lines get fitted by multiple components instead of a single one. We saw in the last two sections that we find increased optical depth values in the densest regions of G24 (panels c and d in Fig. B.7), where we also detect the C¹⁸O line. For these dense regions, we can thus compare the position of the fit component(s) of the ¹³CO emission to the position of the fitted C¹⁸O line. If multiple fit components in ¹³CO are associated with a single C¹⁸O fit component, it can serve as an indication that the ¹³CO emission might suffer from optical depth effects that could have led to the fitting of multiple components. We associate a fit component in ¹³CO with a fit component in C¹⁸O if the centroid position of the former is contained within the FWHM interval of the latter.

We show a map of the number of ¹³CO fit components associated with a single C¹⁸O fit component in Fig. B.7 (e). Within the $W_{\text{C}^{18}\text{O}} = 1 \text{ K km s}^{-1}$ contour, that means the densest part of the G24 region, 71.8% of the C¹⁸O fit components are associated with a single ¹³CO component; 25.5% of the C¹⁸O components are associated with two ¹³CO components, and the remaining 2.8% are associated with three ¹³CO components. Based on these results, we conclude that for about a third of the positions in the most dense region of G24 the decomposition may fit two or three components for what may be a single ¹³CO emission line, whose shape is non-Gaussian due to optical depth effects. Another possibility is that complex line structure is detected in ¹³CO, but not in C¹⁸O, due to differences in sensitivity.

However, the low S/N ratio of the C¹⁸O components makes this analysis rather uncertain. We checked whether the association of a single C¹⁸O component with multiple ¹³CO fit components could be due to broader σ_v values of the C¹⁸O component. The median σ_v value for C¹⁸O components associated with one, two, or three ¹³CO fit components is 1.0, 1.4, and 2.4 km s⁻¹, respectively, and the respective S/N ratio of the C¹⁸O components is 3.2, 3.0, and 2.3. It thus seems likely that the association of multiple ¹³CO fit components with a single C¹⁸O component is at least partly affected by the low S/N ratio of the C¹⁸O components.

Finally, we calculate ¹³CO column densities for the densest region in G24, which can serve as a guideline for when optical depth effects may impact the fitting results. We can calculate ¹³CO column densities including a correction for optical depth effects via (Wilson et al., 2014):

$$N_{\text{CO}}^{13} [\text{cm}^{-2}] = 3 \times 10^{14} \cdot \left(1 - e^{\tau_0^{13}/T_{\text{ex}}}\right)^{-1} \cdot \frac{\tau_0^{13}}{1 - e^{-\tau_0^{13}}} \cdot W_{13\text{CO}}, \quad (\text{B.6})$$

where we plug in the values for $W_{13\text{CO}}$, T_{ex} , and τ_0^{13} shown in Fig. B.7 (a–c). The region within the $W_{\text{C}^{18}\text{O}} = 1 \text{ K km s}^{-1}$ contour has a mean N_{CO}^{13} value of $1.4 \times 10^{16} \text{ cm}^{-2}$ (with minimum and maximum N_{CO}^{13} values of 5.0×10^{15} and $5.1 \times 10^{16} \text{ cm}^{-2}$, respectively). We compared the τ_0^{13} values calculated with Method 2 (Fig. B.7 d) with the corresponding N_{CO}^{13} values but did not find any correlation. However, based on the discussion in this section, we infer that optical depth effects might have an impact on the decomposition if ¹³CO column densities exceed values of $N_{\text{CO}}^{13} \sim 1 \times 10^{16} \text{ cm}^{-2}$.



SUPPLEMENTARY MATERIAL FOR CHAPTER 4

C.1 FURTHER DETAILS ABOUT THE KDA PRIOR

Here we give more details about the KDA prior (Sect. 4.1.3). We describe the method we used to calculate the prior, present the literature results we considered for the prior, and discuss its effect on the distance calculation.

C.1.1 Calculation of priors

In the following we describe the iterative loop that is used to determine priors for the KDA solution (see also Fig. C.1). For a given $(\ell, b, v_{\text{LSR}})$ coordinate, we first determine how many sources N_{src} from a catalogue are associated with this coordinate. For this we define a Gaussian weight using the definition of a Gaussian function:

$$f(x) = a \cdot \exp\left(-4 \cdot \ln(2) \cdot \frac{(x - \mu)^2}{\Theta^2}\right), \quad (\text{C.1})$$

where a , μ , and Θ denote the amplitude, mean position, and FWHM values, respectively. From this definition we construct a Gaussian weight w_g that evaluates to unity at $x = \Theta/2$:

$$w_g(x) = \tilde{a} \cdot \exp(-4 \cdot \ln(2) \cdot x^2), \quad (\text{C.2})$$

with a normalisation factor of $\tilde{a} = \exp(\ln(2))$ and x being the distance to the mean position (in our case $\mu = 0$) in fractions of the FWHM (f_Θ). We can apply this Gaussian weighting straightforwardly along the spectral axis, where $x \equiv f_\Theta = |v_{\text{LSR}}^{\text{src}} - v_{\text{LSR}}| / \Theta_{\text{src}}$, with $v_{\text{LSR}}^{\text{src}}$ and Θ_{src} being the measured centroid velocity and linewidth of the catalogue sources, respectively. We define the weight along the velocity axis w_v as:

$$w_v = \begin{cases} 1, & \text{for } w_g(f_\Theta) \geq 1 \\ w_g(f_\Theta), & \text{for } 1 > w_g(f_\Theta) \geq w_v^{\text{min}} \\ 0, & \text{otherwise,} \end{cases} \quad (\text{C.3})$$

where w_v^{min} is a user-defined threshold. For example, with $w_v^{\text{min}} = 0.125$ all points along the spectral axis for which $|v_{\text{LSR}}^{\text{src}} - v_{\text{LSR}}| > \Theta_{\text{src}}$ receive a weight of $w_v = 0$.

For the spatial association, we use the elliptical or circular FWHM extent of the sources as defined in the respective catalogue. With the following equation we can check whether a point is located within a rotated ellipse:

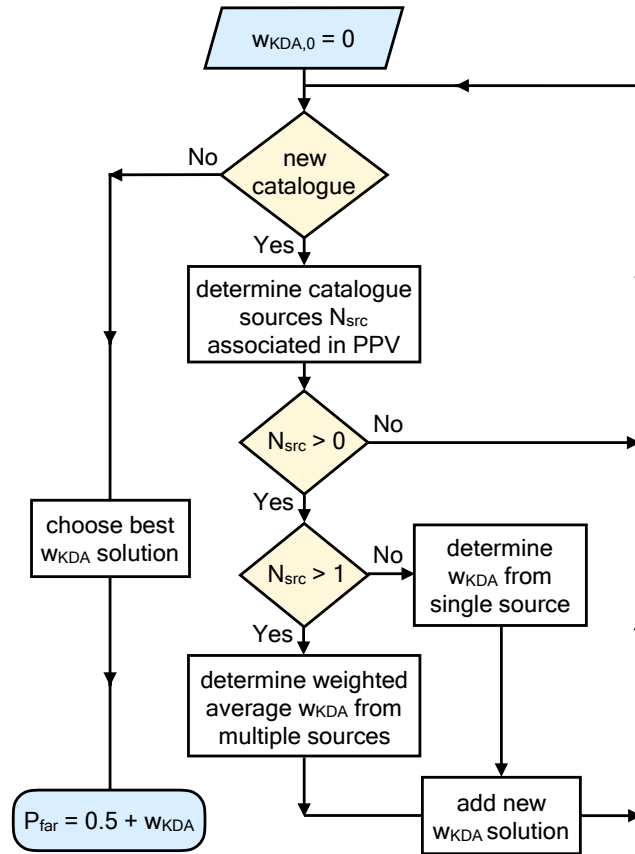


FIGURE C.1: Flowchart outlining how literature distance estimates are used to determine a prior for the KDA solution.

$$\epsilon = \frac{[\cos(\alpha)(x_p - x_0) + \sin(\alpha)(y_p - y_0)]^2}{a^2} + \frac{[\sin(\alpha)(x_p - x_0) + \cos(\alpha)(y_p - y_0)]^2}{b^2}, \quad (\text{C.4})$$

where in our case x_p and y_p refer to the ℓ and b coordinates of our PPV data point and x_0 , y_0 , a , b , and α are the central ℓ and b coordinates, the semi-major and semi-minor axis, and the rotation of the ellipse, respectively. If $\epsilon \leq 1$, the point is located within or on the ellipse. Given that $\sqrt{\epsilon}$ corresponds to the distance to the centre of the source expressed in fractions of its spatial FWHM extent, we can define a weight w_{PP} for the association of Galactic or position-position coordinates with a catalogue source as follows:

$$w_{\text{PP}} = \begin{cases} 1, & \text{for } w_g(\sqrt{\epsilon}) \geq 1 \\ w_g(\sqrt{\epsilon}), & \text{for } 1 > w_g(\sqrt{\epsilon}) \geq w_{\text{PP}}^{\min} \\ 0, & \text{otherwise,} \end{cases} \quad (\text{C.5})$$



where $w_{\text{PP}}^{\text{min}}$ is a user-defined threshold. For example, with $w_{\text{PP}}^{\text{min}} = 0.125$ all points located beyond twice the extent of the source receive a weight of $w_{\text{PP}} = 0$.

We then combine the spectral and spatial weights to a total PPV weight of $w_{\text{PPV}} = w_{\text{PP}} \cdot w_{\text{V}}$. We only retain catalogue sources that have a weight $w_{\text{PPV}} > 0$. If there are no sources from the catalogue that have $w_{\text{PPV}} > 0$ we proceed to the next catalogue and repeat the source association.

If there was at least one catalogue source associated with the coordinate, we calculate w_{KDA} , which gives the weight that the source is located on the near or far distance. The w_{KDA} weight can range from -0.5 (which puts all the weight on the near distance) to 0.5 (which puts all the weight on the far distance). In case of only a single associated catalogue source $w_{\text{KDA}} = w_{\text{PPV}} \cdot f_{\text{N/F}} \cdot w_{\text{CAT}}$, where $f_{\text{N/F}}$ is -0.5 or 0.5 if the catalogue source is associated with the near or far KD solution, respectively, and w_{CAT} is a user-defined weight for the catalogue (see App. C.1.3). If multiple sources are associated, we calculate w_{KDA} as a weighted average:

$$w_{\text{KDA}} = \frac{\sum_{i=1}^{N_{\text{src}}} w_{\text{PPV},i} \cdot f_{\text{N/F},i}}{\sum_{i=1}^{N_{\text{src}}} w_{\text{PPV},i}} \cdot w_{\text{CAT}}. \quad (\text{C.6})$$

After we searched all catalogues, we use the w_{KDA} with the highest absolute value as our final value to determine our prior for the kinematic distance solution with $P_{\text{far}} = 0.5 + w_{\text{KDA}}$. We did not make the final calculation of the weights cumulative or additive as many of the catalogues we use are not fully independent from each other. For example, the CHIMPS catalogue used many of the other catalogues in resolving the KDA for their clumps. In case our routine yields multiple w_{KDA} values with the same absolute value, we calculate the average w_{KDA} value from these solutions. Thus, if for the same clump two catalogues determined different KDA solutions, the resulting P_{far} value is 0.5 , which means that no prior for the KDA will be supplied.

C.1.2 Inferring literature KDA solutions

We use the literature distance information only for prior information on whether the source is located on the near or far side of the Galactic disk. In case one of the catalogues already supplied an information about the KDA resolution (that means if the near or far distance was chosen) we adopt these KDA results. If the KDA resolution was not stated explicitly, we use one of the following two methods to infer it.

METHOD 1: If the corresponding catalogue only gives the information about the heliocentric distance d_{\odot} without any further information on the KDA, we use the relation

$$d_{\odot} = R_0 \cos \ell \pm \sqrt{R_{\text{gal}}^2 - (R_0 \sin \ell)^2} \quad (\text{C.7})$$

to obtain the Galactocentric radius R_{gal} . With R_{gal} , we then establish the near and far kinematic distances, from which we determine the chosen KDA solution. We only attempt to resolve the KDA if the near and far kinematic distances differ by more than 1 kpc; otherwise we remove the source from the catalogue.



METHOD 2: In case the KDA cannot be inferred via Method 1, we use functions contained in the BDC tool to calculate kinematic distance solutions and expected tangent point velocities $v_{\text{LSR}}^{\text{TP}}$ for the catalogue sources. If the v_{LSR} velocity of a catalogue source is within 10 km s^{-1} or is higher than $v_{\text{LSR}}^{\text{TP}}$, we assume that the source is too close to the tangent point to resolve the KDA properly. These sources are subsequently removed from the catalogue.

Next we check for clear KDA solutions. If the v_{LSR} velocity of the source is lower than the near KD solution or higher than the far KD solution we resolve the KDA as ‘N’ (near) or ‘F’ (far), respectively.

For the remaining sources we compare the given catalogue distance to the kinematic distance solutions and the tangent point distance. In case the difference of the literature distance to the tangent point is lower than the differences to both of the kinematic distance solutions, we do not attempt to resolve the KDA and remove the source from the catalogue. Otherwise, we choose the kinematic distance solution that has the smallest difference to the literature distance.

c.1.3 Literature results used in the KDA prior

We now discuss the catalogues that were used in this work to infer priors for the KDA. We required that the catalogues contain information about molecular gas v_{LSR} velocities, either reported directly or reported indirectly via a given kinematic distance. We only retain the catalogue sources for which we could infer whether the near or far distance solution was chosen; we exclude all catalogue entries which were assigned tangent point distances or which had uncertain KDA resolutions. For this work we did not attempt to incorporate distances obtained from alternative distance estimation methods, such as dust extinction mapping, if there was no information about the association with molecular gas. We also chose not to include catalogues based on $^{12}\text{CO} (1-0)$ observations.

Where available, we incorporated measured $^{13}\text{CO} (1-0)$ linewidths for the catalogue sources. If these did not exist, we either settled on linewidth measurements of a higher-density tracer or used median linewidth measurements obtained for comparable sources (i.e. clumps or clouds). We use a $w_{\text{V}}^{\text{min}}$ threshold of 0.125 for all catalogues, which means that we make a spectral association with a catalogue source if $|v_{\text{LSR}}^{\text{src}} - v_{\text{LSR}}| < \Theta_{\text{src}}$. We make a spatial association with sources from the clump catalogues if the (ℓ, b) coordinate of the PPV point is contained within twice the extent of the clump (i.e. $w_{\text{PP}}^{\text{min}} = 0.125$). For the more extended sources of the remaining catalogues, we only make a spatial association if the (ℓ, b) coordinate of the PPV point is located within or close to the elliptical or circular extent of the source (with $w_{\text{PP}}^{\text{min}} = 0.9$)

We give the clump catalogues a higher weight ($w_{\text{CAT}} = 0.75$) than the catalogues of more extended objects, such as molecular clouds and IRDCs ($w_{\text{CAT}} = 0.5$). This was done to favour the KDA information from the clumps on small scales, as the clumps are usually embedded within these more extended objects.

In Table C.1 we give an overview about the catalogues we used as KDA solutions in this work. $N_{\text{src}}^{\text{GRS}}$ gives the number of sources overlapping with the GRS coverage, and N_{Θ} , N_{N} , and N_{F} give the corresponding numbers of sources with measured



TABLE C.1: Overview of the catalogues used as KDA solutions in this work.

Info	$N_{\text{src}}^{\text{GRS}}$	N_{Θ}	N_{N}	N_{F}	$w_{\text{PP}}^{\text{min}}$	$w_{\text{V}}^{\text{min}}$	w_{CAT}	KDAR	Abb.	Ref.
ATLASGAL clumps	1745	426	1221	524	0.125	0.125	0.75	see App. C.1.3	U+18	1, 2, 3
BGPS v1 clumps	146	0	105	41	0.125	0.125	0.75	Method 1	E+12	4, 5, 6
BGPS v2.1 clumps	1046	455	754	292	0.125	0.125	0.75	given	EB+15	7, 8, 9
CHIMPS clumps	3294	3294	2318	976	0.125	0.125	0.75	given	R+19	10
Hi-GAL clumps	4021	0	3536	485	0.125	0.125	0.75	given	E+17	11
COHRS clouds	396	396	262	134	0.9	0.125	0.5	Method 2	C+19	12
GRS clouds	652	652	453	199	0.9	0.125	0.5	Method 1	RD+09	13, 14
GRS clouds (BGPS)	381	381	203	178	0.9	0.125	0.5	Method 1	BH14	15
MSX IRDCs	263	263	261	2	0.9	0.125	0.5	Method 2	S+06	16, 17, 18
GRS H II regions	169	169	49	120	0.9	0.125	0.5	given	A+09	19, 20
WISE H II regions	351	0	72	279	0.9	0.125	0.5	given	A+14	21
SNRs	23	0	17	6	0.9	0.125	0.5	given	R+18	22, 23, 24, 25, 26

Notes. ^(a) (1) Wielen et al. (2012); (2) Urquhart et al. (2014); (3) Urquhart et al. (2018); (4) Rosolowsky et al. (2010); (5) Eden et al. (2012); (6) Eden et al. (2013); (7) Ginsburg et al. (2013); (8) Ellsworth-Bowers et al. (2015); (9) Svoboda et al. (2016); (10) Rigby et al. (2019); (11) Elia et al. (2017); (12) Colombo et al. (2019); (13) Rathborne et al. (2009); (14) Roman-Duval et al. (2009); (15) Battisti & Heyer (2014); (16) Simon et al. (2006b); (17) Simon et al. (2006a); (18) Marshall et al. (2009); (19) Anderson et al. (2009); (20) Anderson & Bania (2009); (21) Anderson et al. (2014); (22) Leahy & Ranasinghe (2018); (23) Ranasinghe & Leahy (2018a); (24) Ranasinghe & Leahy (2018b); (25) Ranasinghe et al. (2018); (26) Green (2019).

linewidths, near, and far KD solutions, respectively. The columns $w_{\text{PP}}^{\text{min}}$, $w_{\text{V}}^{\text{min}}$, and w_{CAT} list the weights we used for the association of catalogue sources (Sect. C.1.1); the KDAR column specifies if the KDA resolution was given in the respective catalogue or how we calculated it otherwise. In the last two columns we give the abbreviation for the catalogues we refer to further on in the text and list the main references used to obtain information about the location, size, velocity, and distance information of the catalogue sources. In the following we discuss the individual catalogues in more detail.

ATLASGAL CLUMPS: [Urquhart et al. \(2018\)](#) presented distance results for clumps from the ATLASGAL survey in the inner Galactic plane ($|l| < 60^\circ$, $|b| < 1.5^\circ$). The catalogue does not contain explicit information on how the KDA was resolved but lists the kinematic distance solutions, the distance estimated with the BDC (v1), and the chosen distance. With that information we could infer the KDA information ('N', 'F') for 6317 clumps. Of these, 4457 clumps have linewidth measurements, of which 3139 were obtained from the SEDIGISM survey (Urquhart et al., in prep.), 668 measurements were taken from [Urquhart et al. \(2018\)](#), and 292 measurements were taken from [Wiener et al. \(2012\)](#). For the remaining clumps with resolved KDAs but missing linewidth information we assume a FWHM linewidth of 3.367 km s^{-1} , which corresponds to the median linewidth computed from the clumps with measurements. We took the size information for the ATLASGAL clumps from [Urquhart et al. \(2014\)](#). In total, 1745 ATLASGAL clumps with resolved KDAs overlap with the GRS coverage.

BGPS CLUMPS (v1): [Eden et al. \(2012\)](#) and [Eden et al. \(2013\)](#) presented KD determinations for clumps of the Bolocam Galactic Plane Survey (BGPS; [Rosolowsky et al., 2010](#)). We only use the sample of 165 BGPS sources whose distances were not inferred via an association with molecular clouds from [Roman-Duval et al. \(2009\)](#). We established the chosen KDA solution via Method 1, using $R_0 = 8.5 \text{ kpc}$ as assumed by [Eden et al. \(2012\)](#) and [Eden et al. \(2013\)](#). We take the corresponding position and size information of these clumps from v1 of the BGPS catalogue ([Rosolowsky et al., 2010](#)). For the linewidth of the clumps we assume a value of $\Theta = 3.316 \text{ km s}^{-1}$, which corresponds to the median linewidth of the BGPS v2.1 sample (see next paragraph).

BGPS CLUMPS (v2.1): [Ellsworth-Bowers et al. \(2015\)](#) resolved the KDA for 1320 BGPS clumps. We took the corresponding position and size information from v2.1 of the BGPS catalogue ([Ginsburg et al., 2013](#)). [Svoboda et al. \(2016\)](#) determined linewidths for 610 of these clumps from NH_3 observations. For clumps the associated ^{13}CO emission has in general broader linewidths than the NH_3 emission ([Wiener et al., 2012](#)). We thus decided to multiply the measured NH_3 linewidths of [Svoboda et al. \(2016\)](#) by a factor of two, which is based on the difference found by [Wiener et al. \(2012\)](#). For the remaining clumps without measured linewidths we assume the median NH_3 linewidth value from the [Svoboda et al. \(2016\)](#) sample corrected by a factor two, which corresponds to 3.316 km s^{-1} and compares very well to the median value from the ATLASGAL sample.



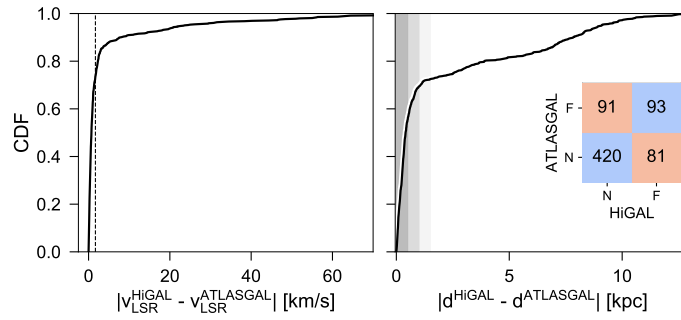


FIGURE C.2: Comparison between 685 associated Hi-GAL and ATLASGAL sources (Urquhart et al., 2018). *Left*: CDF of the absolute difference between the inferred and measured v_{LSR} velocities for the Hi-GAL and ATLASGAL catalogues, respectively. The dashed vertical line indicates the assumed linewidth for the Hi-GAL sources. *Right*: CDF of the absolute difference of reported distances for Hi-GAL and associated ATLASGAL sources. The vertical grey areas indicate distance bins of 0.5 kpc. The inset shows the corresponding confusion matrix for the KDA resolution.

CHIMPS CLUMPS: Rigby et al. (2019) used literature information to resolve the KDA for their sample of clumps compiled from the $^{13}\text{CO}/\text{C}^{18}\text{O}$ (J=3-2) Heterodyne Inner Milky Way Plane Survey (CHIMPS; Rigby et al., 2016). We use 3294 clumps that have the highest reliability flag and a resolved KDA. We take position, size, and spectral information of the clumps from Rigby et al. (2019).

HI-GAL CLUMPS: Elia et al. (2017) presented a compact source catalogue for the Herschel InfraRed Galactic Plane Survey (Hi-GAL), for which KDs were determined via the Brand & Blitz (1993) rotation curve. We only retain the sources for which an external indicator was used to solve the KD (flag ‘G’). The Elia et al. (2017) catalogue does not contain information about the associated v_{LSR} velocities of the sources. We used the function `brand_rotcurve.calc_vlsr` from the kinematic distance package presented in Wenger et al. (2018)¹ to infer the v_{LSR} velocities for the longitude and distance values of the sources in the Elia et al. (2017) catalogue. In Fig. C.2 we benchmark these estimated Hi-GAL v_{LSR} velocities for 685 sources that we could associate with ATLASGAL clumps from Urquhart et al. (2018). We associate a Hi-GAL source with an ATLASGAL clump if their central positions are less than $19.2''$ apart, which corresponds to the ATLASGAL beam size. The left panel in Fig. C.2 shows that the majority of estimated Hi-GAL v_{LSR} velocities match very well with the associated ATLASGAL clump velocities. The fraction of sources for which the v_{LSR} values are not consistent is likely due to wrong associations of spectral lines with the dust features, as there can be multiple molecular gas emission features along the line of sight that the dust feature could be associated with. For this work, we make no attempt to resolve these inconsistent v_{LSR} values. The right panel in Fig. C.2 shows the differences in the estimated distances for the 685 associated sources. Again, for the majority of associated sources the distance values are similar. More important for our context, for 75% of the associated sources the KDA resolution is identical. We take the location and size information for the Hi-GAL clumps from

¹ <https://ascl.net/1712.001>



Elia et al. (2017). For the linewidth, we assume for each clump the median linewidth estimated from the measured values from the ATLASGAL survey, which corresponds to $\Theta = 3.367 \text{ km s}^{-1}$.

COHRS MOLECULAR CLOUDS: Colombo et al. (2019) presented a cloud catalogue for the JCMT CO(3-2) High Resolution Survey (COHRS; Dempsey et al. 2013). We use their fiducial sample of 540 molecular clouds with well-defined distance estimations. We infer best-matching KDA solutions via Method 2, which yielded 396 KDA ('N', 'F') solutions.

GRS MOLECULAR CLOUDS: Roman-Duval et al. (2009) determined distances to 750 clouds from the catalogue of Rathborne et al. (2009) but do not explicitly specify the KDA resolution. Using Method 1 (with $R_0 = 8.5 \text{ kpc}$), we were able to infer the KDA solutions for 652 clouds. We took the position, size, and spectral information of the clouds from Rathborne et al. (2009).

GRS MOLECULAR CLOUDS CROSSMATCHED WITH BGPS CLUMPS: Battisti & Heyer (2014) compiled a catalogue of 437 molecular clouds from the GRS survey, which they associated with BGPS sources from the v1 catalogue (Rosolowsky et al., 2010). They resolve the KDA for their sources but do not explicitly list whether they chose the near or far solution. Using Method 1 (with $R_0 = 8.3 \text{ kpc}$), we could infer the chosen KDA solution for 389 clouds.

MSX IRDCS WITH VELOCITIES FROM GRS: Simon et al. (2006a) determined KDs to 313 IRDCs identified from observations of the *Midcourse Space Experiment* (Simon et al., 2006b), by morphologically matching the IRDCs to ^{13}CO (1–0) emission from the GRS. Simon et al. (2006a) argued that since the IRDCs are seen as extinction features they probably will be located in the foreground and thus always resolve the KDA in favour of the near solution. Marshall et al. (2009) used an alternative approach based on modelling the three-dimensional distribution of interstellar extinction towards 115 of these IRDCs, which allowed them to obtain distances that do not suffer from near/far ambiguities. Whenever these were available, we chose the Marshall et al. (2009) distance determinations over the ones obtained by Simon et al. (2006a). Using Method 2 (Sect. C.1.2), we could resolve the KDA for 272 IRDCs. We take the v_{LSR} and FWHM linewidth information for this sample of IRDCs from Simon et al. (2006a) and take their position and size information from Simon et al. (2006b).

H II REGIONS ASSOCIATED WITH GRS EMISSION: Anderson et al. (2009) associated 301 Galactic H II regions located within the GRS coverage with the corresponding ^{13}CO (1–0) properties. Anderson & Bania (2009) resolved the KDA for 266 of these H II regions using the H I emission/absorption and H I self-absorption methods. We include H II region sources as prior information if one of the following two conditions was fulfilled: the two methods yielded the same KDA resolution; or one of the methods received a high confidence label, in which case we use its KDA solution. We thus retained 169 sources, which had measured associated ^{13}CO (1–0)



properties and a resolved KDA. We take the position, size, and spectral information of the sources from [Anderson et al. \(2009\)](#).

WISE H II REGIONS: [Anderson et al. \(2014\)](#) compiled an H II region catalogue from observations of the *Wide-Field Infrared Survey Explorer* (WISE). Using v2.0 of the catalogue, we select all H II regions with resolved KDAs; we also take the position, size, and v_{LSR} information from this version of the catalogue. For the spectral extent, we use the median linewidth value from the sample of H II regions of [Anderson et al. \(2009\)](#) (see previous paragraph), which corresponds to a value of $\Theta = 4.05 \text{ km s}^{-1}$.

SUPERNOVA REMNANTS: We include KDA solutions for 23 Supernova remnants (SNRs) that have been obtained from H I 21 cm and GRS ^{13}CO line emission ([Ranasinghe & Leahy, 2018a; 2018b; Ranasinghe et al., 2018](#)). In case no information on the spatial extent was given in these works, we adopted the information given in [Leahy & Ranasinghe \(2018\)](#) and [Green \(2019\)](#). For the spectral extent, we assume the average linewidth of 3.6 km s^{-1} that [Rathborne et al. \(2009\)](#) find for their catalogue of molecular clouds of the GRS.

C.1.4 Effect of the KDA prior

In this section we discuss the effect of the KDA prior on the BDC results. For our tests we use the catalogues as detailed in Table C.1, so we include only sources that overlap with the GRS coverage and for which we could infer near or far KDA solutions.

First, we quantify the effect of the w_{CAT} weight on the distance estimation, for the two cases where the spiral arm priors are included ($P_{\text{SA}} = 0.5$) or switched off ($P_{\text{SA}} = 0$). For this test we use only the KDA information from the ATLASGAL sample and do not consider any of the other catalogues. We perform different distance runs with the BDC for the ATLASGAL sample; for each run, we supply the BDC with the correct KDA solutions for the sources and just vary the weight w_{CAT} , which determines the strength of the resulting P_{far} prior. For example, for $w_{\text{CAT}} = 0.5$ a far KDA solution yields $P_{\text{far}} = 0.75$, whereas with $w_{\text{CAT}} = 0.75$ this increases to $P_{\text{far}} = 0.875$. For $w_{\text{CAT}} = 1$ we would thus expect the highest correspondence between our calculated distances and the distances given in [Urquhart et al. \(2018\)](#)². To test how robust the BDC results are against wrong KDA solutions, we also perform distance calculations for which we intentionally supply the incorrect KDA solutions for the ATLASGAL sample.

Table C.2 lists the performance of the BDC results for 20 runs, for which we vary w_{CAT} between the values 0, 0.25, 0.5, 0.75, and 1, use or switch off the P_{SA} prior, and supply either the correct or incorrect KDA solutions. The $\delta(x)$ parameter gives the percentage of calculated distance values whose absolute error is within x kpc of the literature distances; we report $\delta(x)$ for x intervals of ± 0.5 , ± 1.0 , and ± 1.5 kpc. The runs with $w_{\text{CAT}} = 0$ correspond to the default BDC distance estimations that do not consider any prior information on the KDA and thus serve as our benchmarks.

² However, since [Urquhart et al. \(2018\)](#) used an older version of the BDC (v1), we would not expect a perfect correspondence of the distance results even in this best case scenario.

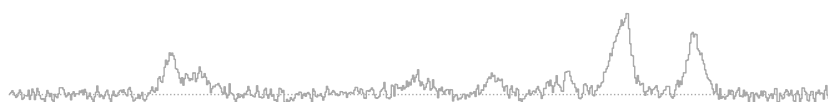


TABLE C.2: BDC results for the ATLASGAL clump sample for different w_{CAT} and P_{SA} values and correct or incorrect KDA priors.

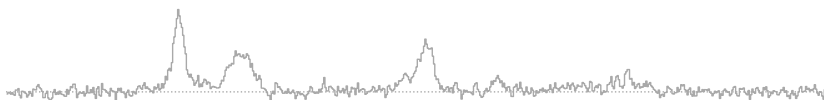
P_{SA}	w_{CAT}	correct KDA			incorrect KDA		
		$\delta(0.5)$ [%]	$\delta(1.0)$ [%]	$\delta(1.5)$ [%]	$\delta(0.5)$ [%]	$\delta(1.0)$ [%]	$\delta(1.5)$ [%]
0.5	0	36.2	56.3	62.7	36.2	56.3	62.7
0.5	0.25	40.9	63.7	70.1	33.4	49.7	55.0
0.5	0.5	46.6	70.8	77.5	28.1	43.6	47.6
0.5	0.75	50.1	75.6	83.3	21.0	32.0	35.9
0.5	1	55.1	83.7	92.6	7.6	10.6	14.2
0	0	37.4	52.3	58.9	37.4	52.3	58.9
0	0.25	44.5	62.6	72.3	23.8	32.3	36.7
0	0.5	53.5	77.0	84.8	16.6	20.7	23.7
0	0.75	59.5	82.7	91.1	8.9	10.7	12.8
0	1	58.3	81.9	91.6	2.4	3.0	5.4

The runs for which we supplied the correct KDA solution show a clear increase in the fraction of matching distances with increasing w_{CAT} value. This is expected, as KDA solutions are more enforced with increasing w_{CAT} values. In the runs where we use the prior for spiral arms ($P_{\text{SA}} = 0.5$), the percentage of matching distance values is less; however, the vast majority of the estimated distances is still close to the literature values.

Unsurprisingly, the supply of incorrect KDA solutions yields wrong distance estimates, especially the higher the w_{CAT} value, that means the more we enforce these KDA solutions. This effect is very strong for the runs where the spiral arm prior was switched off and the prior for the kinematic distances was the dominating factor for the BDC results. Using the prior for the spiral arms can mitigate the negative impact of the incorrect KDA solutions; for $w_{\text{CAT}} = 0.5$ almost half the sources have distance results within 1.5 kpc to the literature distances even though we intentionally forced the BDC to prioritise the wrong KDA solution.

This test demonstrated that the BDC run with $P_{\text{SA}} = 0.5$ is more robust against priors using wrong KDA solutions than the run with $P_{\text{SA}} = 0$. Moreover, we find that w_{CAT} values of 0.5 to 0.75 are preferable values for the catalogue weights, as they offer a good balance between recovery of correct distances with the right KDA solutions for $P_{\text{SA}} = 0$ and robustness against incorrect distances with the wrong KDA solutions for $P_{\text{SA}} = 0.5$.

Next, we want to quantify the effect of using all available KDA information with their corresponding weights (Table C.1). Using the ATLASGAL sample, we again perform different BDC runs with $P_{\text{SA}} = 0.5$ and $P_{\text{SA}} = 0$. For the KDA prior we either use none of the catalogues (giving us a benchmark for the default BDC performance), all KDA solutions from Table C.1 excluding the ATLASGAL catalogue itself, and all KDA solutions including the ATLASGAL catalogue. Figure C.3 shows the BDC results plotted against the literature values for these six BDC runs. Table C.3



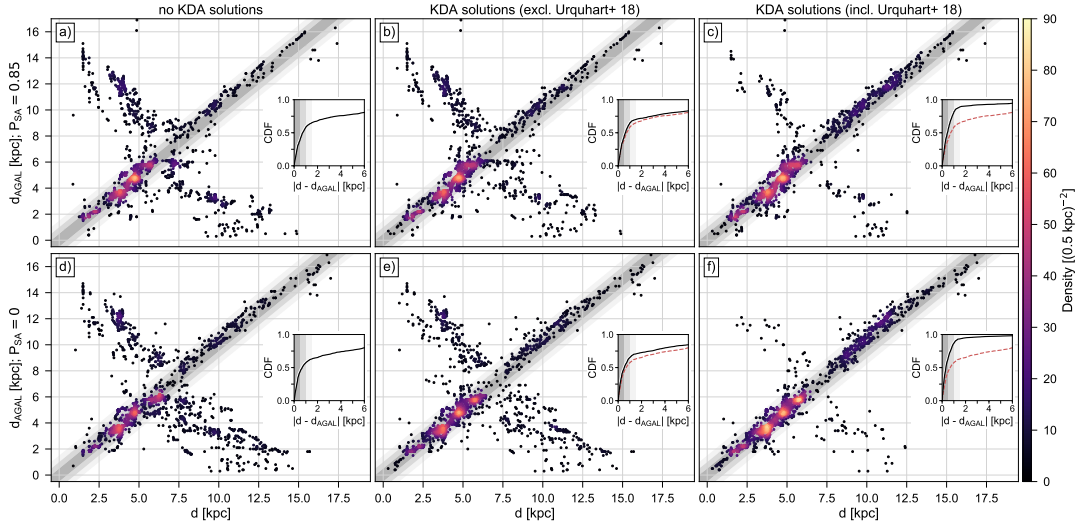


FIGURE C.3: BDC results for the ATLASGAL clump sample plotted against their literature values (d_{AGAL}). The six panels correspond to different settings for the spiral arm and KDA priors. The points are colour-coded by their density. The insets show the CDFs for the difference between the BDC results and the literature distances of the respective panels. The red dashed line in the insets of *panels b and c* and *panels e and f* correspond to the CDFs of *panel a* and *d*, respectively. The grey-shaded areas in the main panels and insets correspond to $|d - d_{\text{AGAL}}|$ intervals of 0.5, 1.0, and 1.5 kpc. See Appendix C.1.4 for more details.

TABLE C.3: BDC results for the ATLASGAL sample for different spiral arm and KDA priors.

KDA	$P_{\text{SA}} = 0.5$			$P_{\text{SA}} = 0$		
	$\delta(0.5)$ [%]	$\delta(1.0)$ [%]	$\delta(1.5)$ [%]	$\delta(0.5)$ [%]	$\delta(1.0)$ [%]	$\delta(1.5)$ [%]
no	39.1	58.5	65.1	43.6	57.4	63.0
excl. U+18	43.7	64.8	70.1	48.9	65.3	70.6
incl. U+18	53.7	81.0	89.1	63.7	86.8	93.4

gives the corresponding percentages of matching distance values within ranges of $\delta(x)$ (with $x = 0.5, 1$, and 1.5 kpc) that are highlighted with the grey-shaded areas in Fig. C.3. The runs which use no KDA solutions (panels a and d) show a large dichotomy between near and far distance solutions. Including all KDA solutions apart from the [Urquhart et al. \(2018\)](#) catalogue itself already manages to improve the correspondence between the distances and indicates that the sources of the remaining catalogues overlap with many of the ATLASGAL clumps. Finally, as expected, the inclusion of the [Urquhart et al. \(2018\)](#) catalogue leads to the best correspondence of the distance results. However, for many sources the spiral arm priors lead to a preference of different KDA resolutions (panel c). By switching the spiral arm prior off, we manage to drastically reduce the instances for which a different KDA solution was favoured. The remaining fraction of clumps for which a different KDA solution was chosen was due to mismatching KDA solutions from different catalogues. For example, [Urquhart et al. \(2018\)](#) give a near distance solution of 3.5 kpc for the clump

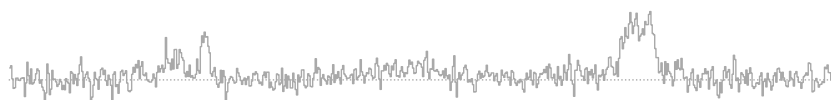


TABLE C.4: BDC results for the remaining catalogues from Table C.1 for different spiral arm and KDA priors.

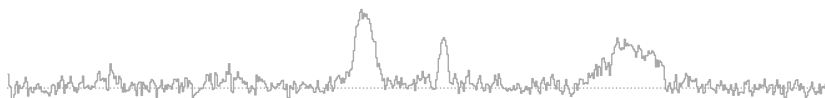
Abb.	$P_{SA} = 0.5$			$P_{SA} = 0$		
	$\delta(1.5)$	$\delta^-(1.5)$	$\delta^+(1.5)$	$\delta(1.5)$	$\delta^-(1.5)$	$\delta^+(1.5)$
	[%]	[%]	[%]	[%]	[%]	[%]
E+12	21.2	45.9	80.8	33.6	67.8	91.1
EB+15	56.6	80.2	88.5	59.1	87.1	92.4
R+19	50.6	79.8	91.3	63.5	90.6	95.7
E+17	51.3	80.6	91.4	62.6	89.3	95.9
C+19	47.0	69.4	74.2	52.3	78.8	84.6
RD+09	38.8	69.3	80.1	52.5	82.5	92.0
BH14	29.8	54.0	65.0	36.0	66.1	76.1
S+06	44.5	74.1	87.5	51.0	76.0	89.4
A+09	25.4	50.3	63.3	30.2	56.8	69.2
A+14	32.2	58.7	68.7	41.9	72.1	83.2
R+18	43.5	78.3	78.3	60.9	91.3	91.3

AGAL020.662-00.139, whereas spatially and spectrally overlapping sources in five other catalogues (A+09, RD+09, BH14, EB+15, E+17) favour a far distance solution, leading to a BDC value of 10.1 kpc.

Finally, we list the performance of the BDC results for the remaining catalogues used for KDA information in Table C.4. We again perform different BDC runs with $P_{SA} = 0.5$ and $P_{SA} = 0$ and give the percentage of sources for which the distance was within a range of 1.5 kpc to the literature distance for the cases where no literature KDA solution is used (labelled δ), and KDA solutions from all catalogues excluding and including the one for which the distances are calculated (labelled δ^- and δ^+ , respectively). We see already an improvement in matching distances for the δ^- runs, which indicates that there is a good overlap between sources from all catalogues. As expected, we see the highest correspondence between the BDC and literature distance results for the runs in which the spiral arm prior is switched off. In conclusion, our tests showed that the BDC runs with supplied literature KDA solutions are able to match the vast majority of distance results from each of the individual catalogues used to infer KDA priors. This result is not self-evident, given that many of these catalogues use different assumptions about the rotation curve parameters. We thus infer that our obtained distance results are consistent with the vast majority of the literature results.

C.2 EFFECTS OF BEAM AVERAGING ON THE OBSERVED LINEWIDTH

We designed the following simplified experiment to test how fluctuations of the line centroids can broaden the linewidth via beam averaging effects. We perform different runs for which we vary the spatial resolution of a given PPV cube to



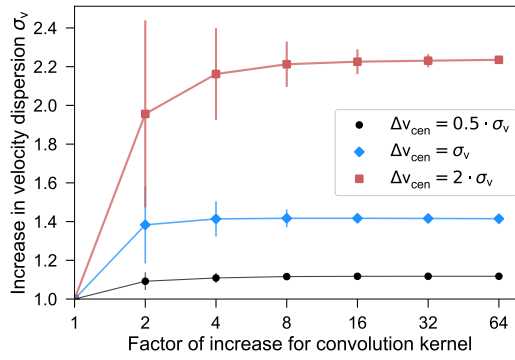


FIGURE C.4: Increase in observed velocity dispersion with decreasing spatial resolution. The points and errorbars show the results of 100 different realisations of a mock PPV cube containing emission lines with identical σ_v values; errorbars indicate 1σ intervals. For each realisation, the standard deviation for the variation of emission line centroids (Δv_{cen}) was varied between 0.5, 1, or 2 times σ_v (indicated in black, blue, and red, respectively). See Appendix C.2 for more details.

simulate observations of regions at different heliocentric distances. For each run we construct PPV cubes with dimension (100, 100, 30) and populate each of the spectra with a single Gaussian component, whose velocity dispersion is two spectral channels. For simplicity we do not assume any noise. The mean position of the Gaussian is centred along the spectral axis with the centroid of the spectrum allowed to vary for each component; the standard deviation of this variation (Δv_{cen}) is set either to 0.5, 1, or 2 times the velocity dispersion. Assuming the pixel size to be equal to the FWHM of the resolution element or beam, we convolve this cube with a 2D Gaussian kernel whose FWHM is set to either 2, 4, 8, 16, 32, or 64 times the pixel size, thus simulating observations of regions at 2 to 64 times the distance of our original cube, which corresponds approximately to the variation present in the GRS. We then determine the velocity dispersion of a Gaussian fit to the central spectrum of the spatially smoothed cube.

Figure C.4 presents the results for 100 different realisations of the PPV cube and shows that the measured σ_v in the spatially smoothed cubes increases significantly with increasing Δv_{cen} . Variations of Δv_{cen} on the order of the velocity dispersion of the emission line in the resolved cube lead to increases in σ_v in the spatially unresolved cubes by a factor of ~ 1.4 .

In real observations Δv_{cen} will not be distributed randomly. Rather, the distribution of line centroids is observed to be highly structured (Henshaw et al., in press) with coherent gradients, which will result in similar effects as in our simplified case. Moreover, variation in the non-thermal contribution to the linewidth can lead to an additional broadening of the lines at coarser spatial resolution. We thus conclude that due to beam averaging effects it is very unlikely that we observe the same population of linewidths in regions located at far distances as in nearby regions, whose emission lines are spatially better resolved.



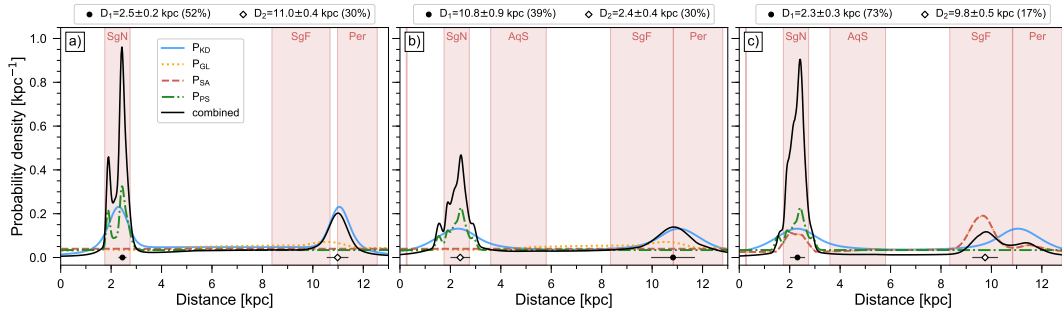


FIGURE C.5: Effect of v_{LSR} uncertainties on BDC results for a source located at $\ell = 35^\circ$, $b = 0.1^\circ$, and $v_{\text{LSR}} = 40 \text{ km s}^{-1}$. The BDC settings are the same for *panels a* and *b*; for *panel c* we included the prior for spiral arms. We increase Δv_{LSR} from 1 km s^{-1} (*panel a*) to 10 km s^{-1} (*panels b* and *c*). The meaning of the lines and symbols is the same as in Fig. 4.2. See App. C.3.1 for more details.

C.3 CHARACTERISATION OF THE BDC PERFORMANCE

Here we give some further details about the performance of the BDC. We also discuss the effect of the KDA and size-linewidth priors (Sects. 4.1.3 and 4.1.4) on our final distance results.

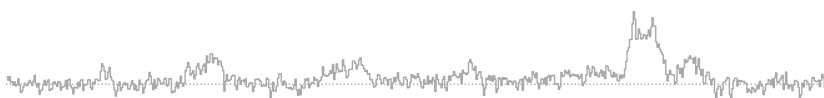
C.3.1 Effect of v_{LSR} uncertainties

Version 2.4 of the BDC allows to supply uncertainties for the v_{LSR} measurement, which can have strong effects on the distance estimation (Fig. C.5). For each fit component, we chose either its estimated v_{LSR} uncertainty or its σ_v value for Δv_{LSR} , whichever was the higher value. The median uncertainty of the Δv_{LSR} values for all fit components was 1.1 km s^{-1} , with an IQR of 0.7 to 1.9 km s^{-1} .

Figure C.5 illustrates the effect of Δv_{LSR} on the distance results. The first two panels (a, b) show distance results obtained with identical BDC settings, where only the supplied uncertainty on the v_{LSR} coordinate was different. Increasing the v_{LSR} uncertainty has multiple effects: the KD peaks get broadened and the association with parallax sources is increased. In our example this causes a shift of the estimated most likely distance from the near to the far KD solution. Finally, panel (c) illustrates the effect of Δv_{LSR} on the association with spiral arms. Larger Δv_{LSR} values lead to an increase in associations with Galactic features. In our example it led to the consideration of the Aquila Spur and Aquila Rift as possible candidates for an association; however this had only a very limited effect on the combined distance PDF.

C.3.2 Distance results without P_{far} priors

Here we discuss the impact of the KDA and size-linewidth priors (see Sect. 4.1.3 and 4.1.4) on our distance results. For this purpose we created four additional BDC runs:



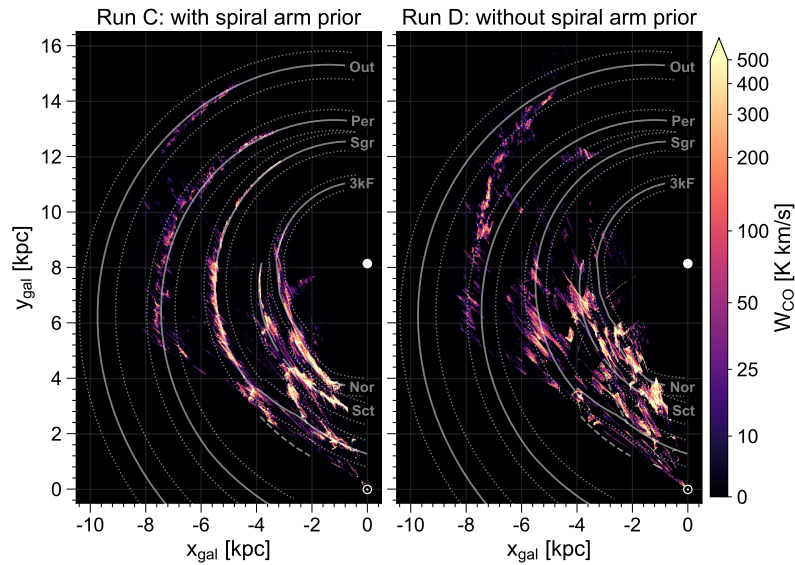


FIGURE C.6: Same as Fig. 4.8 but for the distance results obtained with the default settings of the BDC. When displayed in Adobe Acrobat, it is possible to switch to [the original map](#) (Fig. 4.8), hide the [spiral arm positions](#) and the [grid](#).

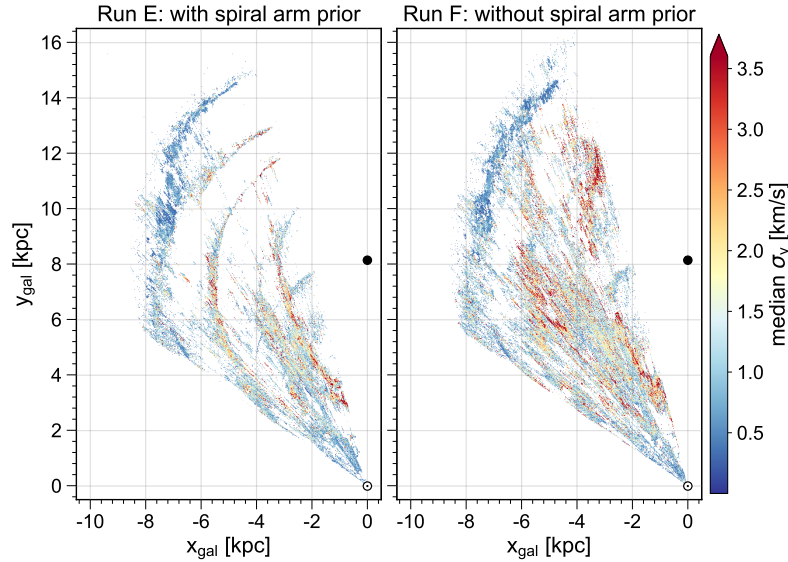
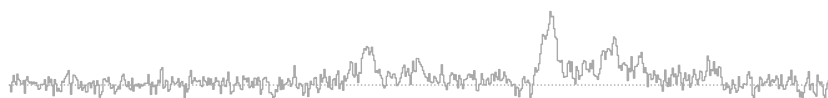


FIGURE C.7: Face-on view of the median velocity dispersion values of Gaussian fit components for the BDC results obtained with (*left*) and without (*right*) the spiral arm prior. The values are binned in 10×10 pc cells and the median was calculated along the z_{gal} axis. The position of the sun and Galactic centre are indicated by the sun symbol and black dot, respectively. When displayed in Adobe Acrobat, it is possible to switch to [the original map](#) (Fig. 4.10), show the [spiral arm positions](#) and hide the [grid](#).



- Run C: Uses the default settings of the BDC, that means $P_{SA} = 0.85$, but does not include the KDA and size-linewidth priors.
- Run D: Same as Run C, but with the SA prior switched off ($P_{SA} = 0$), which also sets $P_{GL} = 0$ as these two priors are combined in the default BDC settings.
- Run E: Same as Run A, but without the size-linewidth prior.
- Run F: Same as Run B, but without the size-linewidth prior.

Figure C.6 shows the map of W_{CO} values for Run C and D. A comparison with Fig. 4.8 reveals substantial differences to Run A and B, respectively. The default BDC settings in Run C lead to a much stronger association with the SA model and the results contain much less emission at close distances ($d < 2$ kpc). However, compared to Run A, Run C does not put emission in between the Perseus and Outer arm. Run D shows that without the KDA and GL priors the distance results contain a higher fraction of emission-free areas, which is especially notable around the far portion of the Sagittarius arm. Without the size-linewidth prior, Run D also puts significantly more emission from close distances towards the Perseus and Outer arm regions. In terms of association with Galactic features: for Run C 13.8% of the emission (and 18.6% of the fit components) were associated with interarm regions, which increased to 25.6% (34.6% of N_{comp}) for Run D.

Figure C.7 shows the resulting σ_v map if we had not used the size-linewidth prior. Since we use this prior only for emission with $v_{LSR} < 20$ km s⁻¹, only positions at the largest R_{gal} values are affected by it. A comparison with Run A and B shows that the size-linewidth prior helps in decreasing the confusion between near and far emission that causes the large fraction of emission lines with narrow linewidths at large distances in Run E and F.

C.3.3 Estimated probabilities, P_{far} weights, and distance choices

Figure C.8 shows a face-on view of the median estimated probability values and the left panel in Fig. C.9 gives the cumulative distribution of all estimated probabilities. These probabilities were estimated from the integrated areas of Gaussian fit components to the combined distance PDF (Sect. 4.1.5). We thus get higher probabilities for regions where the combined distance PDF produced a dominant peak, which however could be caused by negative effects. For example, the near distance solution of the KD prior is cut off for low v_{LSR} values (see Fig. 4.3), thus yielding far distance solutions with high estimated probabilities. The KD prior is also down-weighted for lower R_{gal} values, which could lead to strongly blended KD peaks. This could result in broad Gaussian fits over both of these peaks, with high distance uncertainties and high probability values, which seems to occur at the lowest R_{gal} values (see Fig. 4.21).

The cumulative distribution of the assigned probabilities for the distance values (left panel of Fig. C.9) shows that the chosen distance values from the BDC run with the SA prior have higher associated probabilities. For Run A, 43.8% of the chosen distance values had probabilities > 0.75 and 16.7% of the distance values had probabilities < 0.5 ; for Run B, these fractions change to 33.6% and 21.0%, respectively.



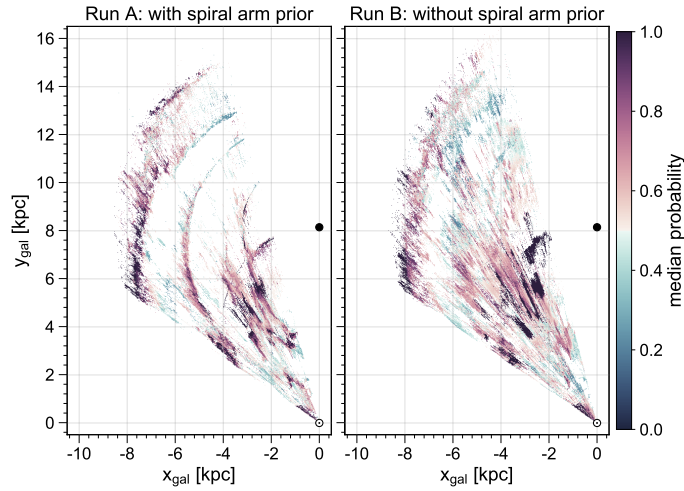


FIGURE C.8: Face-on view of the median probability values from the BDC results obtained with (*left*) and without (*right*) the spiral arm prior. The values are binned in 10×10 pc cells and the median was calculated along the z_{gal} axis. The position of the sun and Galactic centre are indicated by the sun symbol and black dot, respectively. When displayed in Adobe Acrobat, it is possible to show the `spiral arm positions` and hide the `grid`.

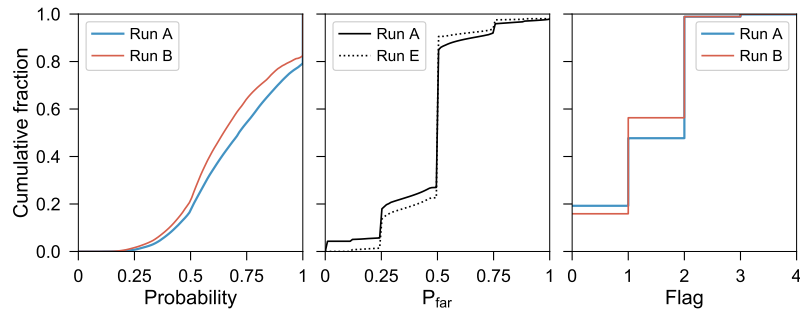


FIGURE C.9: Cumulative distributions for the estimated distance probabilities (*left*), values for the P_{far} prior (*middle*), and choice of the distance values (*right*). See Sect. C.3.3 for more details.

Thus for Run A the Gaussian fits to the combined distance PDF had higher integrated areas, confirming that the addition of the SA prior leads to more well-defined peaks.

The middle panel of Fig. C.9 shows the cumulative distribution of chosen weights for the P_{far} prior for the case where the KDA prior was used (dotted line) and the case where the size-linewidth prior (Sect. 4.1.4) was used in addition to the KDA (solid line). For the case in which P_{far} was only informed by the KDA prior, 23.1% and 7.6% of the fit components received a preference for the near and far KD solution, respectively. If the size-linewidth prior is used in addition to the KDA prior, these percentages increase to 27.5% and 13.3%, respectively.

Finally, the right panel of Fig. C.9 shows the cumulative distribution for the choice of distance values (Sect. 4.1.5). The numbers indicate the following conditions: the distance assignment yielded only one distance solution (0); the associated Gaussian fit of one distance solution did not satisfy the criterion for the amplitude threshold



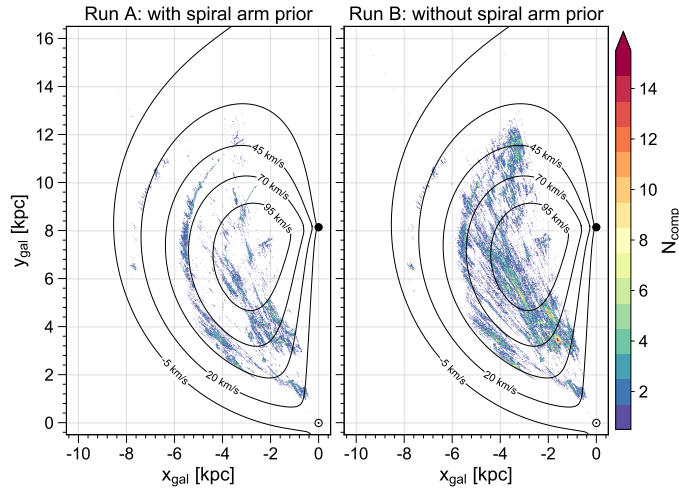
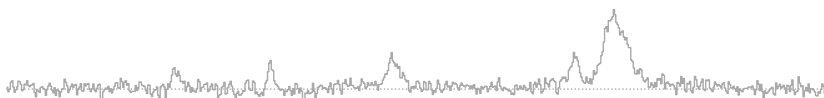


FIGURE C.10: Face-on view of the number of components with distance results that cause an absolute v_{LSR} deviation of more than 10 km s^{-1} compared to the Galactic rotation curve model for the BDC results obtained with (*left*) and without (*right*) the spiral arm prior. The values are binned in $10 \times 10 \text{ pc}$ cells and the values were summed up along the z_{gal} axis. The position of the sun and Galactic centre are indicated by the sun symbol and black dot, respectively. When displayed in Adobe Acrobat, it is possible to show the spiral arm positions, hide the curves of constant projected v_{LSR} , and hide the grid.

(1); the distance solution with the highest probability (i.e. the highest integrated intensity of the associated Gaussian fit) was chosen (2); the distance solution with the lowest absolute distance error was chosen (3); and the near KD solution was picked randomly (4). The cumulative distribution shows that conditions (0), (1), and (2) were responsible for the vast majority of final distance choices (contributing 19.2%, 28.5%, and 51.2% for Run A and 15.9%, 40.4%, and 42.6% for Run B), whereas conditions (3) and (4) only contributed minimally.

c.3.4 Deviation from Galactic rotation curve

Here we quantify the deviation of our distance results from the expected values from the Galactic rotation curve model. These deviations are interesting as they can identify regions with high peculiar velocities. Figure C.10 shows the number of fit components whose estimated distance values caused a deviation of more than 10 km s^{-1} from the expected v_{LSR} value based on the Galactic rotation curve. In Run A and B, 2.2% and 6.2% of the components showed such a large v_{LSR} deviation. Since both panels show similar deviations occurring around the positions of the Sagittarius, Scutum, and Norma arms, it is likely that these differences from pure rotation curve velocities are to a large part due to the effect of the maser parallax sources (see Fig. 4.1). For Run B we can also identify an increase in the number of components with deviating v_{LSR} values inside $R_{\text{gal}} \lesssim 5 \text{ kpc}$. For this region the BDC downweighted the KD prior, so these deviating components might to a large part simply be due to large associated distance uncertainties. A comparison with Fig. 4.21 shows that these regions are indeed associated with increased uncertainty values.



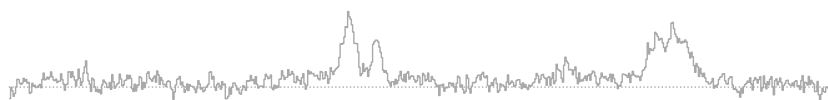
LIST OF SYMBOLS

a_i	amplitude of Gaussian fit component i
b	Galactic latitude
d_{\odot}	heliocentric distance
d_{beam}	physical extent of beam size
f_a	multiplication factor to get maximum amplitude limit for fit components
f_{Θ}	factor determining when FWHM of fit components is flagged as broad
f_{sep}	factor determining the minimum required separation between two fit components
f_w	factor that determines the weight given to neighbouring spectra
F ₁ score	measure of the accuracy for the decomposition of the training set
ℓ	Galactic longitude
N_{chan}	number of channels in a spectrum
N_{comp}	number of fitted Gaussian components in a spectrum
N_{jump}	maximum number of allowed ΔN_{jump} occurrences for a single spectrum
N_{med}	weighted median number of components determined from neighbouring fit solutions
N_{min}	minimum number of spectral channels that the signal intervals in a spectrum must have
N_{pad}	number of spectral channels added to the left and right of signal intervals
N_{refit}	number of refitted spectra
P_{Limit}	probability threshold for assigning spectral feature as noise
p -value	p -value for the null hypothesis that the residual resembles a normal distribution
P_{far}	weight for the kinematic distance ambiguity prior
P_{GL}	weight for the Galactic latitude prior
P_{KD}	weight for the kinematic distance prior
P_{PS}	weight for the parallax sources prior
P_{SA}	weight for the spiral arm prior
R_0	distance to the Galactic centre
R_{gal}	Galactocentric radius
S/N_{min}	minimum S/N ratio for signal peaks in the data
$S/N_{\text{min, fit}}$	minimum S/N ratio for fit components
$S/N_{\text{min, neg}}$	minimum S/N ratio for negative peaks in the spectrum

S/N_{spike}	S/N threshold for noise spikes
SNR_1	S/N threshold used for original spectrum
SNR_2	S/N threshold used for second derivative of smoothed spectrum
T_{ex}	excitation temperature
$T_{\text{B}}, T_{\text{MB}}$	peak main beam brightness temperature
v_{LSR}	radial velocity compared to the local standard of rest
W_{CO}	integrated intensity
w_{CAT}	weight for the catalogue of literature distances
w_{σ}^{far}	weight for the far kinematic distance
w_{σ}^{near}	weight for the near kinematic distance
Z_{gal}	distance from the Galactic midplane
Z_{offset}	offset position of the Sun to the Galactic midplane
α_1	first GAUSSPY smoothing parameter
α_2	second GAUSSPY smoothing parameter
$\Delta\mu_{\text{max}}$	maximum difference in offset positions of fit components for grouping
$\Delta\Theta_{\text{max}}$	maximum difference in FWHM values of fit components for grouping
ΔN_{max}	maximum allowed N_{comp} difference w.r.t. all neighbouring spectra
ΔN_{jump}	maximum allowed N_{comp} difference between individual neighbouring spectra
Θ_i	FWHM value of Gaussian fit component i
Θ_0	circular rotation speed at the position of the Sun
Θ_{min}	minimum value for the FWHM of fit components
Θ_{max}	maximum value for the FWHM of fit components
μ_i	offset or mean position of Gaussian fit component i
ξ	minimum number of spectral channels that a peak has to contain on either side
σ_i	standard deviation of Gaussian fit component i
σ_{rms}	root-mean-square noise of spectrum
$\sigma(T_{\text{A}}^*)$	root-mean-square noise of spectrum in antenna temperature values
$\sigma_{v_{\text{los}}}, \sigma_v$	line of sight velocity dispersion
σ_v^{exp}	expected line of sight velocity dispersion for assumed size-linewidth relationship
$\sigma_{v, \text{med}}$	median velocity dispersion
$\tilde{\sigma}$	standard deviation of σ_{exp}
τ_0^{13}	optical depth for ^{13}CO (1–0) line
χ_{red}^2	reduced chi-squared; chi-squared per degree of freedom
$\mathcal{F}_{\text{neg. res. peak}}$	flag for negative residual features
\mathcal{F}_{Θ}	flag for broad fit components



$\mathcal{F}_{\text{blended}}$	flag for blended fit components
$\mathcal{F}_{\text{residual}}$	flag for fit results not passing normality tests
$\mathcal{F}_{N_{\text{comp}}}$	flag for fit results with incompatible number of components w.r.t. neighbours
\mathcal{F}_{tot}	sum of the $\mathcal{F}_{\text{blended}}$, $\mathcal{F}_{\text{neg. res. peak}}$, \mathcal{F}_{Θ} , $\mathcal{F}_{\text{residual}}$, and $\mathcal{F}_{N_{\text{comp}}}$ flags
$\mathcal{M}_{\sigma_{v_{\text{los}}}, 3D}$	turbulent Mach number
$\mathcal{S}_{\text{data}}$	significance estimate for signal peaks
\mathcal{S}_{fit}	significance estimate for fitted Gaussian components
\mathcal{S}_{min}	minimum significance value for signal peaks and fit components
\mathcal{W}	weight threshold
\mathcal{W}_{min}	minimum weight threshold for termination of phase 2 of the spatially coherent refitting



ACRONYMS

2D	Two-Dimensional
AICc	corrected Akaike Information Criterion
BDC	Bayesian Distance Calculator
CDF	Cumulative Distribution Function
CO	Carbon Monoxide
FWHM	Full Width at Half Maximum
GL	Galactic Latitude
GRS	Galactic Ring Survey
Hi-GAL	<i>Herschel</i> Infrared Galactic plane survey
IQR	Interquartile Range
IRDC	Infrared Dark Cloud
ISM	Interstellar Medium
KD	Kinematic Distance
KDA	Kinematic Distance Ambiguity
LSR	Local Standard of Rest
PDF	Probability Distribution Function
PPV	Position-Position-Velocity
PS	Parallax Sources
PV	Position-Velocity
SA	Spiral Arm
SAA	Spectral Averaging Area
S/N	Signal-to-Noise

PUBLICATIONS

In the following I list all publications I have been involved in during my PhD. This includes first-author papers, co-authored papers, and database entries. Chapter 2 is based on [Riener et al. \(2019\)](#), Chapter 3 is based on [Riener et al. \(2020\)](#), and Chapter 4 is based on Riener et al. (in prep.). Chapters 1 and 5 are partially based on the three aforementioned publications.

REFEREED

Riener, M. et al. (2018). "Gathering dust: A galaxy-wide study of dust emission from cloud complexes in NGC 300." In: *A&A* 612, A81.

Riener, M. et al. (2019). "GAUSSPY+: A fully automated Gaussian decomposition package for emission line spectra." In: *A&A* 628, A78.

Riener, M. et al. (2020). "Autonomous Gaussian decomposition of the Galactic Ring Survey. I. Global statistics and properties of the ^{13}CO emission data." In: *A&A* 633, A14.

REFEREED (CO-AUTHORED)

Henshaw, J.D. et al. (2019). "'The Brick' is not a brick: a comprehensive study of the structure and dynamics of the central molecular zone cloud G0.253+0.016." In: *MNRAS* 285, pp. 2457-2485.

Henshaw, J.D. et al. (in press). "Ubiquitous velocity fluctuations throughout the molecular interstellar medium." In: *Nature Astronomy*.

SUBMITTED / IN PREPARATION

Duarte-Cabral, A. et al. (subm.). "The SEDIGISM survey: Molecular clouds in the inner Galaxy."

Schuller, F. et al. (subm.). "The SEDIGISM survey: first data release and overview of the Galactic structure."

Riener, M. et al. (in prep.). "Autonomous Gaussian decomposition of the Galactic Ring Survey. II. Distance estimates for fit components and distribution of the ^{13}CO gas."

DATABASE ENTRIES

Riener, M. et al. (2017). "VizieR Online Data Catalog J/A+A/612/A81: NGC 300 giant dust clouds (Riener+, 2018)." Originally published in: *A&A* 612, A81.

Riener, M. et al. (2019). "GaussPy+: Gaussian decomposition package for emission line spectra." In: *Astrophysics Source Code Library*, record ascl:1907.020.

Riener, M. et al. (2019). "VizieR Online Data Catalog J/A+A/633/A14: GaussPy+ decomposition of Galactic Ring Survey (Riener+, 2020)." Originally published in: *A&A* 633, A14.



BIBLIOGRAPHY

- Akaike, H. (1973). "Information Theory and an Extension of the Maximum Likelihood Principle." In: ed. by B. N. Petrov & F. Csaki. Proceedings of the 2nd International Symposium on Information Theory, pp. 267–281.
- Anderson, L. D. & T. M. Bania (2009). "Resolution of the Distance Ambiguity for Galactic H II Regions." In: *ApJ* 690.1, pp. 706–719.
- Anderson, L. D. et al. (2009). "The Molecular Properties of Galactic H II Regions." In: *ApJS* 181.1, pp. 255–271.
- Anderson, L. D. et al. (2014). "The WISE Catalog of Galactic H II Regions." In: *ApJS* 212.1, p. 1.
- Anderson, L. D. et al. (2017). "Galactic supernova remnant candidates discovered by THOR." In: *A&A* 605, A58.
- Anderson, L. D. et al. (2019). "A Galactic Plane Defined by the Milky Way H II Region Distribution." In: *ApJ* 871.2, p. 145.
- Andrae, R. et al. (2010). "Dos and don'ts of reduced chi-squared." In: *arXiv e-prints*, arXiv:1012.3754.
- André, P. et al. (2014). "From Filamentary Networks to Dense Cores in Molecular Clouds: Toward a New Paradigm for Star Formation." In: *Protostars and Planets VI*. Ed. by H. Beuther et al., p. 27.
- Arzoumanian, D. et al. (2013). "Formation and evolution of interstellar filaments. Hints from velocity dispersion measurements." In: *A&A* 553, A119.
- Ballesteros-Paredes, J. et al. (2007). "Molecular Cloud Turbulence and Star Formation." In: *Protostars and Planets V*. Ed. by B. Reipurth et al., p. 63.
- Bania, T. M. (1977). "Carbon monoxide in the inner Galaxy." In: *ApJ* 216, pp. 381–403.
- Banks, H. T. & M. L. Joyner (2017). "AIC under the framework of least squares estimation." In: *Applied Mathematics Letters* 74, pp. 33–45.
- Barnes, A. T. et al. (2018). "Similar complex kinematics within two massive, filamentary infrared dark clouds." In: *MNRAS* 475, pp. 5268–5289.
- Barnes, P. J. et al. (2015). "The Three-mm Ultimate Mopra Milky Way Survey. I. Survey Overview, Initial Data Releases, and First Results." In: *ApJ* 812, p. 6.
- Battisti, A. J. & M. H. Heyer (2014). "The Dense Gas Mass Fraction of Molecular Clouds in the Milky Way." In: *ApJ* 780.2, p. 173.
- Beaumont, C. N. et al. (2013). "Quantifying Observational Projection Effects Using Molecular Cloud Simulations." In: *ApJ* 777.2, p. 173.
- Benedettini, M. et al. (2020). "The Forgotten Quadrant Survey. ^{12}CO and ^{13}CO (1-0) survey of the Galactic plane in the range $220^\circ < l < 240^\circ$ $-2.^\circ 5 < b < 0^\circ$." In: *A&A* 633, A147.
- Bergin, E. A. & M. Tafalla (2007). "Cold Dark Clouds: The Initial Conditions for Star Formation." In: *ARA&A* 45.1, pp. 339–396.
- Bergin, E. A. & J. P. Williams (2017). "The Determination of Protoplanetary Disk Masses." In: *Astrophysics and Space Science Library*. Ed. by M. Pessah & O. Gressel. Vol. 445. Astrophysics and Space Science Library, p. 1.

- Bergin, E. A. et al. (2006). "The Thermal Structure of Gas in Prestellar Cores: A Case Study of Barnard 68." In: *ApJ* 645.1, pp. 369–380.
- Berry, D. S. (2015). "FellWalker-A clump identification algorithm." In: *Astronomy and Computing* 10, pp. 22–31.
- Bertin, E. et al. (2002). "The TERAPIX Pipeline." In: *Astronomical Data Analysis Software and Systems XI*. Ed. by D. A. Bohlender et al. Vol. 281. Astronomical Society of the Pacific Conference Series, p. 228.
- Beuther, H. & T. K. Sridharan (2007). "Outflow and Dense Gas Emission from Massive Infrared Dark Clouds." In: *ApJ* 668.1, pp. 348–358.
- Beuther, H. et al. (2012). "Galactic Structure Based on the ATLASGAL 870 μm Survey." In: *ApJ* 747.1, p. 43.
- Bland-Hawthorn, J. & O. Gerhard (2016). "The Galaxy in Context: Structural, Kinematic, and Integrated Properties." In: *ARA&A* 54, pp. 529–596.
- Bolatto, A. D. et al. (2013). "The CO-to-H₂ Conversion Factor." In: *ARA&A* 51.1, pp. 207–268.
- Braiding, C. et al. (2018). "The Mopra Southern Galactic Plane CO Survey—Data Release 3." In: *Publications of the Astronomical Society of Australia* 35, e029.
- Brand, J. & L. Blitz (1993). "The velocity field of the outer galaxy." In: *A&A* 275, pp. 67–90.
- Breitschwerdt, D. & S. Komossa (2000). "Galactic Fountains and Galactic Winds." In: *Ap&SS* 272, pp. 3–13.
- Burkhart, B. et al. (2013). "Hierarchical Structure of Magnetohydrodynamic Turbulence in Position-position-velocity Space." In: *ApJ* 770.2, p. 141.
- Burnham, K. P. & D. R. Anderson (1998). *Model Selection and Inference: A Practical Information-Theoretic Approach*. Vol. 80. Springer-Verlag.
- Burton, M. G. et al. (2013). "The Mopra Southern Galactic Plane CO Survey." In: *PASA* 30, e044.
- Burton, W. B. (1971). "Galactic Structure Derived from Neutral Hydrogen Observations Using Kinematic Models Based on the Density-wave Theory." In: *A&A* 10, p. 76.
- Burton, W. B. (1976). "The morphology of hydrogen and of other tracers in the Galaxy." In: *ARA&A* 14, pp. 275–306.
- Burton, W. B. et al. (1975). "The overall distribution of carbon monoxide in the plane of the Galaxy." In: *ApJ* 202, pp. 30–49.
- Busso, M. et al. (1999). "Nucleosynthesis in Asymptotic Giant Branch Stars: Relevance for Galactic Enrichment and Solar System Formation." In: *ARA&A* 37, pp. 239–309.
- Chen, H. H.-H. et al. (2019). "Droplets. I. Pressure-dominated Coherent Structures in L1688 and B18." In: *ApJ* 877.2, p. 93.
- Cheung, A. C. et al. (1968). "Detection of NH₃ Molecules in the Interstellar Medium by Their Microwave Emission." In: *Phys. Rev. Lett.* 21.25, pp. 1701–1705.
- Cheung, A. C. et al. (1969). "Detection of Water in Interstellar Regions by its Microwave Radiation." In: *Nature* 221.5181, pp. 626–628.
- Clarke, S. D. et al. (2018). "Synthetic C¹⁸O observations of fibrous filaments: the problems of mapping from PPV to PPP." In: *MNRAS* 479, pp. 1722–1746.
- Clemens, D. P. (1985). "Massachusetts-Stony Brook Galactic plane CO survey: the galactic disk rotation curve." In: *ApJ* 295, pp. 422–436.



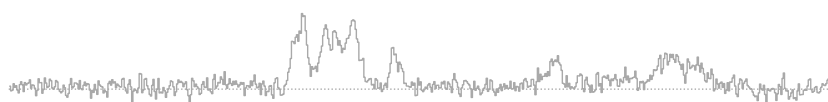
- Clemens, D. P. et al. (1986). "Massachusetts–Stony Brook Galactic Plane CO Survey. II. (I,V) Maps of the First Galactic Quadrant." In: *ApJS* 60, p. 297.
- Colombo, D. et al. (2015). "Graph-based interpretation of the molecular interstellar medium segmentation." In: *MNRAS* 454.2, pp. 2067–2091.
- Colombo, D. et al. (2019). "The integrated properties of the molecular clouds from the JCMT CO(3-2) High-Resolution Survey." In: *MNRAS* 483, pp. 4291–4340.
- Colombo, D. et al. (2014). "The PdBI Arcsecond Whirlpool Survey (PAWS): Environmental Dependence of Giant Molecular Cloud Properties in M51." In: *ApJ* 784.1, p. 3.
- Combes, F. (1991). "Distribution of CO in the Milky Way." In: *ARA&A* 29, pp. 195–237.
- Dame, T. M. (2011). "Optimization of Moment Masking for CO Spectral Line Surveys." In: *ArXiv e-prints*.
- Dame, T. M. & P. Thaddeus (1985). "A wide-latitude CO survey of molecular clouds in the northern Milky Way." In: *ApJ* 297, pp. 751–765.
- Dame, T. M. et al. (2001). "The Milky Way in Molecular Clouds: A New Complete CO Survey." In: *ApJ* 547, pp. 792–813.
- Dempsey, J. T. et al. (2013). "CO (3 - 2) High-resolution Survey of the Galactic Plane: R1." In: *ApJS* 209, p. 8.
- Dénes, H. et al. (2018). "Calibrating the HISA temperature: Measuring the temperature of the Riegel-Crutcher cloud." In: *MNRAS* 479, pp. 1465–1490.
- Dobbs, C. L. et al. (2011). "Why are most molecular clouds not gravitationally bound?" In: *MNRAS* 413.4, pp. 2935–2942.
- Dobbs, C. L. et al. (2014). "Formation of Molecular Clouds and Global Conditions for Star Formation." In: *Protostars and Planets VI*. Ed. by H. Beuther et al., p. 3.
- Draine, B. T. (2011). *Physics of the Interstellar and Intergalactic Medium*.
- Duarte-Cabral, A. & C. L. Dobbs (2016). "What can simulated molecular clouds tell us about real molecular clouds?" In: *MNRAS* 458.4, pp. 3667–3683.
- D'Agostino, R. B. (1971). "An omnibus test of normality for moderate and large sample size." In: *Biometrika* 58, pp. 341–348.
- D'Agostino, R. B. & E. S. Pearson (1973). "Tests for departure from normality." In: *Biometrika* 60, pp. 613–622.
- Eden, D. J. et al. (2012). "Star formation towards the Scutum tangent region and the effects of Galactic environment." In: *MNRAS* 422.4, pp. 3178–3188.
- Eden, D. J. et al. (2013). "Star formation in Galactic spiral arms and the interarm regions." In: *MNRAS* 431.2, pp. 1587–1595.
- Eden, D. J. et al. (2015). "Star formation scales and efficiency in Galactic spiral arms." In: *MNRAS* 452.1, pp. 289–300.
- Elia, D. et al. (2017). "The Hi-GAL compact source catalogue - I. The physical properties of the clumps in the inner Galaxy ($-71.0^\circ < \ell < 67.0^\circ$)." In: *MNRAS* 471.1, pp. 100–143.
- Ellsworth-Bowers, T. P. et al. (2013). "The Bolocam Galactic Plane Survey. VIII. A Mid-infrared Kinematic Distance Discrimination Method." In: *ApJ* 770.1, p. 39.
- Ellsworth-Bowers, T. P. et al. (2015). "The Bolocam Galactic Plane Survey. XII. Distance Catalog Expansion Using Kinematic Isolation of Dense Molecular Cloud Structures with $^{13}\text{CO}(1-0)$." In: *ApJ* 799.1, p. 29.



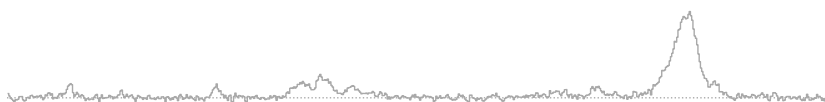
- Elmegreen, B. G. (1987). "Supercloud Formation by Nonaxisymmetric Gravitational Instabilities in Sheared Magnetic Galaxy Disks." In: *ApJ* 312, p. 626.
- Elmegreen, B. G. (2009). "Star Formation in Disks: Spiral Arms, Turbulence, and Triggering Mechanisms." In: *The Galaxy Disk in Cosmological Context*. Ed. by J. Andersen et al. Vol. 254. IAU Symposium, pp. 289–300.
- Elmegreen, B. G. & E. Falgarone (1996). "A Fractal Origin for the Mass Spectrum of Interstellar Clouds." In: *ApJ* 471, p. 816.
- Elmegreen, B. G. & J. Scalo (2004). "Interstellar Turbulence I: Observations and Processes." In: *ARA&A* 42, pp. 211–273.
- Ewen, H. I. & E. M. Purcell (1951). "Observation of a Line in the Galactic Radio Spectrum: Radiation from Galactic Hydrogen at 1,420 Mc./sec." In: *Nature* 168, p. 356.
- Falgarone, E. et al. (1991). "The Edges of Molecular Clouds: Fractal Boundaries and Density Structure." In: *ApJ* 378, p. 186.
- Falgarone, E. et al. (2009). "Intermittency of interstellar turbulence: extreme velocity-shears and CO emission on milliparsec scale." In: *A&A* 507, pp. 355–368.
- Federrath, C. et al. (2010). "Comparing the statistics of interstellar turbulence in simulations and observations. Solenoidal versus compressive turbulence forcing." In: *A&A* 512, A81.
- Federrath, C. et al. (2016). "The Link between Turbulence, Magnetic Fields, Filaments, and Star Formation in the Central Molecular Zone Cloud G0.253+0.016." In: *ApJ* 832.2, p. 143.
- Federrath, C. & R. S. Klessen (2012). "The Star Formation Rate of Turbulent Magnetized Clouds: Comparing Theory, Simulations, and Observations." In: *ApJ* 761.2, p. 156.
- Ferrière, K. M. (2001). "The interstellar environment of our galaxy." In: *Reviews of Modern Physics* 73.4, pp. 1031–1066.
- Field, G. B. et al. (1969). "Cosmic-Ray Heating of the Interstellar Gas." In: *ApJ* 155, p. L149.
- Giannetti, A. et al. (2014). "ATLASGAL-selected massive clumps in the inner Galaxy. I. CO depletion and isotopic ratios." In: *A&A* 570, A65.
- Ginsburg, A. & J. Mirocha (2011). *PySpecKit: Python Spectroscopic Toolkit*. Astrophysics Source Code Library.
- Ginsburg, A. et al. (2013). "The Bolocam Galactic Plane Survey. IX. Data Release 2 and Outer Galaxy Extension." In: *ApJS* 208.2, p. 14.
- Goldsmith, P. F. et al. (2008). "Large-Scale Structure of the Molecular Gas in Taurus Revealed by High Linear Dynamic Range Spectral Line Mapping." In: *ApJ* 680.1, pp. 428–445.
- Gómez, G. C. (2006). "Errors in Kinematic Distances and Our Image of the Milky Way Galaxy." In: *AJ* 132.6, pp. 2376–2382.
- González Lobos, V. & A. M. Stutz (2019). "Gas velocity structure of the Orion A integral-shaped filament." In: *MNRAS* 489.4, pp. 4771–4782.
- Goodman, A. A. et al. (2014). "The Bones of the Milky Way." In: *ApJ* 797.1, p. 53.
- Gould, R. J. & E. E. Salpeter (1963). "The Interstellar Abundance of the Hydrogen Molecule. I. Basic Processes." In: *ApJ* 138, p. 393.



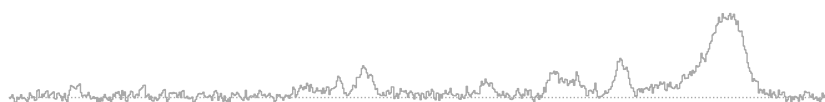
- Gravity Collaboration et al. (2019). "A geometric distance measurement to the Galactic center black hole with 0.3% uncertainty." In: *A&A* 625, p. L10.
- Green, D. A. (2019). "A revised catalogue of 294 Galactic supernova remnants." In: *Journal of Astrophysics and Astronomy* 40.4, p. 36.
- Gum, C. S. et al. (1960). "A 21-cm determination of the principal plane of the Galaxy." In: *MNRAS* 121, p. 132.
- Hacar, A. et al. (2013). "Cores, filaments, and bundles: hierarchical core formation in the L1495/B213 Taurus region." In: *A&A* 554, A55.
- Hacar, A. et al. (2016). "Opacity broadening and interpretation of suprathermal CO linewidths: Macroscopic turbulence and tangled molecular clouds." In: *A&A* 591, A104.
- Haud, U. (2000). "Gaussian decomposition of the Leiden/Dwingeloo survey. I. Decomposition algorithm." In: *A&A* 364, pp. 83–101.
- Heiderman, A. et al. (2010). "The Star Formation Rate and Gas Surface Density Relation in the Milky Way: Implications for Extragalactic Studies." In: *ApJ* 723.2, pp. 1019–1037.
- Heiles, C. & T. H. Troland (2003). "The Millennium Arecibo 21 Centimeter Absorption-Line Survey. II. Properties of the Warm and Cold Neutral Media." In: *ApJ* 586, pp. 1067–1093.
- Hennebelle, P. & E. Falgarone (2012). "Turbulent molecular clouds." In: *A&A Rev.* 20, p. 55.
- Hennebelle, P. & M. Pérault (1999). "Dynamical condensation in a thermally bistable flow. Application to interstellar cirrus." In: *A&A* 351, pp. 309–322.
- Henshaw, J. D. et al. (2014). "The dynamical properties of dense filaments in the infrared dark cloud G035.39-00.33." In: *MNRAS* 440, pp. 2860–2881.
- Henshaw, J. D. et al. (2016a). "Molecular gas kinematics within the central 250 pc of the Milky Way." In: *MNRAS* 457, pp. 2675–2702.
- Henshaw, J. D. et al. (2016b). "Seeding the Galactic Centre gas stream: gravitational instabilities set the initial conditions for the formation of protocluster clouds." In: *MNRAS* 463.1, pp. L122–L126.
- Henshaw, J. D. et al. (2019). "'The Brick' is not a brick: a comprehensive study of the structure and dynamics of the central molecular zone cloud G0.253+0.016." In: *MNRAS* 485.2, pp. 2457–2485.
- Henshaw, J. D. et al. (in press). "Ubiquitous velocity fluctuations throughout the molecular interstellar medium." In: *Nature Astronomy*.
- Hernandez, A. K. et al. (2011). "Mapping Large-scale CO Depletion in a Filamentary Infrared Dark Cloud." In: *ApJ* 738.1, p. 11.
- Heyer, M. H. & C. M. Brunt (2004). "The Universality of Turbulence in Galactic Molecular Clouds." In: *ApJ* 615, pp. L45–L48.
- Heyer, M. & T. M. Dame (2015). "Molecular Clouds in the Milky Way." In: *ARA&A* 53, pp. 583–629.
- Heyer, M. et al. (2009). "Re-Examining Larson's Scaling Relationships in Galactic Molecular Clouds." In: *ApJ* 699.2, pp. 1092–1103.
- Hily-Blant, P. & E. Falgarone (2009). "Intermittency of interstellar turbulence: parsec-scale coherent structure of intense, velocity shear." In: *A&A* 500, pp. L29–L32.



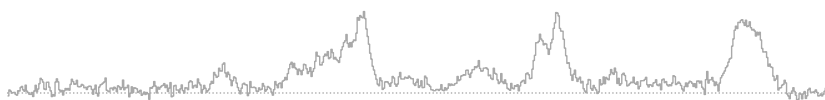
- Hollenbach, D. & E. E. Salpeter (1971). "Surface Recombination of Hydrogen Molecules." In: *ApJ* 163, p. 155.
- Hurvich, C. M. & C. L. Tsai (1989). "Regression and time series model selection in small samples." In: *Biometrika* 76, pp. 297–307.
- Jackson, J. M. et al. (2006). "The Boston University-Five College Radio Astronomy Observatory Galactic Ring Survey." In: *ApJS* 163.1, pp. 145–159.
- Jackson, J. M. et al. (2002). "H I Self-Absorption and the Kinematic Distance Ambiguity: The Case of the Molecular Cloud GRSMC 45.6+0.3." In: *ApJ* 566.2, pp. L81–L84.
- Kainulainen, J. & J. C. Tan (2013). "High-dynamic-range extinction mapping of infrared dark clouds. Dependence of density variance with sonic Mach number in molecular clouds." In: *A&A* 549, A53.
- Kalberla, P. M. W. & J. Kerp (2009). "The HI Distribution of the Milky Way." In: *ARA&A* 47.1, pp. 27–61.
- Kaper, H. G. et al. (1966). "Computer Analysis of Observed Distributions into Gaussian Components." In: *Bull. Astron. Inst. Netherlands* 18, pp. 465–487.
- Kauffmann, J. et al. (2017). "Molecular Line Emission as a Tool for Galaxy Observations (LEGO). I. HCN as a tracer of moderate gas densities in molecular clouds and galaxies." In: *A&A* 605, p. L5.
- Kawata, D. et al. (2019). "Galactic rotation from Cepheids with Gaia DR2 and effects of non-axisymmetry." In: *MNRAS* 482.1, pp. 40–51.
- Keto, E. et al. (2015). "The dynamics of collapsing cores and star formation." In: *MNRAS* 446, pp. 3731–3740.
- Khoperskov, S. et al. (2018). "Bar quenching in gas-rich galaxies." In: *A&A* 609, A60.
- Klessen, R. S. (2011). "Star Formation in Molecular Clouds." In: *EAS Publications Series*. Ed. by C. Charbonnel & T. Montmerle. Vol. 51. EAS Publications Series, pp. 133–167.
- Klessen, R. S. & S. C. O. Glover (2016). "Physical Processes in the Interstellar Medium." In: *Saas-Fee Advanced Course* 43, p. 85.
- Koch, E. W. & E. W. Rosolowsky (2015). "Filament identification through mathematical morphology." In: *MNRAS* 452.4, pp. 3435–3450.
- Kolmogorov, A. N. (1933). "Sulla determinazione empirica di una legge di distribuzione." In: *Giornale dell'istituto Italiano degli Attuari* 4, 83–91 (6.1).
- Kong, S. et al. (2018). "The CARMA-NRO Orion Survey." In: *ApJS* 236.2, p. 25.
- Koyama, H. & S.-i. Inutsuka (2002). "An Origin of Supersonic Motions in Interstellar Clouds." In: *ApJ* 564.2, pp. L97–L100.
- Kramer, C. et al. (1998). "Clump mass spectra of molecular clouds." In: *A&A* 329, pp. 249–264.
- Kritsuk, A. G. et al. (2013). "A supersonic turbulence origin of Larson's laws." In: *MNRAS* 436.4, pp. 3247–3261.
- Krumholz, M. R. et al. (2014). "Star Cluster Formation and Feedback." In: *Protostars and Planets VI*. Ed. by H. Beuther et al., p. 243.
- Krumholz, M. R. (2015). "Notes on Star Formation." In: *arXiv e-prints*, arXiv:1511.03457.
- Kulesa, C. (2011). "Terahertz Spectroscopy for Astronomy: From Comets to Cosmology." In: *IEEE Transactions on Terahertz Science and Technology* 1.1, pp. 232–240.



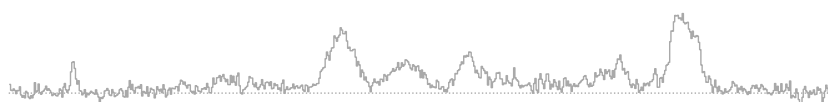
- Kulkarni, S. R. & C. Heiles (1988). "Neutral hydrogen and the diffuse interstellar medium." In: *Galactic and Extragalactic Radio Astronomy*. Ed. by K. I. Kellermann & G. L. Verschuur, pp. 95–153.
- Larson, R. B. (1981). "Turbulence and star formation in molecular clouds." In: *MNRAS* 194, pp. 809–826.
- Leahy, D. A. & S. Ranasinghe (2018). "Evolutionary Models for 15 Galactic Supernova Remnants with New Distances." In: *ApJ* 866.1, p. 9.
- Lilley, A. E. (1955). "The Association of Gas and Dust from 21-CM Hydrogen Radio Observations." In: *ApJ* 121, p. 559.
- Lindner, R. R. et al. (2015). "Autonomous Gaussian Decomposition." In: *AJ* 149, p. 138.
- Liszt, H. S. & W. B. Burton (1981). "Interpretation of CO emission from the galactic molecular cloud ensemble." In: *ApJ* 243, pp. 778–813.
- Liu, H.-L. et al. (2019). "Large-scale periodic velocity oscillation in the filamentary cloud G350.54+0.69." In: *MNRAS* 487.1, pp. 1259–1268.
- Loomis, R. A. et al. (2018). "Detecting Weak Spectral Lines in Interferometric Data through Matched Filtering." In: *AJ* 155.4, p. 182.
- López-Corredoira, M. & F. Sylos Labini (2019). "Gaia-DR2 extended kinematical maps . I. Method and application." In: *A&A* 621, A48.
- Mac Low, M.-M. & R. S. Klessen (2004). "Control of star formation by supersonic turbulence." In: *Reviews of Modern Physics* 76.1, pp. 125–194.
- Mangum, J. G. & Y. L. Shirley (2015). "How to Calculate Molecular Column Density." In: *PASP* 127.949, p. 266.
- Marchal, A. et al. (2019). "ROHSA: Regularized Optimization for Hyper-Spectral Analysis. Application to phase separation of 21 cm data." In: *A&A* 626, A101.
- Marsh, K. A. et al. (2015). "Temperature as a third dimension in column-density mapping of dusty astrophysical structures associated with star formation." In: *MNRAS* 454.4, pp. 4282–4292.
- Marsh, K. A. et al. (2017). "Multitemperature mapping of dust structures throughout the Galactic Plane using the PPMAP tool with Herschel Hi-GAL data." In: *MNRAS* 471.3, pp. 2730–2742.
- Marshall, D. J. et al. (2009). "Distribution and Characteristics of Infrared Dark Clouds Using Genetic Forward Modelling." In: *ApJ* 706.1, pp. 727–737.
- Matzner, C. D. (2002). "On the Role of Massive Stars in the Support and Destruction of Giant Molecular Clouds." In: *ApJ* 566.1, pp. 302–314.
- McKee, C. F. & J. P. Ostriker (1977). "A theory of the interstellar medium: three components regulated by supernova explosions in an inhomogeneous substrate." In: *ApJ* 218, pp. 148–169.
- McKee, C. F. & E. C. Ostriker (2007). "Theory of Star Formation." In: *ARA&A* 45.1, pp. 565–687.
- Mebold, U. (1972). "On the Intercloud H I Gas." In: *A&A* 19, p. 13.
- Miesch, M. S. et al. (1999). "Velocity Field Statistics in Star-forming Regions. I. Centroid Velocity Observations." In: *ApJ* 524.2, pp. 895–922.
- Miville-Deschênes, M.-A. et al. (2017). "Physical Properties of Molecular Clouds for the Entire Milky Way Disk." In: *ApJ* 834.1, p. 57.



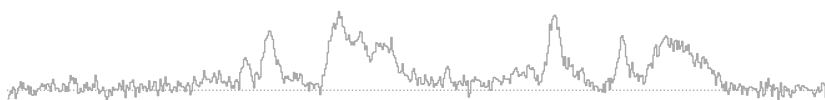
- Molinari, S. et al. (2016a). "Hi-GAL, the Herschel infrared Galactic Plane Survey: photometric maps and compact source catalogues. First data release for the inner Milky Way." In: *A&A* 591, A149.
- Molinari, S. et al. (2016b). "Large-scale latitude distortions of the inner Milky Way disk from the Herschel/Hi-GAL Survey." In: *A&A* 588, A75.
- Moore, T. J. T. et al. (2012). "The effect of spiral arms on star formation in the Galaxy." In: *MNRAS* 426.1, pp. 701–707.
- Mottram, J. C. & C. M. Brunt (2010). "Molecular Cloud Determination in the Northern Galactic Plane." In: *The Dynamic Interstellar Medium: A Celebration of the Canadian Galactic Plane Survey*. Ed. by R. Kothés et al. Vol. 438. Astronomical Society of the Pacific Conference Series, p. 98.
- Murray, C. E. et al. (2018). "The 21-SPONGE H I Absorption Line Survey. I. The Temperature of Galactic H I." In: *ApJS* 238, p. 14.
- Murray, N. (2011). "Star Formation Efficiencies and Lifetimes of Giant Molecular Clouds in the Milky Way." In: *ApJ* 729.2, p. 133.
- Myers, P. C. & V. K. Khersonsky (1995). "On Magnetic Turbulence in Interstellar Clouds." In: *ApJ* 442, p. 186.
- Nakanishi, H. & Y. Sofue (2006). "Three-Dimensional Distribution of the ISM in the Milky Way Galaxy: II. The Molecular Gas Disk." In: *PASJ* 58, pp. 847–860.
- Orkisz, J. H. et al. (2017). "Turbulence and star formation efficiency in molecular clouds: solenoidal versus compressive motions in Orion B." In: *A&A* 599, A99.
- Orkisz, J. H. et al. (2019). "A dynamically young, gravitationally stable network of filaments in Orion B." In: *A&A* 624, A113.
- Ossenkopf, V. & M.-M. Mac Low (2002). "Turbulent velocity structure in molecular clouds." In: *A&A* 390, pp. 307–326.
- Padoan, P. et al. (2014). "The Star Formation Rate of Molecular Clouds." In: *Protostars and Planets VI*. Ed. by H. Beuther et al., p. 77.
- Parker, E. N. (1966). "The Dynamical State of the Interstellar Gas and Field." In: *ApJ* 145, p. 811.
- Penzias, A. A. et al. (1971). "Interstellar $^{12}\text{C}^{16}\text{O}$, $^{13}\text{C}^{16}\text{O}$, and $^{12}\text{C}^{18}\text{O}$." In: *ApJ* 165, p. 229.
- Persic, M. et al. (1996). "The universal rotation curve of spiral galaxies — I. The dark matter connection." In: *MNRAS* 281.1, pp. 27–47.
- Pety, J. et al. (2013). "The Plateau de Bure + 30 m Arcsecond Whirlpool Survey Reveals a Thick Disk of Diffuse Molecular Gas in the M51 Galaxy." In: *ApJ* 779.1, p. 43.
- Pichardo, B. et al. (2000). "On the Effects of Projection on Morphology." In: *ApJ* 532.1, pp. 353–360.
- Pineda, J. L. et al. (2010). "The Relation Between Gas and Dust in the Taurus Molecular Cloud." In: *ApJ* 721, pp. 686–708.
- Pitann, J. et al. (2013). "G048.66-0.29: Physical State of an Isolated Site of Massive Star Formation." In: *ApJ* 766.2, p. 68.
- Pon, A. et al. (2016). "Mid-J CO shock tracing observations of infrared dark clouds. II. Low-J CO constraints on excitation, depletion, and kinematics." In: *A&A* 587, A96.
- Ragan, S. E. et al. (2014). "Giant molecular filaments in the Milky Way." In: *A&A* 568, A73.



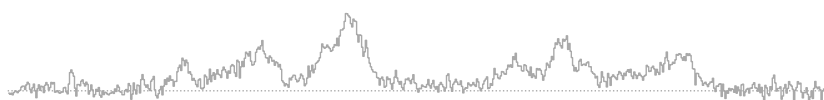
- Ragan, S. E. et al. (2016). "The prevalence of star formation as a function of Galactocentric radius." In: *MNRAS* 462.3, pp. 3123–3129.
- Ragan, S. E. et al. (2018). "The role of spiral arms in Milky Way star formation." In: *MNRAS* 479.2, pp. 2361–2373.
- Ramón-Fox, F. G. & I. A. Bonnell (2018). "Streaming motions and kinematic distances to molecular clouds." In: *MNRAS* 474, pp. 2028–2038.
- Ranasinghe, S. & D. A. Leahy (2018a). "Revised Distances to 21 Supernova Remnants." In: *AJ* 155.5, p. 204.
- Ranasinghe, S. & D. A. Leahy (2018b). "Distances to supernova remnants G20.4+0.1, G24.7-0.6, and G28.6-0.1 and new molecular cloud associations." In: *MNRAS* 477.2, pp. 2243–2250.
- Ranasinghe, S. et al. (2018). "New Distances to Four Supernova Remnants." In: *Open Physics Journal* 4, pp. 1–13.
- Rathborne, J. M. et al. (2009). "Molecular Clouds and Clumps in the Boston University-Five College Radio Astronomy Observatory Galactic Ring Survey." In: *ApJS* 182, pp. 131–142.
- Reid, M. J. et al. (2009). "Trigonometric Parallaxes of Massive Star-Forming Regions. VI. Galactic Structure, Fundamental Parameters, and Noncircular Motions." In: *ApJ* 700.1, pp. 137–148.
- Reid, M. J. et al. (2014). "Trigonometric Parallaxes of High Mass Star Forming Regions: The Structure and Kinematics of the Milky Way." In: *ApJ* 783.2, p. 130.
- Reid, M. J. et al. (2016). "A Parallax-based Distance Estimator for Spiral Arm Sources." In: *ApJ* 823.2, p. 77.
- Reid, M. J. et al. (2019). "Trigonometric Parallaxes of High-mass Star-forming Regions: Our View of the Milky Way." In: *ApJ* 885.2, p. 131.
- Rezaei Kh., S. et al. (2017). "Inferring the three-dimensional distribution of dust in the Galaxy with a non-parametric method. Preparing for Gaia." In: *A&A* 598, A125.
- Rezaei Kh., S. et al. (2018). "Detection of the Milky Way spiral arms in dust from 3D mapping." In: *A&A* 618, A168.
- Rice, T. S. et al. (2016). "A Uniform Catalog of Molecular Clouds in the Milky Way." In: *ApJ* 822, p. 52.
- Ridge, N. A. et al. (2006). "The COMPLETE Survey of Star-Forming Regions: Phase I Data." In: *AJ* 131.6, pp. 2921–2933.
- Riener, M. et al. (2019). "GAUSSPY+: A fully automated Gaussian decomposition package for emission line spectra." In: *A&A* 628, A78.
- Riener, M. et al. (2020). "Autonomous Gaussian decomposition of the Galactic Ring Survey. I. Global statistics and properties of the ^{13}CO emission data." In: *A&A* 633, A14.
- Rigby, A. J. et al. (2016). "CHIMPS: the $^{13}\text{CO}/\text{C}^{18}\text{O}$ ($J = 3 \rightarrow 2$) Heterodyne Inner Milky Way Plane Survey." In: *MNRAS* 456, pp. 2885–2899.
- Rigby, A. J. et al. (2019). "CHIMPS: physical properties of molecular clumps across the inner Galaxy." In: *A&A* 632, A58.
- Rogers, H. & J. M. Pittard (2013). "Feedback from winds and supernovae in massive stellar clusters - I. Hydrodynamics." In: *MNRAS* 431.2, pp. 1337–1351.



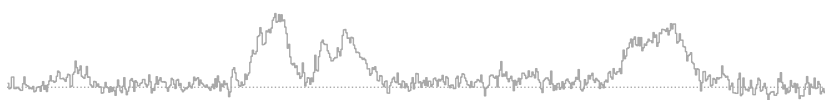
- Roman-Duval, J. et al. (2016). "Distribution and Mass of Diffuse and Dense CO Gas in the Milky Way." In: *ApJ* 818, p. 144.
- Roman-Duval, J. et al. (2009). "Kinematic Distances to Molecular Clouds Identified in the Galactic Ring Survey." In: *ApJ* 699.2, pp. 1153–1170.
- Roman-Duval, J. et al. (2010). "Physical Properties and Galactic Distribution of Molecular Clouds Identified in the Galactic Ring Survey." In: *ApJ* 723.1, pp. 492–507.
- Rosolowsky, E. W. et al. (2008). "Structural Analysis of Molecular Clouds: Dendrograms." In: *ApJ* 679.2, pp. 1338–1351.
- Rosolowsky, E. et al. (2010). "The Bolocam Galactic Plane Survey. II. Catalog of the Image Data." In: *ApJS* 188.1, pp. 123–138.
- Savage, B. D. & J. S. Mathis (1979). "Observed properties of interstellar dust." In: *ARA&A* 17, pp. 73–111.
- Sawada, T. et al. (2012). "Structured Molecular Gas Reveals Galactic Spiral Arms." In: *ApJ* 759.1, p. L26.
- Scalo, J. (1990). "Perception of interstellar structure - Facing complexity." In: *Physical Processes in Fragmentation and Star Formation*. Ed. by R. Capuzzo-Dolcetta et al. Vol. 162. Astrophysics and Space Science Library, pp. 151–176.
- Scalo, J. & B. G. Elmegreen (2004). "Interstellar Turbulence II: Implications and Effects." In: *ARA&A* 42.1, pp. 275–316.
- Schinnerer, E. et al. (2019). "The Gas–Star Formation Cycle in Nearby Star-forming Galaxies. I. Assessment of Multi-scale Variations." In: *ApJ* 887.1, p. 49.
- Schisano, E. et al. (2019). "The Hi-GAL catalogue of dusty filamentary structures in the Galactic Plane." In: *arXiv e-prints*, arXiv:1912.04020.
- Schneider, S. & B. G. Elmegreen (1979). "A catalog of dark globular filaments." In: *ApJS* 41, pp. 87–95.
- Schuller, F. et al. (2017). "SEDIGISM: Structure, excitation, and dynamics of the inner Galactic interstellar medium." In: *A&A* 601, A124.
- Shapiro, P. R. & G. B. Field (1976). "Consequences of a New Hot Component of the Interstellar Medium." In: *ApJ* 205, pp. 762–765.
- Shetty, R. et al. (2012). "The linewidth-size relationship in the dense interstellar medium of the Central Molecular Zone." In: *MNRAS* 425.1, pp. 720–729.
- Shetty, R. et al. (2014). "Interpreting the sub-linear Kennicutt-Schmidt relationship: the case for diffuse molecular gas." In: *MNRAS* 442.3, pp. 2208–2215.
- Simon, R. et al. (2006a). "The Characterization and Galactic Distribution of Infrared Dark Clouds." In: *ApJ* 653.2, pp. 1325–1335.
- Simon, R. et al. (2006b). "A Catalog of Midcourse Space Experiment Infrared Dark Cloud Candidates." In: *ApJ* 639.1, pp. 227–236.
- Smirnov, N. V. (1939). "Estimate of deviation between empirical distribution functions in two independent samples." In: (*Russian*). *Bull. Moscow Univ.* 2, 3–16 (6.1, 6.2).
- Soler, J. D. et al. (2019). "Histogram of oriented gradients: a technique for the study of molecular cloud formation." In: *A&A* 622, A166.
- Solomon, P. M. et al. (1987). "Mass, Luminosity, and Line Width Relations of Galactic Molecular Clouds." In: *ApJ* 319, p. 730.
- Stanimirović, S. & E. G. Zweibel (2018). "Atomic and Ionized Microstructures in the Diffuse Interstellar Medium." In: *ARA&A* 56, pp. 489–540.



- Stanke, T. et al. (2019). "The warm and dense Galaxy - tracing the formation of dense cloud structures out to the Galactic Center." In: *BAAS* 51.3, p. 542.
- Stark, A. A. & J. Brand (1989). "Kinematics of Molecular Clouds. II. New Data on Nearby Giant Molecular Clouds." In: *ApJ* 339, p. 763.
- Straižys, V. et al. (2003). "Interstellar extinction in the direction of the Aquila Rift." In: *A&A* 405, pp. 585–590.
- Stutzki, J. & R. Guesten (1990). "High Spatial Resolution Isotopic CO and CS Observations of M17 SW: The Clumpy Structure of the Molecular Cloud Core." In: *ApJ* 356, p. 513.
- Su, Y. et al. (2019). "The Milky Way Imaging Scroll Painting (MWISP): Project Details and Initial Results from the Galactic Longitudes of 25.°8-49.°7." In: *The Astrophysical Journal Supplement Series* 240, p. 9.
- Sun, J. et al. (2020). "Dynamical Equilibrium in the Molecular ISM in 28 Nearby Star-Forming Galaxies." In: *arXiv e-prints*, arXiv:2002.08964.
- Svoboda, B. E. et al. (2016). "The Bolocam Galactic Plane Survey. XIV. Physical Properties of Massive Starless and Star-forming Clumps." In: *ApJ* 822.2, p. 59.
- Taylor, J. H. & J. M. Cordes (1993). "Pulsar Distances and the Galactic Distribution of Free Electrons." In: *ApJ* 411, p. 674.
- Toomre, A. (1964). "On the gravitational stability of a disk of stars." In: *ApJ* 139, pp. 1217–1238.
- Umemoto, T. et al. (2017). "FOREST unbiased Galactic plane imaging survey with the Nobeyama 45 m telescope (FUGIN). I. Project overview and initial results." In: *PASJ* 69, p. 78.
- Urquhart, J. S. et al. (2014). "ATLASGAL - Complete compact source catalogue: $280^\circ < \ell < 60^\circ$." In: *A&A* 568, A41.
- Urquhart, J. S. et al. (2018). "ATLASGAL - properties of a complete sample of Galactic clumps." In: *MNRAS* 473, pp. 1059–1102.
- VERA collaboration et al. (2020). "The First VERA Astrometry Catalog." In: *arXiv e-prints*, arXiv:2002.03089.
- Vallee, J. P. (1995). "The Milky Way's Spiral Arms Traced by Magnetic Fields, Dust, Gas, and Stars." In: *ApJ* 454, p. 119.
- Vallée, J. P. (2017). "A guided map to the spiral arms in the galactic disk of the Milky Way." In: *The Astronomical Review* 13.3-4, pp. 113–146.
- Wang, K. et al. (2015). "Large-scale filaments associated with Milky Way spiral arms." In: *MNRAS* 450, pp. 4043–4049.
- Wang, Y. et al. (2020). "The HI/OH/Recombination line survey of the inner Milky Way (THOR): data release 2 and H I overview." In: *A&A* 634, A83.
- Weinreb, S. et al. (1963). "Radio Observations of OH in the Interstellar Medium." In: *Nature* 200.4909, pp. 829–831.
- Wenger, T. V. et al. (2018). "Kinematic Distances: A Monte Carlo Method." In: *ApJ* 856.1, p. 52.
- Wiener, M. et al. (2012). "Ammonia from cold high-mass clumps discovered in the inner Galactic disk by the ATLASGAL survey." In: *A&A* 544, A146.
- Williams, J. P. et al. (1994). "Determining Structure in Molecular Clouds." In: *ApJ* 428, p. 693.



- Wilson, B. A. et al. (2005). "A uniform CO survey of the molecular clouds in Orion and Monoceros." In: *A&A* 430, pp. 523–539.
- Wilson, R. W. et al. (1970). "Carbon Monoxide in the Orion Nebula." In: *ApJ* 161, p. L43.
- Wilson, T. L. (1999). "Isotopes in the interstellar medium and circumstellar envelopes." In: *Reports on Progress in Physics* 62.2, pp. 143–185.
- Wilson, T. L. et al. (2014). *Tools of Radio Astronomy*. Springer-Verlag.
- Woosley, S. E. et al. (2002). "The evolution and explosion of massive stars." In: *Reviews of Modern Physics* 74.4, pp. 1015–1071.
- Xu, Y. et al. (2018). "The spiral structure of the Milky Way." In: *Research in Astronomy and Astrophysics* 18.12, p. 146.
- Zhang, B. et al. (2014). "The Parallax of W43: a Massive Star-forming Complex near the Galactic Bar." In: *ApJ* 781.2, p. 89.
- Zhang, M. et al. (2019). "Star-forming content of the giant molecular filaments in the Milky Way." In: *A&A* 622, A52.
- Zhou, C. et al. (2019). "Star formation in IRDC G31.97+0.07." In: *MNRAS* 485, pp. 3334–3351.
- Zucker, C. et al. (2018). "Physical Properties of Large-scale Galactic Filaments." In: *ApJ* 864, p. 153.
- Zucker, C. et al. (2015). "The Skeleton of the Milky Way." In: *ApJ* 815.1, p. 23.
- Zucker, C. et al. (2019). "A Large Catalog of Accurate Distances to Local Molecular Clouds: The Gaia DR2 Edition." In: *ApJ* 879.2, p. 125.
- van Dishoeck, E. F. et al. (1992). "Panel Discussion : the CO/H₂ Abundance Ratio." In: *Astrochemistry of Cosmic Phenomena*. Ed. by P. D. Singh. Vol. 150. IAU Symposium, p. 285.



*Gully Foyle is my name
And Terra is my nation
Deep space is my dwelling place
The stars my destination.*

— Alfred Bester

ACKNOWLEDGMENTS

I would not have been able to write this thesis without the generous help and support of many people. I would like to start by thanking Jouni Kainulainen, Henrik Beuther, and Jonathan Henshaw for their scientific guidance along this journey. Jouni, thank you for your support and giving me the freedom to pursue and work out my own research ideas. Your scientific input and advice was always excellent and spot-on and I am very grateful that you always made time in your schedule when I needed your advice. Henrik, thank you very much for all your help and support throughout these years. It was very reassuring for me to know that you always had an open door for me and would listen to my problems. Thank you for allowing me to take part in your group meetings, for all your helpful contributions and interests in my projects, and for acting as one of the referees for this thesis. Jonny, it was a pleasure to work with you. You were a great moral support throughout my PhD and your contributions and helpful suggestions have been invaluable. I hope we will soon find the time for nice discussions over a couple of beers again.

I would like to thank Christian Fendt for generously agreeing to act as the second referee for this thesis and for organising the excellent IMPRS-HD program. I would also like to thank Friedrich Röpke and Björn-Malte Schäfer for agreeing to be part of the defense committee.

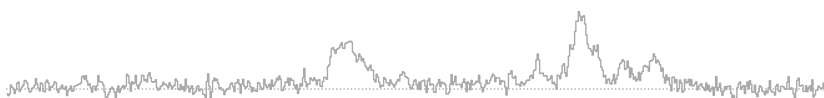
A big thank you to all my co-authors throughout the years, whose detailed reading and precise comments helped to refine and improve my work immensely and changed how I approach new scientific problems for the better. Thanks also to all members of Jouni's and Henrik's group past and present, for the nice scientific atmosphere and interesting discussions throughout the years. Big thanks also to Aida, Asmita, Johnny, Jouni, and Miriam for reading over the thesis and giving me valuable suggestions for improvement.

Next, I would like to thank the people who made my day-to-day life at the institute a pleasure and brightened up my working days. First, all my (extended) Office 225 peeps: I have been lucky in sharing an office with you and it would fill many a page if I were to describe all the fun we had together. Aida, great minds think alike, it was a joy being in the same office as you. I greatly enjoyed our discussions (of which there will be hopefully many more to come), and I will always fondly remember our New York trip. Micah, you became a great buddy, and I hope there is soon an opportunity to discuss rockets and the world over some nice Kwak and Poutine. Miriam, the in-between-work chats with you have always been great and I will miss them. Neven, my K.u.K. (Kuchen und Konditorei) friend, thanks for all the

fun times and tirelessly organising many of our social events. Steffi, my Tesla- and Dino-buddy, you always brightened up the office mood with your visits, I hope we will see each other again soon. Martin (“do I smell/hear/sense coffee?”), your visits to the office were always great fun and your coffee skills are unmatched and were greatly appreciated. Daniele, Diego, Ekatarina, Ismael, Matthias, Mayte: it was a pleasure to have shared the office with all of you. To all my new Elsässer office-peeps, Arianna, Christian, Christoph, Johanna, Josha: even though I haven’t been there for too long I have enjoyed my time with you already immensely, hopefully we have still some fun days coming up (depending on whether Corona allows it).

Victor, my fellow Austrian buddy, the coffee breaks and discussions with you always brightened up my day. Paula (birthday mate!), it was a lot of fun with you and especially that Berlin trip shall be remembered (most delicious brunch ever, however I am still waiting for the Vegan version of *the* Lebanese breakfast). Felix, my neighbour round the corner, keep the jazz alive and remain the cool nice guy you are (also it’s time to check out Thermalbad again). Hector, my funk-and-soul brother, you are a living encyclopaedia for good music, thanks for opening up my musical horizon to the Brazilian classics. To the “Don’t panic”-crew: the pub-quizzes were a helluva lot of fun and our victories shall be remembered (the defeats not so). To my boardgame-peeps (Essen 2019!) – thanks for all the fun evenings and the amazing hours of playing games. To my ARI- and IMPRS peeps, in particular Michael, Sarah, and Marta, it was a lot of fun with you, the 80s nights, *the* Vettters night (need I say more?), and our trips will be fondly remembered. To my friends back in Austria, in particular Lilo and Michi, thanks for being such amazing people, I hope to see you all very soon again.

Finally, I deeply want to thank the most important people of my life. Mama und Papa, danke für eure Unterstützung, ich hoffe es kommt auch weiterhin noch zu vielen Gesprächen über das Universum und die Faszination der Astronomie. Bri, thank you for all your support throughout my life and thanks for always believing in me. I would not be anywhere near where I am today without you, and I shall be forever grateful for what you taught me. To the rest of my family, thank you for always being there when I needed you and your appreciation of and interest in my work. And finally, Asmita, how can I express in words what you mean to me? The fun I have with you, the joy you bring me, and your lovable kindness, where do I even start? There are not enough pages in this world to contain all the thanks and appreciation I have for you – you have made and continue to make me a better man. It is also time to go for some ice cream and watch Jurassic Park again soon, if you ask me.



COLOPHON

This document was typeset using the typographical look-and-feel classicthesis developed by André Miede and Ivo Pletikosić. The style was inspired by Robert Bringhurst's seminal book on typography "*The Elements of Typographic Style*".

Final Version as of April 27, 2020 (classicthesis v4.6).